Control and Readout of High-Dimensional Trapped Ion Qudits

by

Pei Jiang Low

A thesis
presented to the University of Waterloo
in fulfillment of the
thesis requirement for the degree of
Doctor of Philosophy
in
Physics

Waterloo, Ontario, Canada, 2023

Examining Committee Membership

The following served on the Examining Committee for this thesis. The decision of the Examining Committee is by majority vote.

External Examiner:	Boris Blinov Professor, Dept. of Physics, University of Washington
Supervisor(s):	Crystal Senko Associate Professor, Dept. of Physics, University of Waterloo
Internal Member:	Alan Jamison Assistant Professor, Dept. of Physics, University of Waterloo
Internal Member:	Michal Bajcsy Associate Professor, Dept. of Electrical and Computer Engineering, University of Waterloo
Internal-External Member:	Jon Yard Associate Professor, Dept. of Combinatorics and Optimization, Perimeter Institute for Theoretical Physics

Author's Declaration

I hereby declare that I am the sole author of this thesis. This is a true copy of the thesis, including any required final revisions, as accepted by my examiners.

I understand that my thesis may be made electronically available to the public.

Abstract

The trapped ion platform is one of the quantum computing platforms that is at the forefront for realizing large-scale quantum information processing, which is crucial for practically actualizing the advantages of quantum algorithms. Scaling up the trapped ion quantum computing architecture remains a challenge. We explore an alternative avenue in a trapped ion system for increasing the computational Hilbert space other than trapping more ions, which is by increasing the qudit dimension of an ion. Our ion of choice is $^{137}Ba^{+}$, which has a rich energy level structure for high-dimensional qudit encoding. Utilizing the additional energy states found in $^{137}Ba^{+}$ also comes with non-trivial complexities that require careful considerations, which we have solved and report in this thesis. We report on a single-shot state measurement protocol which allows qudit encoding in $^{137}Ba^{+}$ of up to 25 levels, and demonstrate state preparation and measurement of up to 13 levels, which is unprecedented in a trapped ion system.

This thesis is written with hopes that it is complete enough as a guide for readers who wants to work with trapped barium ions. The bring up and calibration methods of equipment parameters are reported in this thesis, along with detailed studies of some experimental observations that may not be intuitively clear. Ion loading via laser ablation is also explored in this work, which is a less commonly used ion loading method. To more effectively load the less abundant ^{137}Ba isotope from a natural abundance source, we employed the resonance enhanced multiphoton ionization process and report on the improved isotope selectivity. Although not directly related to trapped ion quantum information processing, a cost-effective beam pointing stabilization solution that we have developed is presented, which we hope to be helpful to any laboratories with free-space laser beams.

Acknowledgements

Throughout my PhD course in Physics, I had the pleasure of working with many wonderful people. I would first like to thank Crystal Senko for being an excellent advisor. In work and research, Crystal has been open to our suggestions and new ideas, while also being helpful and participating intently when we bring up problems to be solved. She strikes a perfect balance of letting us explore and providing guidance, which is all I could ask for from an advisor. I would also like to thank my advisory committee members, Alan Jamison, Jon Yard, and Michal Bajcsy, who provided helpful feedback on my work that often sparked new ideas for me to try.

My fellow first-generation graduate student and also a friend, Brendan White, has been an excellent lab partner, whom I worked closely with on the works discussed in this thesis. Also special thanks to Rich Rademacher, who was our electronics expert and the electronic systems built by him are wonderful legacies in the laboratory. It has also been a pleasure working with Matthew Day, from whom I had the opportunity to work with on a theoretical noise analysis project, in addition to laboratory work. I learned filter function theory through this project he pioneered, which ends up being useful in many applications, including for error analysis presented in this work. Also thanks to Noah Greenberg, who has always been jovial and helpful in general. Even though having just joined us, Nicholas Zutt has also been a helpful laboratory member and helped review our qudit SPAM paper together with Noah. Although it was brief, I would also like to thank Yvette De Sereville for the time we worked together in the laboratory.

On the active beam stabilizer project, I had the greatest pleasure working with Alexander Gonczaruk, who had been a talented and hardworking undergraduate coop student. Despite having to work remotely due to COVID-19, we had a productive time developing and learning at the same time on coding structures that we were unfamiliar with. Special thanks also goes to Sakshee Patil, who carried out the performance test on the beam stabilizer system.

Being half a globe away from their son/brother must not have easy, especially during COVID-19 times. I want to thank my parents, Low Jhon Iyh and Tan Chon Lew, as well as my brothers, Low Pei Liang, Low Pei Heng and Low Pei Chen, who have been supportive and a great moral support throughout my course. Finally, I have to thank my loving wife, for making the sacrifice to be far away from her family and friends to be with me for my graduate studies, and keeping my stomach full.

Dedication

Dedicated to my wife and family.

Table of Contents

Examining Committee ii

Author's Declaration iii

Abstract iv

Acknowledgements v

Dedication vi

List of Figures xi

List of Tables xv

1 Introduction 1

2 Paul Trap Setup 5

2.1 Four-rod Trap and Vacuum Chamber Setup 5

2.2 Imaging System 7

3 Laser Ablation Barium Ion Loading 9

3.1 Ba and Ba^+ Energy Level Structures 9

3.2 Lasers and Optical Setup for Ion Loading 12

3.2.1 Ion Loading Beam Alignments . . . 15
3.2.2 Ablation Pulse Fluence Calibration . . . 17
3.2.3 Laser Frequency Calibrations for Ion Loading . . . 20
3.3 Higher Laser Intensities Do Not (Necessarily) Lead to Higher Barium Ion Fluorescence Rates . . . 21
3.3.1 Three-level Theoretical Toy Model for Studying Barium Ion Fluorescence Rates . . . 22
3.3.2 Theoretical Simulations of P State Populations of $^{138}Ba^{+}$ and $^{137}Ba^{+}$ 25
3.4 Improved Isotope Selectivity for Ba^{+} Ion Loading . . . 33
3.5 Direct-Ion Loading of Barium Ions . . . 39
3.6 Discussion and Concluding Remarks . . . 41

4 Trapped Ba^{+} Ions As Qudits 43
4.1 Conceptual Control of Ba^{+} $6S_{1/2}$ and $5D_{5/2}$ Energy Levels . . . 44
4.1.1 The Hyperfine $|F, m_F\rangle$ States are Bad Assumptions of $^{137}Ba^{+}$ $5D_{5/2}$ Energy Eigenstates . . . 45
4.1.2 Quadrupole Transitions . . . 48
4.1.3 Relative Transition Strengths in the Intermediate-Field Zeeman Effect 52
4.1.4 Resolved Sideband Cooling . . . 56
4.1.5 Modulation of Transition Frequencies From Trapped Ion Excess Micromotion . . . 58
4.2 Trap Setup for Qudit Experiments . . . 59
4.3 Lasers and Optical Setup for Control of Ba^{+} $5D_{5/2}$ States . . . 60
4.3.1 Initial Laser Beam Alignments for Ba^{+} Control of $5D_{5/2}$ States . . . 62
4.3.2 Initial Frequency Calibration for 1762 nm and 614 nm Lasers . . . 64
4.4 Spectroscopy of $6S_{1/2} \leftrightarrow 5D_{5/2}$ Transitions . . . 69
4.5 Actualization of Utilities of Ba^{+} $6S_{1/2} \leftrightarrow 5D_{5/2}$ Transitions . . . 74
4.5.1 Actualization of 1762 nm Resolved Motional Sideband Cooling . . . 74

4.5.2 1762 nm Transitions for Excess Micromotion Detection and Compensation . . . 78
4.6 State Preparation and Measurement (SPAM) of Trapped Ba^+ Ion Qudits . 80
4.6.1 Qudit Encoding and SPAM Protocol . . . 81
4.6.2 Hardware and Laser Setup for SPAM . . . 84
4.6.3 Optical Pump Fidelity is Dependent on Laser Intensity and Frequency 88
4.6.4 Estimation of $6S_{1/2} \leftrightarrow 5D_{5/2}$ Single π-pulse Transition Errors . . . 89
4.6.5 Efficient Calibration Protocols for 1762 nm Laser Frequencies and Pulse Times . . . 94
4.6.6 SPAM Results and Discussions . . . 98
4.6.7 Concluding Remarks and Outlook . . . 106

5 Cost Effective Beam Stabilizer 108
5.1 Concept and Idea . . . 109
5.2 Stabilization Demonstration . . . 111
5.3 Program Overview . . . 113
5.4 Program Flow - Initialization . . . 114
5.5 Image Processing . . . 116
5.6 Motor Movement . . . 118
5.6.1 Manual Mode . . . 118
5.6.2 Automatic Mode . . . 120
5.7 Additional Details . . . 123
5.7.1 Updating Windows-Pi Shared Variables . . . 124
5.7.2 Emergency Stop for Motors . . . 125
5.8 Other Perks and Potential Developments . . . 126

References 127

APPENDICES 134

A Two-level Transition Equilibrium State **135**

B Writing Your Own Clebsch-Gordan Coefficients Generator **136**

C Script For Detecting the Number of Bright Ions in a 2D Image **139**

D Estimation of Four-rod RF Voltage Amplitude **143**

E $^{133}Ba^{+}$ Loading Attempts **144**

E.1 Loading Attempts With the Low-volume Target 145

E.2 Observation of other excited-state neutral species 149

F Evolution of $^{137}Ba^{+}$ Ion $5D_{5/2}$ Level Energy Eigenstates with Magnetic Field Strengths **153**

G Four-Level Simulations for Studying Fluorescence Flip-Flopping **157**

H A Dynamic Method for Determining Bright/Dark State Photon Count Threshold **159**

I 6-Level Qudit SPAM with $^{138}Ba^{+}$ **161**

J Alternative Interpretation of SPAM Error **163**

K Frequency Resolution Limitation from Finite AWG Memory **165**

L Filter Function Construction for Magnetic Field Noise **167**

List of Figures

2.1 Illustrations of ion trap and vacuum chamber setup. 6

2.2 An illustration of the imaging system. 8

3.1 Barium energy levels. 10

3.2 Illustration of laser setups relevant for ion loading. 13

3.3 Optical setup of the beam paths at the ion trap. 14

3.4 $BaCl_2$ target with a seemingly indented spot highlighted by the red circle. . 18

3.5 Neutral barium and ionic barium fluorescence against pulse fluence. 19

3.6 Three-state toy model simulations of the P state population against laser frequency detunings. 25

3.7 Simulations of $^{138}Ba^+$ and $^{137}Ba^+$ P state populations against laser frequency detunings. 28

3.8 Color maps of empirically collected fluorescence rates against 493 nm and 650 nm carrier laser frequencies of $^{138}Ba^+$ and $^{137}Ba^+$ 29

3.9 Color maps of the laser intensity scan simulation results for $^{138}Ba^+$ and $^{137}Ba^+$. 30

3.10 Color maps of P state population against laser polarizations for $^{138}Ba^+$ and $^{137}Ba^+$. 31

3.11 Spectroscopy of neutral barium fluorescence from the ablated flux. 34

3.12 Aggregated $^{138}Ba^+$ ion chain images ion chain images. 36

3.13 Aggregated $^{137}Ba^+$ ion chain images at low pulse fluence. 37

3.14 Aggregated $^{137}Ba^+$ ion chain images at high pulse fluence. 38

3.15 Trapping probability of $^{138}Ba^+$ using the direct-ion loading method. 40

4.1 Simulated $6S_{1/2} \leftrightarrow 5D_{5/2}$ transition energies and a representative plot of the $5D_{5/2}$ energy eigenstates with increasing magnetic field strengths. 47

4.2 Empirical and theoretically estimated non-zero transition strengths to the $5D_{5/2}$ states from the $|6S_{1/2}, \tilde{F} = 2, m_{\tilde{F}} = 2\rangle$ state, relative to the reduced transition matrix element. 56

4.3 An illustration of the setup for the 1762 nm and 614 nm lasers. 60

4.4 An illustration of an example of the 1762 nm laser frequencies sent to the ion trap and the PDH locking system. 61

4.5 Fluorescence flip-flopping of a $^{138}Ba^+$ ion when the 493 nm, 650 nm, and 1762 nm lasers are turned on 65

4.6 Repump probability against 614 nm laser frequencies. 68

4.7 Pulse sequence for preparing a Ba^+ ion in the $6S_{1/2}$ ground state with the highest magnetic quantum number, and then driving a $6S_{1/2} \leftrightarrow 5D_{5/2}$ transition. 69

4.8 Dark state probability of a $^{138}Ba^+$ and a $^{137}Ba^+$ ion against the 1762 nm driving laser frequency. 70

4.9 Shifted numerically simulated $^{137}Ba^+$ transition frequencies. 72

4.10 Rabi cycling of transitions to the $5D_{5/2}$ states from the $|6S_{1/2}, m = 1/2\rangle$ state in $^{138}Ba^+$. 73

4.11 The dark state probability of $^{138}Ba^+$ against the laser frequency shift from a $\Delta m = 0$ carrier transition frequency. 74

4.12 Pulse sequence for resolved sideband cooling using 1762 nm laser transitions, followed by a coherent 1762 nm transition experiment and a fluorescence readout. 75

4.13 Dark state probability against 1762 nm pulse times with and without cooling sequence. 76

4.14 Dark state probability against 1762 nm laser pulse times, driven at a laser frequency of $\omega_{\Delta m=-1} - \Omega_{RF}$. 78

4.15 Illustration of voltages sent to the four-rod electrodes. 79

4.16 Qudit encoding schemes for $^{137}Ba^+$. 83

4.17 Simplified pulse sequence for one SPAM experiment. 84

4.18 Detailed pulse sequence for one SPAM experiment. 85
4.19 Dark state probability against the 614 nm repump laser frequency. 87
4.20 Illustration and simulation of optical pumping of a four-level toy model. . . 89
4.21 A representative plot of a Rabi flopping experiment for estimating the singple π-pulse transition error. 91
4.22 Rabi cycles of the transition from the $|6S_{1/2}, \tilde{F} = 2, m_{\tilde{F}} = 2\rangle$ state to the $\tilde{F} = 1$ and $\tilde{F} = 2$ states in the $5D_{5/2}$ level. 92
4.23 Rabi cycles of the transition from the $|6S_{1/2}, \tilde{F} = 2, m_{\tilde{F}} = 2\rangle$ state to the $\tilde{F} = 3$ and $\tilde{F} = 4$ states in the $5D_{5/2}$ level. 93
4.24 Plots of transition probability against EOM frequency and shifted transition frequencies against Δf. 96
4.25 Post-selected measurement probability of the 13-level qudit SPAM experiment. 98
4.26 Model noise functional form and plot of the post-selected SPAM error for each prepared state against $\kappa^2\tau_\pi^2$ 102
4.27 Scaling of average SPAM fidelity with qudit dimension with optimal choices of the encoded states and with poor choices. 104

5.1 Schematic and photograph of the cost-effective stabilizer. 109
5.2 Coupling of stepper motors to mirror mounts using custom designed parts. 110
5.3 Graphical user interface (GUI) of our custom written program. 111
5.4 Power output from an optical fiber in a fiber coupler setup. 112
5.5 Schematic of the basic setup of beam stabilizer setup. 113
5.6 Program flow of when the beam stabilization software is first started. . . . 114
5.7 Program flow for processing image obtained from the camera. 116
5.8 Program flow for moving the motors using the software in "Manual Mode". 119
5.9 Program flow of the software in "Automatic Mode" 121
5.10 Program loop for moving a stepper motor. 123
5.11 Threads for sharing data between machines. 125

C.1 Automatic detection of number of ions from a 2D image. 141

E.1 (a) An illustration of the vacuum chamber with a ^{133}Ba enriched salt target. (b) A photograph of the low-volume target. 145

E.2 Neutral barium fluorescence from the low-volume target, sweeping the ablation laser along a line on the target. 146

E.3 Trapping probability of $^{138}Ba^{+}$ from the low-volume target using the direction loading method. 148

E.4 Time-resolved light detection after ablating the low-volume target with a pulse fluence of $3.84\,J/cm^2$. 150

E.5 Time-resolved light detection after ablating the high-volume target with a pulse fluence of $3.84\,J/cm^2$. 151

F.1 Numerical estimations of the $^{137}Ba^{+}$ $\tilde{F} = 1$ and $\tilde{F} = 2$ energy eigenstates in the $5D_{5/2}$ level, expressed in the $|F, m_F\rangle$ basis. 154

F.2 Numerical estimations of the $^{137}Ba^{+}$ $\tilde{F} = 3$ energy eigenstates in the $5D_{5/2}$ level, expressed in the $|F, m_F\rangle$ basis. 155

F.3 Numerical estimations of the $^{137}Ba^{+}$ $\tilde{F} = 4$ energy eigenstates in the $5D_{5/2}$ level, expressed in the $|F, m_F\rangle$ basis. 156

G.1 P state population against the simulated 1762 nm laser detuning in a 4-level toy model. 158

H.1 Dynamic determination of bright/dark state threshold. 160

I.1 6-level qudit SPAM results. (a) The raw fidelities. (b) Post selected fidelities. 162

List of Tables

3.1 Natural abundance of barium isotopes and the first dipole excitation transition frequency shifts. 33

4.1 Relative transition strength factors for $6S_{1/2} \leftrightarrow 5D_{5/2}$ transitions with $\theta_k = 45°$ and $\theta_p = 58°$ at a magnetic field strength of $B_e = 8.35\,\mathrm{G}$ of $^{137}\mathrm{Ba}^{+}$. . . 55

4.2 Examples of measurement outcomes. 82

4.3 Post-selected measurement probability of each prepared state. 99

4.4 Raw measurement probability of each prepared state. 99

4.5 Summary of the encoded states and their corresponding physical atomic states, parameters relevant to the SPAM experiments and post-selected SPAM errors. 100

B.1 An example of Clebsch-Gordan coefficients search table, with the coefficients to be computed. 137

J.1 Raw measurement probability of each prepared state. 164

J.2 Post-selected measurement probability of each prepared state. 164

Chapter 1

Introduction

The utilities of quantum nature of things have been theoretically studied and quantum algorithms have been developed that are shown to be more efficient compared to classical algorithms at solving certain problems, a well known example being Shor's algorithm [1]. These algorithms tackle searching problems by exploiting the ability of a quantum system to be in a superposition of states, and with clever control, they can be made to speed up computational time. The theoretical speed up in quantum algorithms comes in the form of a much lower number of increase in computational gates required for an increase in the computational space compared to classical computing. Therefore, to actualize the practical advantages of quantum algorithms over classical ones, it is imperative for a quantum computer to be able to process information in a large computational space.

Physical systems with controllable quantum states are potential candidates to be used as a quantum computer. Examples include atomic energy states, quantized states of superconducting circuits and polarization states of photons [2]. In order to decide whether a physical platform is a good candidate, in layman's terms, it has to be reliable, fast and as alluded earlier, able to process large scale information. Reliability means that a quantum computer has to be able to produce correct answers consistently, which translates to requiring high fidelities of the quantum operations. The speed of the quantum computer discussed here is not the algorithmic speed, as they run the same quantum algorithms, but the physical speed the computational gates can be performed. In the trapped ion platform, individual ions are trapped in a vacuum with a generated electric field pseudopotential well, typically in a linear chain, and a basic unit of quantum information is encoded in the electronic energy states of an ion [3, 4]. The trapped ion platform is at the forefront of quantum computing performance in terms of the fidelity of computing operations [5, 4, 6], which exceeds the requirement for fault tolerant quantum computing [7].

Another appealing feature of the trapped ion platform is the guarantee that each quantum information carrier is exactly the same to another by nature. This mitigates the problem of error from non-homogeneity of each quantum carrier or the increasing complexities of hardware calibrations required when scaling up the system [8]. However, trapped ion systems face other challenges for scaling up the computational space. An additional quantum information carrier has to be able to have some controllable quantum entanglement with the original system in order to increase the computational space [9]. In a trapped ion system, entanglement between ions is conventionally achieved via shared motional modes due to Coulomb interactions in an ion chain [10, 11], typically driven via laser-ion interactions [5, 12]. A straightforward way to increase the computational space of a trapped ion quantum computer is to add more ions into the chain. As more ions are added into a chain, the total mass of the chain is heavier and lengthens the time required to complete the entangling operations due to limits on laser powers, putting a speed limit on the entangling gates as the computational space scales up [4]. A proposed idea is to split the total number of ions into multiple localized trapped ion chains, and entanglements between ions at different trap regions are done by physically transporting them between trap regions [13]. Another idea which allows entanglement between ions in separate ion traps is via photonic interconnects [14]. Recent developments with laser-free entanglement of trapped ions [15] may also help with the issue of the entanglement gate speed limit for larger ion chains.

A less explored but emerging method for scaling up the computational space of a trapped ion system is to increase the amount of information encoded per ion. Typically, two quantum states are encoded in a quantum information carrier, called a qubit. In a trapped ion, it is not uncommon to find more than two electronic states with long coherence times. The reason for the choice of using only two of the electronic states for encoding are typically to work with electronic states with magnetically insensitive transitions for minimizing errors, called the clock states [5, 16, 17, 18]. Methods to minimize magnetic field noise have been demonstrated [19, 20], and the error from this source is predicted to be made negligible compared to other error sources [21]. Thus, we anticipate that magnetic field noise is not a limiting factor for encoding quantum computational states in more electronic energy levels. By choosing to encode more than two levels in a single information carrier, it is called a qudit, where the d in qudit stands for a general dimension. The progress towards making use of additional atomic energy states has been ongoing [22, 23, 24, 25], and is gaining traction in recent years [12, 26, 27, 28]. Among them is a demonstration of a 5-level qudit-based universal quantum computer, which can be scaled up to 7 levels with $^{40}Ca^{+}$ [12]. Our work focuses on actualizing high-dimensional qudit quantum computers, and we choose an ion species that is rich in the number of energy levels

available for quantum computational state encoding, which is $^{137}Ba^{+}$ [29, 21]. In this work, we show that a 25-level qudit can be encoded in a $^{137}Ba^{+}$ ion, with fully distinguishable single-shot readout, which is a significant increase in the qudit dimension from the previous record [12]. Experimentally, we actualize state preparation and measurement (SPAM) of a 13-level qudit with $^{137}Ba^{+}$. Given a limited number of trapped ions, there is still a limit to the increase in computational space once we use up all the available energy states for encoding for a single ion. However, the qudit encoding approach is not mutually exclusive with efforts to increase more controllable trapped ions, and we anticipate that qudit work can be combined with the aforementioned efforts [13, 14] to massively scale up the computational space. Other than being an avenue for scaling up the computational space, a qudit architecture also provides other benefits such as a more relaxed quantum error correction threshold [30, 31, 32, 33, 34], straightforward quantum simulations for higher spin systems [23, 35], and more efficient qubit gates [36, 37], which serve as additional motivations to pursue this research direction.

The first step to doing any quantum computation with trapped ion is of course, to trap an ion. A common way of loading an ion into an ion trap is via Joule heating of a target in its elemental form using an oven [29, 38, 39, 40, 41, 42, 43, 44, 45]. Here, we explore a less common method for loading barium ions, which is via laser ablation of a target source of the ion to be trapped in its compound form [18, 46, 47]. This method comes with several advantages over the oven heating method, which will be discussed in this thesis. Our main barium isotope of interest, $^{137}Ba^{+}$, has a natural isotopic abundance of 11.2% [48]. In order to have improved isotopic selectivity for barium ion loading, we employ a method known to be useful, which is the two-photon resonance enhanced multiphoton ionization method (REMPI) [38]. The performance of the ion loading selectivity is also characterized in this work, with a robust testing method that we have developed.

This thesis is written in hopes of it being complete enough to be a useful reading material for readers intending to work with or is working with trapped barium ions. I detail the process of bringing up a trapped ion setup for trapping barium ions, starting from the point where the equipment parameters are not calibrated. Any experimental observations that are not intuitively clear or counter-intuitive are also studied and documented in this thesis. Chapter 2 gives a summarized description of the ion trap setup, with the details being published in my previous MSc. thesis [49]. Chapter 3 details the barium ion loading bring up techniques, characterizations of ion loading via laser ablation and performance of isotope-selectivity. Parts of this work in Chapter 3 are published in Ref. [50]. Chapter 4 details the work in actualizing a 13-level qudit control and readout with $^{137}Ba^{+}$, and parts of the work are in preparation to be published as an article [51]. Over the course of my graduate research work in this laboratory, we have engineered many solutions to tackle a

number of issues that surfaced. One of the solutions that we have come up with deals with beam pointing drifts of lasers in a cost-effective manner compared to commercial solutions. We detail the technicalities of this solution in Chapter 5, which we believe would be useful for any laboratory using lasers in free space.

Chapter 2

Paul Trap Setup

The first step to any trapped ion experiments is obviously the ability to trap and detect an ion. Assuming that a way to generate ions at the desired trap location has been figured out (which will be discussed in Chapter 3), the following criteria are needed for an ion trap setup. First, a method to generate an electric field (pseudo)potential is needed to keep an ion trapped in place. Second, the trap has to be in a vacuum environment to minimize collisions of particles with a trapped ion. Third, we need a way to detect or "see" an ion that we have trapped. Most of the work to satisfy these criteria were done during my Master's course in the same laboratory. In this chapter for this thesis, I give a sufficiently complete and updated description of the setup for the reader's general comprehension of the system. For further details of the buildup, I refer the reader to my MSc. thesis [49].

2.1 Four-rod Trap and Vacuum Chamber Setup

We use a four-rod trap with dimensions and voltage setup as shown in Fig. 2.1a. Oscillating voltages at a radio-frequency (RF) of Ω_{RF} and an amplitude of V_{RF} are sent to the four rod electrodes, where one diagonal pair is at a phase π-shifted from the other pair, to generate confining electric pseudopotential in the radial direction. A static (or DC for direct current) voltage of V_S is applied to one pair of the rod electrodes in order to break the ion secular motion degeneracy in the radial plane. For axial confinement, static voltages of V_{N1} and V_{N2} are applied to the two needle electrodes. This generates an electric field that traps ions in a linear chain, commonly called a Paul trap in honor of the inventor of this trapping mechanism, Wolfgang Paul [52]. The ion trapping theory in a Paul trap is described in my MSc. thesis [49].

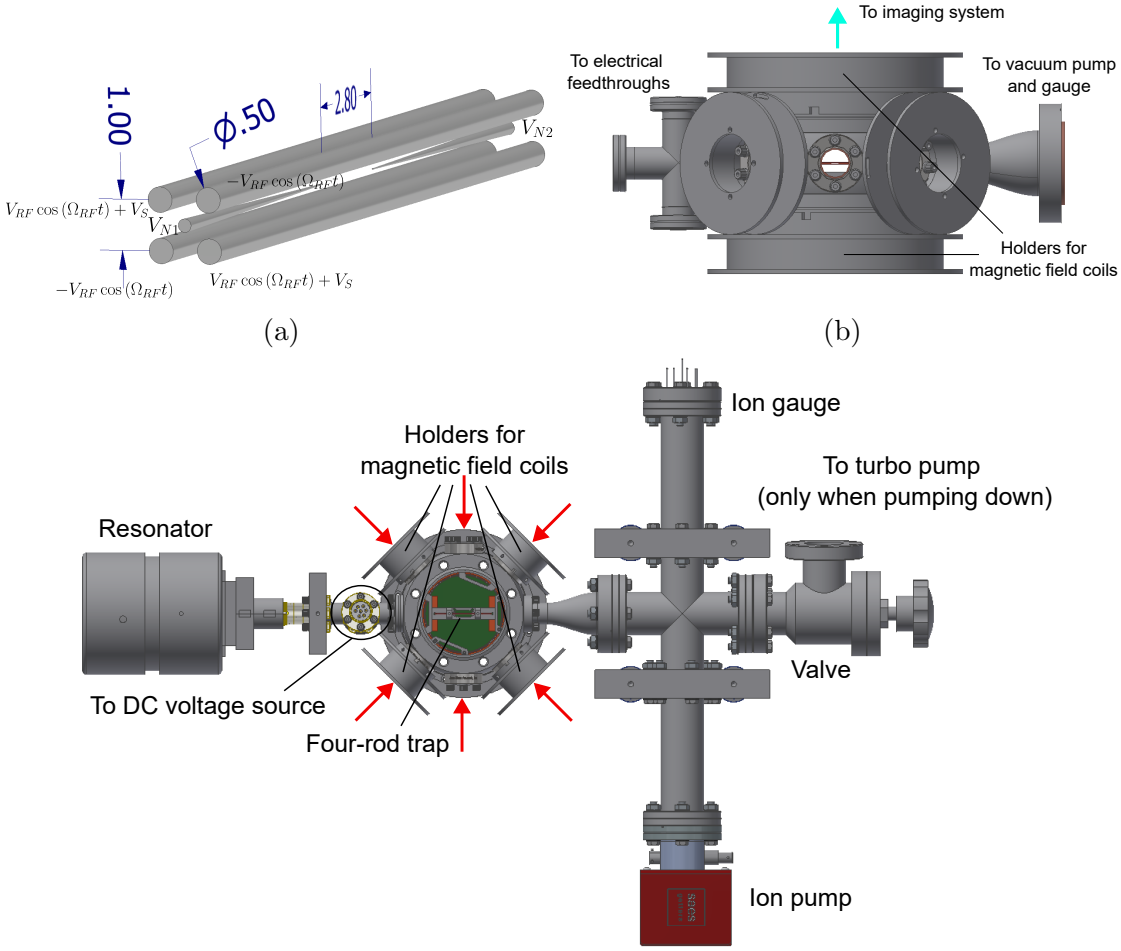

Figure 2.1: (a) An illustration of the four-rod trap used in this work. The units of the dimensions are in millimeters. The lengths of the electrodes in this illustration are truncated to show the critical dimensions close to the trap centre with clarity. A total of six tungsten electrodes are used in the setup, four rods and two needles. The actual lengths of the four rod electrodes are 50 mm. (b) An illustration of the side view of the vacuum chamber setup for our four-rod trap. The four-rod trap is placed at the centre of a 4.5-inch cylindrical vacuum chamber with eight 0.75-inch ports on the sides arranged in a regular octagonal arrangement, with two 3-inch ports at the top and bottom. The electrodes of the trap are visible through the centre viewport in this illustration. (b) An illustration of the top view of the full vacuum chamber setup for our four-rod trap. The top viewport is made invisible to show the internals of the vacuum chamber. Red arrows indicate viewports for laser access.

The trap is housed in an octogonal vacuum chamber, which is pumped down and kept at an air pressure of $\sim 10^{-10}$ mbar as shown in Figs. 2.1b and 2.1c. The top viewport is used for collecting fluorescent light from ions to the imaging system, which is discussed in more detail in Section 2.2. The left port of the cylindrical vacuum chamber is used for electrical connections of the RF and DC voltage sources to the trap electrodes using a flexible printed circuit (FPC). A helical resonator is built to have a resonance at $\Omega_{RF} = 20.772\,\text{MHz}$. For more details on the construction of the helical resonator, the DC voltages sources for the trap electrodes, and how they are connected to the trap electrodes, please see my MSc. thesis at Ref. [49]. The right port is connected to vacuum pump(s) and an ion gauge. Magnetic field coil holders are attached to the diagonal side viewports and also the large vertical viewports of the vacuum chamber. Copper coils are wound around this holders, functioning as electromagnets when currents are passed through them, allowing full directional control of a static magnetic field at the ion position. A non-zero magnetic field strength is required at the ion position in order to break the degeneracy of the atomic states, which is crucial for suppressing coherent dark states [53] so that the ions are visible when driven with lasers (laser fluorescence protocol discussed in Chapter 3) and for quantum computing applications in general (see Chapter 4).

2.2 Imaging System

With an ion trapped, and fluorescing (fluorescence protocol discussed in Chapter 3), we need a setup to collect the fluorescence to image the ion, which is discussed in this section. Figure 2.2 shows the updated setup of the imaging system since the first buildup as detailed in Ref. [49]. The imaging objective is updated to a custom built 1-inch objective with a numerical aperture (NA) of 0.2623. Everything else are still the same as the version in Ref. [49]. The imaging objective is mounted on a three-dimensional translation stage and can freely move unrestricted by the other optical components. The color filter can be freely switched out to select the wavelengths to be imaged. During normal operations, a color filter that allows wavelengths of 493 nm and 554 nm to pass through is put in place. A motorized flip mirror allows us to direct the fluorescent light to a photomultiplier tube (PMT) detector for more sensitive detection of photon counts without spatial resolution, or to a charge-coupled device (CCD) camera which spatially resolves the image. To further optimize the setup, the positions of the CCD camera and the PMT detector can be switched, which I recommend to any reader intending to replicate this setup. This is because we have seen that the position of the ion that is imaged on the CCD camera shifts in the order of pixels as the motorized flip mirror is toggled off and on, which indicates that

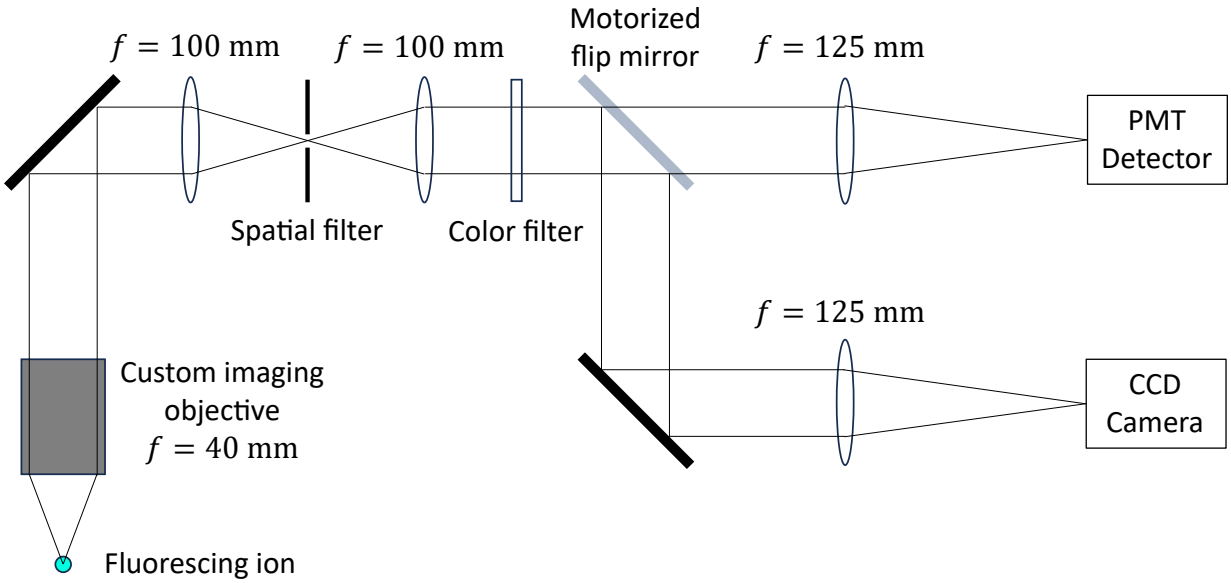

Figure 2.2: An illustration of the imaging system. The dimensions are not drawn to scale.

there is significant enough angular imprecision whenever the flip mirror is toggled. This issue should be resolved with the CCD camera placed in the beam path that is independent of the flip mirror.

Chapter 3

Laser Ablation Barium Ion Loading

In this chapter, I discuss the methods we employed to produce Ba^+ ions from a $BaCl_2$ salt source, and subsequently trap them. Our protocols also come with the advantage of having improved isotope-selectivity for ion loading, which is useful for trapping less abundant isotopes from natural samples.

First, we need to understand the relevant energy levels of Ba and Ba^+ for our protocols, which leads to knowing the laser controls that we need for this work. I describe the details of the laser control setup, and systematic methods to narrow down laser parameters and alignments, starting from a point where all laser parameters and alignments are uncalibrated. This is in hopes that the details are helpful to any readers intending to replicate our work or work with trapped barium ions in general. With our protocols, we demonstrate and characterize improved isotoped-selectivity with a robust testing method that we have developed. An alternative loading method, using direct-ion loading, is also presented in this thesis, which is not isotope-selective, but has a higher loading rate and can be useful for troubleshooting the setup. Parts of this chapter are adapted from Ref. [50].

3.1 Ba and Ba^+ Energy Level Structures

With high-enough pulse fluence, a laser pulse sent to a source target can produce neutral atoms and ejects them from the target [18, 47, 54]. As the atoms reach the centre of the ion trap, they need to be ionized in order to "see" and respond to the electric field pseudopotential well produced by the electrodes in order to be trapped. We ionize the barium atoms via laser excitations. A $6S$ ground-state Ba atom can be driven to the $6P$

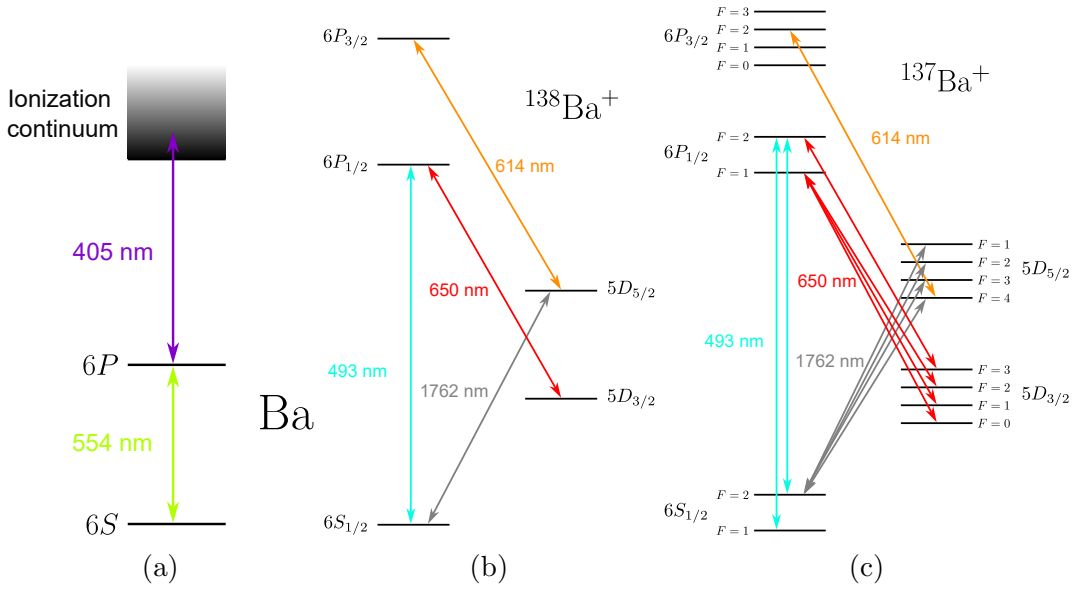

Figure 3.1: (a) Relevant energy levels and laser frequencies for the REMPI protocol used in this work. (b) and (c) Relevant energy levels and laser frequencies of $^{138}Ba^{+}$ and $^{137}Ba^{+}$ used in this work. The 614 nm, 1762 nm lasers and their connected energy levels are not relevant to the discussion in this chapter and will be discussed in Chapter 4.

excited state with a 554 nm laser. This $6P$ excited state is at an energy deficit corresponding to a wavelength of 417 nm from the ionization continuum [55]. Thus, by sending a 554 nm laser and another laser with wavelength < 417 nm (which is 405 nm in this work) simultaneously, a ground-state Ba atom can be ionized via a two-step resonance-enhanced multiphoton ionization (REMPI) process (see Fig. 3.1a). If the ionized barium has a lower kinetic energy than the pseudopotential barrier of the Paul trap, it is trapped.

To be able to detect an ion being in the trap, we need the ion to be giving out light. We make use of the $6P_{1/2}$ excited state of a Ba^+ ion as shown in Figs. 3.1b and 3.1c for this purpose. A Ba^+ ion in the $6P_{1/2}$ state spontaneously decays to the $6S_{1/2}$ ground state 75% of the time, emitting a 493 nm wavelength photon in a random direction. To keep a steady population in the $6P_{1/2}$ level, a 493 nm laser is used to drive the $6S_{1/2} \leftrightarrow 6P_{1/2}$ transition. Since the spontaneous decay rate from the $6P_{1/2}$ level to the $6S_{1/2}$ level is fast, at $95.3\,\mu s^{-1}$ [56], it produces sufficient fluorescence for practical experimental detection, where the fluorescence rate is given by

$$R = \rho_P \gamma_S, \tag{3.1}$$

where ρ_P is the time-averaged population in the $6P_{1/2}$ level and γ_S is the spontaneous decay rate into the $6S_{1/2}$ level. We have thus far ignored another decay path from the $6P_{1/2}$ level, which is to the $5D_{3/2}$ level at a probability of 25%. The $5D_{3/2}$ level has a long decay time of ~ 82 s [57, 29]. Thus, the ion would stop fluorescing once this event occurs. To actually keep a sufficiently-large time-averaged steady state in the $6P_{1/2}$ level, a 650 nm laser which drives the population in the $5D_{3/2}$ level back to the $6P_{1/2}$ level is required.

Freshly trapped ions typically have high kinetic energies, and require cooling down in order to crystallize to an ion chain lattice. The 493 nm and 650 nm transitions also function as Doppler cooling lasers for this purpose. This is done by slightly red-detuning (in the order of 10 MHz) the 493 nm and 650 nm laser frequencies from the transition resonance and sending the lasers to the ions from an angle which addresses all three principal axes of motion.

$^{138}Ba^+$ does not have hyperfine splitting within each J electron angular momentum level as it has zero nuclear spin. Zeeman splittings from typical values of magnetic field strength, which is in the order of 1 G [6, 12, 16, 18], are in the order of 1 MHz. Compared to the transition linewidth of the $6P_{1/2}$ level of ~ 20 MHz, Zeeman energy splittings are small enough such that the $6S_{1/2} \leftrightarrow 6P_{1/2}$ and $5D_{3/2} \leftrightarrow 6P_{1/2}$ transitions each only need a single laser frequency to be able to drive all the states. In contrast, $^{137}Ba^+$ has a nuclear spin of $I = \frac{3}{2}$, which leads to large enough (> 20 MHz) hyperfine energy level splittings to necessitate multiple 493 nm and 650 nm laser frequencies, as shown in Fig. 3.1c. The

choice of $^{137}Ba^{+}$ transitions to drive in order to have fluorescence is not unique, as long as all $6S_{1/2}$ and $5D_{3/2}$ hyperfine levels are driven to any of the $6P_{1/2}$ levels. Our choice of the 493 nm frequencies is to enable optical pumping with a σ_{+}-polarized light of this laser, which will be relevant in Chapter 4 and discussed further in that chapter. Our choice of the 650 nm frequencies will be elaborated in the next section.

3.2 Lasers and Optical Setup for Ion Loading

Fig. 3.2 shows the setup of the apparatus relevant to laser controls required for ion trapping. The resonant transitions between energy levels of barium atoms/ions have finite linewidths and the lasers driving them require precise frequency control. Thus, these lasers, which are the 493 nm, 554 nm and 650 nm, have 1% light picked off to a wavemeter calibrated to the wavelengths of a helium-neon (HeNe) laser, which reads out the laser frequencies using a Fizeau interferometer and feeds back to the piezoelectric actuators of the diffraction gratings inside the laser heads to lock the laser frequencies to our desired set points. Acousto-optic modulators (AOMs) are used for fast switching (in the order of tens of nanoseconds) of the 493 nm and 650 nm lasers, which is required for quantum computing experiments (see Chapter 4 for example). The on/off controls of the 405 nm, 554 nm lasers and the 532 nm pulsed laser do not require precise timings, and motorized mechanical shutters are used. Electro-optic modulators (EOMs) are used in the 493 nm and 650 nm laser setups to generate the additional frequencies required for working with $^{137}Ba^{+}$, as discussed in Chapter 3.1. The half waveplate (HWP) and polarizing beam splitter (PBS) setup for the 493 nm laser allows control of laser powers sent to the combined beam path (used for fluorescence readout and laser cooling) and the optical pump beam path. The optical pump beam path is irrelevant in this chapter and will be discussed in Chapter 4. A HWP and a linear polarizer combinations allow tuning of the 554 nm laser power and 532 nm pulse energy sent to the trap by rotating the HWP. A neutral density (ND) filter is placed in the beam path of the 532 nm pulsed laser going to the $BaCl_2$ target to match the actual sent pulse energy to the sampled pulse energy.

Fig. 3.3 shows how the laser beams are delivered to the ions. The 493 nm optical pump beam path, the 614 nm laser and the 1762 nm laser are irrelevant to this chapter and will only be discussed in Chapter 4. Reflective optics are used to direct and focus the laser beams onto the ion position. This prevents any chromatic shifts of the beams due to refraction, which is useful to us as we are combining lasers of a range of wavelengths to single beams. The absence of chromatic shifts also helps with precise alignments of beam paths by switching a laser for driving ion fluorescence to that beam path for alignments

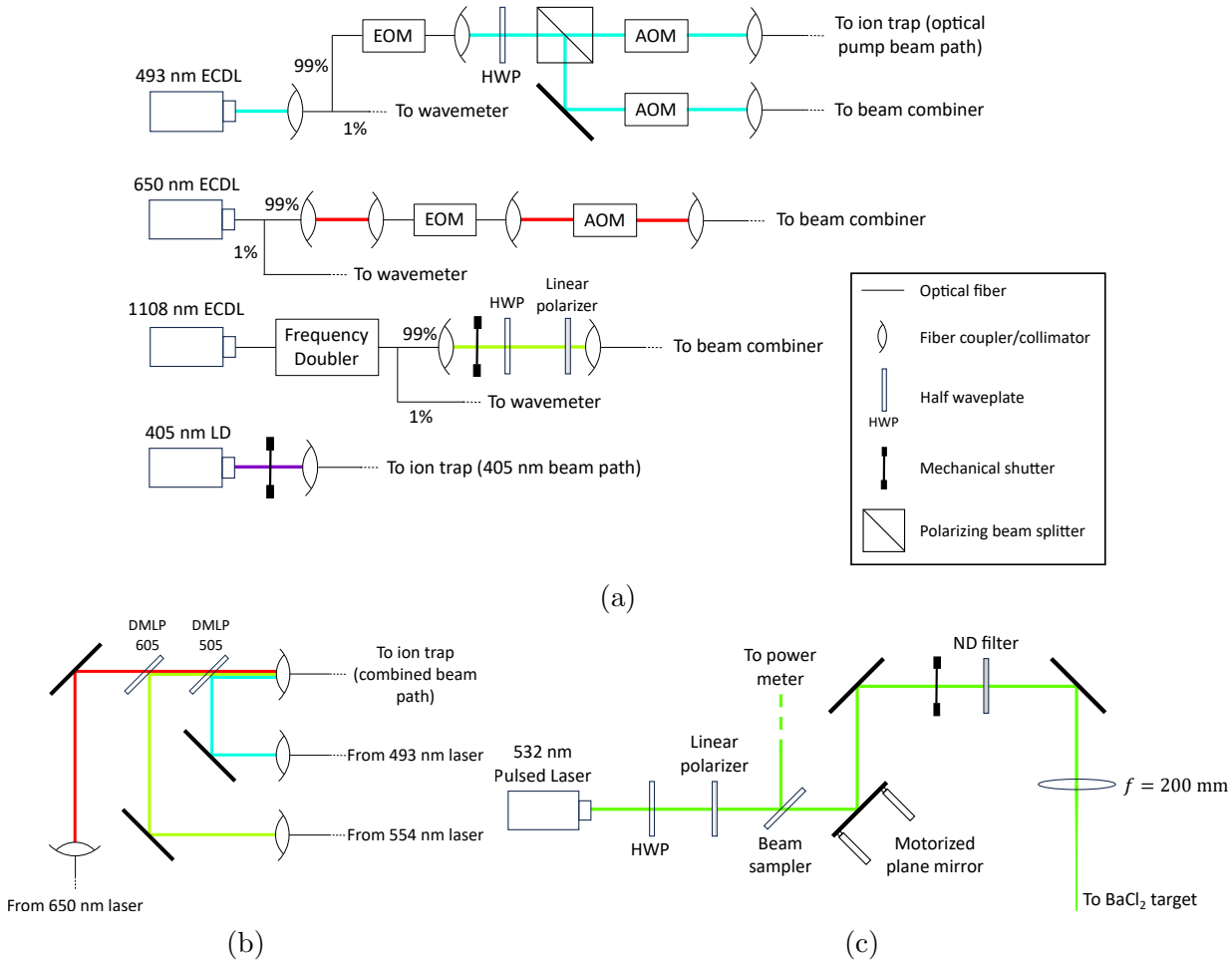

Figure 3.2: Illustration of the setup of lasers relevant for loading ions. Some plane mirrors for geometrical control of laser beams are omitted from this illustration for simplicity. ECDL denotes external cavity diode laser. LD denotes laser diode. DMLP N denotes dichroic mirror (long pass), which allows wavelengths longer than the specified number, N, in nanometers to transmit through. (a) Setups of the continuous wave (CW) lasers. (b) Setup of a free-space beam combiner for combining the 493 nm, 554 nm, and 650 nm lasers to a single beam before being sent to the trap. (c) Setup of the high-power 532 nm pulsed laser with a pulse width of 3 ns to 5 ns for ablating the $BaCl_2$ target.

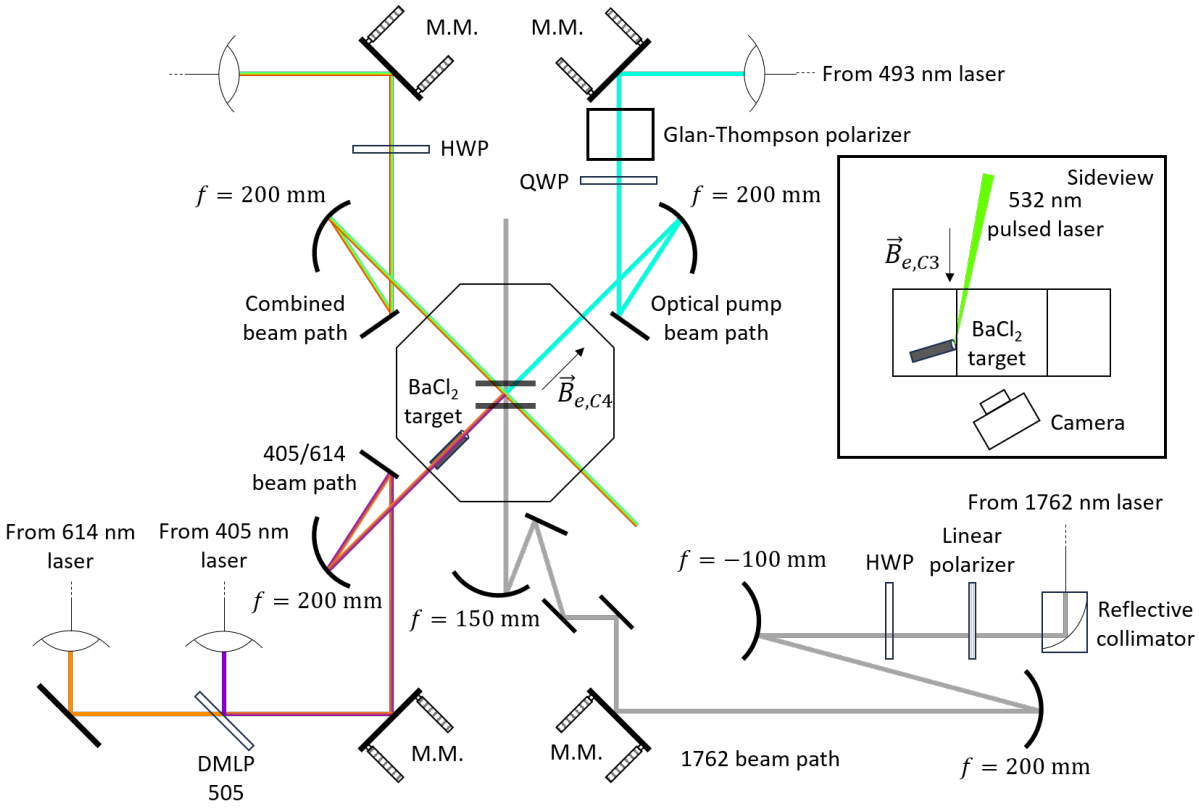

Figure 3.3: Optical setup of the beam paths at the ion trap. The central octogon represents the vacuum chamber, with the four-rod trap in the middle. M.M. denotes a mirror with micrometer actuators for the mount. QWP denotes a quarter waveplate. The spherical concave mirrors focusing the laser beams to the ion are mounted on translation stages to enable fine distance tuning (not shown). An aluminium cup holding $BaCl_2$ is placed in the vacuum chamber acting as a target for laser ablation. The $BaCl_2$ target points towards the ion trap center and is at a distance 14.6 mm from the trap center. The inset shows a sideview of the vacuum chamber to illustrate how the ablation laser beam is sent to the $BaCl_2$ target. A camera is set up to enable viewing of the $BaCl_2$ target. $\vec{B}_{e,C3}$ and $\vec{B}_{e,C4}$ denote the magnetic field directions used in Chapters 3 and 4, unless stated otherwise.

(discussed in Section 3.2.1). The beams are designed to be incident to the spherical concave mirrors at small angles, which is important to minimize aberrations at the beam focus as a spherical surface is only a good approximation of a parabolic surface (which gives a perfect focus from reflection) at small incident angles. Our typical CW laser powers relevant for ion loading at the trap are as follows:

1. 405 nm: in the order of 1 mW, the laser diode power degrades over time.
2. 493 nm (combined beam path): $\sim 35\,\mu W$
3. 554 nm: $1\,\mu W$ to $40\,\mu W$ (tunable with HWP)
4. 650 nm: $\sim 200\,\mu W$

3.2.1 Ion Loading Beam Alignments

Starting from a point where the optical components are roughly set up according to the geometry in Figs. 3.2 and 3.3, I describe how we precisely and systematically narrow down the beam alignments for ion trapping in this section.

The laser alignment for the ablation laser is the simplest, as the laser only needs to hit any spot on the target (with a normal area of around $\pi \times (2\,\text{mm})^2$) in order to generate atom flux. A camera is set up to monitor the salt target as shown in Fig. 3.3. The ablation laser is set to low power and the beam pointing is adjusted using plane mirrors until we see on the camera that it is hitting the target. The size of the beam at the $BaCl_2$ target is estimated by measuring the beam profile focused with an optic with a focal length of $f = 200\,\text{mm}$ beforehand on a separate setup, which turns out to be 196 µm in diameter.

The requirements on the precision and accuracy of the alignments of the combined beam and 405/614 beam are much stricter, as the two beams have to overlap at the Paul trap pseudopotential minimum. The diameters of the beams at the focus, which dictate the length scale of the precision requirement, are estimated to be

$$D_{focus} = \frac{f_{CM}}{f_{FC}} D_{fiber} = \frac{200\,\text{mm}}{10\,\text{mm}} \times 3.3\,\mu\text{m} \approx 70\,\mu\text{m}, \tag{3.2}$$

where f_{CM} is the focal length of the spherical concave mirror, f_{FC} is the focal length of the fiber collimator, D_{fiber} is the mode field diameter of the fiber. The alignment procedure for the combined beam and the 405/614 beam is as follows:

1. Move the imaging objective of the imaging system to look at one of the needle electrodes, and imaging the needle onto the CCD camera as shown in Fig. 2.2.
2. Tune the horizontal actuator of the micrometer mirror mount (M.M.) until light scattering off the needle is observed.
3. Tune the vertical actuator of the M.M. to maximize light scattering on the needle.
4. Tune the horizontal actuator of the M.M. until light scattering on the needle is barely visible.
5. Repeat Steps 3 and 4 until light scattering on Step 3 can no longer be increased.
6. Record the readings of the micrometer scales on the actuators of the M.M.
7. Repeat Steps 1 to 6 for the other needle electrode.
8. Compute the average of the two recorded micrometer scale readings for each actuator. Set the actuators to these readings.

We find that with these procedures, the beam alignments are precise enough to trap ions when the laser frequencies are calibrated, and I would like to thank Matthew Day for coming up with this alignment procedure.

Assuming that other experimental parameters are already calibrated for trapping ions, we can further optimize the beam alignments using the trapped ion fluorescence rate as a metric. For the combined beam path, it is as follows:

1. Set the 493 nm and 650 nm laser frequencies to be further red-detuned (by tens of MHz) from the optimal frequencies for maximizing fluorescence rates (we will see why this is necessary later in Section 3.3).
2. Tune the M.M. actuators to maximize ion fluorescence.

For the 405/614 beam path, since we have no chromatic shifts of the beam pointings in the setup, it can be done as follows:

1. Set the 493 nm and 650 nm laser frequencies to be further red-detuned (by tens of MHz) from the optimal frequencies for maximizing fluorescence rates.

2. Route the 493 nm cooling beam to the 405/614 beam path by unplugging the fiber in Fig. 3.2a labelled "To ion trap (405 nm beam path)" and plugging it into the fiber coupler labelled "To beam combiner" for the 493 nm laser in Fig. 3.2a.

3. Attach a 3D-printed piece with a center hole to the magnetic field holder of the exit viewport.

4. Tune the beam pointing to maximize ion fluorescence, while having the beam pass through the center hole of the 3D-printed piece, so that the beam is exiting through the center of the viewport.

5. Reroute the 405 nm light back to the 405/614 beam path by undoing the change in Step 2.

Although unnecessary for ion loading, the 405 nm light is aligned to be parallel to the direction of the entry and exit viewports of the 405 nm beam as best possible. We will see that this is important for the alignment of the 493 nm optical pump laser for coherent controls of the ion energy states later in Chapter 4.

3.2.2 Ablation Pulse Fluence Calibration

With the laser beams aligned from the previous section, what we need next is barium atom flux for trapping ions. The ablation laser pulse fluence has to be above some threshold for the $BaCl_2$ target to be emitting material from the ablation pulse. Before the laser frequencies are calibrated to enable fluorescence detection of barium atoms or ions, a metric to observe to roughly determine if the laser pulse fluence is high enough is the rise in pressure in the vacuum chamber. We also caution that there may be an upper limit to the ablation pulse fluence for practical uses on a natural $BaCl_2$ target. At $3.84\,\mathrm{J\,cm^{-2}}$, a seemingly indented spot is visible after some pulses on the $BaCl_2$ target as shown in Fig. 3.4. Thus, one should start with small pulse fluences and increase it gradually until noticeable pressure reading increased is observed.

Figure 3.4: $BaCl_2$ target with a seemingly indented spot highlighted by the red circle.

When the 554 nm laser frequency is calibrated (discussed in the next section), we find that the PMT detector of the imaging system is able to detect barium atom fluorescence from the flux produced by ablation. Using the neutral barium fluorescence from the emitted atom flux, we can determine the ablation pulse fluence threshold when the atom flux is produced more accurately, which we find to be about $0.1\,\mathrm{J\,cm^{-2}}$, as shown in Fig. 3.5. With calibrated 493 nm and 650 nm laser frequencies, by turning off the trap voltages to allow charged particles to pass through the trap region, we are also able to pick up barium ion fluorescence from the ablated flux on the PMT when the laser pulse fluence is high enough. The threshold to generate barium ions directly from laser ablation is estimated to be approximately $0.25\,\mathrm{J\,cm^{-2}}$ from the data collected in Fig. 3.5, which is also the pulse fluence threshold to be able to detect pressure increase in our vacuum system.

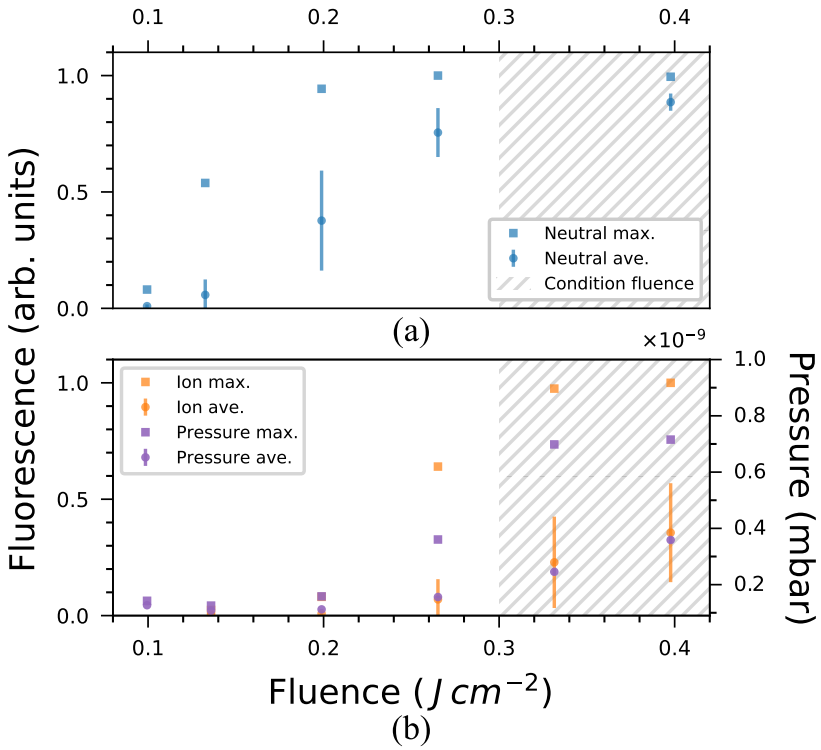

Figure 3.5: (a) Detected fluorescence photon counts from the flux of neutral barium atoms produced by laser ablation. Each pulse fluence data point has a sample size of 120. Neutral max. and ave. denote the maximum and average of the detected photon counts from neutral barium fluorescence from the total sample size. (b) Similar to (a), with the experimental configurations modified to detect fluorescence from barium ions. Also plotted are the pressure readings detected on the ion gauge when the ablation laser is pulsed.

An interesting observation that we see is that for a fresh spot on the $BaCl_2$ target that was never ablated, the pulse fluence threshold to see neutral barium fluorescence is higher, which we have found to be around $0.3\,\mathrm{J\,cm^{-2}}$. After ablating the same spot at this higher pulse fluence for tens or up to a hundred of pulses, the spot may then be producing barium atom flux at a lower pulse fluence. Since this phenomenon appears to be a fresh spot having to be conditioned by higher energy pulses before it can start producing atom flux at lower pulse energies, we call it a conditioning process, although we are not clear on the exact physical dynamics of this observation.

3.2.3 Laser Frequency Calibrations for Ion Loading

With the atom/ion flux and laser beams in place, the laser frequencies can be calibrated. The lasers with strict frequency requirements for ion loading are the 493 nm, 554 nm, and 650 nm lasers. We start by setting the laser frequencies to the reported transition frequencies of ^{138}Ba in past literature [55], taking into account the frequency shift introduced by the AOMs. The 493 nm and 650 nm laser frequencies are set slightly redder then the reported values (by tens of MHz), in order to be able to Doppler cool and trap $^{138}Ba^{+}$ ions. With these values of laser frequencies, we were able to observe noticeable 554 nm fluorescence from barium atom flux. The 554 nm laser frequency is then fine tuned to maximize neutral barium fluorescence from the flux, which should correspond to the transition peak of the barium isotope with the highest abundance, which is ^{138}Ba. We were also able to trap a $^{138}Ba^{+}$ ion using the 493 nm and 650 nm frequency values found from past literature, albeit only with weak fluorescence rate in the order of 10 counts per 100 ms, and we fine tuned the laser frequencies to maximize the ion fluorescence.

Chronologically in the laboratory, the laser frequencies were first calibrated using atom flux produced from a barium oven source, where barium atoms are emitted via resistive heating, when we had a working barium oven. I speculate that it should also be possible to calibrate the laser frequencies with a ablation target source, since we were able to observe atom/ion fluorescence from the flux from laser ablation in Fig. 3.5. An alternative method to calibrate the 493 nm and 650 nm laser frequencies may also be enabled by laser ablation, which is by observing ion fluorescence from the barium ion flux as a metric, which is not available from an oven source.

To calibrate the 554 nm laser frequency for ^{137}Ba, we do a fine spectroscopy of the 554 nm transition in steps of 10 MHz. This is to determine the ^{138}Ba 554 nm fluorescence peak frequency to a precision of 10 MHz. The 554 nm laser frequency is then set to a shift corresponding to the driving a ground state ^{137}Ba to the $6P$ excited state with a total angular momentum of $F = 3/2$, which is known from past literature to be blue of the ^{138}Ba peak by 274.6 MHz [58]. To calibrate the 493 nm and 650 nm laser frequencies for $^{137}Ba^{+}$, from known energy level shifts and hyperfine splittings from past literature [59, 60, 61], we first calculate the EOM frequencies required to drive the desired transitions as shown in Fig. 3.1c based on the scheme we employ. In this work, the 493 nm transitions, which are the $|6S_{1/2}, F = 1\rangle \leftrightarrow |6P_{1/2}, F = 2\rangle$ and $|6S_{1/2}, F = 2\rangle \leftrightarrow |6P_{1/2}, F = 2\rangle$ transitions, are driven by the first red and blue-sidebands generated by the EOM at ± 4012 MHz, and the 493 nm carrier frequency is off-resonant. The $|5D_{3/2}, F = 2\rangle \leftrightarrow |6P_{1/2}, F = 1\rangle$ transition is driven by the carrier frequency of the 650 nm laser, and the other $5D_{3/2}$ to $6P_{1/2}$ transitions are driven by the blue sidebands generated by the EOM. Specifically, the

EOM is used to generate sidebands at 318 MHz, 473 MHz, and 877 MHz, where the blue sidebands drive the $|5D_{3/2}, F = 1\rangle \leftrightarrow |6P_{1/2}, F = 1\rangle$, $|5D_{3/2}, F = 0\rangle \leftrightarrow |6P_{1/2}, F = 1\rangle$, and $|5D_{3/2}, F = 3\rangle \leftrightarrow |6P_{1/2}, F = 2\rangle$ transitions respectively. This EOM setup for the 650 nm is so that the unused sidebands are red of the resonant transitions to prevent heating the ion. Note that the EOM modulation frequencies for the 650 nm laser are slightly off from the reported values [60, 61]. This is set on purpose and the rationale will be discussed in Section 3.3. We then trap a $^{138}Ba^+$ ion. The carrier frequency of the 493 nm is the shifted red by the sideband frequency to be generated by the EOM, and then the EOM is turned on to fluoresce the trapped $^{138}Ba^+$ ion with the laser sideband frequency to calibrate the laser sideband intensity. The electrical power sent to the 493 nm EOM is set to maximize the $^{138}Ba^+$ fluorescence rate. The sideband intensities calibration of the 650 nm laser follow similar steps, except that it is not possible to maximize the $^{138}Ba^+$ fluorescence rate when driving it with sideband frequencies for all the sidebands at the same time. The electrical power sent to the 650 nm EOM for each of the sideband is set to be able to fluoresce $^{138}Ba^+$ with at least 10% of the fluorescence rate compared to the original laser frequency settings for fluorescing $^{138}Ba^+$.

3.3 Higher Laser Intensities Do Not (Necessarily) Lead to Higher Barium Ion Fluorescence Rates

For a simple two-level energy level structure, one ground state and one fast-decaying excited state, the fluorescence rate is expected to monotonically increase with increasing driving laser intensity, until the time-averaged excited state population saturates at 1/2 (see Appendix A). At laser intensities much higher than the saturation intensity, the fluorescence rate will be stable and insensitive to laser frequency changes. In our fluorescence scheme for Ba^+ ions, we will see that this is not the case, due to an additional energy level being involved, which is the $5D_{3/2}$ level. This leads to nuances such as what is alluded in the title of this section. We explore these complexities with theoretical models in this section, in order to gain some insights to what we see or expect to see regarding the characteristics of barium ion fluorescence rates in a laboratory.

3.3.1 Three-level Theoretical Toy Model for Studying Barium Ion Fluorescence Rates

We start by studying a simple model case, which is a three-level system, with the states labelled as $|S\rangle$, $|P\rangle$, and $|D\rangle$. The $|P\rangle$ state has a decay rates of γ_S and γ_D to the $|S\rangle$ and $|D\rangle$ states respectively. The $|S\rangle$ and $|D\rangle$ states are treated as stable states and do not decay. The unperturbed Hamiltonian can be written as

$$\hat{H}_0 = E_S|S\rangle\langle S| + E_P|P\rangle\langle P| + E_D|D\rangle\langle D|, \tag{3.3}$$

where E_j is the energy of state $|j\rangle$, $j \in \{S, P, D\}$. Let two lasers be incident on the system, with Rabi frequencies of Ω_L, and laser angular frequencies of ω_k, where the subscript $L \in \{S, D\}$ indicates laser frequencies that are close to the $|L\rangle \leftrightarrow |P\rangle$ transition. We write the laser frequencies as

$$\begin{aligned} \omega_S &= \omega_{0,S} + \Delta_S \\ \omega_D &= \omega_{0,D} + \Delta_D, \end{aligned} \tag{3.4}$$

where $\omega_{0,L} = (E_P - E_L)/\hbar$ is the resonant frequency of the $|L\rangle \leftrightarrow |P\rangle$ transition. With the assumptions $\Omega_L \ll |\omega_{0,S} - \omega_{0,D}|$ and $\Delta_L \ll |\omega_{0,S} - \omega_{0,D}|$, the resultant Hamiltonian driven by these two lasers can be approximated as

$$\hat{H} = \hat{H}_0 + \hat{H}_{Laser} \tag{3.5}$$

where the Hamiltonian introduced by the lasers is

$$\hat{H}_{Laser} = \Omega_S \cos(\omega_S t)\left(|S\rangle\langle P| + |P\rangle\langle S|\right) + \Omega_D \cos(\omega_D t)\left(|D\rangle\langle P| + |P\rangle\langle D|\right). \tag{3.6}$$

By going to the interaction picture with respect to the Hamiltonian

$$\hat{H}_0' = (E_S - \hbar\Delta_S)|S\rangle\langle S| + E_P|P\rangle\langle P| + (E_D - \hbar\Delta_D)|D\rangle\langle D|, \tag{3.7}$$

and applying the rotating wave approximation ($\Omega_k \ll \omega_k$), the resultant Hamiltonian in the interaction picture is

$$\hat{H}_I = \Delta_S|S\rangle\langle S| + \Delta_D|D\rangle\langle D| + \frac{\Omega_S}{2}\left(|S\rangle\langle P| + |P\rangle\langle S|\right) + \frac{\Omega_D}{2}\left(|D\rangle\langle P| + |P\rangle\langle D|\right) \tag{3.8}$$

Now we write a general state in the three-level system as

$$|\psi_I\rangle = c_S|S\rangle + c_D|D\rangle + c_P|P\rangle. \tag{3.9}$$

Solving the Schrödinger equation, $i\hbar\frac{d}{dt}|\psi_I\rangle = \hat{H}_I|\psi_I\rangle$, gives

$$\begin{aligned}
\frac{d}{dt}c_S &= -i\Delta_S c_S - i\frac{\Omega_S}{2}c_P \\
\frac{d}{dt}c_D &= -i\Delta_D c_D - i\frac{\Omega_D}{2}c_P \\
\frac{d}{dt}c_P &= -i\frac{\Omega_S}{2}c_S - i\frac{\Omega_D}{2}c_D.
\end{aligned} \tag{3.10}$$

Writing the density matrix elements as $\rho_{jj'} = c_j c_{j'}^*$, from Eq. 3.10, we get

$$\begin{aligned}
\frac{d}{dt}\rho_{SS} &= i\frac{\Omega_S}{2}\left(\rho_{SP} - \rho_{PS}\right) \\
\frac{d}{dt}\rho_{DD} &= i\frac{\Omega_D}{2}\left(\rho_{DP} - \rho_{PD}\right) \\
\frac{d}{dt}\rho_{PP} &= -i\frac{\Omega_S}{2}\left(\rho_{SP} - \rho_{PS}\right) - i\frac{\Omega_D}{2}\left(\rho_{DP} - \rho_{PD}\right) \\
\frac{d}{dt}\rho_{SD} &= i\frac{\Omega_D}{2}\rho_{SP} - i\frac{\Omega_S}{2}\rho_{PD} + i\left(\Delta_D - \Delta_S\right)\rho_{SD} \\
\frac{d}{dt}\rho_{SP} &= i\frac{\Omega_S}{2}\left(\rho_{SS} - \rho_{PP}\right) + i\frac{\Omega_D}{2}\rho_{SD} - i\Delta_S\rho_{SP} \\
\frac{d}{dt}\rho_{DP} &= i\frac{\Omega_D}{2}\left(\rho_{DD} - \rho_{PP}\right) + i\frac{\Omega_S}{2}\rho_{DS} - i\Delta_D\rho_{DP}.
\end{aligned} \tag{3.11}$$

Taking into account spontaneous decay from the $|P\rangle$ state, Eq. 3.11 is modified to

$$\begin{aligned}
\frac{d}{dt}\rho_{SS} &= i\frac{\Omega_S}{2}\left(\rho_{SP} - \rho_{PS}\right) + \gamma_S\rho_{PP} \\
\frac{d}{dt}\rho_{DD} &= i\frac{\Omega_D}{2}\left(\rho_{DP} - \rho_{PD}\right) + \gamma_D\rho_{PP} \\
\frac{d}{dt}\rho_{PP} &= -i\frac{\Omega_S}{2}\left(\rho_{SP} - \rho_{PS}\right) - i\frac{\Omega_D}{2}\left(\rho_{DP} - \rho_{PD}\right) - \left(\gamma_S + \gamma_D\right)\rho_{PP} \\
\frac{d}{dt}\rho_{SD} &= i\frac{\Omega_D}{2}\rho_{SP} - i\frac{\Omega_S}{2}\rho_{PD} + i\left(\Delta_D - \Delta_S\right)\rho_{SD} \\
\frac{d}{dt}\rho_{SP} &= i\frac{\Omega_S}{2}\left(\rho_{SS} - \rho_{PP}\right) + i\frac{\Omega_D}{2}\rho_{SD} - i\Delta_S\rho_{SP} - \frac{\gamma_S + \gamma_D}{2}\rho_{SP} \\
\frac{d}{dt}\rho_{DP} &= i\frac{\Omega_D}{2}\left(\rho_{DD} - \rho_{PP}\right) + i\frac{\Omega_S}{2}\rho_{DS} - i\Delta_D\rho_{DP} - \frac{\gamma_S + \gamma_D}{2}\rho_{DP},
\end{aligned} \tag{3.12}$$

which are the optical Bloch equations that allow us to solve for the steady state populations. At equilibrium, the derivatives on the LHS of Eq. 3.12 are zero. Solving Eq. 3.12 for the

state populations in equilibrium, with the equation for normalizing the state population, $1 = \rho_{SS} + \rho_{DD} + \rho_{PP}$, gives the $|P\rangle$ state population of

$$\begin{aligned}\rho_{PP} = \Bigg[& 2 + \frac{4\Delta_S^2 \gamma_S}{\Omega_S^2 (\gamma_S + \gamma_D)} + \frac{4\Delta_D^2 \gamma_D}{\Omega_D^2 (\gamma_S + \gamma_D)} \\ & + \frac{(\gamma_S + \gamma_D)\gamma_S}{\Omega_S^2} + \frac{(\gamma_S + \gamma_D)\gamma_D}{\Omega_D^2} \\ & + \frac{2}{(\gamma_S + \gamma_D)(\Delta_S - \Delta_D)} \left(\frac{\Omega_S^2}{\Omega_D^2} \gamma_D \Delta_D - \frac{\Omega_D^2}{\Omega_S^2} \gamma_S \Delta_S \right) \\ & + \frac{\Omega_S^2 + \Omega_D^2}{4(\Delta_S - \Delta_D)^2 (\gamma_S + \gamma_D)} \left(\gamma_D + \gamma_S + \frac{\Omega_S^2}{\Omega_D^2} \gamma_D + \frac{\Omega_D^2}{\Omega_S^2} \gamma_S \right) \Bigg]^{-1}\end{aligned} \tag{3.13}$$

From Eq. 3.13, the larger the value is in the square bracket, the lower the $|P\rangle$ state population. If we ignore the last two terms inside the square bracket with the $(\Delta_S - \Delta_D)$ denominators, large Rabi frequencies (large Ω_S and Ω_D) saturates ρ_{PP}, and ρ_{PP} is insensitive to laser frequencies (Δ_S and Δ_D). This is because we have effectively ignored the S to D state coherence by ignoring terms that are dependent on $(\Delta_S - \Delta_D)$. Considering all the terms in the square bracket, an immediate implication can be observed, which is when the laser detunings are exact, $\Delta_S = \Delta_D$, we see that ρ_{PP} is zero. This is the electromagnetically induced transparency (EIT) phenomenon. When $(\Delta_S - \Delta_D)$ is small, the last term in the square bracket of Eq. 3.13, $\frac{\Omega_S^2 + \Omega_D^2}{4(\Delta_S - \Delta_D)^2 (\gamma_S + \gamma_D)} \left(\gamma_D + \gamma_S + \frac{\Omega_S^2}{\Omega_D^2} \gamma_D + \frac{\Omega_D^2}{\Omega_S^2} \gamma_S \right)$, dominates over other terms. This term also generally increases with larger laser intensities, which leads to smaller ρ_{PP}. Thus, when the laser frequency detunings are very close to each other, higher laser intensities do not lead to higher fluorescence rates. Eq. 3.13 also implies that the optimal laser frequencies to maximize fluorescence rates are not clear, and are dependent on the laser intensities (see Fig. 3.6).

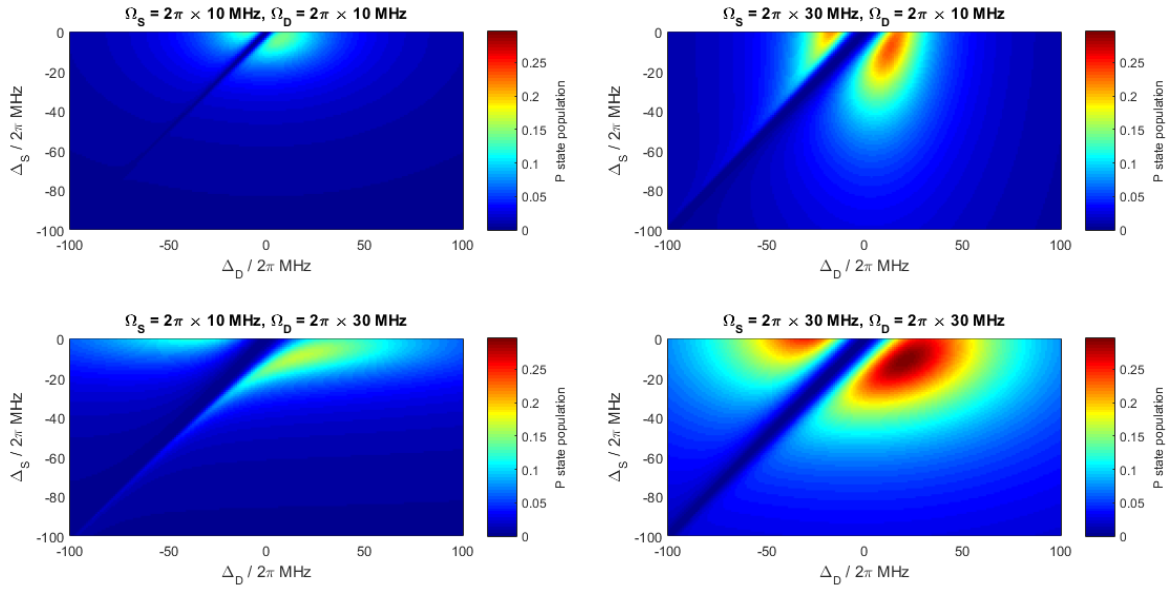

Figure 3.6: Color maps of P state population against laser detunings, Δ_S and Δ_D, simulated using Eq. 3.13 at different laser Rabi frequencies, Ω_S and Ω_D. Barium ion spontaneous decay rates of $\gamma_S = 95.3\,\mu s^{-1}$ and $\gamma_D = 31.0\,\mu s^{-1}$ are used for these simulations. Δ_S is limited to negative values, which is a requirement for Doppler cooling a trapped ion.

3.3.2 Theoretical Simulations of P State Populations of $^{138}Ba^+$ and $^{137}Ba^+$

As discused in Section 3.3.1, our approach to modelling and calculating the excited state population is as follows.

1. Construct the Hamiltonian of the system.
2. Go to the interaction picture in the laser frequencies' reference frame, in order to work with a time-independent Hamiltonian.
3. Construct time derivatives of the energy state density matrix elements using Schrödinger equation.
4. Add spontaneous decay terms to the time derivative equations.

5. Set the time derivatives to zero for the equilibrium condition and together with the requirement that the trace of the density matrix has to be unity, we have a complete set of linear equations to solve for P state population.

To model $^{138}Ba^{+}$ and $^{137}Ba^{+}$ more realistically, I will discuss the additional complexities to be taken into account in each step listed above.

There are not just three energy levels to consider in actual $^{138}Ba^{+}$ and $^{137}Ba^{+}$ ions. In a static magnetic field, $^{138}Ba^{+}$ has two $6S_{1/2}$ states, two $6P_{1/2}$ states and four $5D_{3/2}$ states that are non-degenerate, a total of eight states to be included. Similarly, for $^{137}Ba^{+}$, there are eight $6S_{1/2}$ states, eight $6P_{1/2}$ states, and sixteen $5D_{3/2}$ states, a total of thirty-two states. In the linear Zeeman splitting regime, the angular frequency corresponding to the energy level splittings within each electronic/hyperfine level can be estimated to be

$$\Delta_{Zeeman} = g_K \mu_B B_e m/\hbar \tag{3.14}$$

where g_K is the Landé g-factor, the subscript $K \in \{J, F\}$, where J denotes electronic level, F denotes hyperfine level, μ_B is the Bohr magneton, B_e is the magnetic field strength, m is the magnetic quantum number, and $\hbar$ is the reduced Planck constant. The Landé g-factor is given as

$$\begin{aligned} g_J &= 1 + \frac{J\left(J+1\right) + S\left(S+1\right) - L\left(L+1\right)}{2J\left(J+1\right)} \\ g_F &= g_J \frac{F\left(F+1\right) + J\left(J+1\right) - I\left(I+1\right)}{2F\left(F+1\right)} \end{aligned} \tag{3.15}$$

where J is the total electronic angular momentum number, S is the electron spin number, L is the orbital angular momentum number, F is the total hyperfine angular momentum number, and I is the nuclear spin number. With Eqs. 3.14 and 3.15, we have enough information to determine the frequency detunings of each level to the driving lasers, and we can get to Step 2 in the list of steps to complete the calculations presented above.

The effective Rabi frequencies for the transitions of each energy state also have to be treated carefully for realistic simulations. The relative dipole transition strength for each transition can be derived using Wigner-Eckart theorem.

$$\langle jm|D_q^{(k)}|j'm'\rangle = \langle j'm'kq|jm\rangle \langle j||D^{(k)}||j'\rangle, \tag{3.16}$$

where j is the total angular momentum number, $D_q^{(k)}$ is the q^{th} component of the electric dipole tensor operator, $k = 1$ is the rank of the dipole operator, $\langle j'm'kq|jm\rangle$ is a Clebsch-Gordan coefficient (see Appendix B), and $\langle j||D^{(k)}||j'\rangle$ is the reduced transition matrix

element. Taking into account the laser polarization that is driving the q^{th} component, the actual Rabi frequency for a transition between two states is

$$\Omega_{jmj'm',L} = \sigma_q \langle j'm'kq|jm\rangle \Omega_L, \tag{3.17}$$

where σ_q is the q^{th} component of the laser polarization and the subscript $L \in \{S, D\}$ denotes the electron orbital. In this work, the 493 nm and 650 nm beams are linearly polarized and pointing perpendicularly to the magnetic axis. Let $\theta_L = 0^\circ$ be the polarization angle that minimizes the $q = 0$ component, we have

$$\begin{aligned} \sigma_{\pm,L} &= \cos(\theta_L)/\sqrt{2} \\ \sigma_{0,L} &= \sin(\theta_L). \end{aligned} \tag{3.18}$$

With the Rabi frequency for each transition known, we can get to Step 3 in the list above. To get to Step 4, the branching ratios of the spontaneous decays to each Zeeman state need to be computed, which is straightforward as it is just a factor of Clebsch-Gordan coefficient squared, $|\langle j'm'kq|jm\rangle|^2$, for $^{138}Ba^+$ and a factor of Wigner-Eckart coefficient squared for $^{137}Ba^+$ (See Appendix A of Ref. [49] for derivations of the Wigner-Eckart coefficients).

With all these complexities taken into account, we can get to Step 5. With a total of eight energy levels with $^{138}Ba^+$ and thirty-two energy levels with $^{137}Ba^+$, it is difficult to get an analytical expression for the P state population. So, I use a linear equations solver package in MATLAB, linsolve(), to solve the list of simultaneous linear equations in Step 5 numerically. Keen readers who are curious about how the equations are exactly constructed and the coding approach in this section can study the simulation scripts on the repository at [62].

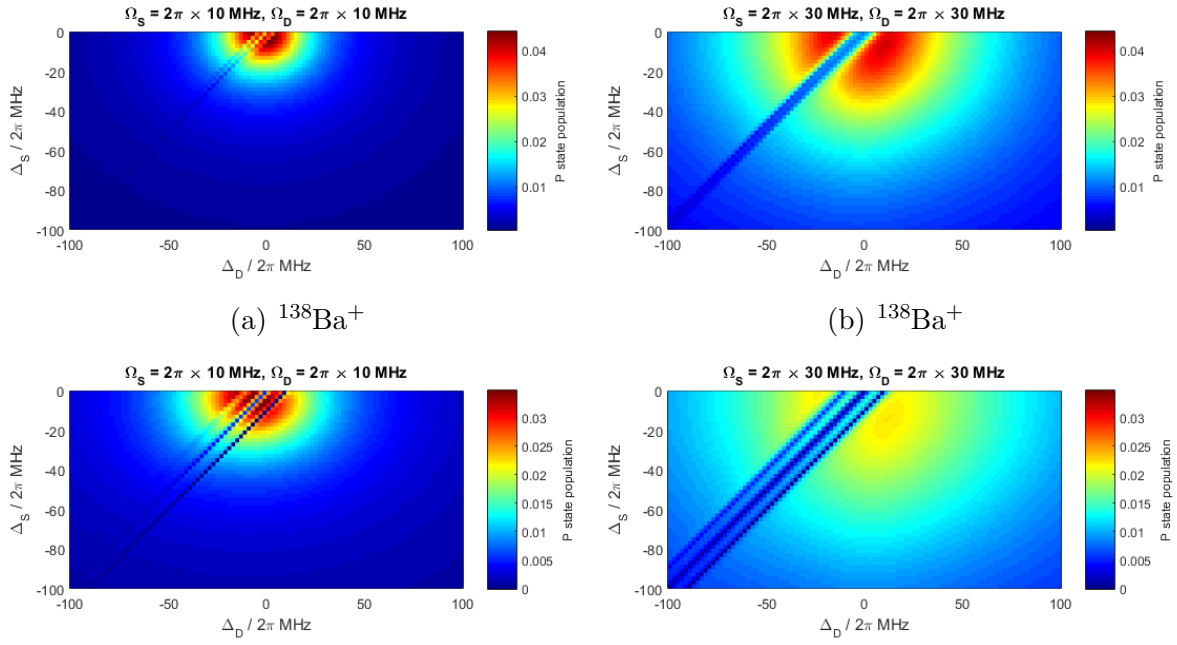

(a) $^{138}Ba^+$ (b) $^{138}Ba^+$

(c) $^{137}Ba^+$ (d) $^{137}Ba^+$

Figure 3.7: Color maps of P state population against laser frequency detunings at different laser Rabi frequencies for $^{138}Ba^+$ ((a) & (b)) and $^{137}Ba^+$ ((c) & (d)). The laser polarization angle is set to $\theta_S = \theta_D = \pi/4$. For (c) & (d), the $|D, F = 2\rangle$ hyperfine level is driven to the $|P, F = 2\rangle$ level instead of the $|P, F = 1\rangle$ level as shown in Fig. 3.1c, as this is what is empirically performed at the time this study is done. The laser frequencies for the $|S, F = 1\rangle \leftrightarrow |P, F = 2\rangle$ and $|S, F = 2\rangle \leftrightarrow |P, F = 2\rangle$ are also have a set 10 MHz detuning from each other, in anticipation to reduce EIT effect (if any) from the ground states. Similarly, the laser frequencies for the $|D, F = 0\rangle \leftrightarrow |P, F = 1\rangle$ and $|D, F = 1\rangle \leftrightarrow |P, F = 1\rangle$ transitions have a set 10 MHz detuning, same for the laser frequencies for the $|D, F = 2\rangle \leftrightarrow |P, F = 2\rangle$ and $|D, F = 3\rangle \leftrightarrow |P, F = 2\rangle$ transition. The Rabi frequencies for the $S \leftrightarrow P$ transition laser frequencies are set to be equal, as is the case for the $D \leftrightarrow P$ transition laser frequencies.

Fig. 3.7 shows the simulation results for $^{138}Ba^+$ and $^{137}Ba^+$. From the results, it can be seen that the effect from EIT is suppressed for $^{138}Ba^+$, from the observation that the P state population is not zero when $\Delta_S = \Delta_D$. This is because for one S state with the same laser detunings with another D state, you can find another Zeeman D state that this S state does not share the same laser detunings with. For $^{137}Ba^+$, the EIT effect is not suppressed

for the $F = 0$ hyperfine state in the D level, as there is only a single Zeeman state in this hyperfine level. Empirically measured fluorescence rates dependence of $^{138}Ba^{+}$ and $^{137}Ba^{+}$ ions also have the same qualitative dependence on the laser frequencies predicted by the simulations, as shown in Fig. 3.8. The fluorescence rate suppression due to the EIT effect when $\Delta_S = \Delta_D$ is obvious from the empirical data. From the data, we can also see that there are upper limits for the 493 nm and 650 nm laser frequencies where the ion stay crystalized and fluorescing. This is due to Doppler heating by the lasers when they are too far blue-detuned. This upper limit for one of the 493 nm and 650 nm lasers is lower if the other laser frequency is bluer, forming fluorescence rate drop-off lines going from top left to bottom right in the color maps.

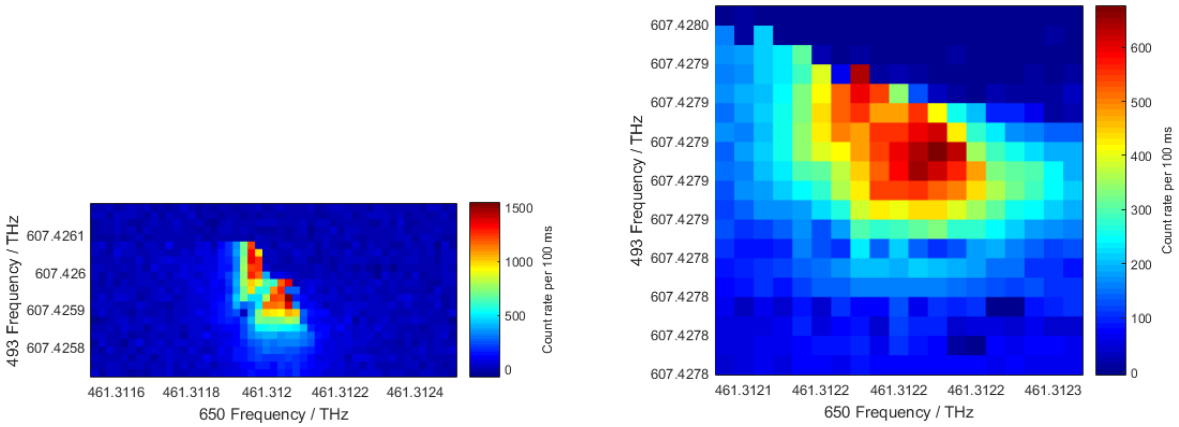

(a) (b)

Figure 3.8: Color maps of empirically collected fluorescence rates against 493 nm and 650 nm carrier laser frequencies of (a) $^{138}Ba^{+}$ and (b) $^{137}Ba^{+}$

Another interesting observation from Fig. 3.7 is that the maximum possible P state population does not increase when the laser Rabi frequencies are increased from $\Omega_S = \Omega_D = 2\pi \times 10\,\text{MHz}$ to $\Omega_S = \Omega_D = 2\pi \times 30\,\text{MHz}$, which is contrary to the simple three-level case as shown in Fig. 3.6. To investigate the P state population dependence on laser intensities, we performed numerical simulations where we scan over a range of 493 nm and 650 nm transition Rabi frequencies. For each combination of 493 nm and 650 nm transition Rabi frequencies, the laser frequencies are scanned in the range from $\Delta_S/2\pi = -100\,\text{MHz}$ to $0\,\text{MHz}$ and $\Delta_D/2\pi = -100\,\text{MHz}$ to $100\,\text{MHz}$ in steps of $10\,\text{MHz}$, and then the frequency combination with the highest P state population is selected.

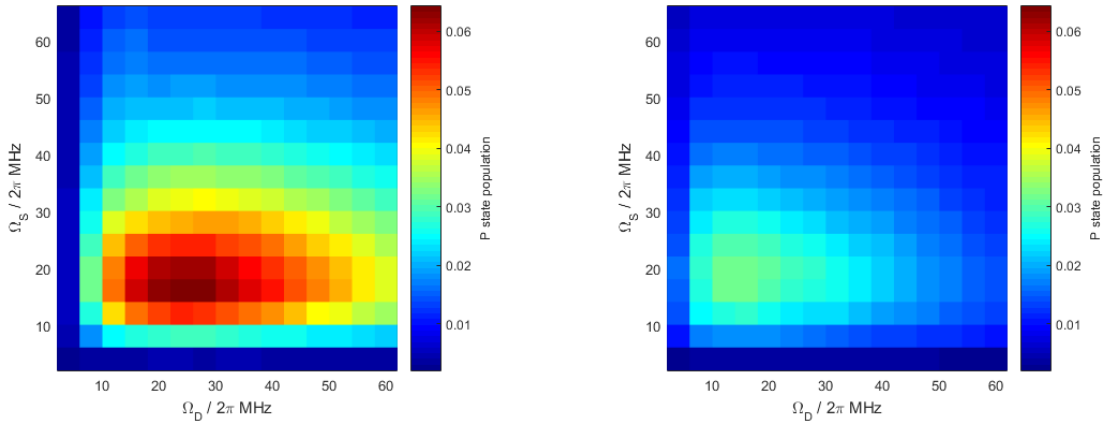

(a) (b)

Figure 3.9: Color maps of the laser intensity scan simulation results for (a) $^{138}Ba^+$ and (b) $^{137}Ba^+$. The polarization angle is chosen to be $\theta_S = \theta_D = \pi/4$.

From Fig. 3.9, we see that there is an optimal point for laser intensities to maximize ion fluorescence, and further increasing any of the laser intensities would lower the P state population. The maximum P state populations also appear to be $\sim 6\%$ and $\sim 3\%$ for $^{138}Ba^+$ and $^{137}Ba^+$ respectively. To compare the simulation results with what we observe empirically, we look at the PMT count rate during ion fluorescence. The count rate (C.R.) of 493 nm light detected on the PMT, collected with our imaging system of $N.A. = 0.2623$, from a Ba^+ ion is

$$C.R. = \frac{\left(1 - \sqrt{1 - N.A.^2}\right) \times \gamma_S \times (Q.E.) \times \rho_P}{2} \tag{3.19}$$

The PMT that we are using to collect ion fluorescence is Hamamatsu H10682-210, which is specified to have a count sensitivity of $4.6 \times 10^5\,\mathrm{s^{-1}\,pW^{-1}}$, which translates to a detection efficiency of $Q.E. = 18.5\%$. In our laboratory, the best $^{138}Ba^+$ and $^{137}Ba^+$ fluorescence rates that we have observed are $C.R. \simeq 20\,\mathrm{ms^{-1}}$ and $C.R. \simeq 10\,\mathrm{ms^{-1}}$ respectively. Using Eq. 3.19, this translates to P state populations of 6.5% and 3.2% for $^{138}Ba^+$ and $^{137}Ba^+$ respectively, which match well with the simulation results.

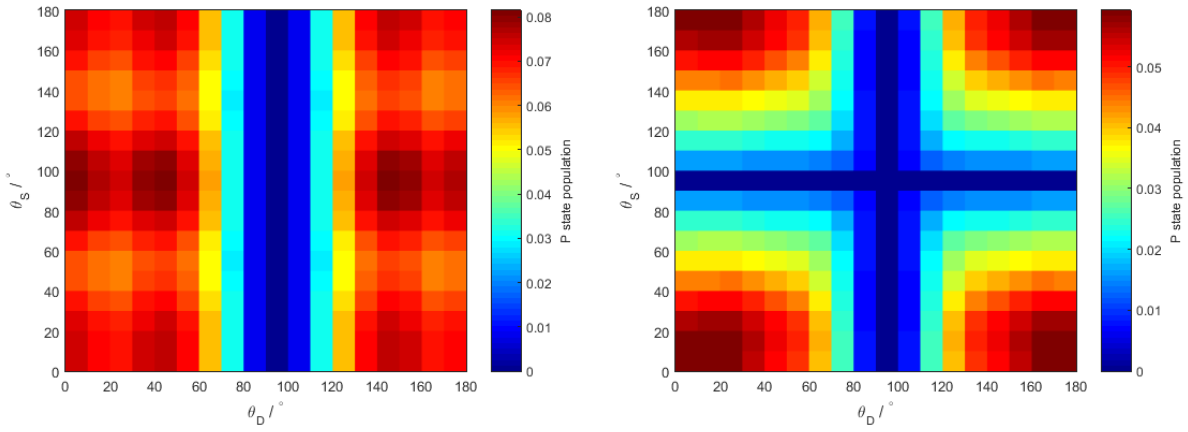

Figure 3.10: Color maps of P state population against laser polarizations for (a) $^{138}Ba^{+}$ and (b) $^{137}Ba^{+}$. (a) The Rabi frequencies are set to $\Omega_S = 2\pi \times 15\,\text{MHz}$ and $\Omega_D = 2\pi \times 25\,\text{MHz}$. (b) The Rabi frequencies are set to $\Omega_S = 2\pi \times 20\,\text{MHz}$ and $\Omega_D = 2\pi \times 15\,\text{MHz}$.

We also studied the fluorescence rate dependence on laser polarizations, by performing similar simulations with the intensity scan simulation, but with the laser intensities fixed and varying laser polarizations instead. From Fig. 3.10, the P state population are largely insensitive to laser polarizations, and have sharp drop off at $\theta_D = \pi/2$. At $\theta_D = \pi/2$, the 650 nm light is π-polarized and can only drive $\Delta m = 0$ transitions. For the $D_{3/2}$ states with $m_J = \pm 3/2$ and $m_F = \pm 3$ in $^{138}Ba^{+}$ and $^{137}Ba^{+}$ respectively, there is no available $6P_{1/2}$ state to drive it to, and thus the state population is stuck in the $D_{3/2}$ level. At $\theta_S = \pi/2$, there is P-state population drop-off for $^{137}Ba^{+}$. This is because the 493 nm light is π-polarized, which would lead to the state population being stuck in the $|6S_{1/2}, F = 2, m_F = 0\rangle$ state as the $|6S_{1/2}, F = 2, m_F = 0\rangle \leftrightarrow |6P_{1/2}, F = 2, m_F = 0\rangle$ transition is forbidden.

To summarize this section, we have studied Ba^{+} fluorescence rates of our ion fluorescence protocol with numerical simulations constructed from optical Bloch equations. From the results, we conclude some important pointers for anyone working with or plans to work with trapped Ba^{+} ions as follows:

1. The optimal laser frequencies for maximizing ion fluorescence are dependent on laser intensities. If you find that the optimal laser frequencies have been drifting, it may not be a fault with your laser frequency locking systems.

2. Higher laser intensities are not always better. There is an optimal point for the laser

intensities for maximal fluorescence, and further increasing them would lower the fluorescence rate.

3. The P state populations are an order of magnitude smaller than the simple two-level case, at $\sim 8\%$ and $\sim 6\%$ for $^{138}Ba^{+}$ and $^{137}Ba^{+}$ respectively. There may be nothing wrong with your imaging system when you have lower photon counts than what you might have intuitively expected.

Technically, we have not done a full parameter scan to search for the true optimal P state population achievable. We did not do a full scan with varying laser polarizations and Rabi frequencies concurrently. For $^{137}Ba^{+}$, we have also fixed the laser frequencies in the same laser (493 nm and 650 nm) to have equal intensities and fixed the frequency modulations for each laser. Thus, we have not done a complete parameter search to definitively conclude points number 2 and 3. However, our empirical observations have been matching the conclusions from the simulations, and we are confident with the implications from the simulation study so far.

3.4 Improved Isotope Selectivity for Ba^+ Ion Loading

Isotope	**Abundance**	$6S \leftrightarrow 6P$ **Transition Frequency Shift** / MHz
132	0.1%	167.9
133	0%	$-23.3(F = 1/2)$ $373.8(F = 3/2)$
134	2.4%	142.8
135	6.6%	$547.3(F = 5/2)$ $326.7(F = 3/2)$ $121.6(F = 1/2)$
136	7.9%	128.02
137	11.2%	$549.5(F = 5/2)$ $274.6(F = 3/2)$ $63.4(F = 1/2)$
138	71.7%	0

Table 3.1: Natural abundance of barium isotopes and the first dipole excitation transition frequency shifts [48, 58]. The $6S \leftrightarrow 6P$ transition frequency shifts are relative to ^{138}Ba. Odd isotopes have nonzero nuclear spin, leading to energy level splittings for different F numbers.

Table 3.1 shows the composition of naturally occurring barium isotopes. ^{137}Ba, which is one of our isotopes of interest, has a lower abundance at 11.2%. To facilitate trapping a desired barium isotope from a natural barium source target, the frequency dependence of the $6S \leftrightarrow 6P$ transitions on the isotopes can be exploited. The 554 nm laser beam path is set up to be perpendicular to the direction of the atom flux from the $BaCl_2$ target as shown in Fig. 3.3, in order to minimize Doppler effects on the spectroscopy of the 554 nm laser on the atom flux. The effect of Doppler broadening on ion loading is speculated to be further suppressed, as only the atoms falling within the crossing overlap of the 554 nm and 405 nm laser beams can be ionized, which is in a length scale of 70 µm. With the $BaCl_2$ salt target being relatively far away from the ion trap center at 14.6 mm, the angular spread of the atom flux that is available for to be ionized is very restricted, to approximately 0.27°, and thus minimizing Doppler broadening effects. By doing a 554 nm laser spectroscopy on ablated

barium atom flux, we obtain resolvable barium isotope fluorescence peaks as shown in Fig. 3.11. To selectively load $^{138}Ba^+$ or $^{137}Ba^+$, we set the 554 nm laser frequencies to their transition peak frequencies respectively. For $^{137}Ba^+$, there are three possible transitions due to hyperfine splittings. We choose the transition to the $F = 3/2$ state as this peak is the best isolated from the transition peaks of other isotopes out of the three transitions.

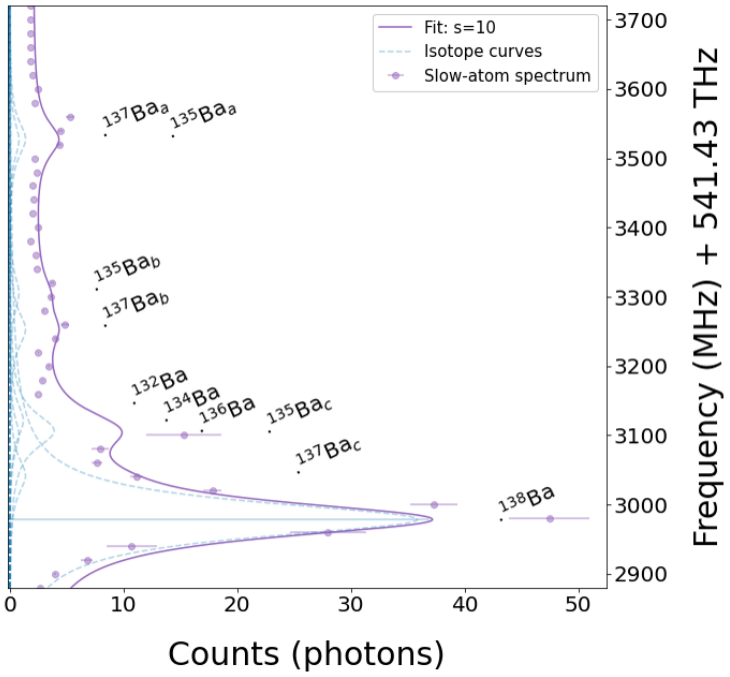

Figure 3.11: Spectroscopy of neutral barium fluorescence from the ablated flux. $s = 10$ denotes the theoretical curve is calculated at 10 times the 554 nm saturation intensity. The photon counts are collected after a time delay of $t > 18\,\mu s$ to minimize Doppler broadening effects. Data analysis performed by Brendan White, see Ref. [63] for details.

To characterize and quantify the ion loading isotope selectivity, we developed a test method as described in the procedure as follows:

1. Set the 493 nm, 554 nm, and 650 nm laser frequencies for the desired isotope to be trapped.

2. Ablate the salt target until at least three bright ions are detected on the CCD camera (see Appendix C for an algorithm to automate the detection of the number of ions).

3. Turn the 650 nm laser off for 1 s and turn it back on.

4. Take a picture on the CCD camera.

5. Repeat Steps 3 and 4 one hundred times.

6. Sum across all the images taken in Step 5. Count the number of bright lattice sites, which is the total number of trapped ions.

Step 3 in the procedure pauses the laser cooling of the ions, which we find to help with scrambling the ion positions. By repeating Step 3 a lot of times, the bright ions have high probabilities of hopping onto all the lattice sites, which were occupied by other dark ions. This method has the benefit of being robust to any other dark ions, be they other elemental ions or molecular ions. Specifically for the experiments for $^{138}Ba^{+}$, $^{134}Ba^{+}$ or $^{136}Ba^{+}$ could be among the bright ions, as we have found that these isotopes will still be fluorescing dimly with the laser frequencies set for fluorescing $^{138}Ba^{+}$. Thus, for each $^{138}Ba^{+}$ experiment, we manually check the images to count the number of ions that are fluorescing brightly at the $^{138}Ba^{+}$ fluorescence rate as the number of trapped $^{138}Ba^{+}$.

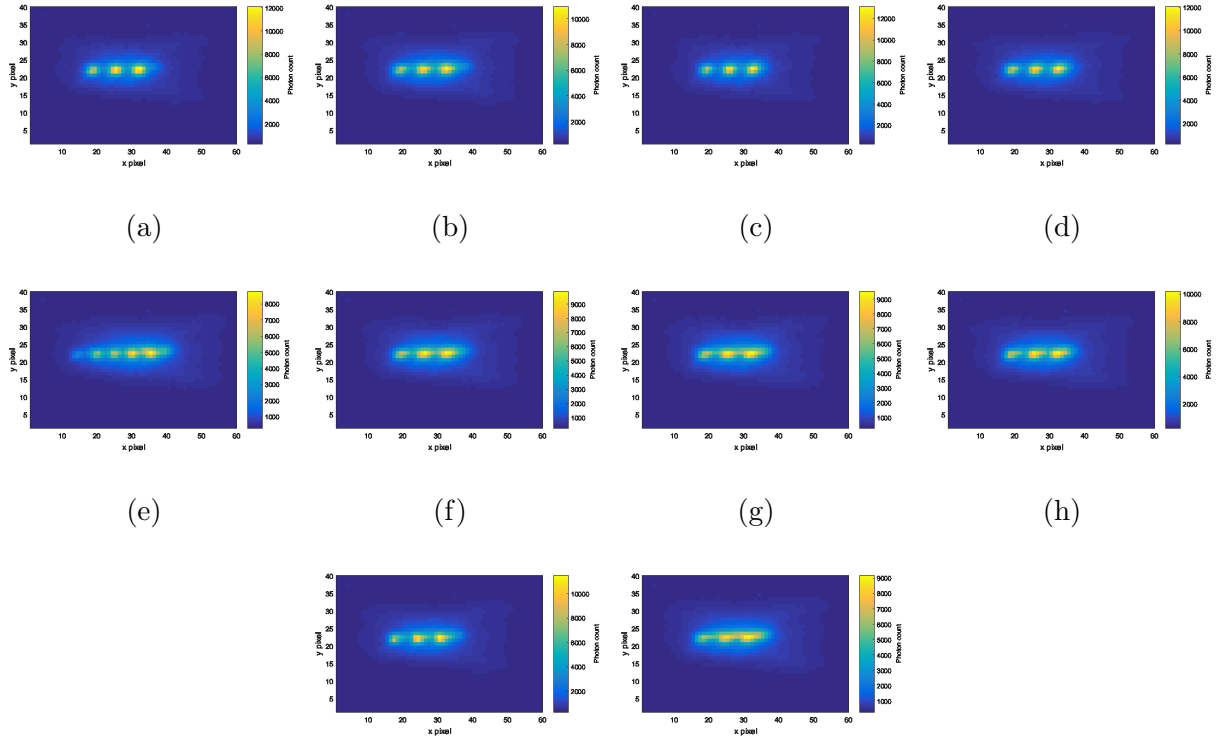

Figure 3.12: $^{138}Ba^{+}$ ion chain images from summing across all images from toggling the repump laser. Each image is a separate experiment. The first excitation laser (554 nm laser) intensity is set to $0.104\,\mathrm{W\,cm^{-2}}$. The total number of ions (bright and dark) are manually counted to be (a) 3, (b) 3, (c) 3, (d) 3, (e) 6, (f) 3, (g) 3, (h) 3, (i) 3, and (j) 3.

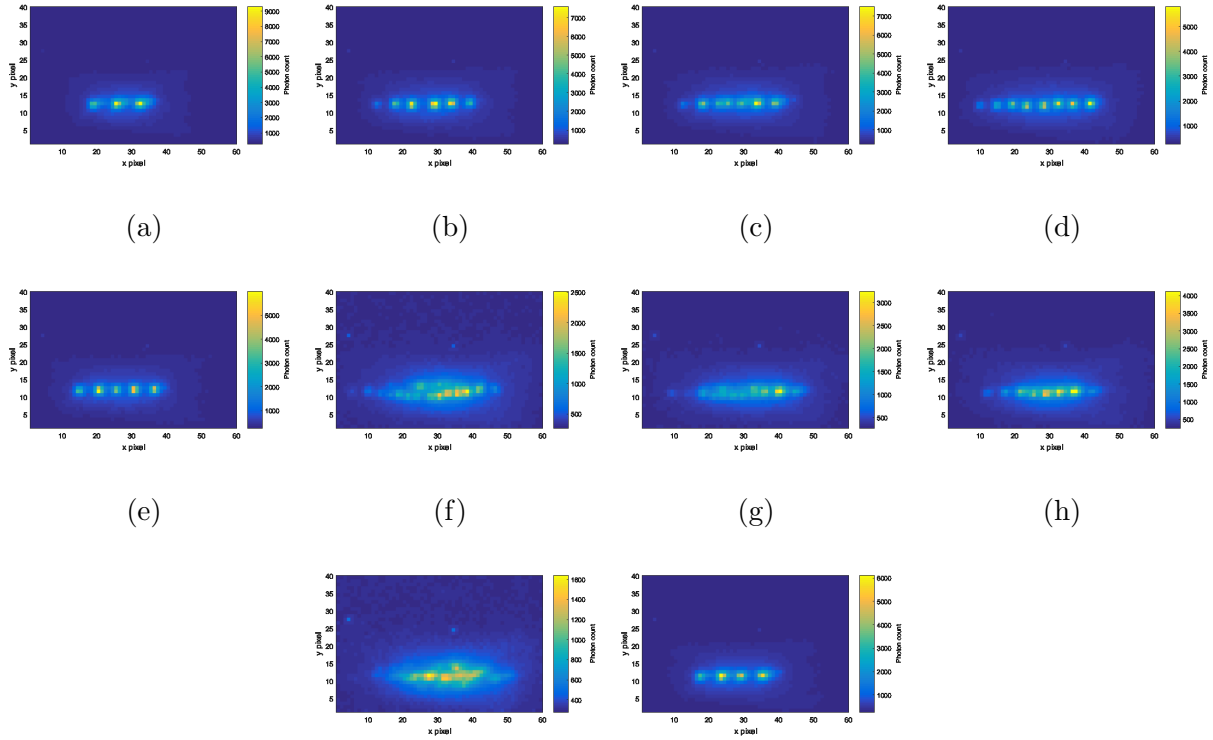

Figure 3.13: $^{137}Ba^{+}$ ion chain images from summing across all images from toggling the repump laser. Each image is a separate experiment. The first excitation laser (554 nm laser) intensity is set to $0.104\,\mathrm{W\,cm^{-2}}$. The total number of ions (bright and dark) are manually counted to be (a) 3, (b) 7, (c) 7, (d) 8, (e) 5, (f) 14, (g) 12, (h) 8, (i) 13, and (j) 4.

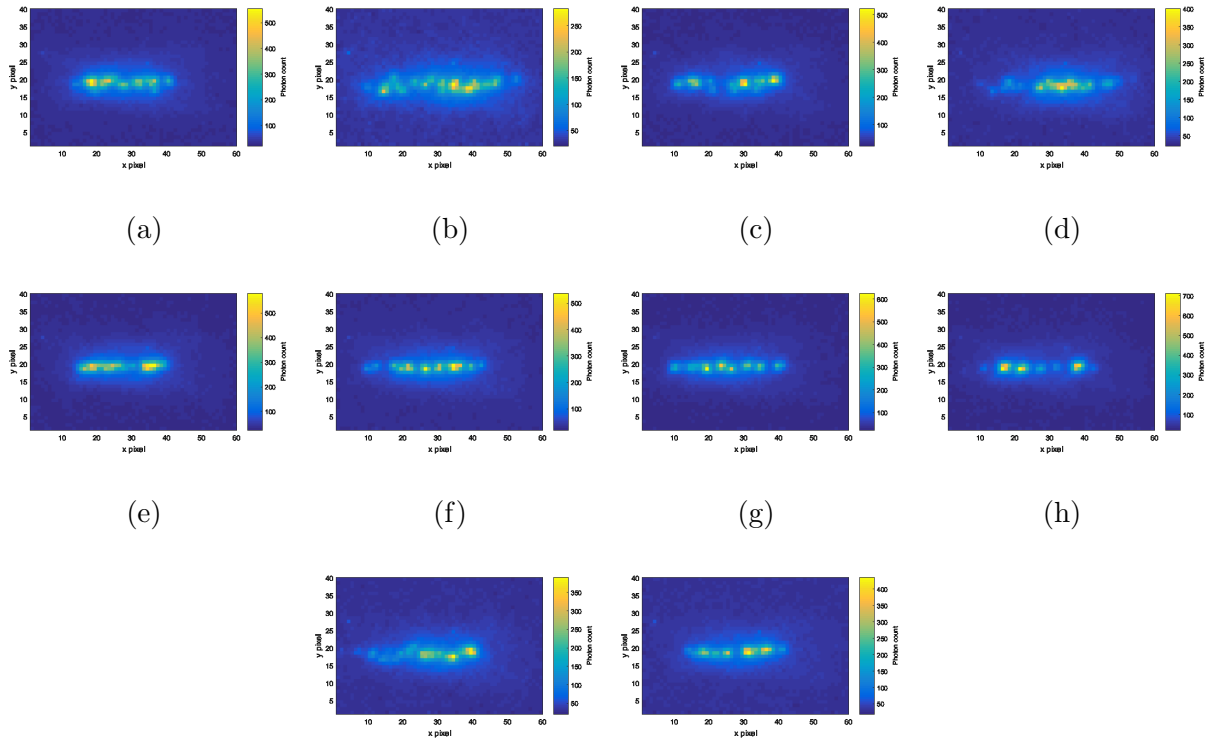

Figure 3.14: $^{137}Ba^{+}$ ion chain images from summing across all images from toggling the repump laser. Each image is a separate experiment. The first excitation laser (554 nm laser) intensity is set to $0.935\,\mathrm{W\,cm^{-2}}$. The total number of ions (bright and dark) are manually counted to be (a) 7, (b) 14, (c) 11, (d) 12, (e) 4, (f) 12, (g) 8, (h) 7, (i) 10, and (j) 8.

For the ion loading isotope selectivity experiments, the ablation pulse fluence was set to $0.25\,\mathrm{J\,cm^{-2}}$, the trap RF voltage amplitude is estimated to be $V_{RF} = 66\,\mathrm{V}$ (see Appendix D for the estimation method), the diagonal rods squeezing voltage is $V_S = 2\,\mathrm{V}$, the needle voltages at $V_{N1} = V_{N1} = 10\,\mathrm{V}$, and a static magnetic field is generated which points in the direction vertical to the vacuum chamber. Fig. 3.12 shows the total lattice sites images of the first ten out of fifty-three isotope selectivity experiments for $^{138}Ba^{+}$ (not all data sets are displayed for brevity, full data sets can be accessed at [64]). Figs. 3.13 and 3.14 show the total lattice sites images for $^{137}Ba^{+}$ at different 554 nm laser powers. We do human manual counting for the total number of lattice sites in Step 6, which may be subject to

uncertainties due to subjectivity of human interpretation, especially for longer ion chains. However, the extent of error from this human uncertainty is not expected to be large, as only about three out of ten experiments for $^{137}Ba^+$ have long chains, and is unlikely to lead to a contrary conclusion that the isotope-selectivity is not significantly improved from the natural ^{137}Ba abundance of 11.2%. The selectivity probability is computed by summing over the total number of trapped desired isotope across all the experiments, divided by the total number of counted lattice sites across all experiments. At 554 nm fluence of $0.104\,W\,cm^{-2}$, out of fifty-three $^{138}Ba^+$ experiments, a total of 185 ions were trapped, with 157 being $^{138}Ba^+$, which gives a selectivity of $85 \pm 3\%$. At 554 nm fluence of $0.104\,W\,cm^{-2}$, out of ten $^{137}Ba^+$ experiments, a total of 81 ions were trapped, with 30 being $^{137}Ba^+$, which gives a selectivity of $37 \pm 5\%$. At 554 nm fluence of $0.935\,W\,cm^{-2}$, out of ten $^{137}Ba^+$ experiments, a total of 93 ions were trapped, with 30 being $^{137}Ba^+$, which gives a selectivity of $32 \pm 5\%$. From these results, the ion loading isotope selectivity is conclusively improved from their natural abundance as shown in Table 3.1.

3.5 Direct-Ion Loading of Barium Ions

In this section, I describe an alternative ion loading method by exploiting the ability of laser ablation to directly generate barium ions, which is a method adopted from Ref. [18]. As shown in Fig. 3.5, at high enough ablation pulse fluence, barium ions are directly released from the $BaCl_2$ target without the need for photoionization. By keeping the ion trap RF voltages off when the ablation event happens, the emitted ions are able to enter the trapping region without being obstructed by the electric pseudopotential barrier of the trap. After some time has passed to allow the emitted ions to arrive at the trapping region, the RF voltages are turned on, and ions with kinetic energies lower than the Paul trap pseudopotential barrier will be trapped. To determine the optimal delay time to turn on the trap RF voltages for direct-ion trapping, we performed a time-resolved scan of trapping probability against the trap RF turn-on time.

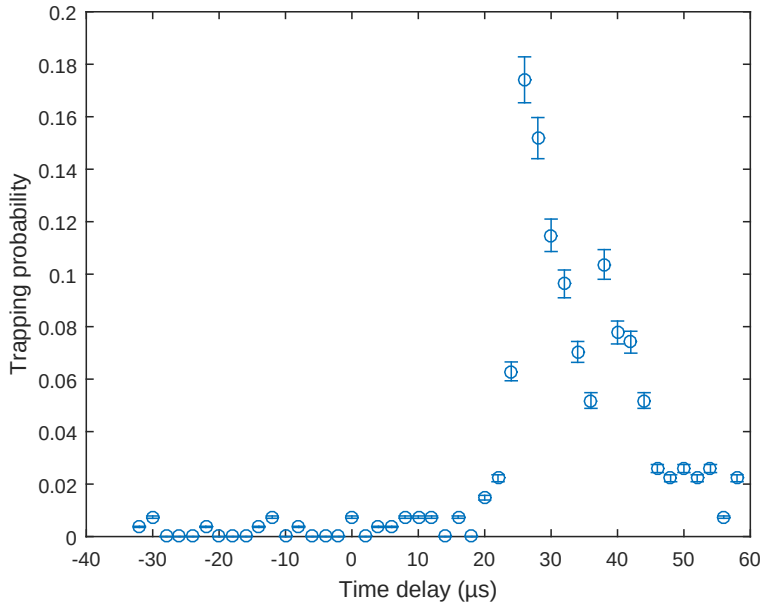

Figure 3.15: Trapping probability of $^{138}Ba^{+}$ using the direct-ion loading method. The horizontal axis denotes the time delay of the trap RF voltage turn-on time from the moment the ablation laser pulse reaches the target. The sample size for each data point is 270. The ablation fluence used is $0.32\,\mathrm{J\,cm^{-2}}$. The trap electrode voltage parameters are the same as what is described in Section 3.4.

From Fig. 3.15, the optimal trap RF turn-on time is 26 µs after the laser ablation event. The optimal trap turn-on time is expected to shift with different trap parameters as it would change the pseudopotential barrier and thus maximum trappable kinetic energy of the ions.

We also investigated the loading efficiency of the direct-ion loading method compared to the REMPI method. A pulse fluence of $0.32\,\mathrm{J\,cm^{-2}}$ is used to ablate on a single spot on the $BaCl_2$ target. The 493 nm, 554 nm and 650 nm laser frequencies are set for trapping and cooling $^{138}Ba^{+}$ ions. First, 300 loading attempts (one ablation pulse per attempt) are performed using the REMPI method. Then, another 300 loading attempts are performed using the direct-ion loading method. The trap RF voltage is turned on 27 µs after the ablation laser hits the target. Lastly, another 300 loading attempts are performed without the REMPI lasers and keeping the trap RF voltages on all the time. This last set of loading attempts serve as a control experiment. We make the assumption that the flux density produced by ablation is consistent throughout these experiments in order to make

direct comparisons of the loading efficiencies of the different loading methods. The loading efficiencies are found to be 15.7%, 39.0% and 1.7% respectively for the REMPI method, the direct-ion loading method and the control experiment respectively. It is interesting that the trapping probability is not zero for the control experiment (which is also observed in non-zero probabilities at negative turn-on times in Fig. 3.15), which I speculate to be due to an ion arriving close to the trapping region during some phase of the oscillating voltage such that the electric field allows the ion to enter the trap region, and then as the ion is going pass the trapping region, the oscillating voltage is in a phase which decelerates the ion, i.e. it is some dynamics that is not predicted by approximating the trap RF voltage as a static pseudopotential. From these results, the direct-ion loading method has an obviously improved trapping efficiency compared to the REMPI method by more then two times. However, direct-ion loading is not isotope selective and is therefore not our main method for loading ions. It is however, useful for troubleshooting the setup as it does not depend on the 405 nm laser beam alignment.

3.6 Discussion and Concluding Remarks

In this chapter, I have described the protocols for trapping barium isotopes using laser ablation. This laser ablation ion loading method comes with a number of remarkable practical benefits compared to a more conventional way of using an oven to drive emission from a metal barium source, especially for barium, which I list as follows:

1. It allows us to prepare the source in a salt form, $BaCl_2$, which is stable in atmospheric environment, as compared to barium metal, which oxidizes rapidly in atmosphere.

2. The atom flux is generated instantaneously upon laser ablation, which leads to potentially quicker trapping of ions.

3. There is practically no heat load on the setup, which may cause drifts in the alignments of the setup due to thermal expansions.

4. Smaller amounts of the source is used up for each ion loading event.

5. No electrical connections and thus access of vacuum electrical feedthroughs are needed for the source.

6. Ions can be generated directly from laser ablation if needed by using high-enough laser pulse fluences, which has some useful applications. Although, some may view

this as a downside as the ion flux may charge up the trap electrodes and push ions away from the RF null, introducing micromotions. However, we do not see this effect from our four-rod trap setup.

Benefit number 4, where small amounts of the source material is used for each loading event is particularly important for ion species that can only be prepared in small amounts. This is the case for $^{133}Ba^+$ as it is radioactive and only small amounts can be installed in a vacuum chamber for health and safety concerns [18]. Loading $^{133}Ba^+$ was our original main motivation for exploring ion loading with laser ablation, but we have yet to successfully trap $^{133}Ba^+$ so far. Details of the loading attempts of $^{133}Ba^+$ can be found in Appendix E.

The loading efficiency depends on a number of experimental parameters, which include the ablation pulse fluence, the 554 nm laser intensity and frequency, and the trap electrode voltages. Using the REMPI process, we find that we can typically reach a loading efficiency of 0.1 to 1 trapped $^{138}Ba^+$ per ablation pulse, and subsequently 0.01 to 0.1 trapped $^{137}Ba^+$ per ablation pulse. The REMPI process also allows improved isotope selective loading of barium isotopes compared to their natural abundances, measured at $85 \pm 3\%$ for $^{138}Ba^+$ and around 35% for $^{137}Ba^+$ in this study. This study lets us answer the question of if relying on isotope selectivity of this current REMPI protocol is sufficient for loading long chains of a single isotope from a natural abundance target, which is not. For loading long chains of isotopes with lower natural abundance, an enriched target with the desired may be required. Alternatively, an isotope-selective laser heating method can be used to expel the unwanted trapped ion isotopes [18], and this improved isotope selectivity loading protocol can be an aid to the overall process of loading a long ion chain of the only desired isotopes.

Chapter 4

Trapped Ba^+ Ions As Qudits

A singly-ionized Ba^+ ion has a metastable $5D_{5/2}$ level, with a spontaneous decay time of 35 s [65]. This decay time is at a time scale much longer than typical trapped ion quantum computing operations [5, 12, 16, 17, 18, 26, 27, 28]. Thus, it is intuitive to think that these metastable states can effectively act as additional coherent ground states, as long as the time scale involving the controls of these states remain negligible compared to the spontaneous decay time. If there is some state measurement protocol that can distinguish quantum information encoded in these stable $6S_{1/2}$ and metastable $5D_{5/2}$ states, then they fulfil a crucial requirement to be used to encode additional computational states. Assuming that there is sufficient control of these states to perform universal single qudit gates and some form of an entangling gate, they can be used for encoding qudits at higher dimensions, effectively increasing the computational Hilbert space. We will see in this chapter that this is indeed the case, and naturally a Ba^+ isotope that has more energy eigenstates in the $6S_{1/2}$ and $5D_{5/2}$ levels can be used for higher dimensional encodings. $^{137}Ba^+$ is a prime candidate for high-dimensional qudit encoding, as there are a total of thirty-two energy eigenstates in the $6S_{1/2}$ and $5D_{5/2}$ levels, which is a reason why this isotope is of interest to us as alluded in Chapter 3.

In this chapter, I describe the work that we have done to actualize coherent controls of the $6S_{1/2}$ and $5D_{5/2}$ states to enable qudit encoding, starting from a point where the experimental parameters are not calibrated. Since the $5D_{5/2}$ states have a long spontaneous decay time, the $6S_{1/2} \leftrightarrow 5D_{5/2}$ transitions have narrow linewidths that are limited only by power broadening. The narrow transition linewidths enable other helpful utilities from the laser control of these transitions, such as resolved sideband cooling and excess micromotion detection, which are also discussed in this chapter. There are also additional complexities with working with the many $^{137}Ba^+$ $6S_{1/2}$ and $5D_{5/2}$ levels, where some commonly applied

approximation methods are no longer valid, which are studied and presented here. Finally, we show that a $^{137}Ba^+$ ion can be used to encode up to 25 levels, and we demonstrate control and readout of a 13-level qudit with $^{137}Ba^+$. Parts of the work in this chapter are adapted from our article in preparation to be published [51].

4.1 Conceptual Control of Ba^+ $6S_{1/2}$ and $5D_{5/2}$ Energy Levels

To ensure that a Ba^+ is in the ground level at the start of an experiment, and not in any of the metastable states, we can wait in the order of minutes in principle to ensure any population in the $5D_{3/2}$ (82 s decay time) or $5D_{5/2}$ (35 s decay time) states decay to the ground state. This is however, not practical for realistic applications, especially when repeat experiments are to be done. To speed this process up, we pump the populations out of the metastable states with dipole transitions. For the $5D_{3/2}$ level, the 650 nm laser is used, as seen before in Chapter 3.1. For the $5D_{5/2}$ level, a 614 nm laser is used, which drives the state population to the $6P_{3/2}$ level (as shown in Figs. 3.1b and 3.1c) and undergoes fast decay to the $6S_{1/2}$ or the $5D_{3/2}$ levels. With both the 614 nm and the 650 nm lasers sent to a Ba^+ ion, the energy state of the ion can be prepared in the ground level quickly.

A Ba^+ ion has multiple states in the $6S_{1/2}$ ground level (two for $^{138}Ba^+$, eight for $^{137}Ba^+$). Without control, a Ba^+ ion in the $6S_{1/2}$ ground energy level can be in any of the states, with equal probabilities. To have control over this randomness of the starting ground state, we choose to optically pump the ground level with a σ_+-polarized 493 nm laser, along with a 650 nm laser to repump the ion out of the $5D_{3/2}$ level. The σ_+-polarized 493 nm laser perpetually drives $\Delta m = +1$ $|6S_{1/2}\rangle \rightarrow |6P_{1/2}\rangle$ transitions, until the ion is in the highest magnetic quantum number state in the $6S_{1/2}$ ground level, where there is no available $\Delta m = +1$ to be driven to in the $6P_{1/2}$ level. This prepares the ion in the $6P_{1/2}$ state with the highest magnetic quantum number, giving us control of the starting point of the ion energy state.

As shown in Figs. 3.1b and 3.1c, the $5D_{5/2}$ level can be accessed from the $6S_{1/2}$ ground state with a quadrupole transition corresponding to a wavelength of 1762 nm. By sending a 1762 nm laser with its frequency tuned to the resonant frequency of a transition between the starting $6S_{1/2}$ state and a $5D_{5/2}$ state allowed by selection rule, a coherent transition is being driven. If we have full control of the pulse timing and the phase of the 1762 nm laser being sent to the ion, then we have full control of the quantum states between the two levels. If we have calibrated the resonant transition frequencies for the other $6S_{1/2} \leftrightarrow 5D_{5/2}$

transitions, then we have full control of the quantum states in the $6S_{1/2}$ and $5D_{5/2}$ levels.

4.1.1 The Hyperfine $|F, m_F\rangle$ States are Bad Assumptions of $^{137}Ba^+$ $5D_{5/2}$ Energy Eigenstates

Taking into account the fine structure splitting, hyperfine structure splitting and Zeeman splitting, the Hamiltonian of an electron orbital (with reference to the electron orbital energy as zero) can be written as

$$\hat{H} = \hat{H}_{FS} + \hat{H}_{HF} + \hat{H}_Z, \tag{4.1}$$

where $\hat{H}_{FS}$, $\hat{H}_{HF}$, and $\hat{H}_Z$ are the fine structure, hyperfine structure, and Zeeman effect Hamiltonian respectively. We first look at $^{138}Ba^+$, we consider the energy levels that we want coherent controls for, which are the $6S_{1/2}$ and $5D_{5/2}$ levels. For $^{138}Ba^+$, there is no nuclear spin and thus $\hat{H}_{HF} = 0$, and only the Zeeman splitting Hamiltonian needs to be considered. In the regime where the Zeeman splittings are much smaller than the fine structure splittings, the energy eigenstates can be approximated to be the fine structure eigenstates of $|J, m_J\rangle$ and $\hat{H}_Z$ is approximated to be

$$\hat{H}_Z = g_J \mu_B B_e \hat{J}_z / \hbar, \tag{4.2}$$

where $\hat{J}_z$ is the projection of the electron total angular momentum onto the magnetic field axis. The fine structure splitting between the $5D_{5/2}$ and the $5D_{3/2}$ is around 24 THz [55], and there is no fine structure splitting in the $6S$ level. The Landé g-factors are in the order of 1 (for the $6S_{1/2}$ and the $5D_{5/2}$ levels, they are approximately $g_J = 2$ [66] and $g_J = 6/5$ [67] respectively), and J_z is in the order of $\hbar$. Thus, the Zeeman energy level splittings is in the order of $\mu_B B_e$, which corresponds to a frequencies in the order of $\frac{\mu_B}{h} B_e \approx (1.4\,\text{MHz/G}) \times B_e$, where h is the Planck constant. For typical magnetic field strengths in a trapped ion experiment, which is in the order of 1 G, the Zeeman splittings is in the order of 1 MHz, which is much lower than the fine structure splitting in the $5D$ level of 24 THz. Therefore, we can accurately approximate the energy eigenstates of the $6S_{1/2}$ and $5D_{5/2}$ levels to be the fine structure eigenstates $|J, m_J\rangle$, and the energy level splittings to be linear with magnetic field strength.

We now consider $^{137}Ba^+$, which has a nuclear spin of $I = 3/2$ and thus a non-zero $\hat{H}_{HF}$ term. The hyperfine splittings $\hat{H}_{HF}$ of the $5D$ levels are in an order of less than 1 GHz [60], which are much lower than the fine splitting of 24 THz. Thus, we can obtain accurate

estimates of the energy level splittings of each fine structure (J) level by considering only the reduced Hamiltonian sub-space.

$$\hat{H}_R = \hat{H}_{HF} + \hat{H}_Z. \tag{4.3}$$

Taking into account the magnetic dipole and electric quadrupole coupling of the nuclear spin and the electron angular momentum, $\hat{H}_R$ can be expressed as

$$\begin{aligned}\hat{H}_R = &\frac{2\pi A_D}{\hbar}\vec{I}\cdot\vec{J} + hB_Q\frac{\frac{3}{\hbar^4}\left(\vec{I}\cdot\vec{J}\right)^2 + \frac{3}{2\hbar^2}\vec{I}\cdot\vec{J} - I\left(I+1\right)J\left(J+1\right)}{2I\left(2I-1\right)J\left(2J-1\right)} \\ &+ \frac{B_e\mu_B}{\hbar}\left(g_J\hat{J}_z + g_I\hat{I}_z\right),\end{aligned} \tag{4.4}$$

where A_D is the magnetic dipole hyperfine structure constant, B_Q is the electric quadrupole hyperfine structure constant, $\vec{I}$ and $\vec{J}$ are the nuclear and electron angular momentum vectors respectively, I and J are the nuclear and electron angular momentum numbers respectively, m_I and m_J are the nuclear and electron angular momenta along the magnetic field axis respectively, and g_I and g_J denote the nuclear and electron g-factor respectively. For the $6S_{1/2}$ level, $A_D = 4018.871\,\text{MHz}$ and $B_Q = 0$ [59]. This leads to a hyperfine splitting of the $F = 1$ and $F = 2$ level to be around 8 GHz, where F is the hyperfine total angular momentum number, $\vec{F} = \vec{J} + \vec{I}$. This is much larger than the Zeeman effect Hamiltonian in the order of $\frac{\mu_B}{h}B_e \approx (1.4\,\text{MHz/G}) \times B_e$ for B_e in the order of 1 G. Thus, the $6S_{1/2}$ energy eigenstates can be approximated with the hyperfine structure eigenstates $|F, m_F\rangle$, with energy level splittings that are linear with B_e for each hyperfine level. For the $5D_{5/2}$ level, $A_D = -12.028\,\text{MHz}$ and $B_Q = 59.533\,\text{MHz}$ [60] (more precise values of the hyperfine constants, including the octupole moment is available at Ref. [68] should simulations with high precision are desired). This leads to a hyperfine energy level splitting in the $F = 3$ and $F = 4$ levels of $\sim 486\,\text{kHz}$ [60], which is smaller than the Zeeman effect Hamiltonian, which is in the order of 1 MHz. Therefore, we cannot approximate the energy eigenstates as the hyperfine $|F, m_F\rangle$ states, and we need to solve 4.4 to find the energy eigenvalues.

We solve Eq. 4.4 for the $5D_{5/2}$ level in the $|I, m_I; J, m_J\rangle = |I, m_I\rangle \otimes |J, m_J\rangle$ basis numerically. The $|I, m_I\rangle$ and $|J, m_J\rangle$ states are expressed in vector forms of dimensions $2I + 1$ and $2J + 1$ respectively, resulting in a vector space dimension for $|I, m_I\rangle \otimes |J, m_J\rangle$ of $(2I + 1)(2J + 1) = 24$. The $\vec{I}\cdot\vec{J}$ operator is expressed in the matrix form as

$$\vec{I}\cdot\vec{J} = \hat{I}_x \otimes \hat{J}_x + \hat{I}_y \otimes \hat{J}_y + \hat{I}_z \otimes \hat{J}_z, \tag{4.5}$$

where

$$
\begin{aligned}
\hat{K}_x &= \frac{1}{2}\left(\hat{K}_+ + \hat{K}_-\right) \\
\hat{K}_y &= -\frac{i}{2}\left(\hat{K}_+ - \hat{K}_-\right) \\
\hat{K}_z &= \sum_{m_K} \hbar m_K |K, m_K\rangle\langle K, m_K| \\
\hat{K}_+ &= \sum_{m_K} \hbar\sqrt{K(K+1) - m_K(m_K+1)}|K, m_K+1\rangle\langle K, m_K| \\
\hat{K}_- &= \sum_{m_K} \hbar\sqrt{K(K+1) - m_K(m_K-1)}|K, m_K-1\rangle\langle K, m_K|,
\end{aligned}
\tag{4.6}
$$

and $K \in \{I, J\}$. Having constructed the Hamiltonian in its matrix representation, the matrix is then diagonalized and the eigenvalues and eigenvectors extracted, which is done using MATLAB's eig() function in this work.

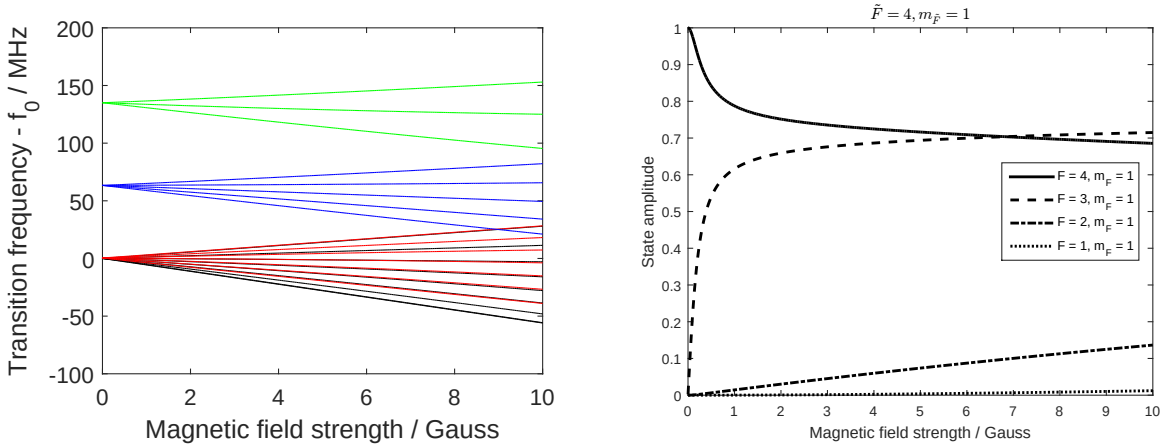

(a) (b)

Figure 4.1: (a) Simulated transition energy levels to the $5D_{5/2}$ states from the $|\tilde{F} = 2, m_{\tilde{F}} = 2\rangle$ state in the $6S_{1/2}$ level. The colored lines denote the $\tilde{F} = 1$ (green), $\tilde{F} = 2$ (blue), $\tilde{F} = 3$ (red), and $\tilde{F} = 4$ (black) states. f_0 is the transition frequency to the $F = 4$ level at zero magnetic field strength. (b) A representative plot of the simulated energy eigenstates, illustrating the mixing of the zero-field eigenstates. The $|\tilde{F} = 4, m_{\tilde{F}} = 1\rangle$ energy eigenstate is expressed in the $|F, m_F\rangle$ basis for magnetic field strengths from 0 to 10 G. Components with zero amplitudes are not plotted.

We define $|J, \tilde{F}, m_{\tilde{F}}\rangle, J \in \{S_{1/2}, 5D_{5/2}\}$ to be the energy eigenstates that approach the hyperfine $|J, F, m_F\rangle$ states at low magnetic field strengths, i.e. $|\tilde{F}, m_{\tilde{F}}\rangle \approx |F, m_F\rangle$ as $B_e \to 0$. From Figure 4.1, it can be seen that the $|5D_{5/2}, \tilde{F}, m_{\tilde{F}}\rangle$ state evolves quickly as B_e increases from 0 G to 0.2 G. The state does not change significantly upon further increase of B_e beyond 1 G. This trend applies to other states with $\tilde{F} = 3$ and $\tilde{F} = 4$ except for states with $m_{\tilde{F}} = \pm 4$ (see Appendix F). If one wishes to work with $^{137}Ba^+$ with its $5D_{5/2}$ energy eigenstates being in the low-magnetic-field $|F, m_F\rangle$ states, the magnetic field has to be lower than 0.2 G. This is however, not practical, as having weak Zeeman splittings disables the ability to perform fluorescence readout and Doppler cooling of the ion (with 493 nm and 650 nm lasers) due to the emergence coherent dark states [53]. Thus, if one wishes to use the $5D_{5/2}$ states in $^{137}Ba^+$ for quantum computing, it may be inevitable to work in the regime where the energy eigenstates of the $5D_{5/2}$ level being significantly different from the hyperfine $|F, m_F\rangle$ states.

4.1.2 Quadrupole Transitions

Starting from a classical picture, the potential energy of a charge distribution, $\rho(\vec{r})$, in an external electric potential energy $V(\vec{r})$ is

$$H_E = \int_{\vec{r}} \rho(\vec{r})\, V(\vec{r})\, d\vec{r} \tag{4.7}$$

Assuming that the charge distribution is centralized and spatial variation in $V(\vec{r})$ is much smaller over the volume of the charge distribution, we can approximate $V(\vec{r})$ with its Taylor expansion about $r = 0$ for the calculation of H_E.

$$H_E = \int_{\vec{r}} \rho(\vec{r}) \left[V(0) + \sum_{r_\alpha} r_\alpha \left.\frac{\partial V}{\partial r_\alpha}\right|_{r=0} + \frac{1}{2} \sum_{r_\alpha} \sum_{r_\beta} r_\alpha r_\beta \left.\frac{\partial^2 V}{\partial r_\beta \partial r_\alpha}\right|_{r=0} + \dots \right] d\vec{r}, \tag{4.8}$$

where $\alpha, \beta \in \{x, y, z\}$ indicate the three-dimensional Cartesian axes. Keeping only the terms up to the second derivatives, we have

$$\begin{aligned} H_E &\approx \int_{\vec{r}} \rho(\vec{r}) \left[V(0) + \sum_{r\alpha} r_\alpha \left.\frac{\partial V}{\partial r_\alpha}\right|_{r=0} + \frac{1}{2} \sum_{r_\alpha} \sum_{r_\beta} r_\alpha r_\beta \left.\frac{\partial^2 V}{\partial r_\beta \partial r_\alpha}\right|_{r=0} \right] d\vec{r} \\ &= V(0) \int_{\vec{r}} \rho(\vec{r})\, d\vec{r} + \sum_{r_\alpha} \left.\frac{\partial V}{\partial r_\alpha}\right|_{r=0} \int_{\vec{r}} \rho(\vec{r})\, r_\alpha d\vec{r} + \frac{1}{2} \sum_{r_\alpha} \sum_{r_\beta} \left.\frac{\partial^2 V}{\partial r_\beta \partial r_\alpha}\right|_{r=0} \int_{\vec{r}} \rho(\vec{r})\, r_\alpha r_\beta d\vec{r}. \end{aligned} \tag{4.9}$$

In Eq. 4.9, the first term is a constant shift of the energy, the second term is the electric dipole energy, and the third term is the electric quadrupole energy. As alluded in the title of this section, we will focus on the quadrupole energy term in this discussion. Now, consider a quantum system of electron orbital states with a finite Hilbert space. Without loss of generality, let the dimension of the Hilbert space be N, we can define an orthonormal basis set $\{|b_j\rangle\}, j \in \{1, 2, \ldots, N\}$, the electric quadrupole energy term can be expressed in an operator form as

$$\begin{aligned}\hat{H}_Q &= \frac{1}{2}\sum_{r_\alpha}\sum_{r_\beta}\left.\frac{\partial^2 V}{\partial r_\beta \partial r_\alpha}\right|_{r=0}\int_{\vec{r}}\rho\left(\vec{r}\right) r_\alpha r_\beta d\vec{r} \\ &= \frac{\mathbf{e}}{2}\sum_{r_\alpha}\sum_{r_\beta}\sum_{j=1}^{N}\sum_{k=1}^{N}\left.\frac{\partial^2 V}{\partial r_\beta \partial r_\alpha}\right|_{r=0}\langle b_j|\hat{r}_\alpha\hat{r}_\beta|b_k\rangle|b_j\rangle\langle b_k|,\end{aligned} \tag{4.10}$$

where $\mathbf{e}$ is the electron charge. Let the external field be a linearly polarized laser field with an electric field amplitude of E_0, represented by

$$E\left(\vec{r},t\right) = E_0\cos\left(\vec{k}\cdot\vec{r}-\omega t\right)\left(\epsilon_x\vec{n}_x+\epsilon_y\vec{n}_y+\epsilon_z\vec{n}_z\right), \tag{4.11}$$

where $\vec{n}_j$ is the unit vector along the j-axis, and ϵ_j is the polarization component along the j-axis, $\sum_j|\epsilon_j|^2 = 1$, $\vec{k}$ is the laser wave vector, ω is the laser frequency, and t is time. The $\left.\frac{\partial^2 V}{\partial r_\beta \partial r_\alpha}\right|_{r=0}$ factor in the quadrupole energy term is then

$$\left.\frac{\partial^2 V}{\partial r_\beta \partial r_\alpha}\right|_{r=0} = E_0\epsilon_\alpha k_\beta\cos\left(\omega t\right). \tag{4.12}$$

Suppose the basis states $\{|b_j\rangle\}$ are also the energy eigenstates of the unperturbed Hamiltonian of the system, with energy eigenvalues of $\{\hbar\omega_j\}$, and that the dipole energy is zero ($\langle b_j|\hat{r}_\alpha|b_k\rangle = 0$). With Eqs. 4.10 and 4.12, the Hamiltonian in the interaction picture with respect to the unperturbed Hamiltonian is

$$\hat{H}_I = \frac{\mathbf{e}E_0}{2}\sum_{r_\alpha}\sum_{r_\beta}\sum_{j=1}^{N}\sum_{k=1}^{N}\epsilon_\alpha k_\beta\langle b_j|\hat{r}_\alpha\hat{r}_\beta|b_k\rangle\cos\left(\omega t\right)e^{i\omega_{jk}t}|b_j\rangle\langle b_k|, \tag{4.13}$$

where $\omega_{jk} = \omega_j - \omega_k$. Suppose that the laser frequency is resonant with one of the transitions, let it be $|b_1\rangle \leftrightarrow |b_2\rangle$, applying the rotating-wave approximation, the Hamiltonian is then

$$\hat{H}_I \approx \frac{\mathbf{e}E_0}{4}\left|\sum_{r_\alpha}\sum_{r_\beta}\epsilon_\alpha k_\beta\langle b_1|\hat{r}_\alpha\hat{r}_\beta|b_2\rangle\right|\left(e^{i\theta_Q}|b_1\rangle\langle b_2| + e^{-i\theta_Q}|b_2\rangle\langle b_1|\right), \tag{4.14}$$

where we have defined $\sum_{r_\alpha}\sum_{r_\beta}\epsilon_\alpha k_\beta\langle b_1|\hat{r}_\alpha\hat{r}_\beta|b_2\rangle = \left|\sum_{r_\alpha}\sum_{r_\beta}\epsilon_\alpha k_\beta\langle b_1|\hat{r}_\alpha\hat{r}_\beta|b_2\rangle\right| e^{i\theta_Q}$. With Eq. 4.14, we have arrived at a familiar form of a Hamiltonian, where transition $|b_1\rangle \leftrightarrow |b_2\rangle$ is being driven coherently with a Rabi frequency of $\Omega = \frac{\mathbf{e}E_0}{2\hbar}\left|\sum_{r_\alpha}\sum_{r_\beta}\epsilon_\alpha k_\beta\langle b_1|\hat{r}_\alpha\hat{r}_\beta|b_2\rangle\right|$. In a system with spherical symmetry, which is true for electron orbitals, it is more convenient to work in the spherical coordinates, and thus converting the Cartesian tensor operators to spherical tensor operators. Converting $\hat{r}_\alpha\hat{r}_\beta$ from a Cartesian rank-2 tensor to a spherical rank-2 tensor gives

$$\begin{aligned}
\hat{r}_x\hat{r}_x &= \frac{1}{2}\hat{T}_2^{(2)} - \frac{1}{\sqrt{6}}\hat{T}_0^{(2)} + \frac{1}{2}\hat{T}_{-2}^{(2)} - \frac{1}{\sqrt{3}}\hat{T}_0^{(0)} \\
\hat{r}_y\hat{r}_y &= -\frac{1}{2}\hat{T}_2^{(2)} - \frac{1}{\sqrt{6}}\hat{T}_0^{(2)} - \frac{1}{2}\hat{T}_{-2}^{(2)} - \frac{1}{\sqrt{3}}\hat{T}_0^{(0)} \\
\hat{r}_z\hat{r}_z &= \frac{2}{\sqrt{6}}\hat{T}_0^{(2)} - \frac{1}{\sqrt{3}}\hat{T}_0^{(0)} \\
\hat{r}_x\hat{r}_y &= \hat{r}_y\hat{r}_x = -\frac{i}{2}\hat{T}_2^{(2)} + \frac{i}{2}\hat{T}_{-2}^{(2)} \\
\hat{r}_x\hat{r}_z &= \hat{r}_z\hat{r}_x = -\frac{1}{2}\hat{T}_1^{(2)} + \frac{1}{2}\hat{T}_{-1}^{(2)} \\
\hat{r}_y\hat{r}_z &= \hat{r}_z\hat{r}_y = \frac{i}{2}\hat{T}_1^{(2)} + \frac{i}{2}\hat{T}_{-1}^{(2)},
\end{aligned} \tag{4.15}$$

where the spherical rank-2 tensor operators, $T_q^{(k)}$, are [69]

$$\begin{aligned}
\hat{T}_0^{(0)} &= -\frac{1}{\sqrt{3}}\left(\hat{r}_x^2 + \hat{r}_y^2 + \hat{r}_z^2\right) \\
\hat{T}_0^{(2)} &= -\frac{1}{\sqrt{6}}\left(-\hat{r}_x^2 - \hat{r}_y^2 + 2\hat{r}_z^2\right) \\
\hat{T}_{\pm1}^{(2)} &= \mp\hat{r}_z\hat{r}_x \pm i\hat{r}_z\hat{r}_y \\
\hat{T}_{\pm2}^{(2)} &= \frac{\hat{r}_x^2 + \hat{r}_y^2}{2} \pm i\hat{r}_x\hat{r}_y.
\end{aligned} \tag{4.16}$$

Plugging Eq. 4.15 into Eq. 4.14 gives

$$\hat{H}_I \approx \frac{\mathbf{e}E_0}{4}\left|\sum_q\sum_{r_\alpha}\sum_{r_\beta}\epsilon_\alpha k_\beta c_{\alpha,\beta,q}\langle b_1|\hat{T}_q^{(2)}|b_2\rangle\right|\left(e^{i\theta_Q}|b_1\rangle\langle b_2| + e^{-i\theta_Q}|b_2\rangle\langle b_1|\right), \tag{4.17}$$

where $c_{\alpha,\beta,q}$ are the coefficients for the corresponding $\hat{T}_q^{(2)}$ operator found in Eq. 4.16, and we have omitted the $\hat{T}_0^{(0)}$ operator as it does not drive transitions between two angular momentum states.

For a quadrupole transition driven only by the q^{th} component, the Hamiltonian is

$$\hat{H}_I \approx \frac{\mathbf{e}kE_0}{4}\left|\langle b_1|\hat{T}^{(2)}_q|b_2\rangle\right|\left|\sum_{r_\alpha}\sum_{r_\beta}\frac{\epsilon_\alpha k_\beta}{k}c_{\alpha,\beta,q}\right|\left(e^{i\theta_Q}|b_1\rangle\langle b_2| + e^{-i\theta_Q}|b_2\rangle\langle b_1|\right). \tag{4.18}$$

The factor $\left|\sum_{r_\alpha}\sum_{r_\beta}\frac{\epsilon_\alpha k_\beta}{k}c_{\alpha,\beta,q}\right|$ is dependent on the geometry of the laser beam pointing and polarization. Evaluating this factor gives us the insight of which q^{th} transition can be driven and how strong, which we will do now. Without loss of generality, let $\vec{k}$ be in the xz-plane, and the angle θ_k to be the angle from the z-axis. This gives

$$\frac{\vec{k}}{k} = \sin(\theta_k)\hat{n}_x + \cos(\theta_k)\hat{n}_z \tag{4.19}$$

Using the property $\vec{k}\cdot\vec{E} = 0$, we have

$$\epsilon_z\cos(\theta_k) = -\epsilon_x\sin(\theta_k). \tag{4.20}$$

Let θ_p be the polarization angle from the xy-plane. We then have

$$\vec{\epsilon} = \cos(\theta_p)\cos(\theta_k)\hat{n}_x + \sin(\theta_p)\hat{n}_y - \cos(\theta_p)\sin(\theta_k)\hat{n}_z \tag{4.21}$$

Using Eqs. 4.15, 4.19 and 4.21, the geometric factor for each q can be derived to be

$$\begin{aligned} g^{(q=0)}(\theta_p,\theta_k) &= \frac{\sqrt{6}}{4}\left|\cos(\theta_p)\sin(2\theta_k)\right| \\ g^{(q=\pm1)}(\theta_p,\theta_k) &= \frac{1}{2}\left|\mp\cos(\theta_p)\cos(2\theta_k) + i\sin(\theta_p)\cos(\theta_k)\right| \\ g^{(q=\pm2)}(\theta_p,\theta_k) &= \frac{1}{4}\left|\cos(\theta_p)\sin(2\theta_k) \mp 2i\sin(\theta_p)\sin(\theta_k)\right| \end{aligned} \tag{4.22}$$

Thus, Eq. 4.18 can be simplified to

$$\hat{H}_I \approx E_0\left|\langle b_1|\hat{Q}_q|b_2\rangle\right| g^{(q)}(\theta_p,\theta_k)\left(e^{i\theta_Q}|b_1\rangle\langle b_2| + e^{-i\theta_Q}|b_2\rangle\langle b_1|\right), \tag{4.23}$$

where I have defined $\hat{Q}_q = \frac{\mathbf{e}k}{4}\hat{T}^{(2)}_q$. From Fig. 3.3, we can see that our wavevector angle of interest is $\theta_k = 45°$. At this wavevector angle, the laser polarization can be tuned to completely suppress $q = 0$ or $q = \pm1$ transitions at $\theta_p = 90°$ and $\theta_p = 0°$ respectively. I note that the $c_{\alpha,\beta,q}$ factors derived in this work differ from Ref. [3], which I used as a study reference, by a constant factor of $\sqrt{\frac{3}{2}}$, which may be due to using a different scaled forms of the spherical tensor operators in Eq. 4.16. The difference in the $c_{\alpha,\beta,q}$ factors also lead to a constant factor difference of the geometric factors $g^{(q}(\theta_p,\theta_k)$ compared to Refs. [70, 71]. Nevertheless, the difference of a constant factor does not change any qualitative analysis in this work.

4.1.3 Relative Transition Strengths in the Intermediate-Field Zeeman Effect

We have seen in Section 4.1.1 that it may be practically inevitable to work with $^{137}Ba^{+}$ in at the the intermediate-field Zeeman effect regime. In this section, we will study how that affects the transition strengths of the $6S_{1/2} \leftrightarrow 5D_{5/2}$ transitions, which we will see to be non-trivial. Substituting an energy eigenstate in the $6S_{1/2}$ level, $|6S_{1/2}, \tilde{F}, m_{\tilde{F}}\rangle$, and an energy eigenstate in the $5D_{5/2}$ level, $|5D_{5/2}, \tilde{F}, m_{\tilde{F}}\rangle$, into $|b_1\rangle$ and $|b_2\rangle$ of Eq. 4.23, we obtain

$$\begin{aligned}\hat{H}_I \approx E_0 \left|\langle 5D_{5/2}, \tilde{F}', m'_{\tilde{F}}|\hat{Q}_q|6S_{1/2}, \tilde{F}, m_{\tilde{F}}\rangle\right| g^{(q)}\left(\theta_p, \theta_k\right) \\ \times \left(e^{i\theta_Q}|5D_{5/2}, \tilde{F}', m'_{\tilde{F}}\rangle\langle 6S_{1/2}, \tilde{F}, m_{\tilde{F}}| + e^{-i\theta_Q}|6S_{1/2}, \tilde{F}, m_{\tilde{F}}\rangle\langle 5D_{5/2}, \tilde{F}', m'_{\tilde{F}}|\right).\end{aligned} \tag{4.24}$$

Using Wigner-Eckart theorem, the $\langle 5D_{1/2}, \tilde{F}', m'_{\tilde{F}}|\hat{Q}_q|6S_{1/2}, \tilde{F}, m_{\tilde{F}}\rangle$ factor can be decomposed into a reduced matrix element independent of q, and a factor that we can compute. To show that, we start by expressing an energy eigenstate $|J, \tilde{F}, m_{\tilde{F}}\rangle$ in the $|m_I, m_J\rangle$ basis. Rewriting $|\tilde{F}_L, m_{\tilde{F},L}\rangle = |L, \tilde{F}, m_{\tilde{F}}\rangle$ for brevity, where $L \in \{S, D\}$ denote the $6S_{1/2}$ and $5D_{5/2}$ levels, we have

$$|\tilde{F}_L, m_{\tilde{F},L}\rangle = \sum_{m_{I,L}, m_{J,L}} c_{m_{I,L}, m_{J,L}}|m_{I,L}, m_{J,L}\rangle. \tag{4.25}$$

Plugging in 4.25 into the factor $\langle \tilde{F}_D, m_{\tilde{F},D}|\hat{Q}_{q=m_{\tilde{F},D}-m_{\tilde{F},S}}|\tilde{F}_S, m_{\tilde{F},S}\rangle$ gives

$$\begin{aligned}&\langle \tilde{F}_D, m_{\tilde{F},D}|\hat{Q}_{q=m_{\tilde{F},D}-m_{\tilde{F},S}}|\tilde{F}_S, m_{\tilde{F},S}\rangle \\ &= \sum_{m_{I,D}, m_{J,D}} \sum_{m_{I,S}, m_{J,S}} c^*_{m_{I,D}, m_{J,D}} c_{m_{I,S}, m_{J,S}} \langle m_{I,D}, m_{J,D}|\hat{Q}_{q=m_{\tilde{F},D}-m_{\tilde{F},S}}|m_{I,S}, m_{J,S}\rangle.\end{aligned} \tag{4.26}$$

Since the electric quadrupole operator $\hat{Q}_q$ only acts on the electron angular momentum, and thus only the $|m_J\rangle$ sub-space, Eq. 4.26 can be rewritten as

$$\begin{aligned}&\langle \tilde{F}_D, m_{\tilde{F},D}|\hat{Q}_{q=m_{\tilde{F},D}-m_{\tilde{F},S}}|\tilde{F}_S, m_{\tilde{F},S}\rangle \\ &= \sum_{m_{I,D}, m_{J,D}} \sum_{m_{I,S}, m_{J,S}} c^*_{m_{I,D}, m_{J,D}} c_{m_{I,S}, m_{J,S}} \langle m_{J,D}|\hat{Q}_{q=m_{J,D}-m_{J,S}}|m_{J,S}\rangle \delta_{m_{I,S} m_{I,D}}.\end{aligned} \tag{4.27}$$

From Wigner-Eckart theorem, we have

$$\begin{aligned}
&\langle m_{J,D}|\hat{Q}_{q=m_{J,D}-m_{J,S}}|m_{J,S}\rangle \\
&= \langle J_D = 5/2, m_{J,D}|\hat{Q}_{q=m_{J,D}-m_{J,S}}|J_S = 1/2, m_{J,S}\rangle \\
&= \langle J_S = 1/2, m_{J,S}; k = 2, q = m_{J,D} - m_{J,S}|J_D = 5/2, m_{J,D}\rangle\langle J_D||\hat{Q}||J_S\rangle.
\end{aligned} \tag{4.28}$$

The $\langle J_S = 1/2, m_{J,S} = 1/2; k = 2, q = m_{J,D} - m_{J,S}|J_D = 5/2, m_{J,D}\rangle$ term is the Clebsch-Gordan coeffcient for coupling angular momenta J_S and k to get J_D, which we can compute (see Appendix B). With Eqs. 4.27 and 4.28, we have

$$\begin{aligned}
&\langle \tilde{F}_D, m_{\tilde{F},D}|\hat{Q}_{q=m_{\tilde{F},D}-m_{\tilde{F},S}}|\tilde{F}_S, m_{\tilde{F},S}\rangle \\
&= \langle J_D||\hat{Q}||J_S\rangle \sum_{m_{I,D},m_{J,D}} \sum_{m_{I,S},m_{J,S}} c^*_{m_{I,D},m_{J,D}} c_{m_{I,S},m_{J,S}} \delta_{m_{I,S}m_{I,D}} \\
&\times \langle J_S = 1/2, m_{J,S}; k = 2, q = m_{J,D} - m_{J,S}|J_D = 5/2, m_{J,D}\rangle \\
&= \langle J_D||\hat{Q}||J_S\rangle\langle \tilde{F}_S, m_{\tilde{F},S}; k = 2, q = m_{\tilde{F},D} - m_{\tilde{F},S}|\tilde{F}_D, m_{\tilde{F},D}\rangle,
\end{aligned} \tag{4.29}$$

where we have defined

$$\begin{aligned}
&\langle \tilde{F}_S, m_{\tilde{F},S}; k = 2, q = m_{\tilde{F},D} - m_{\tilde{F},S}|\tilde{F}_D, m_{\tilde{F},D}\rangle \\
&= \sum_{m_{I,D},m_{J,D}} \sum_{m_{I,S},m_{J,S}} c^*_{m_{I,D},m_{J,D}} c_{m_{I,S},m_{J,S}} \delta_{m_{I,S}m_{I,D}} \\
&\times \langle J_S = 1/2, m_{J,S}; k = 2, q = m_{J,D} - m_{J,S}|J_D = 5/2, m_{J,D}\rangle.
\end{aligned} \tag{4.30}$$

Since the $c_{m_{I,L},m_{J,L}}$ coefficients can be computed numerically as described in Section 4.1.1, the $\langle \tilde{F}_S, m_{\tilde{F},S}; k = 2, q = m_{\tilde{F},D} - m_{\tilde{F},S}|\tilde{F}_D, m_{\tilde{F},D}\rangle$ factor can be computed.

Finally, with Eqs. 4.24 and 4.29, the quadrupole transition Hamiltonian can be expressed as

$$\begin{aligned}
\hat{H}_I \approx E_0 &\left|\langle J_D||\hat{Q}||J_S\rangle\langle \tilde{F}_S, m_{\tilde{F},S}; k = 2, q = m_{\tilde{F},D} - m_{\tilde{F},S}|\tilde{F}_D, m_{\tilde{F},D}\rangle\right| g^{(q)}(\theta_p, \theta_k) \\
&\times \left(e^{i\theta_Q}|\tilde{F}_D, m_{\tilde{F},D}\rangle\langle \tilde{F}_S, m_{\tilde{F},S}| + e^{-i\theta_Q}|\tilde{F}_S, m_{\tilde{F}_S}\rangle\langle \tilde{F}_D, m_{\tilde{F},D}|\right).
\end{aligned} \tag{4.31}$$

Between any two $6S_{1/2} \leftrightarrow 5D_{5/2}$ transitions, the relative transition strengths (ignoring the common factors E_0 and $\left|\langle J_D||\hat{Q}||J_S\rangle\right|$ in Eq. 4.31) is

$$g^{(q)}(\theta_p, \theta_k)\,\langle \tilde{F}_S, m_{\tilde{F},S}; k = 2, q = m_{\tilde{F},D} - m_{\tilde{F},S}|\tilde{F}_D, m_{\tilde{F},D}\rangle. \tag{4.32}$$

As discussed in Section 4.1.2, the 1762 nm laser polarization can be tuned to fully suppress the $\Delta m = 0$ or $\Delta m = \pm 1$ transitions, which is undesirable for us. We set the laser polarization angle to $\theta_p = 58°$ so that all q transitions can be driven. Using Eq. 4.32, at $\theta_k = 45°$, $\theta_p = 58°$ and a magnetic field strength of $B_e = 8.35\,\mathrm{G}$ (see Section 4.4 for magnetic field strength estimation in our setup), the relative transition strengths from any $6S_{1/2}$ state to any $5D_{5/2}$ state are calculated and summarized in Table 4.1. The relative transition strengths from the $|6S_{1/2}, \tilde{F} = 2, m_{\tilde{F}} = 2\rangle$ are plotted in Fig. 4.2 and compared to empirically collected data (see Section 4.6.4), which shows good agreement with the theoretical model.

$5D_{5/2}$ state	$6S_{1/2}$ state							
	$\tilde{F}=1$			$\tilde{F}=2$				
	$m_{\tilde{F}}=-1$	$m_{\tilde{F}}=0$	$m_{\tilde{F}}=1$	$m_{\tilde{F}}=-2$	$m_{\tilde{F}}=-1$	$m_{\tilde{F}}=0$	$m_{\tilde{F}}=1$	$m_{\tilde{F}}=2$
$\tilde{F}=1, m_{\tilde{F}}=1$	0.262	0.137	0.070	0	0.065	0.057	0.048	**0.028**
$\tilde{F}=1, m_{\tilde{F}}=0$	0.189	0.188	0.120	0.084	**0.018**	**0.018**	0.035	0.047*
$\tilde{F}=1, m_{\tilde{F}}=-1$	0.136	0.170	0.206	0.066	0.062	0.040	**0.024**	0
$\tilde{F}=2, m_{\tilde{F}}=2$	0	0.239	0.121	0	0	0.124	0.103	0.071*
$\tilde{F}=2, m_{\tilde{F}}=1$	0.128	0.148	0.176	0	0.136	**0.010**	0.070	0.089*
$\tilde{F}=2, m_{\tilde{F}}=0$	0.158	0.071	0.182	0.097	0.084	0.083	**0.010**	0.089*
$\tilde{F}=2, m_{\tilde{F}}=-1$	0.191	0.038	0.189	0.124	**0.003**	0.067	0.096	0
$\tilde{F}=2, m_{\tilde{F}}=-2$	0.169	0.200	0	0.128	0.100	0.067	0	0
$\tilde{F}=3, m_{\tilde{F}}=3$	0	0	0.166	0	0	0	0.283	**0.004**
$\tilde{F}=3, m_{\tilde{F}}=2$	0	0.060	0.129	0	0	0.222	0.166	0.038*
$\tilde{F}=3, m_{\tilde{F}}=1$	**0.016**	0.076	0.118	0	0.140	0.218	0.085	0.045*
$\tilde{F}=3, m_{\tilde{F}}=0$	**0.028**	0.099	0.087	0.067	0.194	0.189	**0.005**	0.040*
$\tilde{F}=3, m_{\tilde{F}}=-1$	0.052	0.100	0.063	0.124	0.239	0.093	0.040	0
$\tilde{F}=3, m_{\tilde{F}}=-2$	0.077	0.103	0	0.214	0.189	**0.006**	0	0
$\tilde{F}=3, m_{\tilde{F}}=-3$	0.130	0	0	0.268	0.069	0	0	0
$\tilde{F}=4, m_{\tilde{F}}=4$	0	0	0	0	0	0	0	0.328*
$\tilde{F}=4, m_{\tilde{F}}=3$	0	0	0.124	0	0	0	0.078	0.268*
$\tilde{F}=4, m_{\tilde{F}}=2$	0	0.062	0.117	0	0	**0.001**	0.157	0.238*
$\tilde{F}=4, m_{\tilde{F}}=1$	**0.022**	0.085	0.116	0	**0.024**	0.058	0.221	0.159*
$\tilde{F}=4, m_{\tilde{F}}=0$	0.040	0.114	0.088	**0.021**	**0.006**	0.142	0.209	0.099*
$\tilde{F}=4, m_{\tilde{F}}=-1$	0.073	0.116	0.065	**0.030**	0.047	0.198	0.178	0
$\tilde{F}=4, m_{\tilde{F}}=-2$	0.102	0.118	0	**0.030**	0.131	0.244	0	0
$\tilde{F}=4, m_{\tilde{F}}=-3$	0.162	0	0	**0.005**	0.285	0	0	0
$\tilde{F}=4, m_{\tilde{F}}=-4$	0	0	0	0.328	0	0	0	0

Table 4.1: Relative transition strength factors $g^{(q)}(\theta_p, \theta_k)\langle \tilde{F}_S, m_{\tilde{F},S}; k=2, q=m_{\tilde{F},D}-m_{\tilde{F},S}|\tilde{F}_D, m_{\tilde{F},D}\rangle$ for $6S_{1/2} \leftrightarrow 5D_{5/2}$ transitions with $\theta_k = 45°$ and $\theta_p = 58°$ at a magnetic field strength of $B_e = 8.35\,\mathrm{G}$ of $^{137}Ba^+$. Non-zero values lower than 0.03 are in bold texts. The value of 0.03 is determined by empirically observing that the transitions weaker than this have large errors due to decoherence from the SPAM experiments in this work, which is also a value that is approximately an order of magnitude lower than the strongest transitions. *Transitions used in this work.

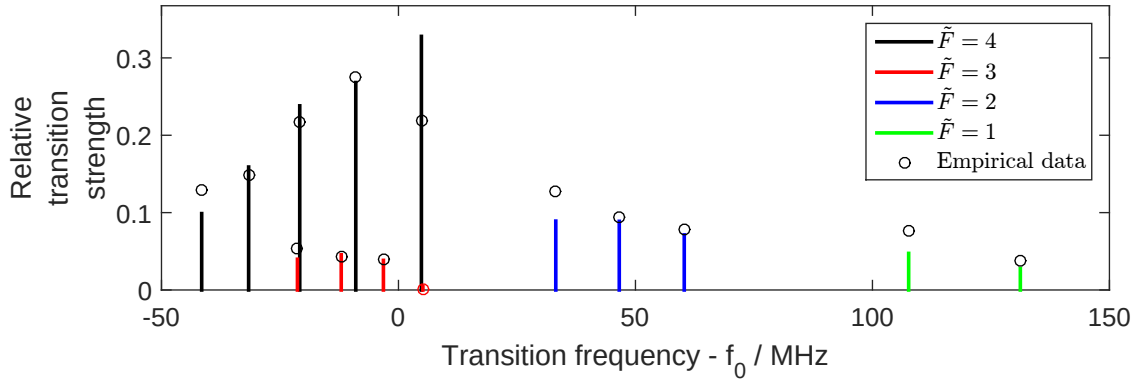

Figure 4.2: Theoretically estimated non-zero transition strengths to the $5D_{5/2}$ states from the $|6S_{1/2}, \tilde{F} = 2, m_{\tilde{F}} = 2\rangle$ state, relative to the reduced transition matrix element. The empirical data are scaled values of the measured Rabi frequencies. The error bars of the empirical data are smaller than the plot markers and are not plotted. The $|\tilde{F} = 3, m_{\tilde{F}} = 3\rangle$ relative transition strength is too weak to be clearly visible on the plot or accurately estimated experimentally due to coherence time limitations. The red marker is an upper bound of the empirically measured Rabi frequency for this transition.

4.1.4 Resolved Sideband Cooling

Consider a system with 2 internal electronic states and moving in a one-dimensional simple harmonic oscillator, which is a simplified model for a trapped ion. The static Hamiltonian can be expressed as

$$\begin{aligned} \hat{H} &= \hat{H}_{0,E} + \hat{H}_{0,M} \\ \hat{H}_{0,E} &= \hbar\omega_0 |0\rangle\langle 0| + \hbar\omega_1 |1\rangle\langle 1| \\ \hat{H}_{0,M} &= \hbar\omega_M \left(\hat{a}^\dagger \hat{a} + \frac{1}{2}\right) \end{aligned} \tag{4.33}$$

where $\hat{H}_{0,E}$ is the Hamiltonian of the internal energy states, $\hat{H}_{0,M}$ is the Hamiltonian of the motional states, $\hbar\omega_l$ is the internal energy of state $|l\rangle$, $l \in \{0, 1\}$, ω_M is the motional frequency, $\hat{a}^\dagger$ and $\hat{a}$ are the raising and lowering operators respectively of a quantum harmonic oscillator. Suppose that a laser field introducing a perturbation with the Hamiltonian of

$$\hat{H}_{int} = \hbar\Omega \cos\left(k\hat{x} - \omega t\right) \left(|0\rangle\langle 1| + |1\rangle\langle 0|\right). \tag{4.34}$$

This modifies the total Hamiltonian to

$$\hat{H} = \hat{H}_{0,E} + \hat{H}_{0,M} + \hat{H}_{int}. \tag{4.35}$$

In the interaction picture with respect to the static Hamiltonian, $\hat{H}_{0,E} + \hat{H}_{0,M}$, the Hamiltonian is

$$\hat{H}_I = \frac{\hbar\Omega}{2}\left(e^{-i\omega t}e^{ik\hat{x}_I} + e^{i\omega t}e^{-ik\hat{x}_I}\right)\left(e^{-i\omega_{10}t}|0\rangle\langle 1| + e^{i\omega_{10}t}|1\rangle\langle 0|\right), \tag{4.36}$$

where $\omega_{10} = \omega_1 - \omega_0$ and $\hat{x}_I$ is the position operator in the interaction picture. For small $kx \ll 1$, we can perform Taylor expansion on $e^{ik\hat{x}_I}$ and keeping only the first order term as an approximation, giving

$$\begin{aligned}\hat{H}_I \approx{}& \frac{\hbar\Omega}{2}\left(e^{-i\omega t} + e^{i\omega t}\right)\left(e^{-i\omega_{10}t}|0\rangle\langle 1| + e^{i\omega_{10}t}|1\rangle\langle 0|\right)\\ &+ i\frac{\hbar k\Omega}{2}\left(e^{-i\omega t}\hat{x}_I - e^{i\omega t}\hat{x}_I\right)\left(e^{-i\omega_{10}t}|0\rangle\langle 1| + e^{i\omega_{10}t}|1\rangle\langle 0|\right)\end{aligned} \tag{4.37}$$

Expressing the position operator in terms of the raising and lowering operator gives

$$\hat{x}_I = \sqrt{\frac{\hbar}{2\mathbf{m}\omega_M}}\left(e^{i\omega_M t}\hat{a}^\dagger + e^{-i\omega_M t}\hat{a}\right) \tag{4.38}$$

where $\mathbf{m}$ is the mass of the particle, which in our case is an ion. With Eq. 4.38, Eq. 4.36 can be expressed as

$$\begin{aligned}\hat{H}_I \approx{}& \frac{\hbar\Omega}{2}\left(e^{-i\omega t} + e^{i\omega t}\right)\left(e^{-i\omega_{10}t}|0\rangle\langle 1| + e^{i\omega_{10}t}|1\rangle\langle 0|\right)\\ &+ i\frac{\hbar\eta\Omega}{2}\left(e^{-i\omega t} - e^{i\omega t}\right)\left(e^{i\omega_M t}\hat{a}^\dagger + e^{-i\omega_M t}\hat{a}\right)\left(e^{-i\omega_{10}t}|0\rangle\langle 1| + e^{i\omega_{10}t}|1\rangle\langle 0|\right),\end{aligned} \tag{4.39}$$

where we have introduced the Lamb-Dicke parameter

$$\eta = k\sqrt{\frac{\hbar}{2\mathbf{m}\omega_M}}. \tag{4.40}$$

From, Eq. 4.39, there are three interesting values for the laser frequencies. With rotating wave approximation, which is valid when $\Omega \ll \omega_M$ and $\Omega \ll \omega_{10}$, we have

$$\begin{aligned}\hat{H}_I &\approx \frac{\hbar\Omega}{2}\left(|0\rangle\langle 1| + |1\rangle\langle 0|\right), \quad \omega = \omega_{10}\\ \hat{H}_I &\approx i\frac{\hbar\eta\Omega}{2}\left(-\hat{a}|0\rangle\langle 1| + \hat{a}^\dagger|1\rangle\langle 0|\right), \quad \omega = \omega_{10} + \omega_M\\ \hat{H}_I &\approx i\frac{\hbar\eta\Omega}{2}\left(-\hat{a}^\dagger|0\rangle\langle 1| + \hat{a}|1\rangle\langle 0|\right), \quad \omega = \omega_{10} - \omega_M\end{aligned} \tag{4.41}$$

When $\omega = \omega_{10}$, it is the usual Hamiltonian for driving a resonant transition between the two internal levels with a Rabi frequency of Ω. When $\omega = \omega_{10} - \omega_M$, it is driving the state from $|0\rangle$ to $|1\rangle$ with a reduction of one quantum of phonon, called a motional red sideband transition. If the motional state is in a pure Fock state $|n\rangle$, then the red sideband Rabi frequency is $\eta\Omega\sqrt{n}$. Conversely, when $\omega = \omega_{10} + \omega_M$, it is a motional blue sideband transition.

For the barium ion energy level structure shown in Fig. 3.1b and 3.1c, the $6S_{1/2} \leftrightarrow 5D_{5/2}$ transitions are expected to have narrow transition linewidths limited only by power broadening. The transition linewidth is expected to be much lower than 1 MHz, which is the order of secular motional frequency of our trapped ion. With resolvable sideband, the motional red sideband can be driven from the $6S_{1/2}$ level to the $5D_{5/2}$ to remove one motional quantum. The ion internal state can then be reset to the $6S_{1/2}$ level by pumping with 614 nm and 650 nm light as described in Section 4.1. A $6S_{1/2} \leftrightarrow 5D_{5/2}$ red sideband transition can be driven again to remove another motional quantum. Assuming that the 614 nm and 650 nm light pumping process has minimal heating effects, this process can be continuously repeated to perpetually remove motional state quanta until it reaches the $|n = 0\rangle$ motional Fock state. We will later see how this is actualized in this work in Section 4.5.1.

4.1.5 Modulation of Transition Frequencies From Trapped Ion Excess Micromotion

When there is some imperfection in the trapped ion voltages or electrode geometry, the ion can be moving at the electrode RF frequency Ω_{RF}, called the excess micromotion. A common cause of this effect is the offset of the electric pseudopotential minimum to the point with zero electric field from the oscillating saddle potential generated by the RF voltage, called the RF null. To study the effect of excess micromotion on a two-level transition, we model the Hamiltonian as follows. The interaction Hamiltonian introduced by a laser field is as shown in Eq. 4.34. A trapped ion excess micromotion moves at a constant amplitude [49], and we can model the motion as

$$x(t) = x_0 \cos(\Omega_{RF} t), \tag{4.42}$$

The interaction Hamiltonian is then

$$\begin{aligned} \hat{H}_{int} &= \hbar\Omega \cos(kx_0 \cos(\Omega_{RF} t) - \omega t)\,(|0\rangle\langle 1| + |1\rangle\langle 0|) \\ &= \frac{\hbar\Omega}{2}\left(e^{-i\omega t} e^{ikx_0 \cos(\Omega_{RF} t)} + e^{i\omega t} e^{-ikx_0 \cos(\Omega_{RF} t)}\right)(|0\rangle\langle 1| + |1\rangle\langle 0|) \end{aligned} \tag{4.43}$$

Using the Jacobi-Anger expansion, we can expand $e^{ikx_0\cos(\Omega_{RF}t)}$ as

$$e^{ikx_0\cos(\Omega_{RF}t)} = \sum_{n=-\infty}^{\infty} i^n J_n(kx_0)\, e^{in\Omega_{RF}t}, \tag{4.44}$$

where $J_n(kx_0)$ is the n^{th} Bessel function of the first kind. Going to the interaction picture, the Hamiltonian can now be expressed as

$$\begin{aligned}\hat{H}_I = \sum_{n=-\infty}^{\infty} i^n \frac{\hbar\Omega}{2} J_n(kx_0)\left(e^{-i\omega t}e^{in\Omega_{RF}t} + (-1)^n e^{i\omega t}e^{in\Omega_{RF}t}\right) \\ \times \left(e^{-i\omega_{10}t}|0\rangle\langle 1| + e^{i\omega_{10}t}|1\rangle\langle 0|\right).\end{aligned} \tag{4.45}$$

When the laser frequency is $\omega = \omega_{10} + m\Omega_{RF}, m \in \mathbb{Z}$, with rotating wave approximation, the Hamiltonian is then

$$\hat{H}_I \approx i^m \frac{\hbar\Omega}{2} J_m(kx_0)\left(|1\rangle\langle 0| + (-1)^m |0\rangle\langle 1|\right) \tag{4.46}$$

From Eq. 4.46, we can coherently drive the $|0\rangle \leftrightarrow |1\rangle$ transition at some integer multiples of the RF drive frequency from the carrier resonance, with Rabi frequencies of $\Omega J_m(kx_0)$. With larger excess micromotion, x_0, and subsequently larger $J_m(kx_0)$, leads to larger Rabi frequencies at the transition frequencies modulated by excess Hamiltonian. Since our trap RF voltage frequency is at $\sim 20\,\text{MHz}$, we expect to be able to resolve the excess-micromotion-modulated transitions with the $6S_{1/2} \leftrightarrow 5D_{5/2}$ transitions in a Ba^+ ion. Therefore, by measuring the excess-micromotion-modulated Rabi frequencies, it is a useful metric to detect imperfections in the ion trap or the minimum pseudopotential shift from the RF null. The realization of this utility will be discussed in Section 4.5.2.

4.2 Trap Setup for Qudit Experiments

This is a brief section that only describes the trap parameters that are used in this chapter, which has some changes from Chapter 3. The vacuum chamber has an air pressure of $1\times10^{-10}\,\text{mbar}$. RF voltages with an estimated amplitude of $V_{RF} = 230\,\text{V}$ and a frequency of $\Omega_{RF} = 20.772\,\text{MHz}$ are sent to the 4-rod electrodes. Static voltages of $V_S = 3\,\text{V}$ are sent to one pair of the diagonal rods to break the degeneracy of the ion radial secular motional frequencies. $10\,\text{V}$ of static voltage is applied to the needle electrodes for axial confinement. The magnetic field direction is set to $\vec{B}_{e,C4}$ in Fig. 3.3. This setup results in a trapped $^{137}Ba^+$ with radial secular motional frequencies of $1.2\,\text{MHz}$ and $1.4\,\text{MHz}$, and an axial motional frequency of $10\,\text{kHz}$.

4.3 Lasers and Optical Setup for Control of Ba^+ $5D_{5/2}$ States

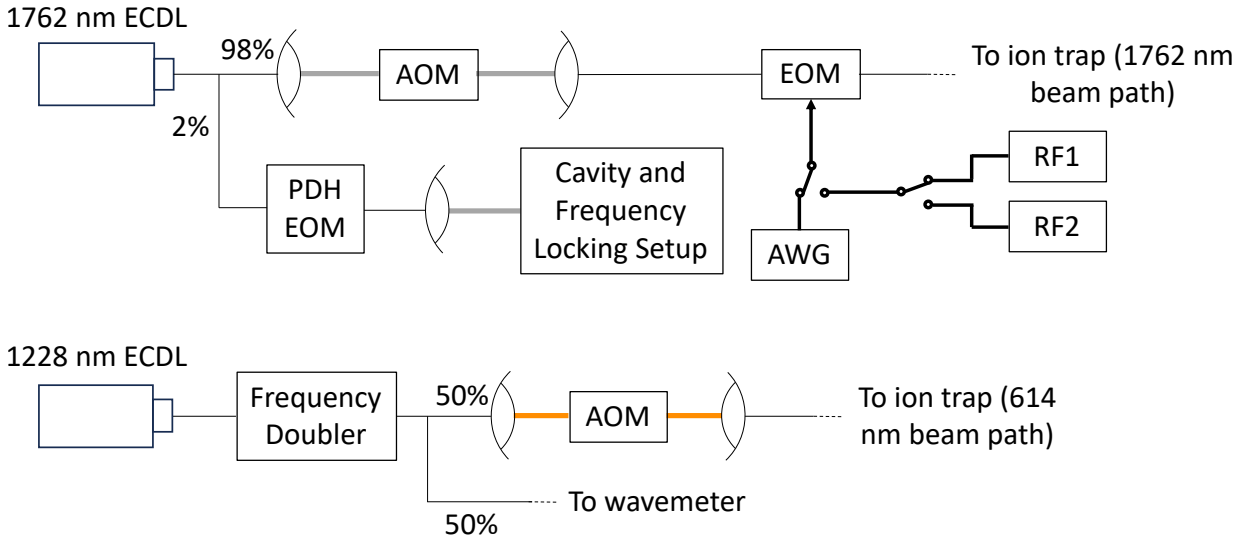

Figure 4.3: An illustration of the setup for the 1762 nm and 614 nm lasers. Optics for geometrical control of the laser beams are omitted. Thicker lines denote electrical connections instead of optical fibers. PDH EOM denotes the EOM for generating frequency sidebands for the Pound-Drever-Hall (PDH) frequency locking technique. AWG denotes an arbitrary waveform generator, which is the frequency source for the EOM of the 1762 nm light going to the ion trap during normal operations. The 1762 nm main beam EOM frequency source can be switched to other RF frequency synthesizers (labelled RF1 and RF2) using fast RF switchs.

Fig. 4.3 shows a simplified illustration of the setups of the 1762 nm and 614 nm lasers before they are sent to the ion trap in Fig. 3.3. The 1762 nm laser has 2% light picked off to be used for frequency locking with a setup built by Stable Laser Systems (SLS). In this frequency locking setup, the picked off laser is referenced and locked to a temperature-controlled Fabry–Pérot cavity in vacuum using the Pound-Drever-Hall (PDH) method. The PDH modulation signal sent to the PDH EOM for extracting the PDH readout function is hard-coded to be 5 MHz. An additional variable RF frequency (labelled as offset frequency by SLS, indicating offset to the Fabry–Pérot cavity mode) can be sent to the PDH EOM on top of the 5 MHz signal to generate a laser frequency sideband to be locked to a Fabry–Pérot cavity mode frequency, ω_{cavity}, instead of the carrier frequency. This

enables the 1762 nm laser carrier frequency, $\omega_{carrier}$, sent to the ion trap to be stabilized to any desired frequencies by choosing any offset frequency, Δ_{PDH}, to be sent to the PDH EOM, i.e. $\omega_{carrier} = \omega_{cavity} + \Delta_{PDH}$, where the sign of Δ_{PDH} dictates whether the blue or red-sideband of the PDH EOM offset frequency is chosen to be locked to the cavity mode. For normal operations, the 1762 nm laser carrier frequency is set to be off resonant to any $6S_{1/2} \leftrightarrow 5D_{5/2}$ transition frequencies, $\omega_{transition}$, and the EOM in the main power path of the 1762 nm laser generates a first-order frequency sideband resonant to the transition to be driven. The carrier frequency to be locked to is chosen such that the sideband modulation frequency to be generated for the main power EOM, Δ_{EOM}, is within the bandwidth allowed by hardware and the higher order sidebands from the EOM are not close to any $6S_{1/2} \leftrightarrow 5D_{5/2}$ transitions. Fig. 4.4 summarizes an example of 1762 nm EOMs frequency modulation setup for normal operations as described earlier. Driving the transitions with an EOM sideband allows fast switching of the sideband frequencies and thus the transitions to be driven, as opposed to driving them with the carrier frequency. The 614 nm laser has 50% light picked off to a wavemeter for readout of the laser frequency and feedback for frequency locking. The main power beam paths of both 1762 nm and 614 nm lasers pass through AOMs, which allow fast on/off switch of the laser beams at the ion trap.

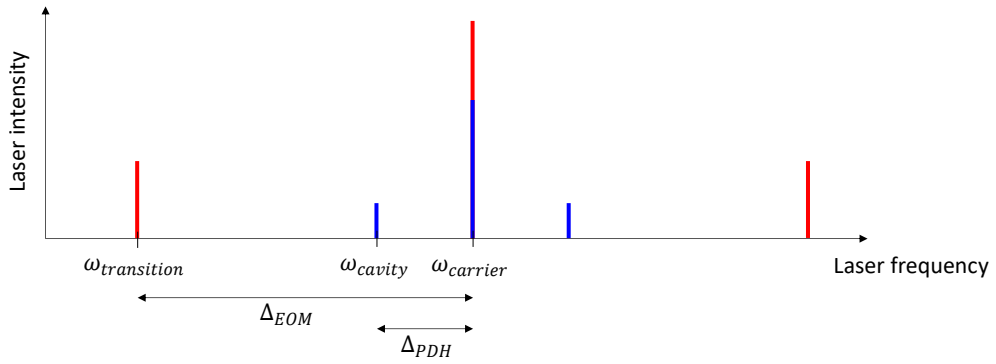

Figure 4.4: An illustration of an example of the 1762 nm laser frequencies sent to the ion trap (red lines) and the PDH locking system (blue lines). In this example, the red sideband of the PDH EOM frequency is locked to a Fabry–Pérot cavity mode, and the red sideband of the main laser power EOM is used to drive an energy level transition.

At the ion trap, as shown in Fig. 3.3, the 1762 nm and 614 nm laser output powers are 2.0 mW and 15 µW respectively. The 1762 nm laser is collimated with a reflective collimator, to allow light of other wavelengths to be collimated through the same beam path as well, which helps with beam alignments (discussed in Section 4.3.1). The 1762 nm laser beam is sent to the ion at an angle perpendicular to the four-rod trap axial axis to

minimize coupling of the transitions to the axial motional mode. At the ion position, the beam diameter is estimated to be focused to a size of

$$D_{focus} = \frac{f_{CM}}{f_{FC}} \frac{|f_{T1}|}{|f_{T2}|} D_{fiber} = \frac{150\,\text{mm}}{33\,\text{mm}} \frac{100\,\text{mm}}{200\,\text{mm}} 10.1\,\mu\text{m} \approx 23\,\mu\text{m}, \tag{4.47}$$

where f_{T1} and f_{T2} are the focal lengths of the first and second optics in the telescope setup. The 1762 nm beam direction as shown in Fig. 3.3 is chosen to minimize coupling to the axial motional mode of the ion. The 614 nm beam is combined with the 405 nm laser beam path with a dichroic mirror and focused to an estimated beam diameter of 53 µm at the ion.

To be able to send a σ_+-polarized 493 nm light to the ion for optical pumping (as described in Section 4.1), a static magnetic field is generated parallel to the optical pumping beam in Fig. 3.3. A Glan-Thompson polarizer is used to ensure the beam is highly linearly polarized before reaching the QWP. The QWP is set to an angle which converts a linearly polarized light to a circularly polarized light. The beam is then focused at the ion at a beam diameter estimated to be 70 µm.

4.3.1 Initial Laser Beam Alignments for Ba^+ Control of $5D_{5/2}$ States

In this section, I describe the methods we employed to align the laser beams relevant to the coherent controls of the $6S_{1/2}$ and $5D_{5/2}$ states, up to the point where we can detect the beams are reaching the ions, but not necessarily fully fine-tuned to match the centre of the beam profile to the ion position. The methods to further optimize the laser beam pointings are discussed in Section 4.6.2.

First, a $^{138}Ba^+$ ion is trapped. To align the 493 nm optical pump beam, the following procedure is done:

1. The magnetic field direction is switched to being vertical to the vacuum chamber to ensure the magnetic field axis perpendicular to the 493 nm optical pump beam, so that the beam will fluoresce the ion with any polarization.

2. The 493 nm optical pump beam pointing is then tuned to completely overlap with the 405 nm light beam path without the Glan-Thompson polarizer and the QWP in place.

3. The 493 nm light in the combined beam path is then turned off, but keeping the 650 nm light on, so that the ion would fluoresce if the 493 nm optical pump beam is aligned to the ion. We find that it is always sufficiently aligned to see ion fluorescence driven by the 493 nm optical pump beam after Step 2 is done.

4. Tune the 493 nm optical pump beam pointing to maximize fluorescence on the ion.

5. Set up the Glan-Thompson polarizer and the QWP in place, ensuring the back reflected 405 nm and 493 nm beams go back to the themselves to ensure the 493 nm beam is perfectly perpendicular on the QWP.

Since the 405 nm beam is already aligned to be parallel to the magnetic field coils along its direction of propagation (see Chapter 3.2.1), the 493 nm optical pump beam will be parallel to the magnetic field during optical pumping operations. To generate a circularly polarized 493 nm, the vertical magnetic field coils are turned off and the coils parallel to the optical pumping beam are turned on. The QWP is then rotated until fluorescence on the ion is minimized.

To align the 614 nm beam to the ion, the following procedure is done:

1. The 614 nm beam path collimator and the redirecting plane mirror for it are mounted on tunable mirror mounts. These two mirror mounts are used to independently tune the 614 nm path without affecting the 405 nm beam path. The 614 nm laser beam is tuned to perfectly overlap with the 405 nm beam.

2. The 650 nm laser for the combined beam path is rerouted to the 614 nm beam path.

3. The 493 nm laser in the combined beam path is turned on, together with the 650 nm laser, so that the trapped ion will fluoresce when the 614 nm beam path is aligned. We find that fluorescence is always visible after Step 1 is done.

4. Further optimize the beam pointing by tuning the mirror mounts used in Step 1 by maximizing ion fluorescence.

5. Reroute the 650 nm light to the combined beam path and the 614 nm laser to the 614 nm beam path.

To align the 1762 nm beam to the ion, the following procedure is done:

1. The 650 nm laser for the combined beam path is rerouted to the 1762 nm beam path.

2. The method for aligning the beam to the approximate trap center using the M.M. scale readings by observing the scattering of light on the trap needle electrodes as discussed in Chapter 3.2.1 is done.

3. The 493 nm laser in the combined beam path is turned on, together with the 650 nm laser, so that the trapped ion will fluoresce when the 1762 nm beam path is aligned.

4. Further optimize the beam pointing by maximizing ion fluorescence while making sure the beam exits through the center of the exit viewport.

5. Reroute the 650 nm light to the combined beam path and the 1762 nm laser to the 1762 nm beam path.

4.3.2 Initial Frequency Calibration for 1762 nm and 614 nm Lasers

Due to the long spontaneous decay time of the $5D_{5/2}$ level, the transition linewidth from the $6S_{1/2}$ level is extremely narrow at sub-Hz and only broadened by power broadening. Therefore, one might intuitively think that the search for the range of 1762 nm frequencies that is close to the $6P_{1/2} \leftrightarrow 5D_{5/2}$ will be a long and arduous process. This is, fortunately, not the case as there is a method to allow us to see fluorescence response from the ion even when the 1762 nm is off-resonant by hundreds of megahertz. This is done by turning the 493 nm, 650 nm, and 1762 nm lasers on at the same time. When the 1762 nm laser frequency is within a resonant transition frequency in the order of ~ 100 MHz, we observe flip-flopping of the ion fluorescence between bright and dark as shown in Fig. 4.5. The flip-flopping rate of the ion fluorescence increases as the 1762 nm laser frequency is closer to a resonant transition, which helps narrowing down the range of 1762 nm to within ~ 100 MHz of the resonant transitions. An inconclusive attempt to study this phenomenon by modelling it with optical Bloch equations is presented in Appendix G.

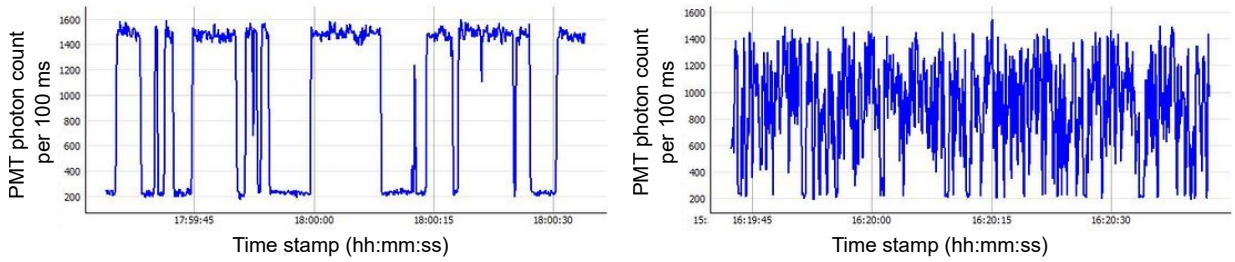

(a) (b)

Figure 4.5: Fluorescence flip-flopping of a $^{138}Ba^{+}$ ion when the 493 nm, 650 nm, and 1762 nm lasers are turned on, with the 1762 nm laser frequency detuning at (a) ~ 200 MHz and (b) < 50 MHz.

With the wide frequency response of the bright/dark states flip-flopping, starting from a point where the 1762 nm laser resonant frequencies are not known, we can calibrate the 1762 nm laser frequency to within ~ 50 MHz of the transition lines systemically with the following procedure:

1. The 1762 nm laser main power output is sent to a wavemeter instead of the trap. The 1762 nm laser head parameters (piezoelectric voltage for the grating actuator, laser current and laser temperatures) are tuned to obtain a frequency reading reported by past literature for the $6S_{1/2} \leftrightarrow 5D_{5/2}$ transition [55].

2. Reroute the 1762 nm laser back to the ion trap. The EOM for the 1762 nm laser main beam path is turned off, so that there is only one laser frequency going to the ion trap.

3. A Ba^{+} ion of the desired isotope is trapped.

4. Tune the piezoelectric offset voltage of the 1762 nm laser head with the 493 nm, 650 nm, and 1762 nm lasers turned on, until the bright/dark state flip-flopping of the ion is observed.

5. Tune the piezoelectric offset voltage to maximize the bright/dark state flip-flopping rate. Note this piezoelectric offset voltage value.

6. Using the laser controller for the 1762 nm laser, set the piezoelectric voltage to be scanning periodically at some small amplitudes, which we typically set to 0.4 V, to do a periodic scanning of the laser frequency. A spike in the transmitted signal through

the PDH Fabry–Pérot cavity can be observed when the periodic frequency scanning scans through a laser frequency corresponding to a cavity mode.

7. Turn the PDH EOM off and tune the piezoelectric offset voltage, with the periodic scan running, tune the piezoelectric offset voltage until the cavity mode frequency, ω_{cavity}, closest to the laser frequency that drives the bright/dark state flip-flopping is found. The bright/dark state flip-flopping may go away at this step as the cavity mode frequency is not guaranteed to be close to the transition frequencies.

8. Starting from a low modulation frequency for the PDH EOM such that the blue/red sideband is within the piezoelectric periodic scan range to transmit through the cavity, which we typically use 20 MHz, increase the modulation frequency in small steps and tune the piezoelectric offset voltage in the direction towards the transition frequency found in Step 5 while keeping the PDH EOM blue/red sideband transmitting through the cavity.

9. Note the modulation frequency for the PDH EOM when the bright/dark state flip-flopping phenomenon returns. This is the difference between the transition frequency and the closest cavity mode frequency, $\Delta_{TC} = \omega_{transition} - \omega_{cavity}$.

10. Choose a desired modulation frequency for the 1762 nm main power EOM for driving the transitions, compute the corresponding value for $\Delta_{PDH} = \Delta_{TC} - \Delta_{EOM}$. Lock the laser frequency to this PDH EOM sideband, which would turn off the piezoelectric periodic scanning.

11. Send the modulation frequency Δ_{EOM} to the main laser power EOM, verify that the bright/dark state flip-flopping phenomenon is observed.

To calibrate the 614 nm laser frequency, we first set the frequency to the $5D_{5/2} \leftrightarrow 6P_{3/2}$ transition reported from past literature [55]. We find that with this, it is enough to stop the bright/dark state flip-flopping phenomenon (always bright) when the 614 nm laser is turned on together with the 493 nm, 650 nm, and 1762 nm lasers. While the exact 1762 nm transition lines are not found, for finer calibration of the 614 nm laser frequency, the following procedure is done:

1. The 493 nm and 650 nm lasers are kept on through the whole sequence in this procedure.

2. Pulse the 1762 nm light for a time similar to the time scale of the bright/dark state flip-flopping rate, which we find 200 ms to be appropriate for our setup.

3. Collect and record the photon counts on the PMT detector.

4. Pulse the 614 nm laser for a set repump time.

5. Collect and record the photon counts on the PMT detector.

6. Repeat Steps 1 to 5 to obtain a statistically significant number of data points.

7. Repeat Steps 1 to 6 for other 614 nm laser frequencies.

8. From the data set collected, we perform post selection of the data by selecting only the data points where the ion is dark in Step 3, as these are the cases where the state population is measured to be in $5D_{5/2}$ before the 614 nm pulse.

9. With the post-selected data, the probability where the ion is detected to be bright at Step 5 is computed. The 614 nm laser frequencies with the highest probabilities are close to the resonant $5D_{5/2} \leftrightarrow 6P_{3/2}$ transition frequencies.

To differentiate between bright and dark states in Steps 8 and 9, a threshold photon count needs to be determined. As discussed in Chapter 3.3, Ba^+ ion fluorescence rate is sensitive to 493 nm and 650 nm laser intensities and frequencies. Depending on the stability of the apparatus, Ba^+ ion fluorescence rate may not be consistent, which we find to be the case for our setup, and the fluorescence rates can vary from day to day. Therefore, we have developed a dynamic method of determining a photon count threshold for differentiating bright and dark states, which is presented in Appendix H.

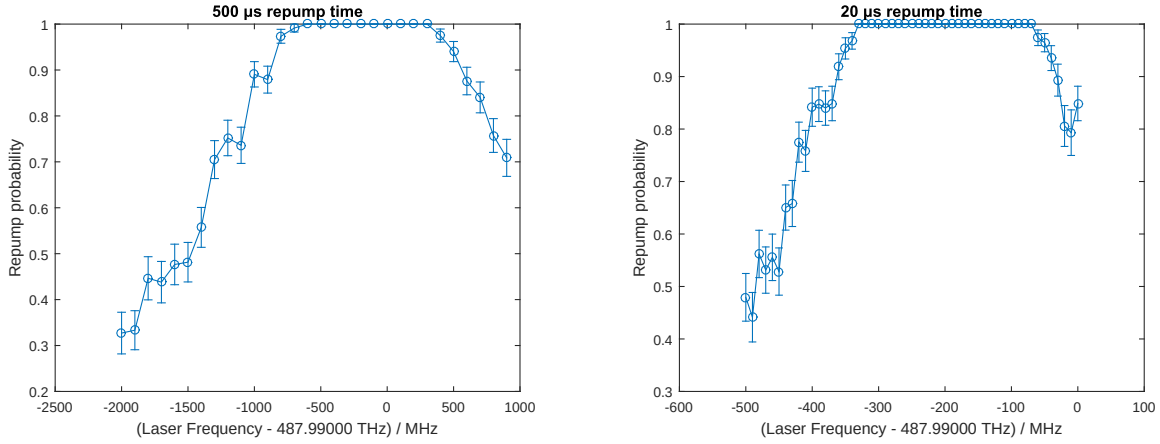

(a) (b)

Figure 4.6: Repump probability against 614 nm laser frequencies at 614 nm pulse times of (a) 500 µs and (b) 20 µs.

Fig. 4.6 shows the result of frequency scans 614 nm laser on a $^{138}Ba^{+}$ ion. 200 repeat experiments were done for each data point. Post-selected data (low counts on first PMT reading, before repump) averages to be about 120 samples. An obvious repump probability peak is observed in the frequency domain, with the peak narrowing at shorter 614 nm pulse times.

4.4 Spectroscopy of $6S_{1/2} \leftrightarrow 5D_{5/2}$ Transitions

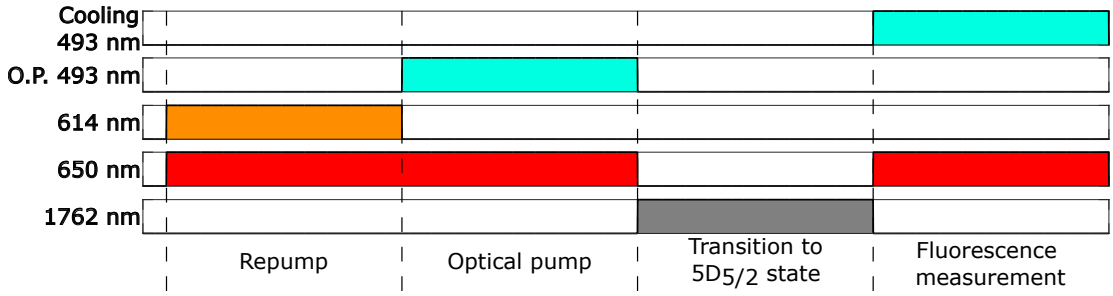

Figure 4.7: Pulse sequence for preparing a Ba^+ ion in the $6S_{1/2}$ ground state with the highest magnetic quantum number, and then driving a $6S_{1/2} \leftrightarrow 5D_{5/2}$ transition. O.P. denotes optical pump. The pulse times are not drawn to scale.

With the 614 nm laser frequency calibrated to repump the $5D_{5/2}$ state quickly and the 493 nm optical pump beam circularly polarized, the following pulse sequence as shown in Fig. 4.7 can be done to find the $6S_{1/2} \leftrightarrow 5D_{5/2}$ transition lines. The 1762 nm laser pulse time is set to some value from an initial guess to be much longer than the resonant Rabi periods of the transitions, which we chose to be 1 ms. If the 1762 nm laser frequency falls within the linewidth due to power broadening of a resonant frequency, there will be a significant probability of the state population being in the $5D_{5/2}$ level after the pulse sequence and is measured to be dark.

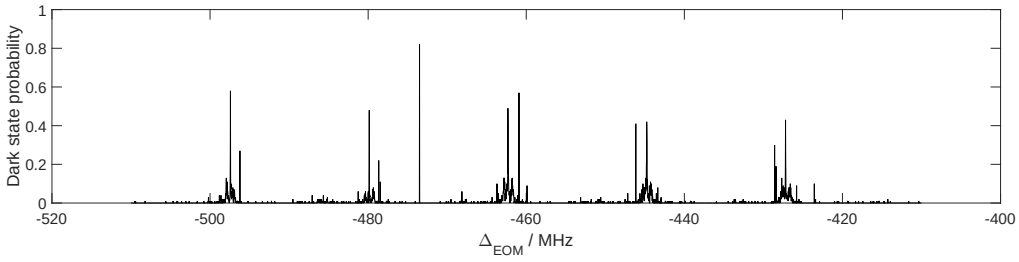

(a)

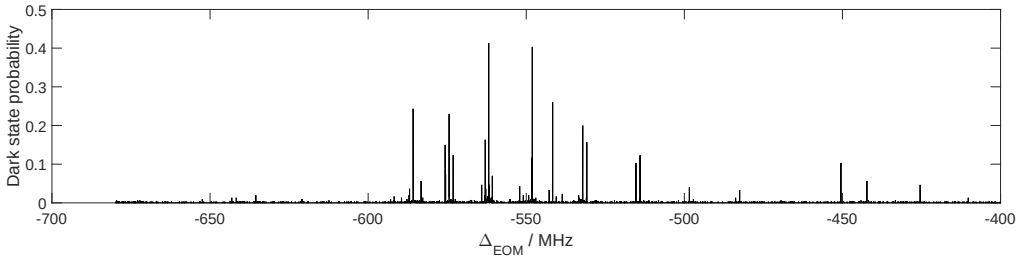

(b)

Figure 4.8: Dark state probability of (a) a $^{138}Ba^{+}$ and (b) a $^{137}Ba^{+}$ ion against the 1762 nm driving laser frequency, which is generated with an EOM modulation at Δ_{EOM} from the laser carrier frequency.

Fig. 4.8a shows the dark state probabilities against Δ_{EOM} in steps of 20 kHz for $^{138}Ba^{+}$, where the pulse sequence in Fig. 4.7 is repeated 100 times for each value of Δ_{EOM}. Five equally spaced dark state probability peaks can be observed, corresponding to the five $\Delta m = -2$ to 2 of quadrupole transitions. From Section 4.3.1, we only know that the 493 nm repump beam is circularly polarized, which means it could be σ_{-} or σ_{+}-polarized. To check that, we compare the change in the transition with the highest transition frequency when we flip the magnetic field direction of the chamber. The transition with the highest transition frequency is

$$\omega_{SD,max} = \omega_{SD,0} + \frac{\mu_B B_e}{\hbar} \left(g_{J,D} \left(m_S + 2 \right) - g_{J,S} m_S \right), \tag{4.48}$$

where $\omega_{SD,0}$ is the transition frequency without Zeeman splitting. For the energy levels at hand, $g_{J,D} = 6/5$ and $g_{J,S} = 2$, giving

$$\omega_{SD,max} = \omega_{SD,0} + \frac{\mu_B B_e}{\hbar} \left(-\frac{4}{5} m_S + \frac{12}{5} \right), \tag{4.49}$$

Thus, we choose the direction of the magnetic field with a lower highest 1762 nm transition

frequency to prepare the state in the $6S_{1/2}$ state with the highest magnetic quantum number.

The same procedure was done for $^{137}Ba^{+}$ and the results are shown in Fig. 4.8b. The assignments of the $6S_{1/2} \leftrightarrow 5D_{5/2}$ transitions to the dark state probability peaks are not as clear in this case. To be able to assign $6S_{1/2} \leftrightarrow 5D_{5/2}$ transitions to these peaks, we match the measured resonant peak with the highest frequency to the transition to the highest energy level in $5D_{5/2}$ allowed by the selection rule, which is the $|6S_{1/2}, \tilde{F} = 2, m_{\tilde{F}} = 2\rangle \leftrightarrow |5D_{5/2}, \tilde{F} = 1, m_{\tilde{F}} = 1\rangle$ transition. Then, we numerically compute the $5D_{5/2}$ energy levels for a range of magnetic field strengths, and pick out the magnetic field strength where all the other measured resonant peaks are intersecting with some numerically computed energy levels, as shown in Fig. 4.9. This lets us determine assign the measured resonant frequencies to the corresponding $6S_{1/2} \leftrightarrow 5D_{5/2}$ transitions and the magnetic field strength at the same time.

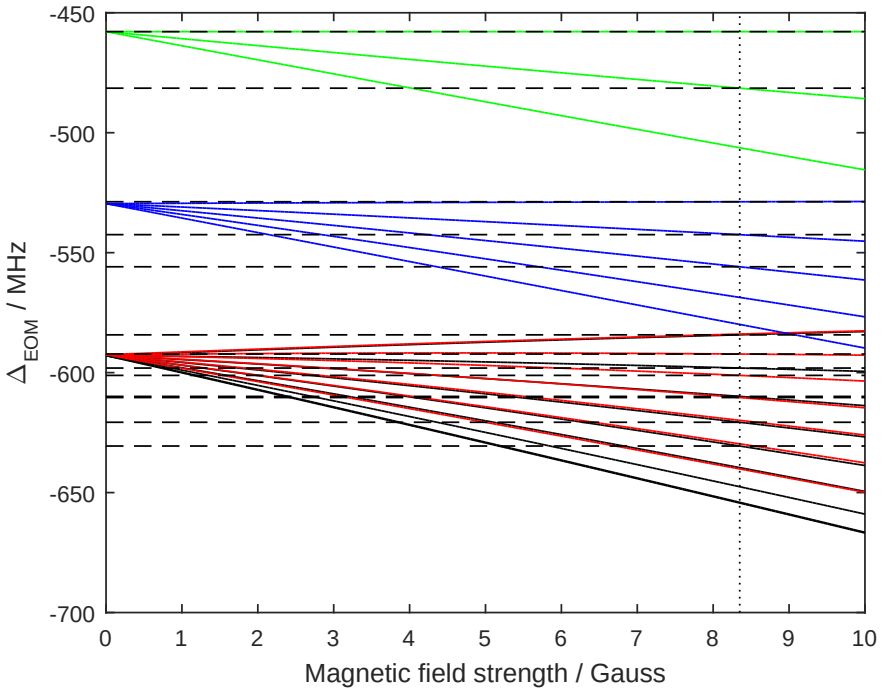

Figure 4.9: Solid lines: numerically simulated $^{137}Ba^{+}$ transition frequencies, shifted to match the $|6S_{1/2}, \tilde{F} = 2, m_{\tilde{F}} = 2\rangle \leftrightarrow |5D_{5/2}, \tilde{F} = 1, m_{\tilde{F}} = 1\rangle$ transition to the highest measured transition frequency for a range of magnetic field strengths. The colors denote the $\tilde{F} = 1$ (green), $\tilde{F} = 2$ (blue), $\tilde{F} = 3$ (red) and $\tilde{F} = 4$ (black) levels. Dashed lines: Empirically measured $^{137}Ba^{+}$ transition frequencies. Dotted line: The magnetic field where all the measured transition frequencies intersect the numerically simulated energy levels, which is $B_e = 8.35\,\mathrm{G}$.

With the $6S_{1/2} \leftrightarrow 5D_{5/2}$ transitions found, we can drive coherent transitions between a $6S_{1/2}$ state and a $5D_{5/2}$ by choosing Δ_{EOM} corresponding to the transition frequency. By varying the pulse time of the 1762 nm laser in the pulse sequense as shown in Fig. 4.7, we observe Rabi cycling of the states as shown in Fig. 4.10 below for $^{138}Ba^{+}$, which lets us determine the Rabi frequencies of each transition.

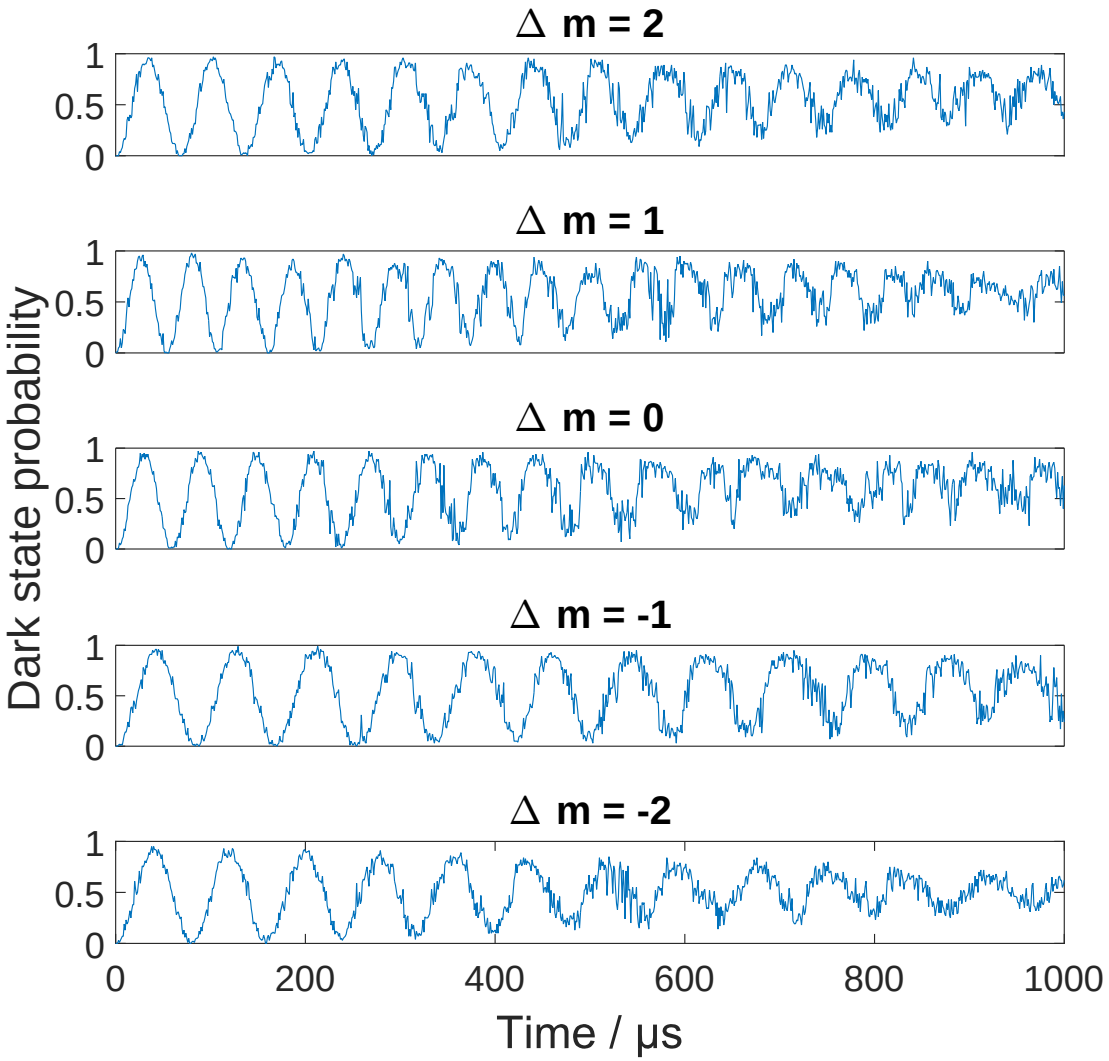

Figure 4.10: Rabi cycling of transitions to the $5D_{5/2}$ states from the $|6S_{1/2}, m = 1/2\rangle$ state in $^{138}Ba^{+}$.

4.5 Actualization of Utilities of Ba^+ $6S_{1/2} \leftrightarrow 5D_{5/2}$ Transitions

As discussed in Sections 4.1.4 and 4.1.5, we expect to be able to resolve the 1762 nm transitions modulated by ion motions, and extract useful functions from them. We demonstrate the actualization of these utilities in this section.

4.5.1 Actualization of 1762 nm Resolved Motional Sideband Cooling

By doing a spectroscopy of the 1762 nm transitions at around a carrier peak at finer frequency steps, we can resolve the secular motional sidebands clearly as shown in Fig. 4.11 below.

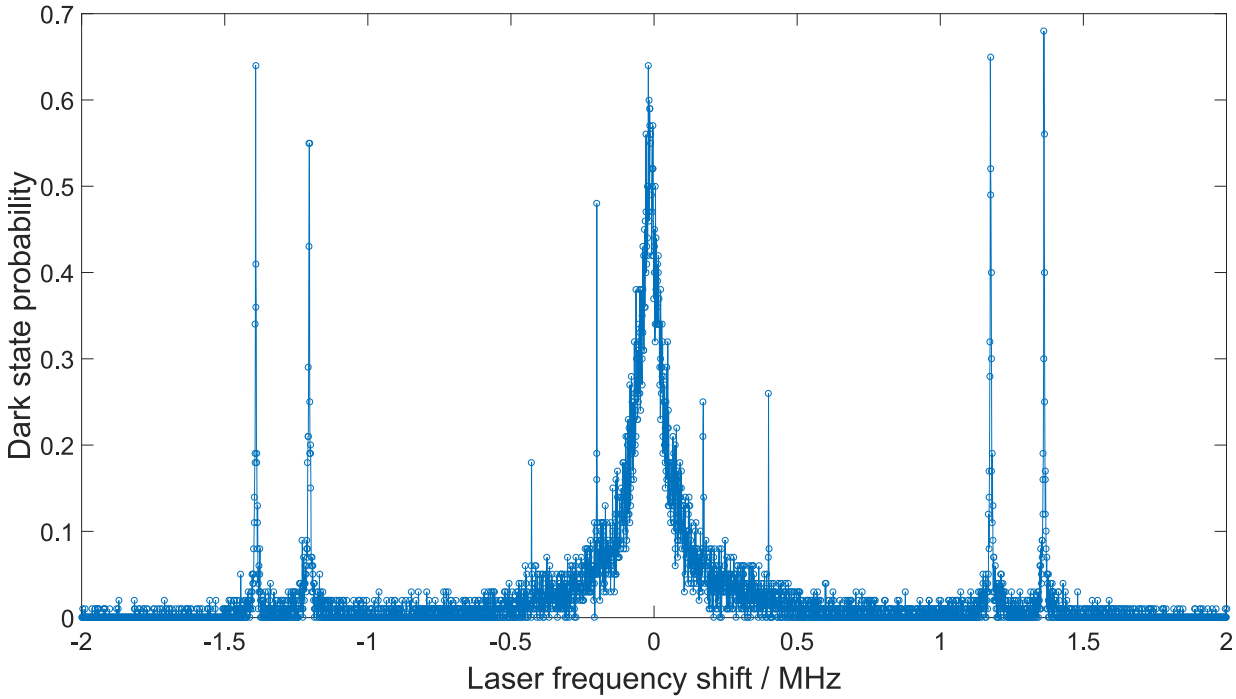

Figure 4.11: The dark state probability of $^{138}Ba^+$ against the laser frequency shift from a $\Delta m = 0$ carrier transition frequency. The sample size for each data point is 100. Frequency step size is 1 kHz.

The carrier frequency has the highest transition Rabi frequency and is thus power broadened the most in the spectrum. The red and blue sidebands of the two secular motional frequencies are clearly resolved in Fig. 4.11, at 1.2 MHz and 1.4 MHz. The higher motional frequency at 1.4 MHz corresponds to the axis of static voltage squeezing by the rod electrodes, V_S, as shown in Fig. 2.1a, and vice versa. To cool the desired motion of the ion along the desired axis, the corresponding red sideband frequency is driven. The following pulse sequence as shown in Fig. 4.12 below shows the actualization of the resolved sideband cooling protocol as described in Section 4.1.4.

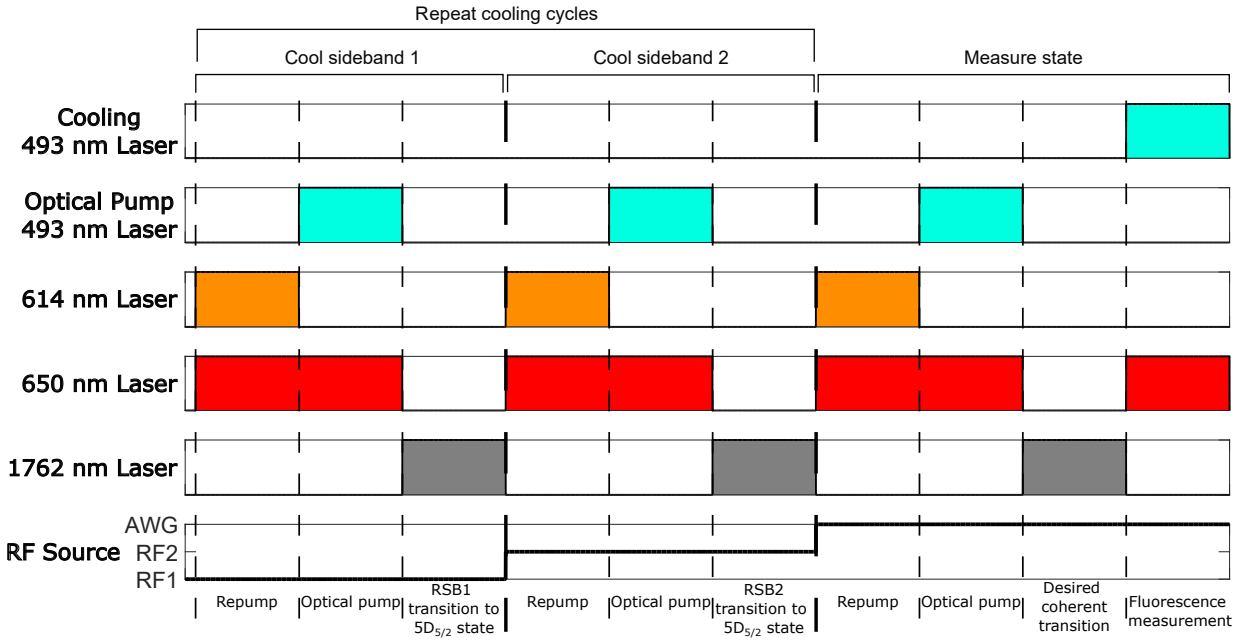

Figure 4.12: Pulse sequence for resolved sideband cooling using 1762 nm laser transitions, followed by a coherent 1762 nm transition experiment and a fluorescence readout.

The pulse sequence in Fig. 4.12 is separated into three sections by thick dashed lines. The first section of the pulse sequence reduces the motional quantum of the first radial axis by one for a successful transition to the $5D_{5/2}$ state, and the second section is for the second radial axis. The cooling sequence of the first and second sections are repeated for perpetual cooling of the ion. The third section of the pulse sequence does a coherent transition on the desired transition of the experiment after cooling and then perform a measurement readout. To be able to change the 1762 nm laser frequency quickly during the pulse sequence, the RF source for the main 1762 nm power EOM is switched using

a fast RF switch between the AWG, RF1 and RF2 as shown in Fig. 4.3, with RF1 and RF2 being used for driving the cooling sideband transitions and the AWG for the desired transition.

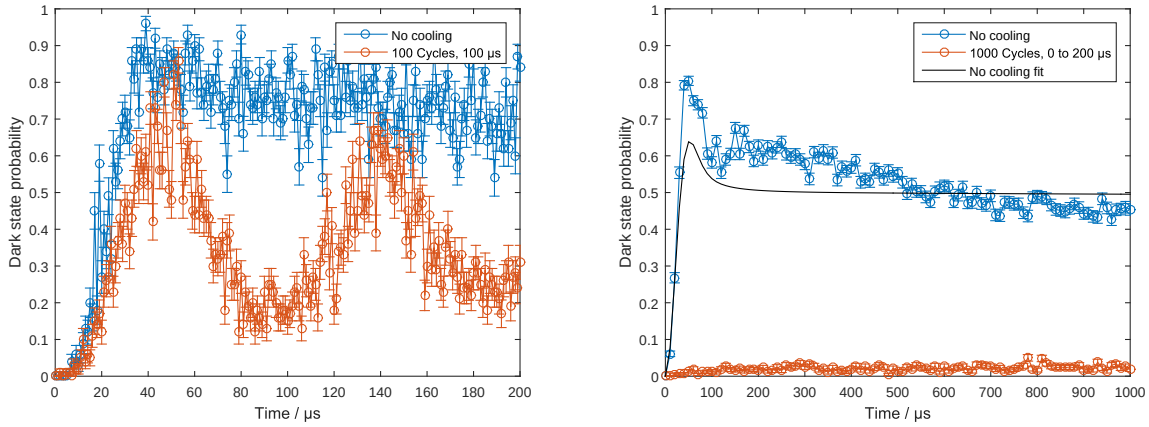

(a) (b)

Figure 4.13: Dark state probability against 1762 nm pulse times with and without cooling sequence on a 1.2 MHz red sideband of a $^{138}Ba^{+}$ $\Delta m = 0$ transition. (a) Constant 1762 nm pulse time at 100 µs is used for the cooling cycle, cooling cycles repeated 100 times. (b) Varying 1762 nm pulse times from 0 µs to 200 µs, at increments of 0.2 µs, totalling 1000 cooling cycles.

Figure 4.13 shows the 1762 nm laser pulse time scans of a $^{138}Ba^{+}$, $\Delta m = 0$, 1.2 MHz red sideband transition, with and without the cooling sequence cycles as discussed earlier. At the time these experiments were carried out, the 1762 nm laser main power EOM was not set up and the transition was driven by the laser carrier frequency, by locking to the first sideband of the PDH EOM at $\Delta_{PDH} = \omega_{transition} - \omega_{carrier}$ at the cavity (see Section 4.3). Since the transition to be driven after the cooling cycles is the same, at the 1.2 MHz red sideband of a $^{138}Ba^{+}$ $\Delta m = 0$ transition, and we are cooling only one of the axes in these experiments, the frequency switching protocol as described in Fig. 4.12 is not needed. Without cooling, assuming that the ion motional state is in a thermal mixed state, the red sideband transition probability follows the function

$$P\left(\text{Dark}\right) = \sum_{n}^{\infty} T_{\bar{n}}\left(n\right) \sin^2\left(\eta\Omega\sqrt{n}t\right), \tag{4.50}$$

where $T_{\bar{n}}(n)$ is the thermal mixed state probability distribution with an average phonon number $\bar{n}$.

$$T_{\bar{n}}(n) = \frac{\bar{n}^n}{(\bar{n}+1)^{n+1}}. \tag{4.51}$$

From Eq. 4.50, the $5D_{5/2}$ state transition probability as a function of laser pulse time is a combination of many different Rabi cycles at different Rabi frequencies, weighted by the motional Fock state distribution. This eliminates the oscillatory feature of the $5D_{5/2}$ state transition probability, as seen in Figs. 4.13a and 4.13b when no cooling cycles are performed. Eq. 4.50 is used to fit the data points without cooling cycles in Fig. 4.13b. The carrier transition Rabi frequency is measured to be $\Omega = 2\pi \times 111\,\text{kHz}$ for this transition (not shown). The Lamb-Dicke parameter is calculated using Eq. 4.40, taking into account that the wavevector direction is at an angle of 45° to the motional axis, to be $\eta = 0.014$. With these values, the functional fit of Eq. 4.50 to the data points give an average phonon number of $\bar{n} = 140 \pm 20$ when no resolved sideband cooling is performed. The high average phonon number of $\bar{n} = 140 \pm 20$ indicates that our Doppler laser cooling is probably not optimized and further cooling (enabled by resolved sideband cooling) is required for quantum operations that are sensitive to the motional states.

In Figs. 4.13a, the 1762 nm pulse time is fixed to 100 µs during the cooling cycles. This results in an oscillatory feature with transition probability troughs at pulse times in multiples of 100 µs. This is likely because a phonon Fock state with negligible or zero transition probabilities at $t = 100\,\mu\text{s}$ is stuck in that state and cannot be cooled further. This converges the distribution of the phonon to be accumulated in Fock states with Rabi frequencies $\eta\Omega\sqrt{n} \times 100\,\mu\text{s} = 2m\pi, m \in \mathbb{Z}$. If $\eta\Omega\sqrt{n} \times 100\,\mu\text{s} = 2m\pi$ for a phonon Fock state, then $\eta\Omega\sqrt{n} \times 200\,\mu\text{s} = 2m\pi$ is also automatically satisfied, which manifests as a second transition probability trough at $t = 200\,\mu\text{s}$, and troughs at further laser pulse times in multiples of 100 µs are expected. Therefore, the laser pulse times in the cooling cycles should be varied in this cooling protocol, in order to prevent any stuck phonon Fock states and cool the ion as close as possible to the zero phonon Fock state. Fig. 4.13b shows the results with cooling pulses varying from 0 µs to 200 µs in steps of 0.2 µs for each cycle, and it is obvious that the red sideband transition probability is significantly suppressed. Since there are indications that the phonon Fock state distribution is no longer in a thermal state distribution after resolved sideband cooling from Fig. 4.13a, I do not assume a thermal mixed state for the results in Fig. 4.13b after the cooling process. I quantify the cooling performance by computing the probability that the ion is in the zero phonon Fock state, which is calculated as follows. First, I compute the average of the dark state probability over the range of pulse times after the initial rise time from $t = 0$, which I estimate to be

$t > 200\,\mu s$. The zero phonon Fock state probability is then computed using

$$P(|n=0\rangle) = 1 - 2\,\langle P_{t>200\,\mu s}(\text{Dark})\rangle\,, \tag{4.52}$$

where $\langle\cdot\rangle$ denote average across laser pulse times. From the calculations, we have $P(|n=0\rangle) = 4.6 \pm 0.2\%$, which is significantly cooler than the temperature of the ion pre-cooling.

4.5.2 1762 nm Transitions for Excess Micromotion Detection and Compensation

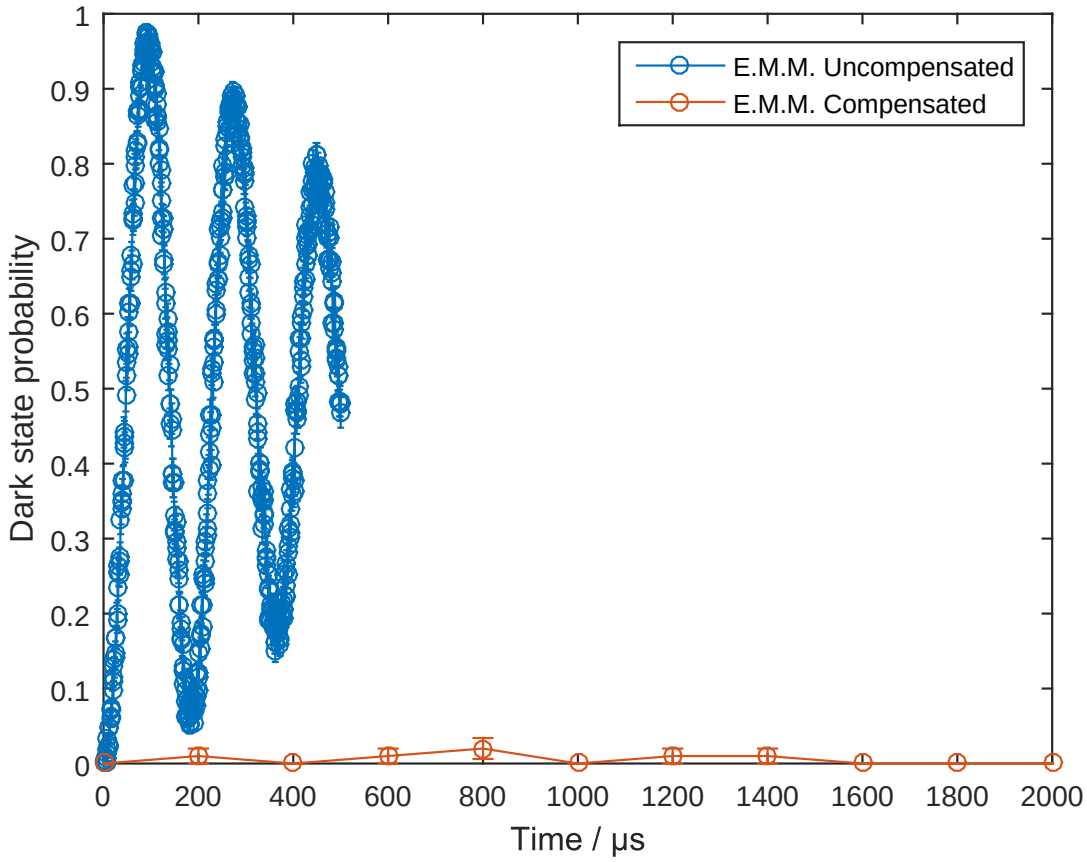

Figure 4.14: Dark state probability against 1762 nm laser pulse times, driven at a laser frequency of $\omega_{\Delta m=-1} - \Omega_{RF}$, where $\omega_{\Delta m=-1}$ is a resonant $\Delta m = -1$ $6S_{1/2} \leftrightarrow 5D_{5/2}$ transition of $^{138}Ba^{+}$. E.M.M. denotes excess micromotion.

The derivations in Section 4.1.5 predicts that we can observe Rabi cycling of a $6S_{1/2} \leftrightarrow 5D_{5/2}$ transition at laser frequencies detuned from the carrier resonance in integer multiples of Ω_{RF} if the ion is moving with a sufficiently large excess micromotion amplitude. This is indeed the case, as seen from Fig. 4.14 for the E.M.M. uncompensated case, where the laser frequency is set to Ω_{RF} red of a $\Delta m = -1$ $6S_{1/2} \leftrightarrow 5D_{5/2}$ transition in $^{138}Ba^{+}$. A common cause for this excess micromotion is a mismatch of the pseudopotential minimum to the RF null, which can be compensated with DC voltages sent to the rod electrodes.

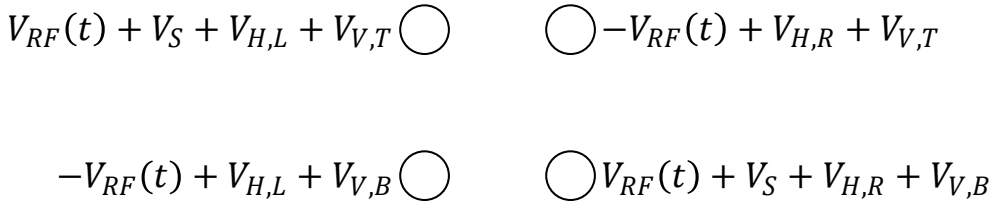

Figure 4.15: Illustration of voltages sent to the four-rod electrodes, including voltages for excess micromotion compensation.

Fig. 4.15 shows an illustration of voltages sent to the four-rod trap electrodes. $V_{V,T}$ and $V_{V,B}$ displaces the ion in the vertical direction, where the subscripts T and B denote top and bottom electrodes respectively. $V_{H,L}$ and $V_{H,R}$ displaces the ion in the horizontal direction, where the subscripts L and R denote left and right electrodes respectively. Our voltage sources are set up such that the DC voltages on the electrodes can only have positive values, i.e. $V_{V,T}, V_{V,B}, V_{H,L}, V_{H,R} > 0\,\mathrm{V}$. Let us define

$$\begin{aligned} |V_V| &= \begin{cases} V_{V,T}, & V_V < 0 \\ V_{V,B}, & V_V \geq 0 \end{cases} \\ |V_H| &= \begin{cases} V_{H,R}, & V_H < 0 \\ V_{V,L}, & V_H \geq 0 \end{cases} . \end{aligned} \tag{4.53}$$

The procedure for excess micromotion compensation is performed as follows:

1. Set the 1762 nm laser frequency to be Ω_{RF} detuned from a resonant $6S_{1/2} \leftrightarrow 5D_{5/2}$ transition.

2. Set V_V to some starting voltage, $V_V = V_{start}$, run a laser pulse time scan of the experiment as shown in Fig. 4.7, starting from $t = 0$ over some long enough range of pulse times, at least one order of magnitude larger than the Rabi cycle period of the resonant carrier transition. We typically set it to be a few milliseconds.

3. Compute the average of the photon counts collected by the PMT detector across all 1762 nm laser pulse times for the data collected in Step 2.

4. Increase V_V by some voltage step, $V_V \rightarrow V_V + \Delta V$.

5. Repeat Steps 1 to 4, until some end point of the voltage scan range $V_V = V_{end}$.

6. Set V_V to the voltage value which gives the highest average PMT count computed in Step 3.

7. Repeat Steps 1 to 6 for the horizontal voltage, replacing V_V with V_H in the procedure.

When the ion is shifted to be close enough to the RF null, the excess micromotion amplitude is minimal and the Rabi frequency is low. With a sufficiently low Rabi frequency, the ion stays mostly in the ground $6S_{1/2}$ state over the range of scanned laser pulse times in Step 2, resulting in high averaged PMT counts in Step 3. Otherwise, the averaged PMT counts are approximately half of the bright state PMT count. This lets us pinpoint the compensation DC voltages to push the ion to the RF null in Step 6. It is also important to compensate for the vertical displacement first, as the excess micromotion moves mostly in the horizontal direction, parallel to the 1762 nm laser wavevector and thus stronger motional coupling to the laser, when it is displaced vertically from the RF null. With the excess micromotion compensated, the transition modulated by excess micromotion is significantly suppressed as shown in the E.M.M. compensated data from Fig. 4.14.

4.6 State Preparation and Measurement (SPAM) of Trapped Ba^+ Ion Qudits

Up until this point in this chapter, we have explored how the $6S_{1/2}$ and $5D_{5/2}$ states can be coherently manipulated with laser controls. In this section, we construct a protocol for performing state preparation and measurement (SPAM) of a qudit system using these controls, which are necessary functions for a quantum computer. The same protocol applies to both $^{138}Ba^+$ and $^{137}Ba^+$ isotopes, and SPAM can be performed in the same manner. We will focus the discussion on $^{137}Ba^+$ in this section, which is the isotope with more stable and metastable energy states for high-dimensional qudit encodings, and a brief summary of the $^{138}Ba^+$ results are relegated to Appendix I.

4.6.1 Qudit Encoding and SPAM Protocol

We have seen that a σ_+-polarized 493 nm light optically pumps a Ba^+ ion to the $6S_{1/2}$ state with the highest magnetic quantum number. Thus, it is natural to encode the computational $|0\rangle$ state in the $|6S_{1/2}, \tilde{F} = 2, m_{\tilde{F}} = 2\rangle$ state of $^{137}Ba^+$ in our scheme. The ability to perform universal single qudit gates is enabled by any two of the encoded states being connected by a series of two-level transitions that we can control [72, 73, 74]. Thus, it is natural to encode the states in the $5D_{5/2}$ level that are directly accessible with a quadrupole transition from the $|6S_{1/2}, \tilde{F} = 2, m_{\tilde{F}} = 2\rangle$ state as the next computational states, and any two computational states are connected via two two-level transitions via the $|0\rangle$ state. These $5D_{5/2}$ states directly accessible from the $|6S_{1/2}, \tilde{F} = 2, m_{\tilde{F}} = 2\rangle$ state are also connected to the other states in the $6S_{1/2}$ level, and so on, giving us access to any states in the $6S_{1/2}$ and $5D_{5/2}$ levels in at most three transitions as implied by Table 4.1. This gives us the ability to perform universal single qudit gates on a 32-level qudit. However, we will see later, during the qudit measurement protocol in this work, not all 32 states are fully distinguishable, and the number of levels that can be encoded is limited by the number of states that are distinguishable in a single-shot by the measurement process.

The general state preparation process is straightforward. First, the $^{137}Ba^+$ ion is optically pumped to the $|6S_{1/2}, \tilde{F} = 2, m_{\tilde{F}} = 2\rangle$ state. Then, at most three sequential 1762 nm laser π-pulses with the corresponding frequencies that connect the $|6S_{1/2}, \tilde{F} = 2, m_{\tilde{F}} = 2\rangle$ state to the desired state to be prepared are sent to the ion. This completes the state preparation process.

Now, we describe a protocol we use to perform qudit state measurements. $^{137}Ba^+$ emits fluorescence when it is driven by 493 nm and 650 nm lasers if the ion is in the $6S_{1/2}$ state. It does not fluoresce if the ion is in any of the encoded $5D_{5/2}$ states. We make use of this property to construct a single-shot qudit measurement process, which is described in the sequence below. The process consists of multiple steps, but we characterize it as single-shot in the sense that the projected quantum state can be determined definitively in a single run of the measurement protocol.

1. Without loss of generality, the $|0\rangle$ state is assigned as one of the $6S_{1/2}$ states. Any population of the encoded states in the $6S_{1/2}$ level other than state $|0\rangle$ is brought up to a corresponding unencoded $5D_{5/2}$ state by sending π-pulses of 1762 nm laser with frequencies resonant to the desired transitions in sequence. This is commonly called a shelving process.

2. The 493 nm and 650 nm lasers are turned on to check for fluorescence. The ion is measured to be in the qudit state $|0\rangle$ if fluorescence is observed at this step.

3. The population corresponding to the next computational state $|n\rangle$ in $5D_{5/2}$ is brought down to one of the $6S_{1/2}$ states by sending a π-pulse of 1762 nm laser with the corresponding transition frequency. We call this a de-shelving process.

4. Step 2 is repeated to check for fluorescence. The ion is measured to be in the qudit state $|n\rangle$ if fluorescence is observed for the first time at this step, as exemplified in Table 4.2.

5. Steps 3 and 4 are repeated until all states are de-shelved and checked for fluorescence.

Experiment	Measurement step												
	$\|0\rangle$	$\|1\rangle$	$\|2\rangle$	$\|3\rangle$	$\|4\rangle$	$\|5\rangle$	$\|6\rangle$	$\|7\rangle$	$\|8\rangle$	$\|9\rangle$	$\|10\rangle$	$\|11\rangle$	$\|12\rangle$
1	D	D	D	B	D	D	D	D	D	D	D	D	D
2	D	D	D	B	B	B	B	B	B	B	B	B	B
3	D	D	D	D	D	D	D	D	D	D	D	D	D

Table 4.2: Examples of measurement outcomes. B and D denote that the ion is detected as bright and dark respectively. The de-shelving process in the measurement sequence as described in the main text is performed in ascending order of the encoded states. Experiments 1 and 2 are interpreted as measuring the system to be in state $|3\rangle$. Experiment 3 is regarded as a measurement failure and is removed from the data set for the post-selected SPAM results. In this experiment, the deshelving process is simultaneously a reshelving process (see Fig. 4.18). An alternative interpretation that treats Experiment 2 as a measurement failure rather than a measurement of the state $|3\rangle$ is discussed in Appendix J.

From this measurement sequence, it can be seen that at least $d_S - 1$ levels in the $5D_{5/2}$ level has to be left unencoded in Step 1 of the measurement process to have full distinguishability, where d_S is the number of computational states encoded in the $6S_{1/2}$ level. Let N_D be the total number of states in the shelve ($5D_{5/2}$ in this case) level, the maximum number of shelve states that can be encoded is $d_D = N_D - (d_S - 1)$, giving the maximum possible qudit dimension of $d_S + d_D = N_D + 1$. For $^{137}Ba^+$, $N_D = 24$ and thus a maximum number of 25 levels can be encoded with this scheme.

Table 4.2 shows representative examples of possible measurement outcomes. Experiment 3 in Table 4.2 is a directly detectable failure of the measurement procedure. This is arguably a less critical error than misdiagnosing the quantum state, as the user directly knows an error has occurred and can rerun the computation. In this thesis, we will present

both the raw SPAM results and the post-selected SPAM results, where measurement outcomes such as Experiment 3 are excluded from the data sample, but further data analysis will only be performed on the post-selected SPAM results.

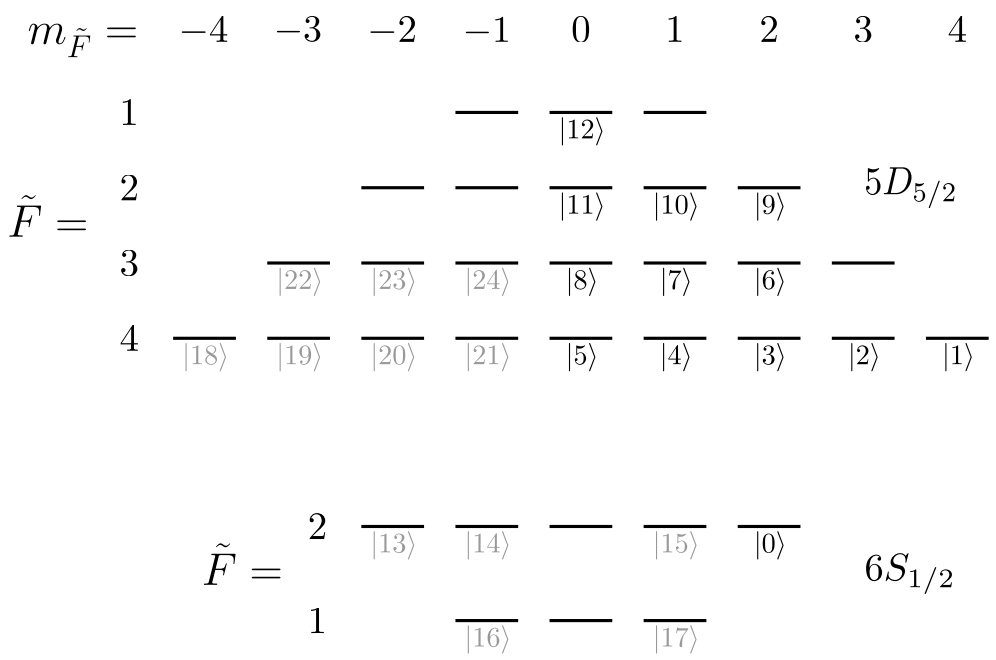

Figure 4.16: Qudit encoding schemes for $^{137}Ba^{+}$. Black texts indicate the encoding scheme employed in this work for $^{137}Ba^{+}$. All states with sufficiently strong (resulting in π-pulse transition fidelity of $\geq 75\%$, discussed later in main text) allowed transitions to the $5D_{5/2}$ level from $|0\rangle$ are encoded. Gray texts indicate a possible extension of the encoding scheme to up to 25 levels, where the additional states are chosen arbitrarily.

In this work, we encode the $|6S_{1/2}, \tilde{F} = 2, m_{\tilde{F}} = 2\rangle$ state as the $|0\rangle$ state and any $5D_{5/2}$ states directly accessible from the $|0\rangle$ state with a single quadrupole transition as computational states. We exclude the states that have transition strengths that are too weak or with bad π-pulse transition fidelity ($< 75\%$, see Section 4.6.4), which are the $|5D_{5/2}, \tilde{F} = 3, m_{\tilde{F}} = 3\rangle$ and $|5D_{5/2}, \tilde{F} = 1, m_{\tilde{F}} = 1\rangle$ states. This totals 13 encoded states as shown in Fig. 4.16. For this encoding, at most one quadrupole transition in the state preparation step is required and the shelving process in Step 1 of the measurement procedure is unnecessary. The $6S_{1/2}$ ground state chosen for the de-shelving process is also fixed to be $|6S_{1/2}, F = 2, m_F = 2\rangle$ for convenience. The pulse sequence to perform SPAM on this 13-level qudit is summarized in Fig. 4.17 below.

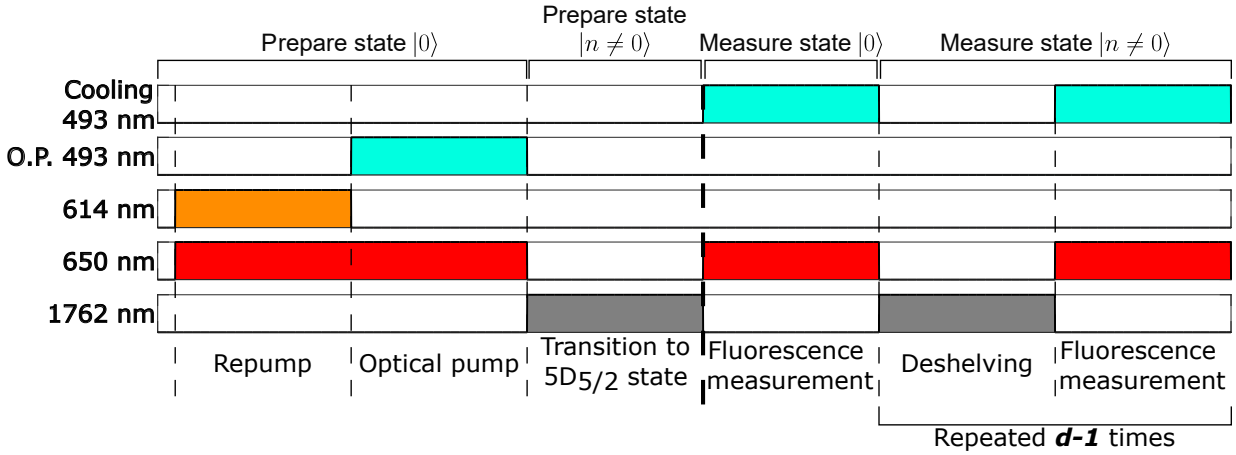

Figure 4.17: Simplified pulse sequence for one SPAM experiment for a prepared state $|n\rangle$ of a d-dimensional qudit, demonstrated in this work for $d = 13$. O.P. denotes optical pumping. The time axis is not drawn to scale. The pulse sequences to the left and right of the bold dashed line are the state preparation and state measurement processes respectively. The 1762 nm laser pulse for the state preparation step is only needed if the prepared state is not $|0\rangle$. For a detailed pulse sequence relevant to the experimental apparatus, see Fig. 4.18.

4.6.2 Hardware and Laser Setup for SPAM

To be able to carry out the pulse sequence as shown in Fig. 4.17, the ability to quickly switch the 1762 nm driving laser frequency for twelve different transitions is required. This is accomplished by a function in our AWG, where it can store a table of different periodic waveforms in its memory. The output waveform can be cycled in the waveform table from one waveform to the next by sending an external DC voltage trigger to the AWG, which allows easy control of the timings in the pulse sequence. We configure 13 waveforms to be saved in the AWG waveform table, each generating an EOM modulated sideband frequency Δ_{EOM} corresponding to a $|0\rangle \leftrightarrow |n\rangle$ resonant transition of our 13-level qudit. For the waveform corresponding to the $|0\rangle$ state, some Δ_{EOM} value that is far off-resonant to any $6S_{1/2} \leftrightarrow 5D_{5/2}$ transitions is set. To save 13 periodic waveforms with a constant AWG clock rate in the limited memory of the AWG, our frequency resolution is limited to 1 kHz (see Appendix K). With this AWG setup, the detailed pulse sequence to perform our 13-level qudit SPAM is presented in Fig. 4.18 below.

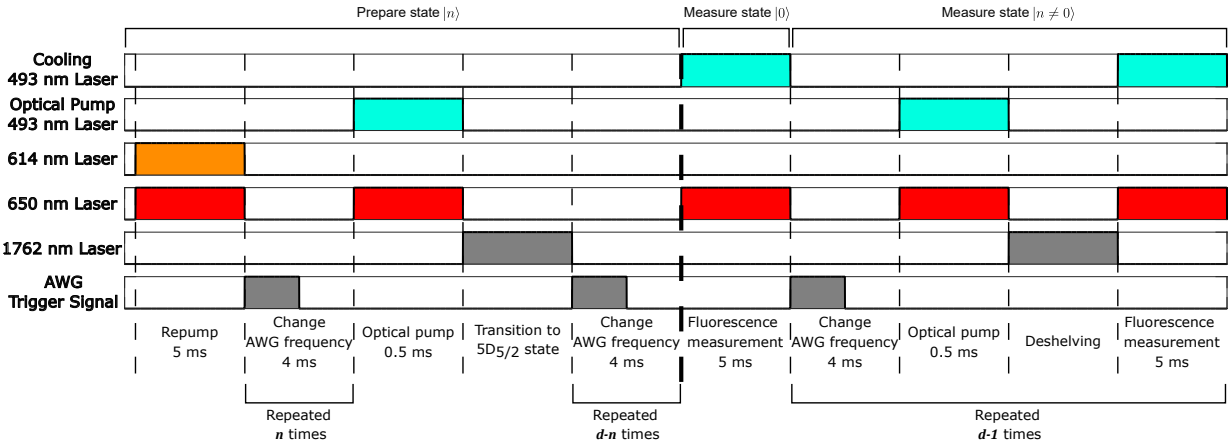

Figure 4.18: Pulse sequence for one SPAM experiment for a prepared $|n\rangle$ state of a d-dimensional qudit demonstrated in this work. The time axis is not drawn to scale. The pulse sequences to the left and right of the bold dashed line are the state preparation and state measurement processes respectively. A list of d individual frequencies corresponding to the transitions for each encoded state in a d-dimensional qudit is set in the AWG, and frequency switching is achieved by the AWG trigger signal. The optical pumping step in the measurement process is technically unnecessary for the measurement procedure described in the main text. It is present in this work for investigating another method of determining a measured state, which we have found to be less robust than what is described in the main text (see Appendix J).

Having a short 1762 nm π-pulse transition is important to minimize decoherence effects during state preparation of $|n \neq 0\rangle$ states. Therefore, it is important to ensure high 1762 nm laser intensity at the ion. We do this by optimizing the laser beam pointing as follows. Δ_{EOM} is set to correspond to a resonant $|6S_{1/2}, \tilde{F} = 2, m_{\tilde{F}} = 2\rangle \leftrightarrow |5D_{5/2}\rangle$ transition and the Rabi cycling pulse sequence in Fig. 4.7 is run repeatedly with 1762 nm laser pulse time set lower than the current π-pulse time. The 1762 nm laser beam pointing is then tuned to minimize the photon count detected by the PMT detector. The lower photon count at the PMT detector is due to the dark state probability being increased at the probe pulse time due to the shortening of a Rabi cycle period when the incident laser intensity is increased.

It is also important to ensure that the optical pump 493 nm laser beam is parallel to the magnetic field axis, as it being off-axis would introduce other polarization components of the laser (σ_- and π polarizations, which is also referred to as σ_0 polarization in an earlier chapter). This error reduces the population in the $|6S_{1/2}, \tilde{F} = 2, m_{\tilde{F}} = 2\rangle$ state after the optical pump process. One might think that we can perform the protocol to prepare

the state in $|n \neq 0\rangle$ and measure the dark state probability as a metric to systematically optimize the optical pump beam pointing, but we find this to be difficult due to the optical pump fidelity being dependent on laser intensity as well (see Section 4.6.3). Thus, we optimize the optical pump beam pointing geometrically as described in Section 4.3.1, and find that it is sufficient for demonstrating qudit SPAM.

We only have a single 614 nm frequency in our setup, and we set it to be resonant to the $|5D_{5/2}, \tilde{F} = 4, m_{\tilde{F}} = 2\rangle \leftrightarrow |6P_{3/2}, \tilde{F} = 2\rangle$ transition. This frequency is chosen so that all the other encoded $5D_{5/2}$ states except $|5D_{5/2}, \tilde{F} = 4, m_{\tilde{F}} = 4\rangle$ can be driven to the $|6P_{3/2}, \tilde{F} = 2\rangle$ level at relatively small frequency detunings, and a repump time of 500 µs is sufficient for these states. The $|5D_{5/2}, \tilde{F} = 4, m_{\tilde{F}} = 4\rangle \leftrightarrow |6P_{3/2}, \tilde{F} = 2\rangle$ transition is forbidden and the $|5D_{5/2}, \tilde{F} = 4, m_{\tilde{F}} = 4\rangle$ state can only be driven to the $|6P_{3/2}, \tilde{F} = 3\rangle$ level. For the experiments which involve the $|5D_{5/2}, \tilde{F} = 4, m_{\tilde{F}} = 4\rangle$ state, the repump time is increased to 5 ms. To calibrate the 614 nm laser to the desired $|5D_{5/2}, \tilde{F} = 4, m_{\tilde{F}} = 2\rangle \leftrightarrow |6P_{3/2}, \tilde{F} = 2\rangle$ transition, the experiments with the pulse sequence in Fig. 4.7 is done with the 1762 nm laser frequency set to drive the $|6P_{1/2}, \tilde{F} = 2, m_{\tilde{F}} = 2\rangle \leftrightarrow |5D_{5/2}, \tilde{F} = 4, m_{\tilde{F}} = 2\rangle$ transition and with a π-pulse time. The repump time is set to some value lower than the saturation time for repumping the state in order to be able to resolve the transition peaks, which we chose to be 100 µs. The results of this 614 nm frequency scan experiment is shown in Fig. 4.19 below.

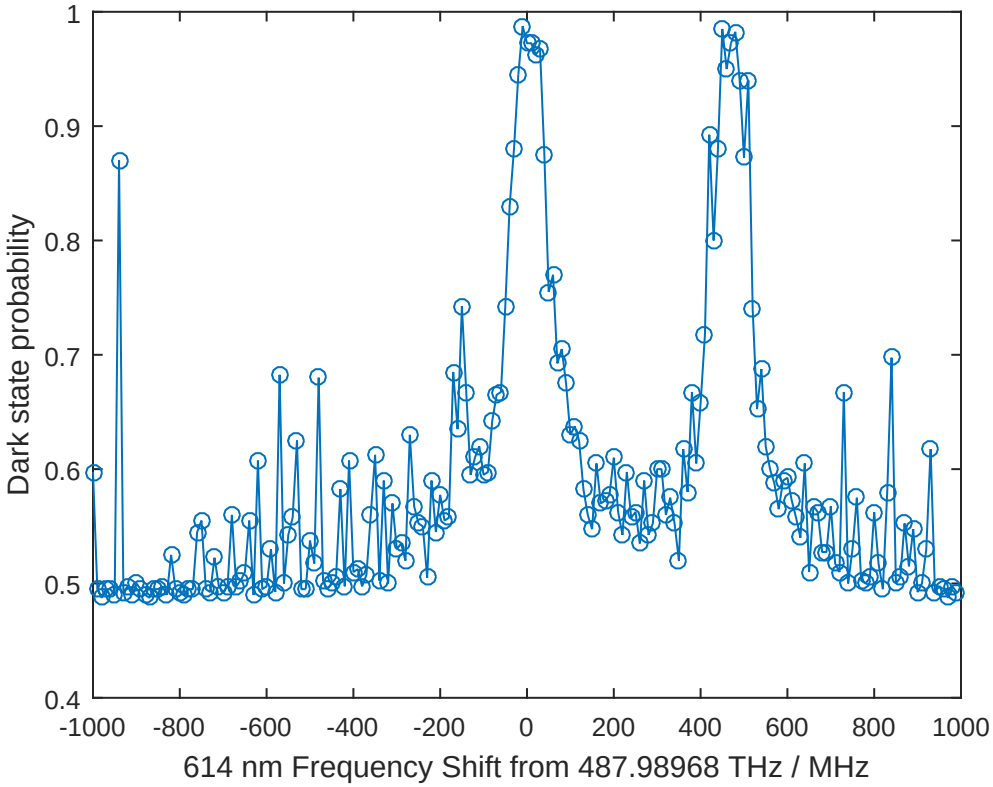

Figure 4.19: Dark state probability against the 614 nm repump laser frequency. The 1762 nm laser frequency and pulse times are set to perform a π-pulse transition from the $|6S_{1/2}, \tilde{F} = 2, m_{\tilde{F}} = 2\rangle$ state to the $|5D_{5/2}, \tilde{F} = 4, m_{\tilde{F}} = 2\rangle$ state. The repump time is set to 100 µs.

The central peak in Fig. 4.19 corresponds to the 614 nm frequency resonant to the $|5D_{5/2}, \tilde{F} = 4, m_{\tilde{F}} = 2\rangle \leftrightarrow |6P_{3/2}, \tilde{F} = 2\rangle$ transition and the peak that is around 470 MHz blue of it is the transition to the $|6P_{3/2}, \tilde{F} = 3\rangle$ level. It is interesting to note that although $|F = 4\rangle \leftrightarrow |F = 2\rangle$ is dipole forbidden, $|\tilde{F} = 4\rangle \leftrightarrow |F = 2\rangle$ is not in general, as $|\tilde{F} = 4\rangle$ states are superposition states of hyperfine F states.

4.6.3 Optical Pump Fidelity is Dependent on Laser Intensity and Frequency

In this section, we explore how sensitive is an optical pumping performance to other laser parameters, which are the frequency detuning and intensity, given that the optical pumping light is not perfectly polarized (it is trivial for the perfectly polarized case). We model the problem using optical Bloch equations as we did in Chapter 3.3. In this case, I construct a toy model of four states as shown in Fig. 4.20a, where I have ignored the D states.

The time derivatives of the state amplitudes are then constructed as follows.

$$\begin{aligned}
\frac{d}{dt}c_{S1} &= -i\Delta c_{S1} - i\frac{\sigma_0\Omega}{2}c_{P1} - i\frac{\sigma_+\Omega}{2}c_{P2} \\
\frac{d}{dt}c_{S2} &= -i\Delta c_{S2} - i\frac{\sigma_-\Omega}{2}c_{P1} - i\frac{\sigma_0\Omega}{2}c_{P2} \\
\frac{d}{dt}c_{P1} &= -i\frac{\sigma_0\Omega_S}{2}c_{S1} - i\frac{\sigma_-\Omega_S}{2}c_{S2} \\
\frac{d}{dt}c_{P2} &= -i\frac{\sigma_+\Omega_S}{2}c_{S1} - i\frac{\sigma_0\Omega_S}{2}c_{S2},
\end{aligned} \tag{4.54}$$

and the time derivatives of the density matrix elements are

$$\begin{aligned}
\frac{d}{dt}\rho_{S1S1} &= c_{S1}\frac{d}{dt}c^*_{S1} + c^*_{S1}\frac{d}{dt}c_{S1} + \frac{\gamma}{2}\left(\rho_{P1P1} + \rho_{P2P2}\right) \\
\frac{d}{dt}\rho_{S2S2} &= c_{S2}\frac{d}{dt}c^*_{S2} + c^*_{S2}\frac{d}{dt}c_{S2} + \frac{\gamma}{2}\left(\rho_{P1P1} + \rho_{P2P2}\right) \\
\frac{d}{dt}\rho_{P1P1} &= c_{P1}\frac{d}{dt}c^*_{P1} + c^*_{P1}\frac{d}{dt}c_{P1} - \gamma\rho_{P1P1} \\
\frac{d}{dt}\rho_{P2P2} &= c_{P2}\frac{d}{dt}c^*_{P2} + c^*_{P2}\frac{d}{dt}c_{P2} - \gamma\rho_{P2P2} \\
\frac{d}{dt}\rho_{S1S2} &= c_{S1}\frac{d}{dt}c^*_{S2} + c^*_{S2}\frac{d}{dt}c_{S1} \\
\frac{d}{dt}\rho_{S1P1} &= c_{S1}\frac{d}{dt}c^*_{P1} + c^*_{P1}\frac{d}{dt}c_{S1} - \frac{\gamma}{2}\rho_{S1P1} \\
\frac{d}{dt}\rho_{S1P2} &= c_{S1}\frac{d}{dt}c^*_{P2} + c^*_{P2}\frac{d}{dt}c_{S1} - \frac{\gamma}{2}\rho_{S1P2} \\
\frac{d}{dt}\rho_{S2P1} &= c_{S2}\frac{d}{dt}c^*_{P1} + c^*_{P1}\frac{d}{dt}c_{S2} - \frac{\gamma}{2}\rho_{S2P1} \\
\frac{d}{dt}\rho_{S2P2} &= c_{S2}\frac{d}{dt}c^*_{P2} + c^*_{P2}\frac{d}{dt}c_{S2} - \frac{\gamma}{2}\rho_{S2P2}
\end{aligned} \tag{4.55}$$

where we have assumed a spontaneous decay branching ratio of $\frac{1}{2}$ for each P state to an S state.

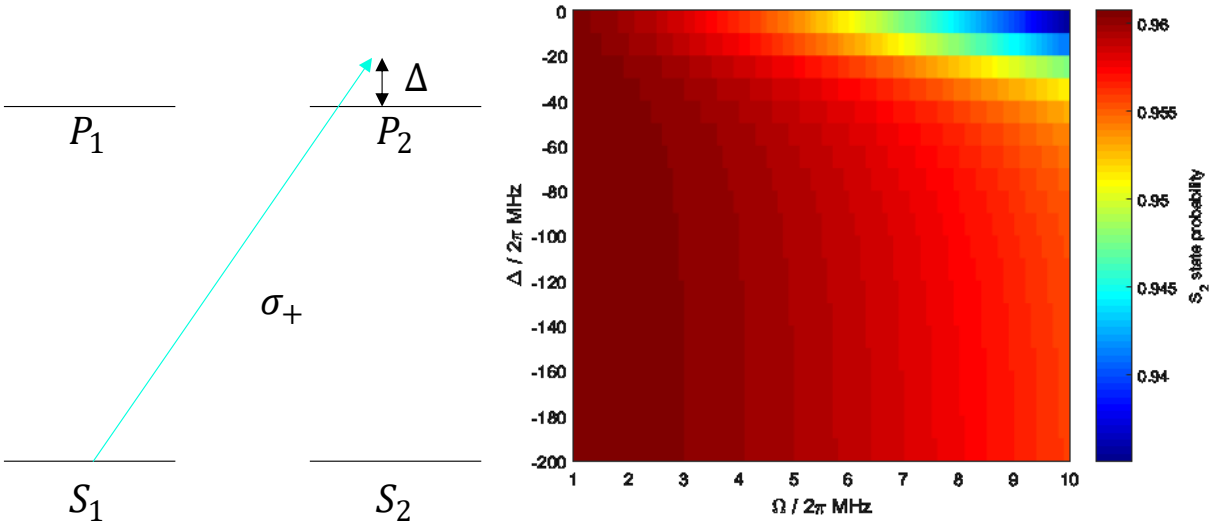

(a) (b)

Figure 4.20: (a) An illustration of the four-level toy model. (b) Color map of S_2 state probability against laser frequency and intensity.

For the simulations, we set $\gamma = 95.3\,\mu s^{-1}$, and 2% in the σ_- and σ_0 polarization each. From the simulations as shown in Fig. 4.20b, it shows that the S_2 steady state population decreases with increasing laser intensity and also lower laser frequency detunings, which are the main takeaways of this toy model study. These have important implications in terms of how we should approach laser alignments as described in the earlier section for example.

4.6.4 Estimation of $6S_{1/2} \leftrightarrow 5D_{5/2}$ Single π-pulse Transition Errors

With the hardware and lasers set up for driving $^{137}Ba^+$ $|6S_{1/2}, \tilde{F} = 2, m_{\tilde{F}} = 2\rangle$ state to the $5D_{5/2}$ states, we perform Rabi cycling experiments for each transition to the encoded states to investigate 1762 nm π-pulse transition fidelities. The Rabi cycling experimental procedure is as follows:

1. The waveform frequency from the AWG for the 1762 nm laser EOM sideband is set to the resonant frequency of a chosen 2-state transition.

2. The pulse sequence to prepare $^{137}Ba^{+}$ in the $|6S_{1/2}, \tilde{F} = 2, m_{\tilde{F}} = 2\rangle$ state is sent to the ion.

3. Once the $|6S_{1/2}, \tilde{F} = 2, m_{\tilde{F}} = 2\rangle$ state is prepared, the 1762 nm laser is turned on for some time t.

4. The fluorescence lasers are turned on and the ion fluorescence is collected in the PMT for some time, which we set to be 5 ms.

5. Steps 2-4 are repeated to obtain a large enough sample size to determine the probability of the ion being dark, which we chose to be 100 times.

6. Step 5 is repeated for a range of pulse times that cover at least half a Rabi cycle for all transitions, which is $t = 0\,\mu s$ to $t = 500\,\mu s$ in our case, in sufficiently fine time steps, which we set to be 1 µs.

The data points around the first transition probability peak of the Rabi flopping data are used to fit to the function as shown in Equation 4.56,

$$p(t) = A\cos^2\left(\frac{\pi\,(t - t_{peak})}{2t_{scale}}\right) + C \tag{4.56}$$

where A, C, t_{peak} and t_{scale} are scalar parameters that are allowed to vary to fit the function to the data points. Specifically, data points from $t = t_{peak,r}/2$ to $t = 3t_{peak,r}/2$, where $t_{peak,r}$ is the time where the data point has the highest measured transition probability in the first Rabi flopping peak, are selected for functional fitting. From the functional fit, the single π-pulse transition error is estimated to be $\epsilon_\pi = 1 - A - C$. This functional fit is also used to determine and calibrate the π-pulse times, which we set to t_{peak}.

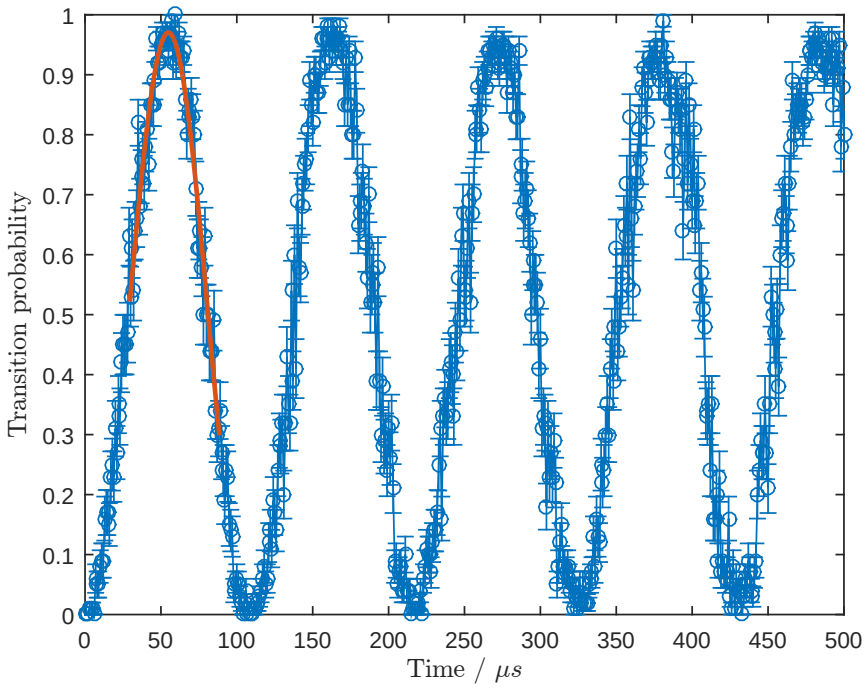

Figure 4.21: A representative plot of a Rabi flopping experiment for estimating the singple π-pulse transition error. The data shown is the transition to the $|5D_{5/2}, \tilde{F} = 4, m_{\tilde{F}} = 1\rangle$ state. Circles denote the experimental data points, and the red solid line is the functional fit using Equation 4.56.

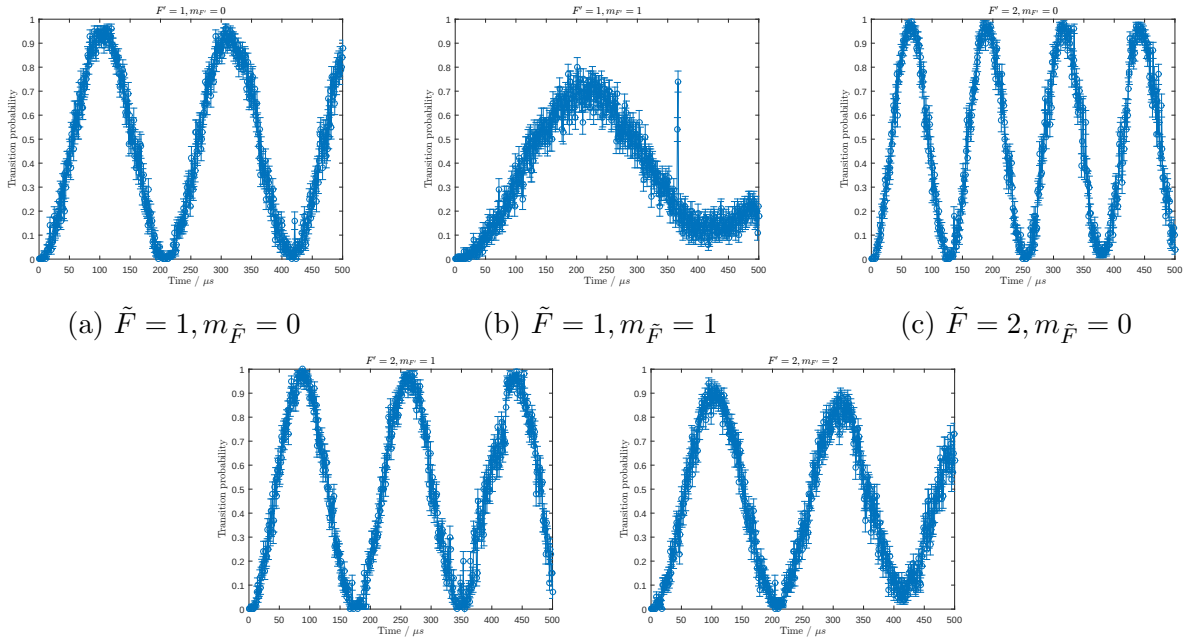

(a) $\tilde{F} = 1, m_{\tilde{F}} = 0$ (b) $\tilde{F} = 1, m_{\tilde{F}} = 1$ (c) $\tilde{F} = 2, m_{\tilde{F}} = 0$

(d) $\tilde{F} = 2, m_{\tilde{F}} = 1$ (e) $\tilde{F} = 2, m_{\tilde{F}} = 2$

Figure 4.22: Rabi cycles of the transition from the $|6S_{1/2}, \tilde{F} = 2, m_{\tilde{F}} = 2\rangle$ state to the $\tilde{F} = 1$ and $\tilde{F} = 2$ states in the $5D_{5/2}$ level.

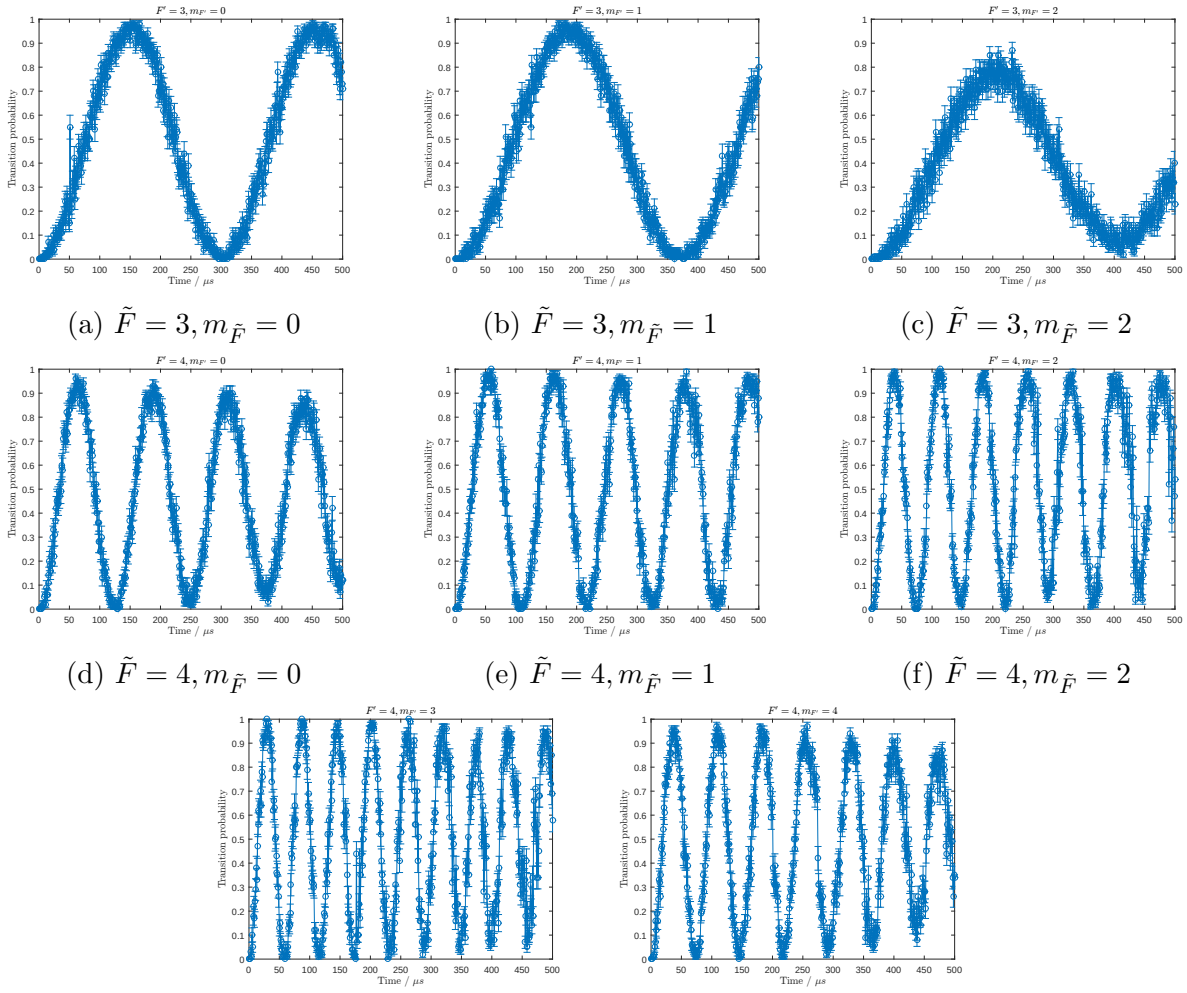

(a) $\tilde{F} = 3, m_{\tilde{F}} = 0$ (b) $\tilde{F} = 3, m_{\tilde{F}} = 1$ (c) $\tilde{F} = 3, m_{\tilde{F}} = 2$

(d) $\tilde{F} = 4, m_{\tilde{F}} = 0$ (e) $\tilde{F} = 4, m_{\tilde{F}} = 1$ (f) $\tilde{F} = 4, m_{\tilde{F}} = 2$

(g) $\tilde{F} = 4, m_{\tilde{F}} = 3$ (h) $\tilde{F} = 4, m_{\tilde{F}} = 4$

Figure 4.23: Rabi cycles of the transition from the $|6S_{1/2}, \tilde{F} = 2, m_{\tilde{F}} = 2\rangle$ state to the $\tilde{F} = 3$ and $\tilde{F} = 4$ states in the $5D_{5/2}$ level.

From Fig. 4.22, we can immediately see that the transition fidelity to the $|5D_{5/2}, \tilde{F} = 1, m_{\tilde{F}} = 1\rangle$ state is low and is not included for the SPAM experiments. The estimations of the transition errors are summarized in a later section in Section 4.6.6, where they will be discussed together with the SPAM results.

4.6.5 Efficient Calibration Protocols for 1762 nm Laser Frequencies and Pulse Times

The 1762 nm laser main power EOM frequencies for driving resonant $6S_{1/2} \leftrightarrow 5D_{5/2}$ transitions may drift due to drifts in the PDH Fabry–Pérot cavity dimensions from thermal effects or drifts in the magnetic field strengths. The 1762 nm laser pulse times to drive a π-pulse transition for each of the transition may also drift due to drifts in the laser power. Thus, to ensure optimal state preparation fidelities, the 1762 nm laser frequencies and pulse times need to be calibrated before experiments. We developed calibration processes which do not scale with qudit dimensions for $d \geq 6$, and thus show that this is not a practical concern for scaling up to higher-dimensional qudits.

The frequency calibration process employed in this work requires empirically determining $6S_{1/2} \leftrightarrow 5D_{5/2}$ transition frequencies for only 3 of the encoded states, regardless of the dimension of the qudit. The first transition frequency is the transition with the lowest magnetic field strength sensitivity, f_{offset}, which is to the $|5D_{5/2}, \tilde{F} = 2, m_{\tilde{F}} = 1\rangle$ state in this work. The other 2 transition frequencies are transitions with the largest magnetic fields strength sensitivity with respect to each other, f_{low} and f_{high}, which are to the $|5D_{5/2}, \tilde{F} = 4, m_{\tilde{F}} = 0\rangle$ and $|5D_{5/2}, \tilde{F} = 4, m_{\tilde{F}} = 4\rangle$ states in this work. The transition frequencies for some other state $|n\rangle$ encoded in the $5D_{5/2}$ level, f_n, are determined via Eq. 4.57,

$$f_n = h\left(\boldsymbol{a_n}, \Delta f, f_{offset}\right) \tag{4.57}$$

where $\boldsymbol{a_n} = (a_{n,1}, a_{n,2}, \ldots a_{n,N})$ is a list of parameters for the function $h\left(\boldsymbol{a_n}, \Delta f, f_{offset}\right)$ and $\Delta f = f_{high} - f_{low}$. We find that setting $h\left(\boldsymbol{a_n}, \Delta f, f_{offset}\right)$ as a linear function is sufficient for calibrating the transition frequencies for the drifts that we experience. So, we use

$$h\left(\boldsymbol{a_n}, \Delta f, f_{offset}\right) = a_{n,1}\Delta f + f_{offset} + a_{n,2}. \tag{4.58}$$

To determine the parameters $a_{n,1}$ and $a_{n,2}$, the transition frequency of each transition to the encoded $5D_{5/2}$ states are determined empirically. The experimental procedure to determine a transition frequency for the 1762 nm laser is as follows:

1. The waveform amplitude from the AWG for the 1762 nm laser EOM sideband is lowered to the point where the magnitude of power broadening is in the order of 1 kHz, so that we can resolve the resonant frequencies to a resolution of 1 kHz.

2. The pulse sequence to prepare $^{137}Ba^{+}$ in the $|6S_{1/2}, \tilde{F} = 2, m_{\tilde{F}} = 2\rangle$ state is sent to the ion.

3. Once the $|6S_{1/2}, \tilde{F} = 2, m_{\tilde{F}} = 2\rangle$ state is prepared, the 1762 nm laser is turned on for a time that is longer than the coherence time in our system. We set it to 3 ms in this work.

4. The fluorescence lasers are turned on and the ion fluorescence is collected in the PMT detector for a set time, which we set to 5 ms. If the 1762 nm laser frequency is resonant, there is around 0.5 probability of the ion not fluorescing.

5. Steps 2-4 are repeated to obtain a large enough sample size to determine the probability of the ion being dark, which we chose to be 400 in this work.

6. Steps 5 is repeated for the EOM frequencies from -50 kHz to 50 kHz from the previously determined resonant frequency in steps of 10 kHz, assuming that the frequencies have not drifted more than ± 50 kHz.

7. The AWG frequency where the average PMT count is the lowest from Step 6 is determined. Fine frequency scan in steps of 1 kHz is scanned from -10 kHz to 10 kHz of this frequency.

8. From the fine frequency scan, the transition probability against EOM frequency data is fit with a Lorentzian function, and the centre of the Lorentzian function is set as the resonant frequency (see Figure 4.24a).

We rely on natural drifts of our setup and collect sets of empirically determined $6S_{1/2} \leftrightarrow 5D_{5/2}$ transitions on different days. With a large enough data sets, linear regression is performed for each transition frequency, f_n, to obtain the parameters $a_{n,1}$ and $a_{n,2}$ (see Figure 4.24b).

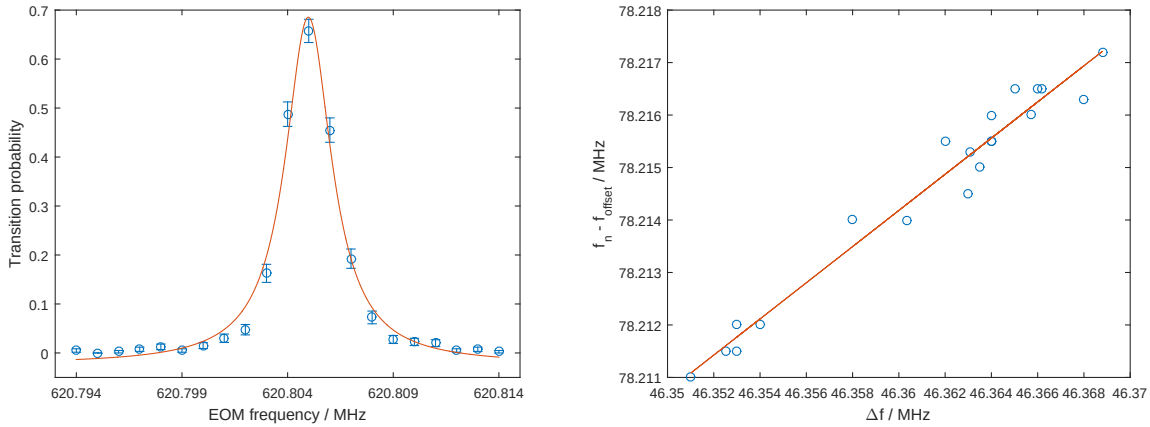

(a) (b)

Figure 4.24: (a) A representative plot of transition probability against EOM frequency for the transition to $|5D_{5/2}, \tilde{F} = 4, m_{\tilde{F}} = 1\rangle$. The data points are fit to a Lorentzian function to determine the resonant frequency of a $6S_{1/2} \leftrightarrow 5D_{5/2}$ transition. (b) A representative plot of shifted transition frequencies against Δf for the transition to $|5D_{5/2}, \tilde{F} = 4, m_{\tilde{F}} = 1\rangle$. Each data point is an empirically determined transition frequency on different days or different times. Linear regression is performed to determine the parameters $a_{n,1}$ and $a_{n,2}$.

In principle, it is possible to empirically determine only 2 transition frequencies, f_{low} and f_{high}, using this technique, and set $f_{offset} = f_{low}$. This leads to a different set of parameters $\boldsymbol{a_n}$ that are still sufficient information to determine f_n. However, since f_{low} is magnetically sensitive, it can drift during the calibration process and lead to offset errors for other calibrated frequencies f_n. Empirically, we observe that determining a transition frequency that is insensitive to magnetic field as the offset frequency, f_{offset}, is required for optimal results.

To perform fast π-pulse time calibrations, we develop a protocol as follows. From Eq. 4.31, the ratio of the Rabi frequencies between two transitions, $|j\rangle \leftrightarrow |i\rangle$ and $|j'\rangle \leftrightarrow |i'\rangle$ with the same $\Delta m = q$ is a constant value of

$$R_{i'j',ij} = \frac{\Omega_{i'j'}}{\Omega_{ij}} = \frac{\langle j'; k = 2, q|i'\rangle}{\langle j; k = 2, q|i\rangle} \tag{4.59}$$

which is independent of the laser parameters. The resonant Rabi frequencies and thus the $R_{i'j',ij}$ ratios can be empirically measured in the laboratory. During the calibration process to determine π-pulse times, for each initial state $|j\rangle$ and each $\Delta m = q$, only Rabi

frequency measurement of one transition, let it be Ω_{ij}, needs to be performed. Then, the Rabi frequencies of the rest of the transitions with the same $\Delta m = q$ can be computed using

$$\Omega_{i'j'} = R_{i'j',ij}\Omega_{ij} \tag{4.60}$$

For a quadrupole transition, $q \in \{-2, -1, 0, 1, 2\}$. Thus, at most Rabi frequencies of five transitions, one for each q value, need to be measured empirically during the calibration process, regardless of the qudit dimension d.

The scheme discussed here assumes that the actual Rabi frequencies are sufficiently close to the resonant Rabi frequencies, which does not necessarily hold true in an experimental setup. With some laser frequency detuning δ from resonance, the actual Rabi frequency is

$$\Omega' = \sqrt{\Omega^2 + \delta^2} \tag{4.61}$$

In this work, the resolution of the laser frequency is restricted to 1 kHz due to the limitation of the AWG memory size, and the weakest transition used in this work has a Rabi frequency of 2.5 kHz. Thus, the assumption $\Omega' \approx \Omega$ does not hold true consistently, and this π-pulse calibration scheme is not used in this work.

The actual π-pulse times calibration protocol is similar to what is done in Section 4.6.4. Instead of scanning a full range 500 µs of the 1762 nm pulse times, the laser pulse time is scanned from 0.5 to 1.5 times the π-pulse times of the previously found values for each transition. The functional form in Eq. 4.56 is then used to fit the data points to extract t_{peak} as the calibrated π-pulse times. This Rabi cycling experiment is done for transitions to all the encoded states during the calibration process.

4.6.6 SPAM Results and Discussions

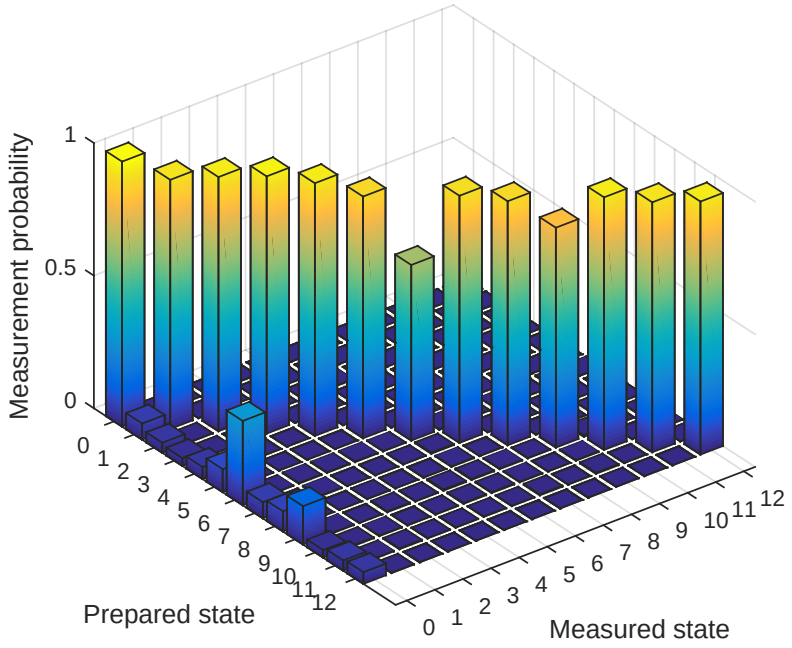

Figure 4.25: Post-selected measurement probability of the 13-level qudit SPAM experiment.

Fig. 4.25 summarizes the post-selected SPAM experimental results, where the cases when no bright state is detected throughout the measurement sequence are removed from the data set. For the raw SPAM results, where the cases with no bright states detected are counted as errors, see Table 4.4. The average raw and post-selected SPAM errors are computed to be $13.1 \pm 0.3\%$ and $8.3 \pm 0.3\%$ respectively for a 13-level qudit. The raw data sets and analysis scripts for this work can be found in the repository linked at Ref. [75].

Prepared state	Measured state												
	$\|0\rangle$	$\|1\rangle$	$\|2\rangle$	$\|3\rangle$	$\|4\rangle$	$\|5\rangle$	$\|6\rangle$	$\|7\rangle$	$\|8\rangle$	$\|9\rangle$	$\|10\rangle$	$\|11\rangle$	$\|12\rangle$
$\|0\rangle$	0.999	0.001	0	0	0	0	0	0	0	0	0	0	0
$\|1\rangle$	0.061	0.939	0	0	0	0	0	0	0	0	0	0	0
$\|2\rangle$	0.038	0.001	0.958	0.001	0	0	0.002	0	0	0	0	0	0
$\|3\rangle$	0.029	0.001	0	0.970	0	0	0	0	0	0	0	0	0
$\|4\rangle$	0.045	0	0	0	0.953	0	0	0	0	0	0	0	0
$\|5\rangle$	0.087	0.001	0	0	0	0.911	0	0	0.001	0	0	0	0
$\|6\rangle$	0.318	0.001	0.003	0.003	0.003	0.001	0.662	0.003	0.001	0.001	0	0.004	0.001
$\|7\rangle$	0.061	0	0.002	0	0	0.001	0.004	0.932	0	0	0	0	0
$\|8\rangle$	0.076	0	0	0.001	0	0	0.002	0	0.920	0	0	0.001	0
$\|9\rangle$	0.145	0.002	0	0.003	0.001	0.005	0.003	0.002	0.001	0.829	0.007	0	0.001
$\|10\rangle$	0.029	0.003	0.002	0	0.001	0.003	0.003	0.002	0	0.002	0.952	0	0.002
$\|11\rangle$	0.039	0.002	0.003	0.001	0.001	0.001	0.001	0.004	0	0.004	0	0.942	0.001
$\|12\rangle$	0.044	0.001	0	0	0	0	0	0	0	0.001	0	0	0.954

Table 4.3: Post-selected measurement probability of each prepared state from SPAM experiments used to plot Fig. 4.25. See Table 4.4 for the raw measurement probabilities.

Prepared state	Measured state													
	$\|0\rangle$	$\|1\rangle$	$\|2\rangle$	$\|3\rangle$	$\|4\rangle$	$\|5\rangle$	$\|6\rangle$	$\|7\rangle$	$\|8\rangle$	$\|9\rangle$	$\|10\rangle$	$\|11\rangle$	$\|12\rangle$	Null
$\|0\rangle$	0.999	0.001	0	0	0	0	0	0	0	0	0	0	0	0
$\|1\rangle$	0.059	0.911	0	0	0	0	0	0	0	0	0	0	0	0.030
$\|2\rangle$	0.037	0.001	0.941	0.001	0	0	0.002	0	0	0	0	0	0	0.018
$\|3\rangle$	0.029	0.001	0	0.960	0	0	0	0	0	0	0	0	0	0.010
$\|4\rangle$	0.044	0	0	0	0.926	0	0	0	0.002	0	0	0	0	0.028
$\|5\rangle$	0.080	0.001	0	0	0	0.841	0	0	0	0.001	0	0	0	0.077
$\|6\rangle$	0.252	0.001	0.002	0.002	0.002	0.001	0.525	0.002	0.001	0.001	0	0.003	0.001	0.207
$\|7\rangle$	0.058	0	0.002	0	0	0.001	0.004	0.887	0	0	0	0	0	0.048
$\|8\rangle$	0.071	0	0	0.001	0	0	0.002	0	0.861	0	0	0.001	0	0.064
$\|9\rangle$	0.126	0.002	0	0.003	0.001	0.004	0.003	0.002	0.001	0.722	0.006	0	0.001	0.129
$\|10\rangle$	0.027	0.003	0.002	0	0.001	0.003	0.003	0.002	0	0.002	0.897	0	0.002	0.058
$\|11\rangle$	0.037	0.002	0.003	0.001	0.001	0.001	0.001	0.004	0	0.004	0	0.897	0.001	0.049
$\|12\rangle$	0.043	0.001	0	0	0	0	0	0	0	0.001	0	0	0.929	0.026

Table 4.4: Raw measurement probability of each prepared state from SPAM experiments. The sample size is 1000. Null indicates that all fluorescence readouts during the measurement procedure are dark and no valid computational state output is obtained.

From Fig. 4.25 and Table 4.3, we observe that when an error occurs, where the measured state is not the intended state to be prepared, the state is measured to be in the $|0\rangle$ state most of the time. This indicates that the error is mostly at the state preparation stage, where the π-pulse transition fails to drive the ion to the intended $5D_{5/2}$ state. The large variations in the SPAM errors for different transitions indicate the major source of error is something that affects each transition to different extents, which led to the conjecture that the magnetic field noise is the major source of error, since each transition has a different magnetic field sensitivity, as summarized in Table 4.5.

Computational state	Atomic State	SPAM error	Relative magnetic field sensitivity / MHz G^{-1}	π-pulse time / µs	Estimated single transition error
$\|0\rangle$	$\|6S_{1/2}, \tilde{F}=2, m_{\tilde{F}}=2\rangle$	0.001	NA	NA	NA
$\|1\rangle$	$\|5D_{5/2}, \tilde{F}=4, m_{\tilde{F}}=4\rangle$	0.061	2.7992	37.2	0.075
$\|2\rangle$	$\|5D_{5/2}, \tilde{F}=4, m_{\tilde{F}}=3\rangle$	0.042	1.1202	29.7	0.016
$\|3\rangle$	$\|5D_{5/2}, \tilde{F}=4, m_{\tilde{F}}=2\rangle$	0.030	−0.3554	37.5	0.023
$\|4\rangle$	$\|5D_{5/2}, \tilde{F}=4, m_{\tilde{F}}=1\rangle$	0.047	−1.7009	54.9	0.030
$\|5\rangle$	$\|5D_{5/2}, \tilde{F}=4, m_{\tilde{F}}=0\rangle$	0.09	−2.9234	63.0	0.07
$\|6\rangle$	$\|5D_{5/2}, \tilde{F}=3, m_{\tilde{F}}=2\rangle$	0.34	1.7050	204.8	0.23
$\|7\rangle$	$\|5D_{5/2}, \tilde{F}=3, m_{\tilde{F}}=1\rangle$	0.068	0.5718	188.3	0.050
$\|8\rangle$	$\|5D_{5/2}, \tilde{F}=3, m_{\tilde{F}}=0\rangle$	0.080	−0.5672	151.2	0.049
$\|9\rangle$	$\|5D_{5/2}, \tilde{F}=2, m_{\tilde{F}}=2\rangle$	0.17	2.0094	104.5	0.11
$\|10\rangle$	$\|5D_{5/2}, \tilde{F}=2, m_{\tilde{F}}=1\rangle$	0.047	0.3026	87.3	0.030
$\|11\rangle$	$\|5D_{5/2}, \tilde{F}=2, m_{\tilde{F}}=0\rangle$	0.058	−1.3707	64.1	0.026
$\|12\rangle$	$\|5D_{5/2}, \tilde{F}=1, m_{\tilde{F}}=0\rangle$	0.046	−0.7373	105.4	0.054
NA	$\|5D_{5/2}, \tilde{F}=1, m_{\tilde{F}}=1\rangle$	NA	1.9462	215	0.31
NA	$\|5D_{5/2}, \tilde{F}=3, m_{\tilde{F}}=3\rangle$	NA	2.7988	$\sim$ 2000*	NA

Table 4.5: Table summarizing the encoded states and their corresponding physical atomic states, parameters relevant to the SPAM experiments and post-selected SPAM errors. The relative magnetic field sensitivities are the magnetic field sensitivities of the $5D_{5/2}$ states to the magnetic field sensitivity of the $|6S_{1/2}, \tilde{F}, m_F = 2\rangle$ state. The magnetic field sensitivities are computed by taking the numerical first order derivatives of the simulated energy levels as shown in Section 4.1.1 at $B_e = 8.35\,\mathrm{G}$. The single transition errors are estimated from the functional fits of Rabi cycles as described in Section 4.6.4. *This value is estimated from relative transition strengths using Table 4.1, and not measured empirically.

We can see that there may be some correlation of the SPAM error to the transition magnetic field strength sensitivities and π-pulse times from Table 4.5 at first glance. To further investigate the possible relation of the SPAM error to magnetic field noise, we construct an error model as follows. The post-selected SPAM error for a given prepared state $|n \neq 0\rangle$ due to decoherence from magnetic field noise is

$$\varepsilon_{SPAM} = \frac{\varepsilon_\pi}{\varepsilon_\pi + (1 - \varepsilon_\pi)^2}, \tag{4.62}$$

where ε_π is the error for a single π-pulse transition. Using filter function theory [76, 77], ε_π can be expressed as (see Appendix L)

$$\varepsilon_\pi \approx \frac{1}{\pi} \int_0^\infty \frac{1}{\omega^2} S(\omega) F(\omega) \, d\omega \tag{4.63}$$

which is a spectral overlap of the transition frequency noise power spectral density (PSD), $S(\omega)$, with the filter function of the target operation, $F(\omega)$.

We model the PSD of the magnetic field noise, which we assume to be proportional to the transition-frequency noise, to be a $1/f$-noise with a prominent peak at the mains electricity alternating current (AC) frequency and a baseline white noise,

$$S(\omega) = \begin{cases} h_a/\omega_0, & \omega < \omega_0 \\ h_{peak}, & \omega_{AC} - \Delta\omega_{AC}/2 < \omega < \omega_{AC} + \Delta\omega_{AC}/2 \\ h_a/\omega + h_b, & \text{Otherwise} \end{cases}, \tag{4.64}$$

where h_a is the scaling coefficient of the $1/f$-noise component, h_b is the baseline white noise, h_{peak} is the noise PSD peak at the mains electricity frequency, ω_0 is some threshold Fourier frequency such that noise PSD does not go to infinity at low Fourier frequencies to keep the model physical, ω_{AC} is the mains electricity frequency and $\Delta\omega_{AC}$ is the width of the mains electricity noise peak. For a π-pulse transition, the filter function can be approximated as (see Appendix L)

$$F(\omega) = \begin{cases} 4\frac{\omega^2}{\Omega^2}, & \omega < \Omega \\ 2, & \omega \geq \Omega \end{cases} \tag{4.65}$$

Assuming that $\omega_{AC} < \Omega$, evaluating Equation 4.63 with Equations 4.64 and 4.65 gives

$$\begin{aligned} \varepsilon_\pi &= \frac{4}{\pi}\left(\frac{5h_a}{4\Omega^2} + \frac{h_a}{\Omega^2}\ln\left(\frac{\Omega}{\omega_0}\right) + \frac{h_b}{\Omega^2}(\Omega - \omega_0) - \frac{h_a}{\Omega^2}\ln\left(\frac{\omega_{AC} + \Delta\omega_{AC}/2}{\omega_{AC} - \Delta\omega_{AC}/2}\right)\right. \\ &\left. - \frac{h_b}{\Omega^2}\Delta\omega_{AC} + \frac{h_b}{2\Omega} + \frac{h_{peak}}{\Omega^2}\Delta\omega_{AC}\right) \\ &\approx \frac{4}{\pi\Omega^2}\left(\frac{5h_a}{4} + h_a\ln\left(\frac{\Omega}{\omega_0}\right) + h_{peak}\Delta\omega_{AC}\right) + \frac{6h_b}{\pi\Omega}, \end{aligned} \tag{4.66}$$

where we have made the approximations $\omega_0 \ll \Omega$, $\Delta\omega_{AC} \ll \omega_{AC}$ and $h_b \ll \Omega^2\Delta\omega_{AC}$. From Equation 4.66, there are 2 asymptotic behavior. In the regime where $\Omega \ll \frac{2K}{3h_b}$, where $K = \frac{5h_a}{4} + h_a\ln\left(\frac{\Omega}{\omega_0}\right) + h_{peak}\Delta\omega_{AC}$, $\varepsilon_\pi \propto \frac{1}{\Omega^2}$. In the regime where $\Omega \gg \frac{2K}{3h_b}$, $\varepsilon_\pi \propto \frac{1}{\Omega}$. Since it is commonly reported that the mains electricity AC noise is a dominant error source [20, 29], it is reasonable to assume that we are in the $\Omega \ll \frac{2K}{3h_b}$ regime in this work as well.

In the time domain, assuming that the fluctuation in the magnetic field strength is sufficiently small, the transition frequency shift of 2 energy states can be estimated to be linear, i.e.

$$\Delta\nu(t) \propto \kappa B_e(t), \tag{4.67}$$

where $\Delta\nu\,(t)$ denotes the transition frequency shift, κ is the linear magnetic field sensitivity and B_e is the magnetic field strength. This implies that the PSD of the transition frequency shift, which is the transition-frequency noise to be proportional to κ^2, i.e.

$$S\,(\omega) = \left|\Delta\hat{\nu}\,(\omega)\right|^2 \propto \kappa^2. \tag{4.68}$$

With the π-pulse time being inversely proportional to the Rabi frequency, $\tau_\pi \propto 1/\Omega$, Eqs. 4.66 and 4.68, in the $\Omega \ll \frac{2K}{3h_b}$ regime, we have

$$\varepsilon_\pi \propto \kappa^2\tau_\pi^2, \tag{4.69}$$

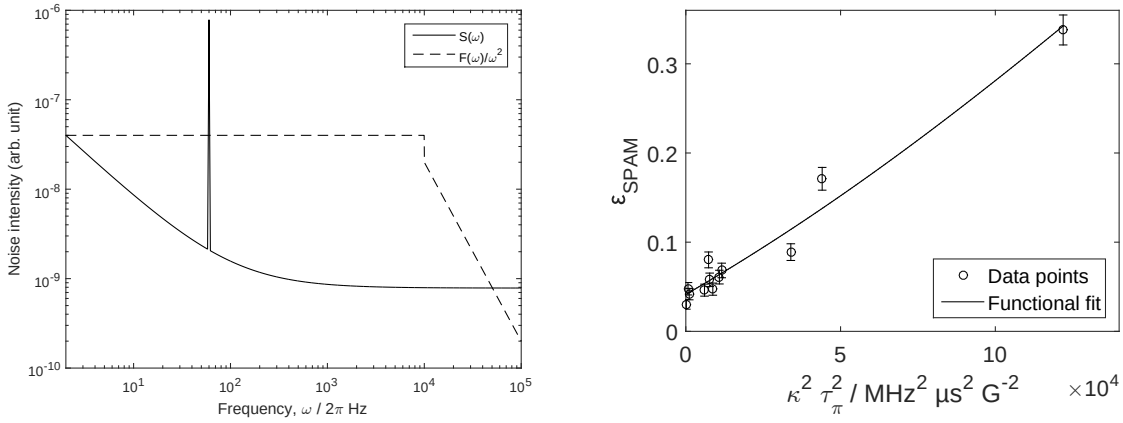

(a) (b)

Figure 4.26: (a) Diagrammatic representation of the functional forms of the frequency noise power spectral density, $S(\omega)$, and the filter function of a π-pulse transition, $F(\omega)$, used for error analysis in this work. (b) Plot of the post-selected SPAM error for each prepared state from Fig. 4.25 against $\kappa^2\tau_\pi^2$, which we identify as the relevant figure of merit for errors induced by magnetic field fluctuations. κ is the magnetic field sensitivity and τ_π is the π-pulse time. An obvious positive correlation of ε_{SPAM} with $\kappa^2\tau_\pi^2$ is observed, indicating agreement with Eq. 4.69. Eqs. 4.62 and 4.69 with an additional freely varying parameter for the vertical intercept are used to fit the data.

The scaling of ϵ_{SPAM} with $\kappa^2\tau_\pi^2$ as shown in Fig. 4.26b shows agreement with this error model, which supports the notion that magnetic field noise is a major source of error in this work. The vertical intercept of $\epsilon_{SPAM} = 0.041 \pm 0.006$ in Fig. 4.26b may indicate that around 4% of the error comes from other sources. From Eq. 4.62, for small ϵ_π, $\epsilon_{SPAM} \approx \epsilon_\pi$.

By comparing ϵ_{SPAM} with the empirically measured ϵ_π in Table 4.5, for $\epsilon_\pi < 0.1$, ϵ_{SPAM} is larger than ϵ_π by $1.5 \pm 2\%$ on average. We suspect that this 1.5% error may come from calibration drifts and 614 nm light leakage. We speculate that the majority of the rest of the remaining error to be from unclean laser polarization from the optical pumping step, but the available data in this work does not allow accurate quantitative estimations of the remaining errors. A more advanced state preparation protocol, by pumping out the unwanted $6S_{1/2}$ states with 1762 nm transitions [6], has been shown to reduce optical pumping errors to below 10^{-4}, and can be applied in the future extension of this work to mitigate optical pumping errors.

The sources of error discussed above make up most of the SPAM error in this work. The rest of the error sources are difficult to be analyzed empirically due to the large uncertainties of the two estimated sources of errors. Other known error sources are theoretically computed in this work and they are indeed relatively small. The longest time a state stays shelved in $5D_{5/2}$ level during the SPAM process in this work is around 120 ms. This leads to an estimated upper bound error of around $e^{0.12/35} \approx 0.3\%$ due to spontaneous emission from the $5D_{5/2}$ level. The transitions with transition frequencies closest to each other are the transitions to the $|5D_{5/2}, \tilde{F} = 4, m_{\tilde{F}} = 2\rangle$ and $|5D_{5/2}, \tilde{F} = 3, m_{\tilde{F}} = 0\rangle$ states, which are separated by around $\Delta = 475$ kHz. With $6S_{1/2} \leftrightarrow 5D_{5/2}$ transition Rabi frequencies of around $\Omega = 10$ kHz, the estimated error due to off-resonant transition is around $\frac{\Omega^2}{\Omega^2+\Delta^2} = 0.04\%$. The photon count threshold to determine bright or dark ion states is set to 11 counts for the SPAM data set in this work. The average photon count of the data points below this threshold, which we estimate to be the dark state average photon count, is 0.651 ± 0.002. The average photon count of the data points above this threshold, which we estimate to be the bright state average photon count, is 27.87 ± 0.05. Assuming Poisson distributions for dark and bright state photon counts, we have an upper bound of 0.025% for bright/dark state discrimination error.

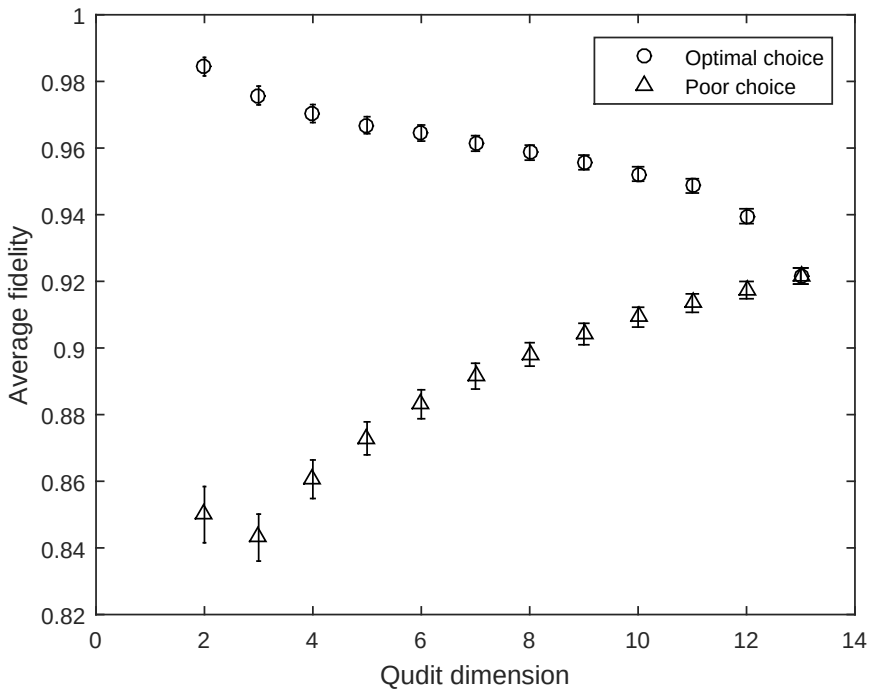

Figure 4.27: Scaling of average SPAM fidelity with qudit dimension with optimal choices of the encoded states and with poor choices. For the optimal choice, the $|6S_{1/2}, F = 2, m_F = 2\rangle$ state and $d-1$ states with the best π-pulse transition fidelities are chosen as the computational states. For the poor choice, the $d-1$ states with the worst π-pulse transition fidelities are chosen instead. This illustrates that the scaling of the fidelity is largely dependent on the fidelity of the additional π-pulse transition and not inherent to the qudit dimension.

It should be noted that the SPAM error only scales with the encoded qudit dimension if the additional encoded state has worse π-pulse transition error. Qudit SPAM error does not increase inherently with increasing qudit dimensions, as long as the decay time of the metastable states remains negligible compared to the SPAM operation time. Figure 4.27 illustrates this point, where you can have the average SPAM fidelity increase with qudit dimensions by making poor choices for qudit encoding.

The finding that the magnetic field noise error is our major source of error is a good sign, as we have not put in any effort in addressing magnetic field noise in this work. Thus, they are expected to be large. The fact that we do not see any other large sources of error

indicates that we did not run into any unprecedented large errors related to scaling up the qudit dimensions, and therefore we are not seeing any evidence that inherently prohibits qudit scaling. As alluded in Chapter 1, methods to mitigate magnetic field noise are known. Magnetic field noise can be reduced passively via setting up magnetic shielding around the ion trap, and using permanent magnets as the source of magnetic field. This method has been shown to to be able to reduce magnetic field noise to a level of $\leq 2.7 \times 10^{-8}$ G [19], which is estimated to contribute to an error level lower than light scattering error from hyperfine Raman transitions [21]. It is known that the alternating current (AC) of the mains electricity contribute a significant level of magnetic field fluctuation. This magnetic field fluctuation can be compensated actively by generating an oscillating magnetic field at the mains electricity AC frequency with the appropriate amplitude and phase that counters the fluctuation. Electromagnets can be used to generate this magnetic field and significant improvements of the coherent times from 70 µs to 2500 µs in a $^{40}Ca^{+}$ qubit have been demonstrated [20].

The measurement time of around 100 ms is relatively long for typical trapped ion quantum operations [5, 12, 16, 17, 18]. The main contributors to the measurement time are the AWG trigger and fluorescence steps. The AWG trigger time is an artificial limitation from the method we employed in this work for switching the 1762 nm laser EOM frequency from the AWG (see Section 4.6.2). To speed up this process, in principle, it is possible to program and generate a single arbitrary waveform which changes in frequency according to the timings of the deshelving steps. This bypasses the 4 ms AWG external signal trigger step in this work. The fluorescence time in this work is set to be comparable to the AWG signal trigger times to maximize collected photon counts of bright ions without significant compromise to the overall measurement time. If the 1762 nm laser frequency switching time is reduced, the fluorescence time can be reduced as well, as long as it does not significantly impact the error from distinguishing bright and dark states. From Ref. [6], it is demonstrated that a fluorescence collection time of 350 µs is possible with $^{137}Ba^{+}$. Thus, with these efforts, it should be possible to reduce the overall measurement time significantly, to $d \times 350$ µs, and the measurement time scales linearly as the qudit dimension. With the measurement time reduced, the main contributor to the SPAM experimental time could be the state preparation procedure, which is dominated by the repump time. The repump time is long due to the dipole transition from the $|5D_{5/2}, \tilde{F} = 4, m_{\tilde{F}} = 4\rangle$ state to the $|6P_{3/2}, F = 2\rangle$ state being forbidden. Thus, to access the $6P_{3/2}$ level from the $|5D_{5/2}, \tilde{F} = 4, m_{\tilde{F}} = 4\rangle$ state, it has to go to the $|6P_{3/2}, F = 3\rangle$ state, which is roughly 400 MHz detuned, and therefore requiring a long transition time. The transition frequencies of the rest of the encoded states to the $|6P_{3/2}, F = 2\rangle$ state are only detuned in the order of 10 MHz, and a repump time in the order of 100 µs is sufficient. To reduce the

repump time to the order of 100 µs, an EOM can be set up to generate an additional frequency that is resonant to the $|5D_{5/2}, \tilde{F} = 4, m_{\tilde{F}} = 4\rangle \leftrightarrow |6P_{3/2}, F = 3\rangle$ transition, and further reduction in repump time is possible with more effort towards increasing 614 nm laser intensity at the ion.

4.6.7 Concluding Remarks and Outlook

In this work, we have demonstrated high-level qudit encoding and SPAM of up to 13 levels using a $^{137}Ba^+$ ion with average raw and post-selected SPAM errors of $13.1 \pm 0.3\%$ and $8.3 \pm 0.3\%$ respectively. Calibration protocols of the laser parameters for SPAM that do not scale with qudit dimensions are also demonstrated, which have important practical implications for scaling up qudit dimensions. The major source of SPAM error in this work is the magnetic field noise. However, this should not be a major roadblock for this qudit protocol, as the methods to rectify magnetic field noise are known. Implementing these methods in our setup will be one of the main efforts in the future advancement of this qudit work.

We have thus far demonstrated SPAM with $^{137}Ba^+$ in this work. To build a functioning quantum computer, the ability to perform single qudit gates and entangling gates are required. The encoding scheme and the state manipulation presented in this work is similar to the study in Ref. [12] using $^{40}Ca^+$. Universal qudit quantum computing has been demonstrated in that work. Therefore, it is reasonable to suggest that the implementation of single qudit and entangling gates for $^{137}Ba^+$ can be similar to $^{40}Ca^+$ and straightforward. Since any two states in the $6S_{1/2}$ and $5D_{5/2}$ levels of a Ba^+ ion can be connected by a sequence of two-level transitions, universal single qudit gates for states in the $^{137}Ba^+$ $5D_{5/2}$ can be straightforwardly implemented with precise phase and timing control of the 1762 nm laser [72, 73, 74]. Entangling gates can also be implemented directly with 1762 nm lasers, provided that the state coherence time is long enough. For faster entangling gates, Raman transitions between the $6S_{1/2}$ hyperfine states using high-power 532 nm lasers can be used. These efforts towards actualizing high-dimensional universal qudit quantum computing with $^{137}Ba^+$ are our main objectives for the continuity of this work.

Another milestone for the continuity of this work, which I predict to be within reach in the near future, is extending $^{137}Ba^+$ qudit encoding to up to 25-levels. This can be done by performing multiple 1762 nm π-pulse transitions for state preparation, but the fidelity will be limited due to large error from magnetic field noise. An alternative method is to be able to prepare the ion in some $6S_{1/2}$ state other than $|6S_{1/2}, \tilde{F} = 2, m_{\tilde{F}} = 2\rangle$ via other means. One method is by driving hyperfine transitions in the $6S_{1/2}$ level using

a microwave or via laser Raman transitions. Another method is to perpetually pump the undesired $6S_{1/2}$ states to the $6P_{3/2}$ level and let it spontaneously decay until it reaches the desired prepared state in the $6S_{1/2}$ state with 1762 nm, 614 nm, and 650 nm lasers. As long as any $6S_{1/2}$ state can be prepared with high fidelity, we only need a single 1762 nm transition to prepare it in any $5D_{5/2}$ states, which would let us achieve 25-level SPAM with similar average fidelity as we have now, even without reducing magnetic field noise.

Chapter 5

Cost Effective Beam Stabilizer

In this chapter, I discuss a solution that we have developed in the laboratory for solving the problem point laser beam pointing drifts. It is somewhat disconnected from the main trapped ion work, but beam pointing drifts are a common problem in any laboratory using free-space laser beams and may be an of interest for any readers encountering this problem. This invention allows the user to solve the problem of slow laser beam drifts using cost-effective and commercially accessible components.

5.1 Concept and Idea

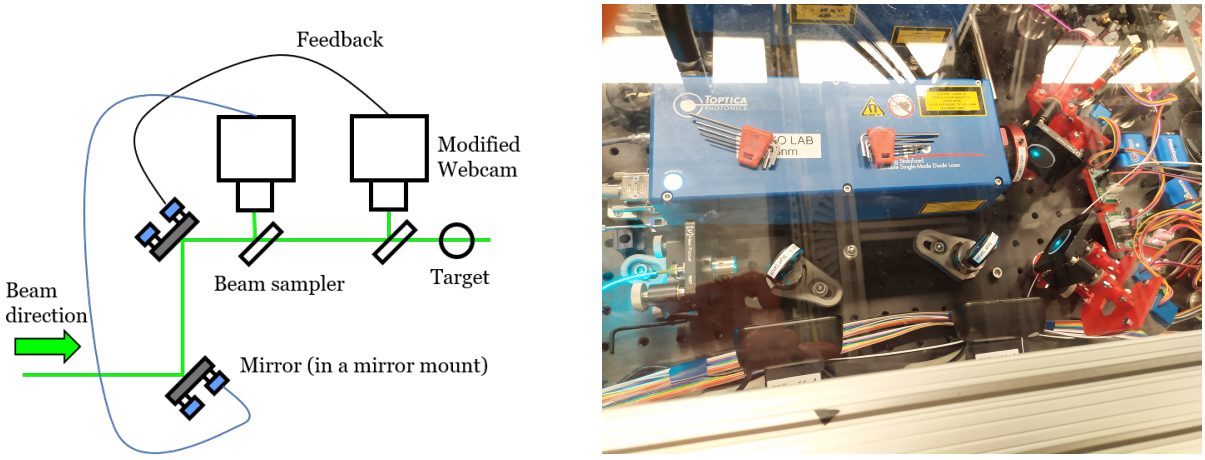

(a) (b)

Figure 5.1: (a) Schematic of the cost-effective stabilizer. Two mirrors on mirror mounts, each with a horizontal and a vertical actuators, provide full control of the laser beam pointing. Each mirror mount is motorized with hobby-level motors for automation. Two beam samplers pick off a small percentage of the laser power at two different points along the laser beam path. The picked off beams are directed into their respective modified webcams. The modified webcams detect the coordinates of the beams and provide feedback to the mirror mounts for beam stabilization. (b) A photograph of the setup used to stabilize the beam pointing from a laser head.

The beam pointing of a laser beam can be fully defined by being directed by 2 mirror mounts, each with a horizontal and a vertical actuators (see Figure 5.1). The 4 actuators provide the 4 degrees of freedom required to fully define a straight line in a 3-dimensional space, thus giving full control of the laser beam pointing. To automate the process of beam pointing control, the actuators on the mirror mounts have to be motorized. We have invented a cost-effective method to achieve this. We custom-designed plastic parts that enables the user to attach hobby-level stepper motors, which are cheap and easily commercially accessible, to manual mirror mounts. This method allows the user to motorize any typical manual mirror mounts (from Thorlabs, Newport, etc.) by only slightly changing the design of the plastic parts. The stepper motors are driven and digitally controlled by a Raspberry Pi.

(a)

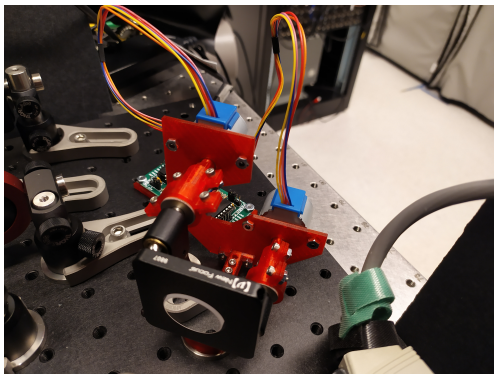

(b)

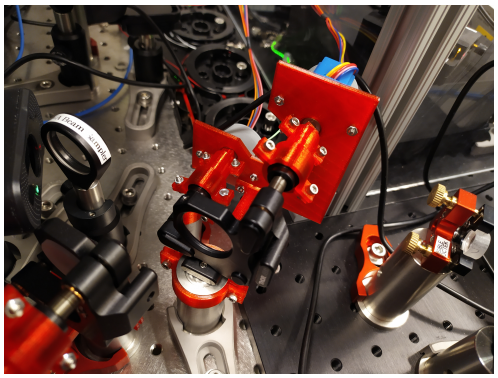

(c)

Figure 5.2: Coupling of stepper motors to mirror mounts using custom designed parts. (a) Plastic parts for motor-mount coupling. (b) A Newfocus mirror mount coupled with stepper motors. (c) A Thorlabs mirror mount coupled with stepper motors.

To be able to do active beam stabilization, feedback to the stepper motors are required.

To achieve this, small portions of power of the laser beams are picked-off at 2 different points along the laser beam path with beam samplers. Each picked-off beam are sent to a modified webcam. The webcams are modified by removing the their lenses and attaching a neutral density filter to filter off background light. The 2 webcams provide the necessary coordinates at 2 different points along the beam path required to fully define a straight line. By using the coordinates of the laser beam on 2 different webcams as feedback for the stepper motors, active stabilization of the laser beam is possible.

We have written the program to interface with the webcams and stepper motors, which we consider to be our invention. Active beam stabilization is achieved using this program and demonstrated in Section 5.2. With this method, any commercially available USB webcams can be used, which lends to cost-effectiveness and ease of access.

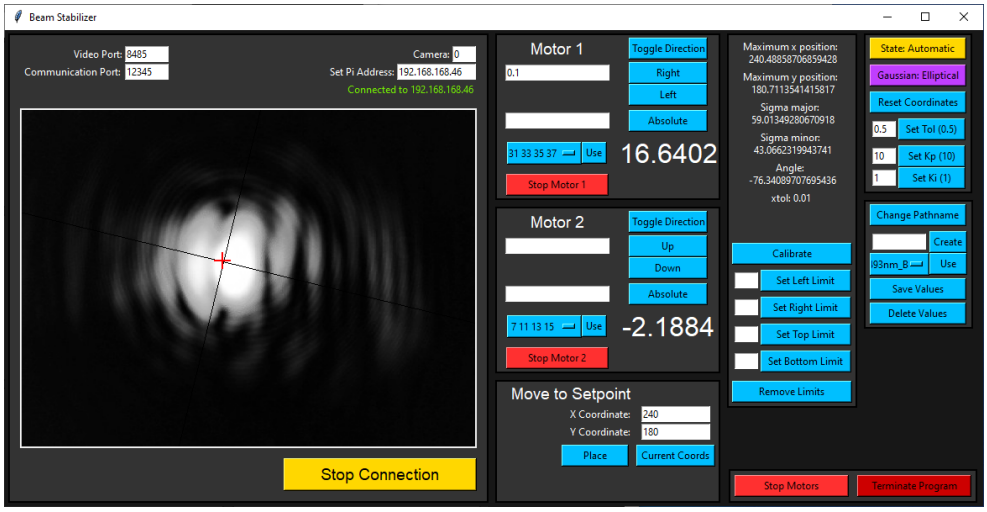

Figure 5.3: Graphical user interface (GUI) of our custom written program. It runs on Windows and is Python-based.

5.2 Stabilization Demonstration

We have demonstrated the performance of our cost-effective beam stabilizer in a fiber coupler setup. In a fiber coupler setup, a laser beam is sent through a collimator, which focuses the laser light into a optical fiber tip. The laser power output from the optical fiber is largely dependent on the beam pointing of the laser in the fiber coupler setup. This is because the fiber tip is small (in the order of microns) and slight displacements or

angular deviations of the laser beam would cause the laser to miss the tip. Therefore, by monitoring the laser power at the optical fiber output, the beam pointing stability can be assessed.

We set up an artificial source of beam destabilization by moving the beam randomly using a motorized mirror mount before the beam stabilizer setup. With the artificial destabilization, the power output from the fiber is monitored with the beam stabilizer turned on and off. As seen in Figure 5.4, the power output has greatly different trends with and without the beam stabilizer turned on. With the beam stabilization turned on, the output power is stable at around 11 µW. Without the beam stabilization, the output power varies wildly.

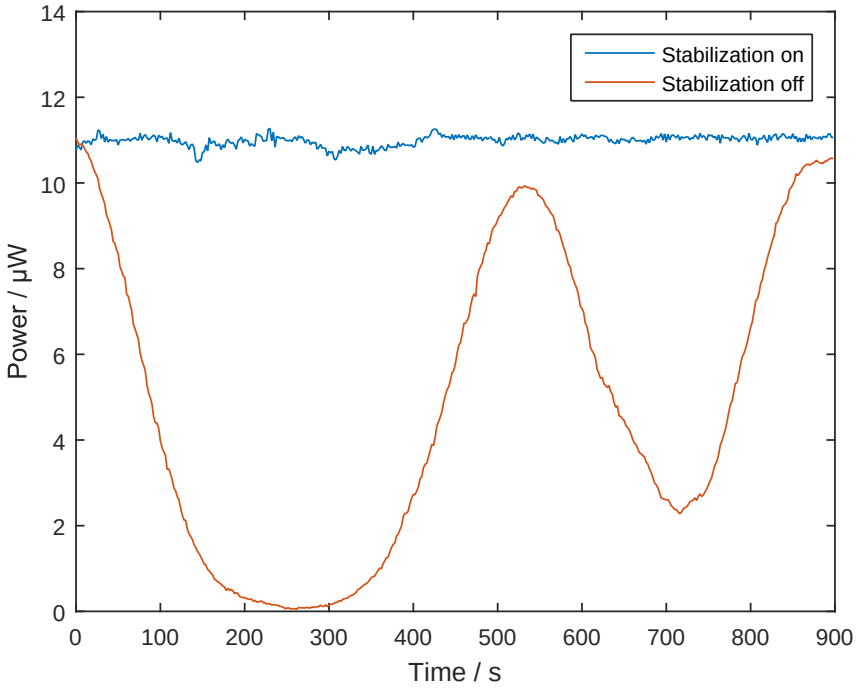

Figure 5.4: Power output from an optical fiber in a fiber coupler setup. An artificial source of beam drift is introduced into the system. With the active beam stabilization turned on, the output power is stable at around 11 µW. With the beam stabilizer turned off, the power output varies wildly.

5.3 Program Overview

The basic setup of our cost-effective beam stablizer (controlling only 1 mirror mount) consists of 1 Windows machine, a Raspberry Pi, a webcam and 2 stepper motors. The Raspberry Pi has to be on the same network as the Windows machine, so that they can talk to each other. This can be done either via WiFi or ethernet connections. A webcam and 2 stepper motors are connected to the Raspberry Pi. The webcam is connected via USB and the stepper motors are connected through the Pi's GPIO pins.

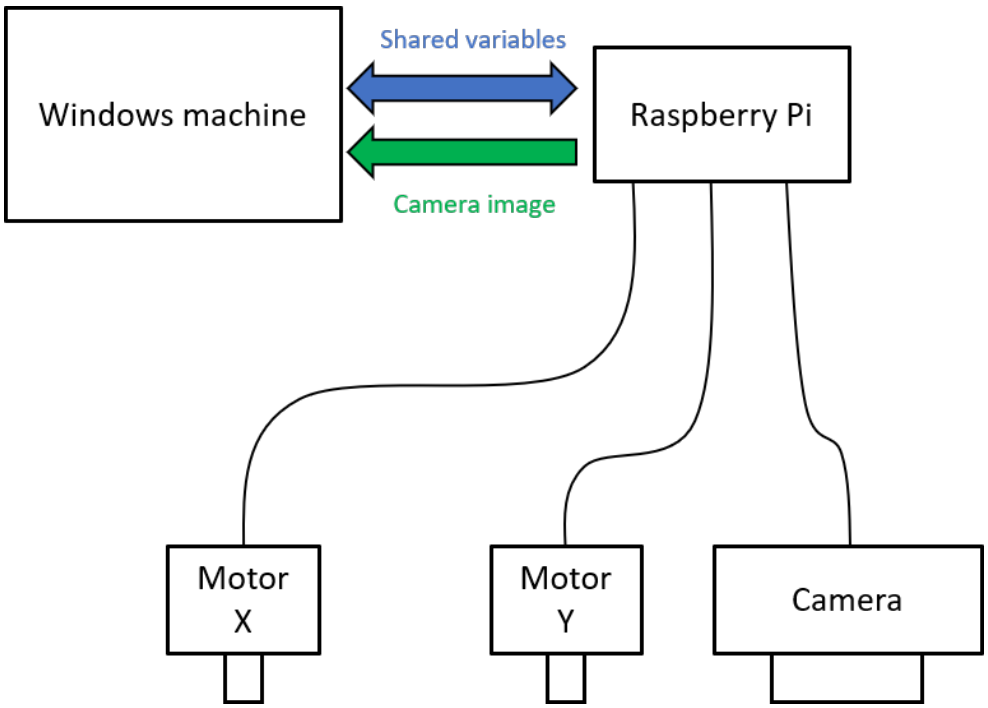

Figure 5.5: Schematic of the basic setup of beam stabilizer setup. The hardware consists of a Windows machine, a Raspberry Pi, 2 stepper motors and 1 camera.

There are 2 running scripts for our cost-effective beam stabilizer - one running on a Windows machine and another one running on a Raspberry Pi. The script on the Pi collects images from the webcam and sends the images to the Windows machine. The Pi script also controls the stepper motor voltages to move the motors. The script on the Windows machine runs the GUI of the program. The Windows script runs the computations to calculate the parameters of a 2D Gaussian function when it is used to fit the images received from the Pi. This gives the coordinates of the laser beam on the webcam. The

Windows script also decides the motors to move, at which directions, at what speed, and sends the commands to the Pi.

5.4 Program Flow - Initialization

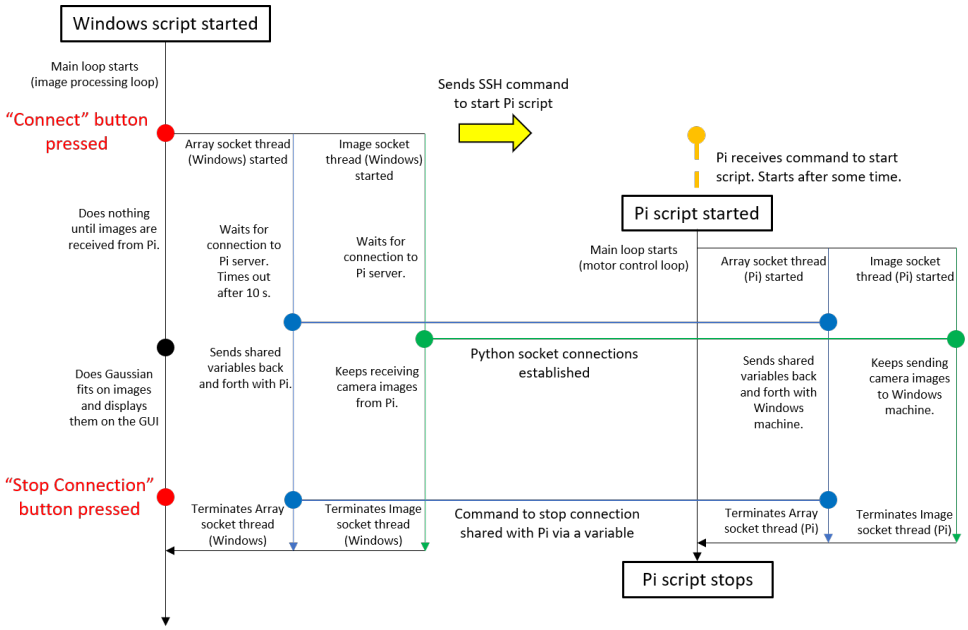

Figure 5.6: Program flow of when the beam stabilization software is first started. See text for detailed descriptions.

The script on the Windows machine is run first. It launches a GUI using Python's tkinter module. The script starts the main loop of processing the acquired images. However, the loop does not do anything until the Windows machine's connection to a Pi running the beam-stabilizer script is established. On the GUI, there are entries for the "Video port", "Communication port", "Camera" and "Set Pi Address". The video port is the port that is used for sending the webcam images from the Pi to the Windows machine. The video port is chosen to be 8485 by default. The communication port is the port used for sending and receiving the variables being used by both machines. This port is chosen to be 12345 by default. The "Camera" entry chooses the webcam to be used. Since we only use 1 camera per Pi, the "Camera" entry is usually set to 0. The "Set Pi Address" entry requires the

IP address of the Raspberry Pi, as the name suggests. Once these 4 entries are set, the "Connect" button is pressed.

Once the "Connect" button is pressed, the Windows machine sends the command to run the beam-stabilizer script on the Pi specified by the address in the entry "Set Pi Address" via SSH. At the same time, the "Array socket thread (Windows)" and the "Image socket thread (Windows)" are run in parallel with the image-processing main loop on the Windows machine. The "Array socket thread (Windows)" is a thread that runs continuously to exchange variables that are shared by both the Windows machine and the Pi using Python's socket module. This is the communication thread that uses the port 12345. The "Image socket thread (Windows)" is a thread that runs continuously to receive camera images from the Pi. This is the communication thread that uses the port 8485. On the Windows machine, both "Array socket thread (Windows)" and "Image socket thread (Windows)" act as clients and seek to establish connections with the socket servers at the Pi. Once the connections to the servers are established, the threads run their continuous loops and functions accordingly. If a long enough time has passed (hard-coded to be 10 seconds) after the "Array socket thread (Windows)" is started without being able to establish a connection to the Pi server, both "Array socket thread (Windows)" and "Image socket thread (Windows)" terminate and the script goes back to the state when it is first started, where only the main loop for processing images is running. While trying to connect to the Pi or when the connection has already established, the user has the choice to terminate the threads, "Array socket thread (Windows)" and "Image socket thread (Windows)", manually from the GUI by pressing the "Stop Connection" button as well, which will return the script the the initial state when it is first started.

On the Pi side, the Pi script runs 3 parallel threads continuously when it is started. The "Pi main thread" controls the stepper motor voltages. The "Array socket thread (Pi)" is the server sends and receives an array of variables shared by both the Pi and the Windows machine. The "Image socket thread" is the server that captures images from the webcam using Python's OpenCV module and sends the images to the Windows machine.

When the connection is established, the Pi continuously sends the images acquired from the camera to the Windows machine. The Windows machine receives the images and perform 2D elliptical or circular (select-able by the user on the GUI) Gaussian function fits on the images and display the images and the fit parameters on the GUI. The script also draws an angled crosshair on top of the image that marks the maximum intensity point from the fit parameters. The angle of the crosshair is dependent on the fitted angle parameter of a 2D elliptical Gaussian fit, marking the major and minor axes of the ellipse. It displays a normal straight crosshair if a circular Gaussian fit is chosen.

5.5 Image Processing

For each image received from the Pi by the Windows machine, a 2D Gaussian function fit is performed to find the fit parameters. The least_squares function from Python's scipy module is used to do the function fit. Since the least_squares function utilizes a non-linear regression method, initial guess of the function parameters are required. In addition, the initial guess cannot be too far off from the global optimal fit, as the parameters may converge to some local optimum that is not the true global optimal parameters due to the nature of non-linear regression.

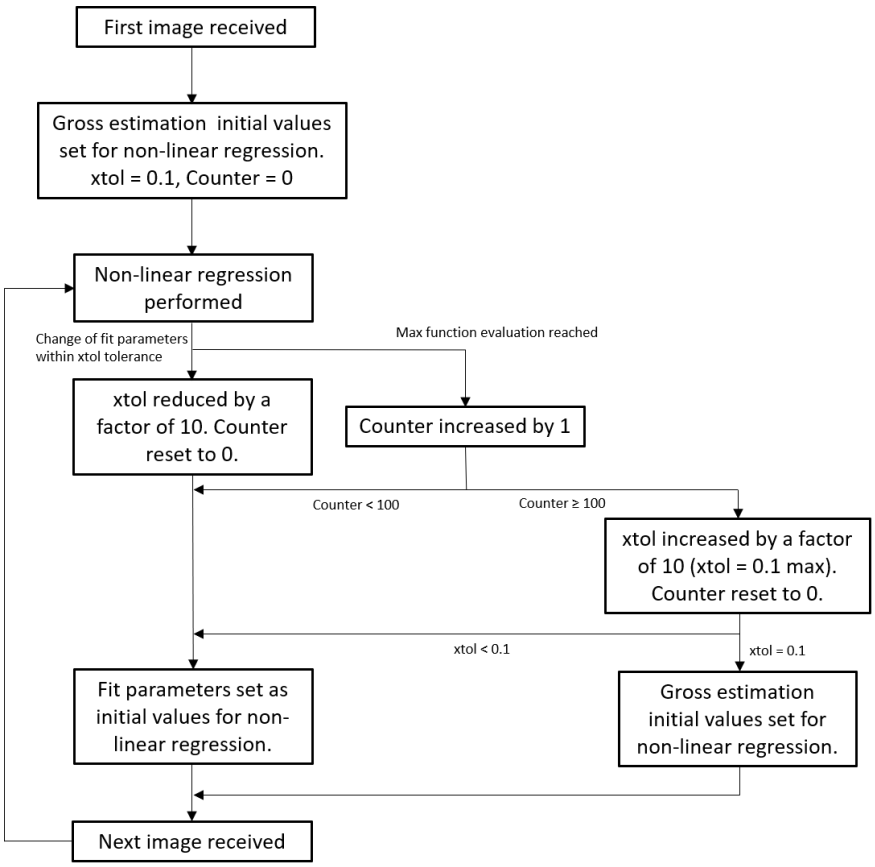

Figure 5.7: Program flow for processing image obtained from the camera. See text for detailed descriptions.

For the first image received from the Pi, the initial guess of the fit parameters are grossly estimated. For the initial guess of the amplitude parameter, it is set to 100. This

is because the maximum count of a single pixel on a typical camera using integer format is 255, 100 is approximately half of that. For the beam width, which is the σ parameter, the initial guess is set to 50. This is because the typical pixel size of a webcam is approximately 6 micron, 50 pixels correspond to roughly 0.3 mm, which is close enough to a typical laser beam radius. The beam angle initial guess is set to 0. The initial guess of the intensity offset of the Gaussian function is set to 0 as the background counts are expected to be low since the webcam is covered by a neutral-density filter. For the initial guesses of the maximum x and y positions of the Gaussian function, they are taken from the median of the indices of the pixels with the highest count in the image. By taking the median of the indices, the guess of the beam position will still be accurate even when the laser intensity is saturated on the camera.

In the least_squares function, the maximum number of function evaluation is set to a low number of 3. This is because we want this process to be fast for a smooth frame rate on the GUI and fast response time of the beam-stabilizer. The downside of having a low maximum number of function evaluation is that the non-linear regression may end prematurely before the parameters converge to to accurate values. This is circumvented by using the fitted parameters from the previous image for the subsequent image. For a laser that is stable on the camera, all the images are nearly identical. Thus, by iterating the process of using the fitted parameters of the previous image for the subsequent image, the initial guess and resultant fitted parameters still converge to the accurate values over time.

There is a problem that could arise from the iteration of using the resultant fit parameters from the previous image for the initial guess of the next image, which is when the resultant fit parameters from the previous image are inaccurate initial guess of the parameters for the next image. This could happen when the laser is not initially turned on in the previous image and turned on in the subsequent image. Another case this could be happening is when the laser beam is being moved quickly. Then, the initial guess of the parameters are not accurate, the problem of converging to non-globally optimal values arises again. In these cases, we want to revert the initial guess of the parameters to the gross estimations as described by paragraph 2 of this section. To solve this problem, we utilize the "xtol" option of the least_squares function. The "xtol" parameter quantifies the tolerance for termination by the change of the fit parameters. If the magnitude of the change of the fit parameters are smaller than the threshold defined by "xtol" in the non-linear regression iterations, the non-linear regression terminates as a "successful fit". The "xtol" value is initially set to 0.1. If a non-linear regression fit terminates due to the fit parameters changing by magnitudes smaller than that defined by "xtol" (as opposed to reaching the maximum number of function evaluation), the "xtol" value is reduced by a

factor of 10. If non-linear regressions that terminate due to reaching the allowed maximum number of function evaluation 100 times consecutively, "xtol" in increased by a factor of 10, to a maximum value of 0.1. If non-linear regressions that terminate due to reaching the allowed maximum number of function evaluation 100 times consecutively while the "xtol" value is 0.1, the initial guess of the parameters will be reverted to the gross estimations as described by paragraph 2 in this section. These steps prevent the parameter fit to be stuck in a non-global optimum when there are large changes in the images.

With these techniques in place, we find that the fit parameters are accurate every time we send a laser to the camera when the setup is tested and being used in our lab.

5.6 Motor Movement

Each stepper motor that we use has 4 voltage pins that power the electromagnets in the motor. The 4 pins are turned on in a sequence of patterns to move the rotor. The GPIO pins of the Raspberry Pi is used to supply the voltages to the stepper motors. The rotational speed of the rotor is controlled by the time delay between the patterns in the pin voltage sequence. By default, the time delay is set to 1 ms for fast movement.

For each stepper motor, there are 2 variables shared by the Windows and Pi machines (through the "Array socket thread") that dictate the motor movement. They are both boolean variables, the first variable dictates whether to move or not to move the motor clockwise - it moves when the variable is set to "True", does not move when it is set to "False". Likewise, the second variable dictates whether to move the motor anticlockwise. When both parameters are "True" or both are "False", the motor does not move. The motor movement control in the script is done this way so that it is responsive to changes by the user. Since the "Array socket thread" runs independently in parallel with other functions, the motor movement variables are updated in the speed of the loop. Thus, the motors can be moved or stopped quickly by setting the motor movement variables to "True" or "False".

5.6.1 Manual Mode

By default, the script is set to "Manual Mode", where the motor movements are not controlled by any feedback, and are controlled by manual entries from the user. There are 2 ways to move a motor manually from the GUI. The first is by setting an absolute displacement to move the motor to. The script on the Windows machine reads the current

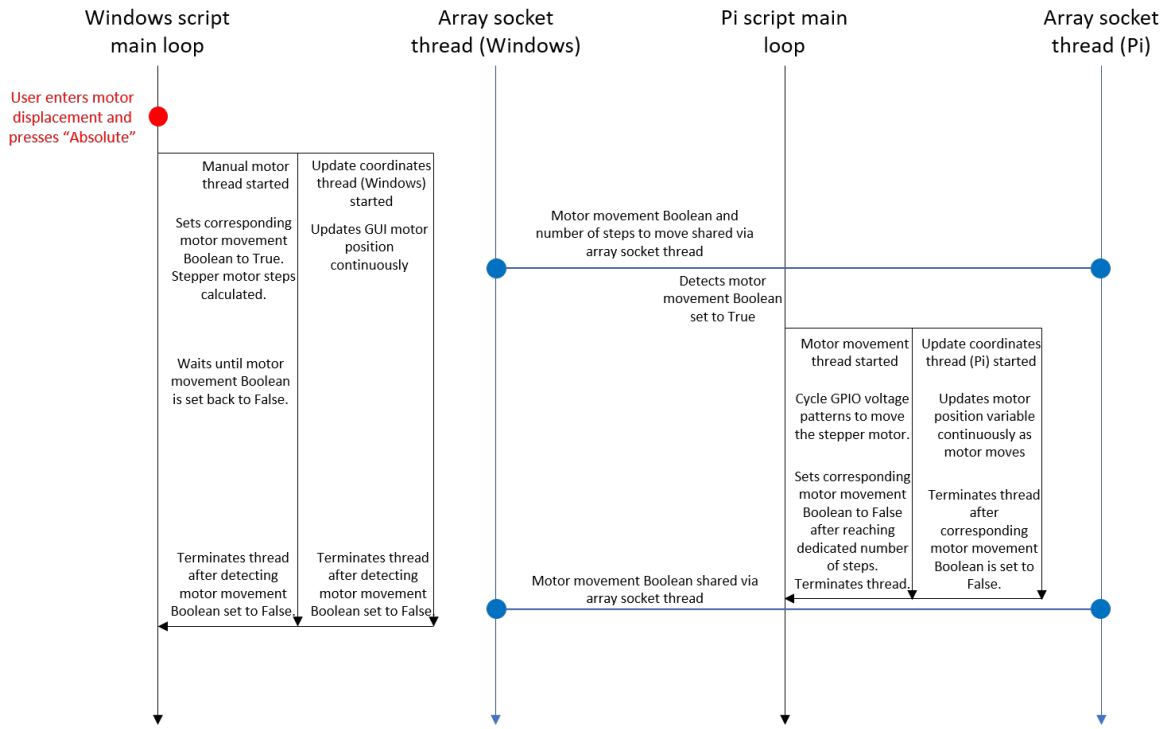

Figure 5.8: Program flow for moving the motors using the software in "Manual Mode". See text for details.

positions of the motor from a text file when it is first started. If it is the first time the program is being used and there is no text file for the motor positions, the program will default the motor positions to 0 and create the text file. When the entry for the absolute displacement is entered by the user and the "Absolute" button is pressed, 2 new threads are started in the Windows script. A "Manual motor thread" starts the motor movement and waits for the dedicated number of steps to finish. The "Update coordinates thread (Windows)" updates the positions of the motors on the GUI in parallel with other processes. In the "Manual motor thread", the number of steps to move the motor by and in which direction based on its current position. Then, the corresponding motor movement variable is set to "True" (if the resultant number of steps to move by is non-zero), and the number of steps to move by is shared as a variable with the Pi machine as well through the "Array socket thread". 2 parallel threads are then started on the Pi machine - the "Motor movement thread" and the "Update coordinates thread (Pi)". In the "Motor movement thread", the script cycles the PI GPIO pin voltage patterns to move the motor. The motor

then moves with the default delay time between voltage pin patterns of 1ms. At the same time, the motor positions are tracked and updated in "Update coordinates thread (Pi)" while the motors are moving, and the values are shared with the Windows machine through the "Array socket thread (Windows)". The "Update coordinates thread (Windows)" on the Windows machine then updates the GUI with the new values. After the number of steps to move has reached, the Pi machine sets the corresponding motor movement boolean variable from "True" back to "False", and the motor stops moving. Then, the specific threads for moving the motor are terminated - "Manual motor thread", "Motor movement thread", "Update coordinates thread (Windows)" and "Update coordinates thread (Pi)".

The second way for manual movement is to move the motor relative to its current position. The user sets the relative displacement of the motor in the GUI and presses either the "Left" or "Right" button ("Up" or "Down" button for the beam vertical steering motor). The "Left" or "Right" ("Up" or "Down") button dictates whether the motor moves clockwise or anticlockwise, and the corresponding motor movement boolean variable is set to "True". The relative displacement is also shared with the Pi as a variable to dictate the number of stepper motor steps. The rest of the procedure on how the motor moves is the same as the first case (move by absolute displacement).

If the user wishes to stop the motors before the motors reach the set number of steps to move, it can be done by pressing the "Stop Motor X" button on the GUI, where "X" is either "1" or "2" depending on the motor to be stopped. If the user wants to stop both motors, the "Stop Motors" button does that. By pressing the "Stop Motor X" button, the Windows machine sets both the motor movement boolean variables of the corresponding motor to False, which terminates the motor movement loop on the Pi machine.

5.6.2 Automatic Mode

On the GUI, the user can switch the program from "Manual Mode" to "Automatic Mode". "Automatic Mode" is the mode that is used for active beam stabilization. In this mode, the motors move such that the maximum x and y positions of the Gaussian function fit on the image matches the set point that is set by the user.

First, the user has to place the set point of the coordinates to move the beam to (in units of camera pixels). This is done on the GUI entries in the "Move to Setpoint" frame. Once the "Place" button is pressed, a parallel thread is started on the Windows machine that assigns the x and y coordinates entries on the GUI to some variables in the Windows machine. Then, a red crosshair is created as an overlay on top of the camera image that marks the setpoint. Once the setpoint is created, the motors will start moving to match the

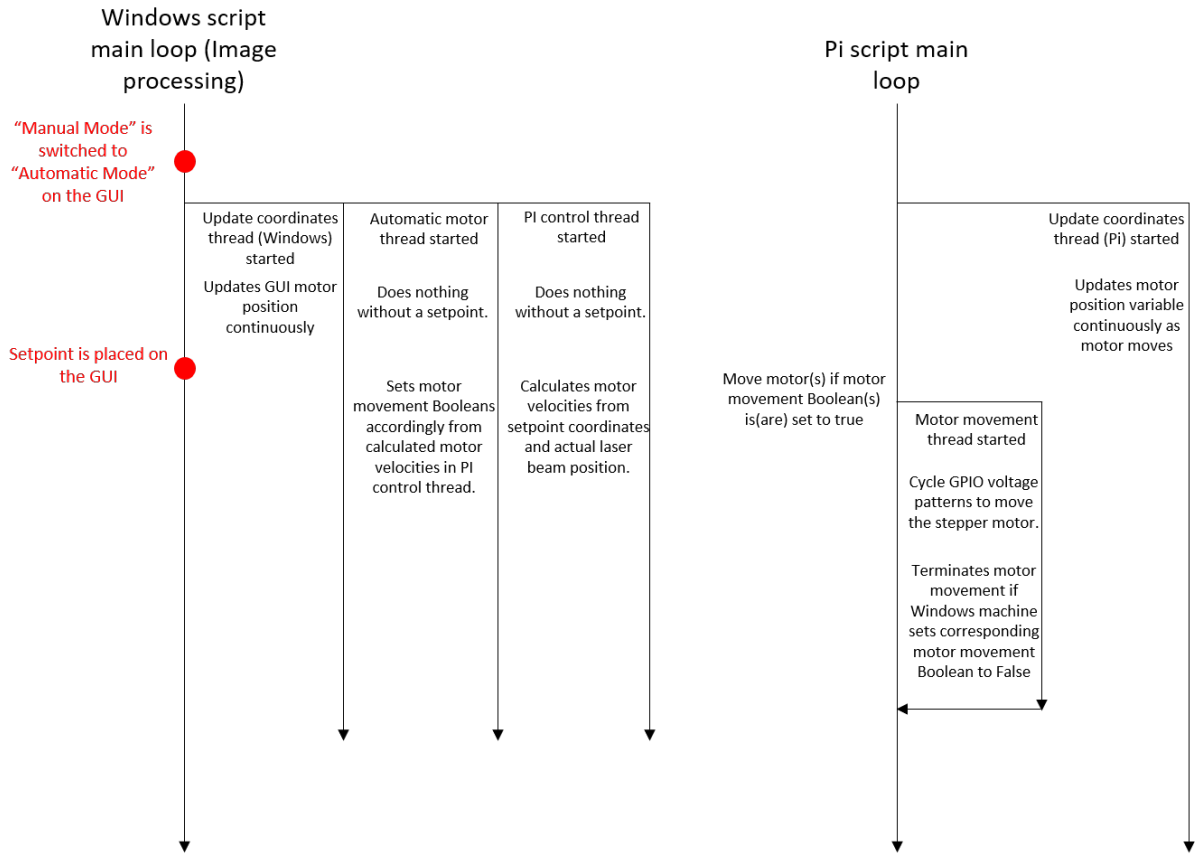

Figure 5.9: Program flow of the software in "Automatic Mode", which is the mode used for active beam stabilization. The "Array socket threads" sharing the variables are not shown. See text for further details.

beam coordinates from the image Gaussian fit to the setpoint coordinates. If the setpoint crosshair is not created yet while in "Automatic Mode", the motors do not move.

When the program is switched to "Automatic Mode", 3 threads on the Windows machine are started that runs in parallel with the main loop, "Array socket thread (Windows)" and "Image socket thread (Windows)". The first thread is the "Update coordinates thread (Windows)", which is as described in Section 5.6.1. The second thread is the "Automatic motor thread", which sets the motor movement boolean variables to True or False depending on certain conditions from the feedback of the cameras. The third thread is the "PI control thread", which calculates the speeds of the motors using principles of a PI control loop.

In the "Automatic motor thread", an infinite loop runs which checks the difference between the setpoint coordinate and the beam position from the Gaussian fit constantly. If the difference between the setpoint and the actual beam position along an axis (x or y) is less than a certain threshold set by the user on the GUI (default value is 0.5 pixel), no motors will be set to move. This is to prevent artificial jittering of the beam due to random fluctuations of the parameters from the Gaussian fit. Other than the setpoint difference threshold, if the motor speed is too slow (which is calculated in the "PI control thread", elaborated later in this section), which is currently hard-coded to be 1 second delay time between the sequence of pin patterns, then the motors are not set to move as well. This is to prevent the system from becoming too unresponsive when there's a long wait time for the motor movement to finish. If the setpoint difference is larger than the threshold and the motor speed is fast enough, then the corresponding motors are set to move. The motor(s) to be moved and the direction(s) of the motor movement depends on the value(s) of the motor velocity calculated in the "PI control thread".

In the "PI control thread", the motor velocities for the motors controlling the x (horizontal) and y (vertical) alignment of the beam are calculated. The speeds of the motors are slower the closer the beam is to the setpoint. This is done so that the ability of the system to actively stabilize slow beam drifts is largely independent of the processing speed of the Windows machine running the program. If a Windows machine is unable to run the main image processing loop as described in Section 5.5 at a faster refresh rate than the (constant) step rate of the stepper motors, the beam will keep overshooting the setpoint and not stabilize. Thus, by making the stepper motor step rates (i.e. motor speeds) variable with the difference between the beam position and the setpoint, Windows machines with slower processing speeds can stabilize a laser beam as well. The exact formula to compute the motor velocity is

$$v_x = K_P \left(x_{set} - x_{actual,n}\right) + K_I \sum_{i=n-499}^{n} \left(x_{set} - x_{actual,i}\right) / 500 \tag{5.1}$$

where v_x is the motor velocity, x_{set} is the setpoint coordinate, $x_{actual,i}$ is the actual coordinate of the i^{th} image frame, the subscript n denotes the current index, K_P is the proportional coefficient and K_I is the integral coefficient. The K_P and K_I coefficients can be set by the user in the GUI, they are defaulted to be 10 and 1 respectively. The delay time between the patterns in the pin voltage sequence is then calculated by $t_{delay} = 1/v_x$, which will be in units of seconds.

On the Pi side, when the program is switched to "Automatic Mode", the "Update coordinates thread (Pi)" is started. Then, whenever a motor movement boolean variable is set

to True from the Windows machine, a new thread is started that moves the corresponding motor in the corresponding direction by cycling the stepper motor pins through a sequence of voltage patterns. Between pin voltage patterns, the time delay is variable and is set by t_{delay} as discussed earlier. In the script, the time delay is implemented by cycling through a while loop with a counter, with a 1 ms wait time in each loop, until the counter multiplied by 1 ms equals or exceeds t_{delay}. It is done this way instead of just programming the script to wait a total of t_{delay} to keep the stabilization process responsive. t_{delay} is continuously updated from the "PI control thread" on the Windows machine. Thus, if the program is scripted to wait a total of t_{delay} in one go, it may not be using the most up-to-date t_{delay} as more images are processed while the motor is waiting.

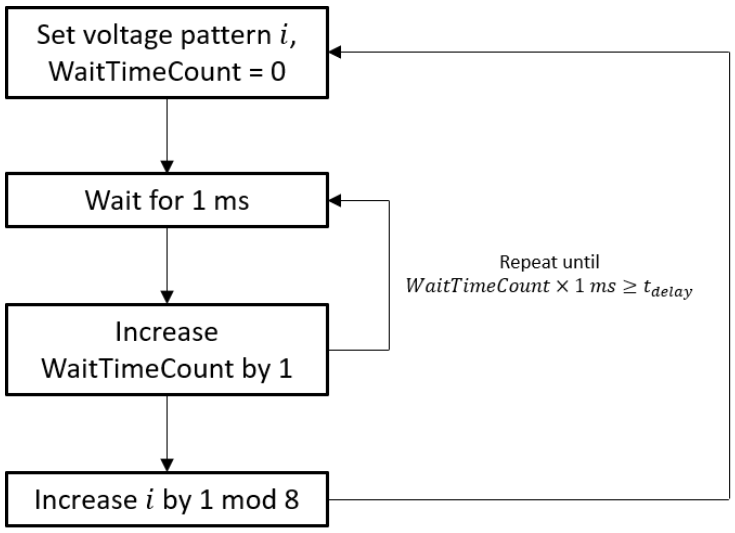

Figure 5.10: Program loop for moving a stepper motor. The loop continues indefinitely as long as its corresponding motor movement Boolean is set to True.

5.7 Additional Details

Additional details for the program that are technical to programming and not fundamental to the active beam stabilization framework are presented in this section.

5.7.1 Updating Windows-Pi Shared Variables

There are some intricacies involved in updating variable values that are shared by the Windows and Pi machines. If one were to simply have the "Array socket threads" send the shared variables back and forth between the 2 machines and just updating the variables on individual machines without any timing synchronization, there could be cases where the updated variables are overwritten by the old variables received from the opposing machine. Thus, dummy variables are used to declare when the individual machine is receiving data from the opposing machine and when the individual machine is updating shared variables. When shared variables need to be updated, a new thread is run to do the process. The script in the thread declares that it is updating shared variables and checks to see if the machine is receiving data. If it is, the machine will wait until it has finished receiving data before updating the shared variables. After updating the shared variables, the script removes the declaration that it is updating shared variables and exits the thread. In the "Array socket thread", it checks if the machine is updating shared variables and waits for the update to be finished before sending the data and receiving new data. This way, the timing is synchronized and the system will not drop shared variable updates.

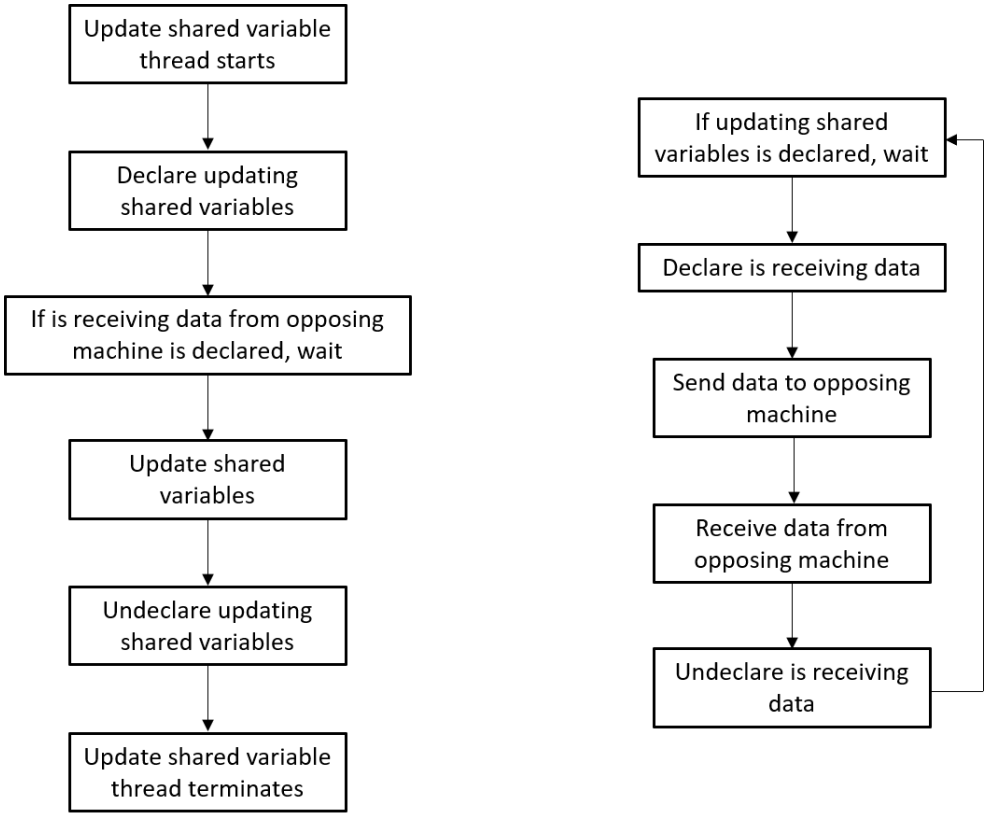

Figure 5.11: (Left) The program sequence of the thread that is launched every time a shared variable has to be updated. (Right) Program sequence for sending and receiving data in "Array socket threads". These sequences prevent unintended overwrite of the shared variables. See text for details.

5.7.2 Emergency Stop for Motors

In "Automatic Mode", the motor movements are dictated by the Windows machine, including the command to stop motor movements by using the motor movement boolean variables shared between the 2 machines. If the connection from the Pi to the Windows machine is somehow disconnected while the booleans are set such that a motor is moving, the motor will continue moving without end, which is detrimental for laser beam alignment. To prevent this, in "Array socket thread (Pi)", it checks if data is received successfully from the Windows machine in every loop. If the Pi fails to receive data, the Pi script does not enter the loops that move motors.

5.8 Other Perks and Potential Developments

With our setup, aside from using it for active beam stabilization, a laser beam can be steered remotely using the GUI as long as the user has access to the computer that is controlling the stepper motors. This makes remote optical alignment possible, which is a perk especially in the recent pandemic situation.

A potential development for the future could be automating beam alignment processes using the setup. An example would be the fiber coupling process. By using the output power from the optical fiber as feedback, it is possible to design an automated script that couples the light into a fiber optimally.

References

[1] P.W. Shor. Polynomial-time algorithms for prime factorizationand discrete logarithms on a quantum computer. *SIAM J. COMPUT.*, 26(5):1484–1509, 1997.

[2] T. D. Ladd, F. Jelezko, R. Laflamme, Y. Nakamura, C. Monroe, and J. L. Oâ€™Brien. Quantum computers. *Nature*, 464(7285):45–53, Mar 2010.

[3] D.F.V. James. Quantum dynamics of cold trapped ions with application to quantum computation. *Applied Physics B*, 66(2):181–190, Feb 1998.

[4] Colin D. Bruzewicz, John Chiaverini, Robert McConnell, and Jeremy M. Sage. Trapped-ion quantum computing: Progress and challenges. *Applied Physics Reviews*, 6(2):021314, 2019.

[5] J. P. Gaebler, T. R. Tan, Y. Lin, Y. Wan, R. Bowler, A. C. Keith, S. Glancy, K. Coakley, E. Knill, D. Leibfried, and D. J. Wineland. High-Fidelity Universal Gate Set for $^{9}Be^{+}$ Ion Qubits. *Phys. Rev. Lett.*, 117:060505, Aug 2016.

[6] Fangzhao Alex An, Anthony Ransford, Andrew Schaffer, Lucas R. Sletten, John Gaebler, James Hostetter, and Grahame Vittorini. High Fidelity State Preparation and Measurement of Ion Hyperfine Qubits with $I > \frac{1}{2}$. *Phys. Rev. Lett.*, 129:130501, Sep 2022.

[7] Robert Raussendorf and Jim Harrington. Fault-Tolerant Quantum Computation with High Threshold in Two Dimensions. *Phys. Rev. Lett.*, 98:190504, May 2007.

[8] Stephan G. J. Philips, Mateusz T. MÄ. . . dzik, Sergey V. Amitonov, Sander L. de Snoo, Maximilian Russ, Nima Kalhor, Christian Volk, William I. L. Lawrie, Delphine Brousse, Larysa Tryputen, Brian Paquelet Wuetz, Amir Sammak, Menno Veldhorst, Giordano Scappucci, and Lieven M. K. Vandersypen. Universal control of a six-qubit quantum processor in silicon. *Nature*, 609(7929):919–924, Sep 2022.

[9] M.A. Nielsen and I.L. Chuang. *Quantum Computation and Quantum Information: 10th Anniversary Edition*. Cambridge University Press, 2010.

[10] J. I. Cirac and P. Zoller. Quantum Computations with Cold Trapped Ions. *Phys. Rev. Lett.*, 74:4091–4094, May 1995.

[11] A. Sørensen and K. Mølmer. Entanglement and quantum computation with ions in thermal motion. *Phys. Rev. A*, 62:022311, Jul 2000.

[12] Martin Ringbauer, Michael Meth, Lukas Postler, Roman Stricker, Rainer Blatt, Philipp Schindler, and Thomas Monz. A universal qudit quantum processor with trapped ions. *Nature Physics*, 18(9):1053–1057, Sep 2022.

[13] D. Kielpinski, C. Monroe, and D. J. Wineland. Architecture for a large-scale ion-trap quantum computer. *Nature*, 417(6890):709–711, Jun 2002.

[14] C. Monroe, R. Raussendorf, A. Ruthven, K. R. Brown, P. Maunz, L.-M. Duan, and J. Kim. Large-scale modular quantum-computer architecture with atomic memory and photonic interconnects. *Phys. Rev. A*, 89:022317, Feb 2014.

[15] R. Srinivas, S. C. Burd, H. M. Knaack, R. T. Sutherland, A. Kwiatkowski, S. Glancy, E. Knill, D. J. Wineland, D. Leibfried, A. C. Wilson, D. T. C. Allcock, and D. H. Slichter. High-fidelity laser-free universal control of trapped ion qubits. *Nature*, 597(7875):209–213, Sep 2021.

[16] S. Olmschenk, K. C. Younge, D. L. Moehring, D. N. Matsukevich, P. Maunz, and C. Monroe. Manipulation and detection of a trapped Yb^+ hyperfine qubit. *Phys. Rev. A*, 76:052314, Nov 2007.

[17] T. P. Harty, D. T. C. Allcock, C. J. Ballance, L. Guidoni, H. A. Janacek, N. M. Linke, D. N. Stacey, and D. M. Lucas. High-Fidelity Preparation, Gates, Memory, and Readout of a Trapped-Ion Quantum Bit. *Phys. Rev. Lett.*, 113:220501, Nov 2014.

[18] D. Hucul, J. E. Christensen, Eric R. Hudson, and Wesley C. Campbell. Spectroscopy of a Synthetic Trapped Ion Qubit. *Phys. Rev. Lett.*, 119:100501, Sep 2017.

[19] T. Ruster, C. T. Schmiegelow, H. Kaufmann, C. Warschburger, F. Schmidt-Kaler, and U. G. Poschinger. A long-lived Zeeman trapped-ion qubit. *Applied Physics B*, 122(10):254, Sep 2016.

[20] Han Hu, Yi Xie, and Man chao Zhang et al. Compensation of low-frequency noise induced by power line in trapped-ion system. *PREPRINT (Version 1) available at Research Square*, May 2022.

[21] Pei Jiang Low, Brendan M. White, Andrew A. Cox, Matthew L. Day, and Crystal Senko. Practical trapped-ion protocols for universal qudit-based quantum computing. *Phys. Rev. Res.*, 2:033128, Jul 2020.

[22] A. Smith, B. E. Anderson, H. Sosa-Martinez, C. A. Riofrío, Ivan H. Deutsch, and Poul S. Jessen. Quantum Control in the Cs $6S_{1/2}$ Ground Manifold Using Radio-Frequency and Microwave Magnetic Fields. *Phys. Rev. Lett.*, 111:170502, Oct 2013.

[23] C. Senko, P. Richerme, J. Smith, A. Lee, I. Cohen, A. Retzker, and C. Monroe. Realization of a Quantum Integer-Spin Chain with Controllable Interactions. *Phys. Rev. X*, 5:021026, Jun 2015.

[24] F. M. Leupold, M. Malinowski, C. Zhang, V. Negnevitsky, A. Cabello, J. Alonso, and J. P. Home. Sustained State-Independent Quantum Contextual Correlations from a Single Ion. *Phys. Rev. Lett.*, 120:180401, May 2018.

[25] M. Malinowski, C. Zhang, F. M. Leupold, A. Cabello, J. Alonso, and J. P. Home. Probing the limits of correlations in an indivisible quantum system. *Phys. Rev. A*, 98:050102, Nov 2018.

[26] D. T. C. Allcock, W. C. Campbell, J. Chiaverini, I. L. Chuang, E. R. Hudson, I. D. Moore, A. Ransford, C. Roman, J. M. Sage, and D. J. Wineland. omg blueprint for trapped ion quantum computing with metastable states. *Applied Physics Letters*, 119(21), 11 2021. 214002.

[27] Pavel Hrmo, Benjamin Wilhelm, Lukas Gerster, Martin W. van Mourik, Marcus Huber, Rainer Blatt, Philipp Schindler, Thomas Monz, and Martin Ringbauer. Native qudit entanglement in a trapped ion quantum processor. *Nature Communications*, 14(1):2242, Apr 2023.

[28] O. Băzăvan, S. Saner, M. Minder, A. C. Hughes, R. T. Sutherland, D. M. Lucas, R. Srinivas, and C. J. Ballance. Synthesizing a $\hat{\sigma}_z$ spin-dependent force for optical, metastable, and ground-state trapped-ion qubits. *Phys. Rev. A*, 107:022617, Feb 2023.

[29] M. R. Dietrich, N. Kurz, T. Noel, G. Shu, and B. B. Blinov. Hyperfine and optical barium ion qubits. *Phys. Rev. A*, 81:052328, May 2010.

[30] E. T. Campbell, H. Anwar, and D. E. Browne. Magic-state distillation in all prime dimensions using quantum Reed-Muller codes. *Phys. Rev. X*, 2:041021, Dec 2012.

[31] E. T. Campbell. Enhanced fault-tolerant quantum computing in d-Level systems. *Phys. Rev. Lett.*, 113:230501, Dec 2014.

[32] R. S. Andrist, J. R. Wootton, and H. G. Katzgraber. Error thresholds for Abelian quantum double models: Increasing the bit-flip stability of topological quantum memory. *Phys. Rev. A*, 91:042331, Apr 2015.

[33] Adrian Hutter, Daniel Loss, and James R Wootton. Improved HDRG decoders for qudit and non-Abelian quantum error correction. *New Journal of Physics*, 17(3):035017, mar 2015.

[34] Fern H. E. Watson, Hussain Anwar, and Dan E. Browne. Fast fault-tolerant decoder for qubit and qudit surface codes. *Phys. Rev. A*, 92:032309, Sep 2015.

[35] Bárbara Andrade et al. Engineering an effective three-spin Hamiltonian in trapped-ion systems for applications in quantum simulation. *Quantum Sci. Technol. 7 034001*, April 2022.

[36] B. P. Lanyon, M. Barbieri, M. P. Almeida, T. Jennewein, T. C. Ralph, K. J. Resch, G. J. Pryde, J. L. O'Brien, A. Gilchrist, and A. G. White. Simplifying quantum logic using higher-dimensional Hilbert spaces. *Nature Phys.*, 5:134–140, 2008.

[37] T. C. Ralph, K. J. Resch, and A. Gilchrist. Efficient Toffoli gates using qudits. *Phys. Rev. A*, 75:022313, Feb 2007.

[38] N. Kjærgaard, L. Hornekær, A. M. Thommesen, Z. Videsen, and M. Drewsen. Isotope selective loading of an ion trap using resonance-enhanced two-photon ionization. *Appl. Phys. B Lasers Opt.*, 71(2):207–210, 2000.

[39] S. Gulde, D. Rotter, P. Barton, F. Schmidt-Kaler, R. Blatt, and W. Hogervorst. Simple and efficient photo-ionization loading of ions for precision ion-trapping experiments. *Appl. Phys. B Lasers Opt.*, 73(8):861–863, 2001.

[40] R. G. DeVoe and C. Kurtsiefer. Experimental study of anomalous heating and trap instabilities in a microscopic ^{137}Ba ion trap. *Phys. Rev. A*, 65(6):8, 2002.

[41] A. V. Steele, L. R. Churchill, P. F. Griffin, and M. S. Chapman. Photoionization and photoelectric loading of barium ion traps. *Phys. Rev. A*, 75(5), 2007.

[42] B. Wang, J. W. Zhang, C. Gao, and L. J. Wang. Highly efficient and isotope selective photo-ionization of barium atoms using diode laser and LED light. *Opt. Express*, 19(17):16438, 2011.

[43] G. Leschhorn, T. Hasegawa, and T. Schaetz. Efficient photo-ionization for barium ion trapping using a dipole-allowed resonant two-photon transition. *Appl. Phys. B Lasers Opt.*, 108(1):159–165, 2012.

[44] R. D. Graham, S.-P. Chen, T. Sakrejda, J. Wright, Z. Zhou, and B. B. Blinov. A system for trapping barium ions in a microfabricated surface trap. *AIP Advances*, 4(5):057124, 2014.

[45] T. G. Ballance, J. F. Goodwin, B. Nichol, L. J. Stephenson, C. J. Ballance, and D. M. Lucas. A short response time atomic source for trapped ion experiments. *Rev. Sci. Instrum.*, 89(5), 2018.

[46] G. Vrijsen, Y. Aikyo, R. F. Spivey, I. V. Inlek, and J. Kim. Efficient isotope-selective pulsed laser ablation loading of $^{174}Yb^{+}$ ions in a surface electrode trap. *Opt. Express*, 27(23):33907, 2019.

[47] S. Olmschenk and P. Becker. Laser ablation production of Ba, Ca, Dy, Er, La, Lu, and Yb ions. *Appl. Phys. B Lasers Opt.*, 123(4):1–6, 2017.

[48] Michael Berglund and Michael E. Wieser. Isotopic compositions of the elements 2009 (IUPAC Technical Report). *Pure and Applied Chemistry*, 83(2):397–410, 2011.

[49] Pei Jiang Low. *Tolerable Experimental Imperfections for a Quadrupole Blade Ion Trap and Practical Qudit Gates with Trapped Ions*. MSc thesis, University of Waterloo, 2019. Available at `https://uwspace.uwaterloo.ca/handle/10012/15163`.

[50] Brendan M. White, Pei Jiang Low, Yvette de Sereville, Matthew L. Day, Noah Greenberg, Richard Rademacher, and Crystal Senko. Isotope-selective laser ablation ion-trap loading of $^{137}Ba^{+}$ using a $BaCl_2$ target. *Phys. Rev. A*, 105:033102, Mar 2022.

[51] Pei Jiang Low, Brendan White, and Crystal Senko. Control and Readout of a 13-level Trapped Ion Qudit, 2023.

[52] Wolfgang Paul. Electromagnetic traps for charged and neutral particles. *Rev. Mod. Phys.*, 62:531–540, Jul 1990.

[53] D. J. Berkeland and M. G. Boshier. Destabilization of dark states and optical spectroscopy in Zeeman-degenerate atomic systems. *Phys. Rev. A*, 65:033413, Feb 2002.

[54] K. Sheridan, W. Lange, and M. Keller. All-optical ion generation for ion trap loading. *Applied Physics B*, 104(4):755–761, Sep 2011.

[55] J. J. Curry. Compilation of Wavelengths, Energy Levels, and Transition Probabilities for Ba I and Ba II. *Journal of Physical and Chemical Reference Data*, 33(3):725–746, 2004.

[56] A. Kramida, Yu. Ralchenko, J. Reader, and and NIST ASD Team. NIST Atomic Spectra Database (ver. 5.10), [Online]. Available: `https://physics.nist.gov/asd` [2023, June 17]. National Institute of Standards and Technology, Gaithersburg, MD., 2022.

[57] T. W. Koerber, M. H. Schacht, K. R. G. Hendrickson, W. Nagourney, and E. N. Fortson. rf Spectroscopy with a Single Ba^+ Ion. *Phys. Rev. Lett.*, 88:143002, Mar 2002.

[58] W. A. van Wijngaarden and J. Li. Hyperfine splittings and isotope shifts of (6s)21S0→(6s6p) 1P1 transition in barium. *Canadian Journal of Physics*, 73(7-8):484–488, 1995.

[59] R. Blatt and G. Werth. Precision determination of the ground-state hyperfine splitting in $^{137}Ba^+$ using the ion-storage technique. *Phys. Rev. A*, 25:1476–1482, Mar 1982.

[60] Roger E. Silverans, Gustaaf Borghs, Peter De Bisschop, and Marleen Van Hove. Hyperfine structure of the 5d ^2D_J states in the alkaline-earth Ba ion by fast-ion-beam laser-rf spectroscopy. *Phys. Rev. A*, 33:2117–2120, Mar 1986.

[61] Petrine Villemoes, Arne Arnesen, Filip Heijkenskjöld, and Anders Wannstrom. Isotope shifts and hyperfine structure of 134-138Ba II by fast ion beam-laser spectroscopy. *Journal of Physics B*, 26:4289–4299, 1993.

[62] Pjl thesis scripts and data. `https://doi.org/10.5281/zenodo.8209202`, 2023.

[63] Brendan Bramman. *Ablation loading and qudit measurements with barium ions*. PhD thesis, University of Waterloo, 2023.

[64] Selectivity ablation data. `https://doi.org/10.5281/zenodo.6029079`, 2022.

[65] A. A. Madej and J. D. Sankey. Quantum jumps and the single trapped barium ion: Determination of collisional quenching rates for the $5d^2D_{5/2}$ level. *Phys. Rev. A*, 41:2621–2630, Mar 1990.

[66] K. H. Knöll, G. Marx, K. Hübner, F. Schweikert, S. Stahl, Ch. Weber, and G. Werth. Experimental g_J factor in the metastable $5D_{3/2}$ level of Ba^+. *Phys. Rev. A*, 54:1199–1205, Aug 1996.

[67] N. Kurz, M. R. Dietrich, Gang Shu, T. Noel, and B. B. Blinov. Measurement of the Landé g factor of the $5D_{5/2}$ state of Ba ii with a single trapped ion. *Phys. Rev. A*, 82:030501, Sep 2010.

[68] Nicholas Lewty, Boon Leng Chuah, Radu Cazan, Bijaya Sahoo, and Murray Barrett. Experimental determination of the nuclear magnetic octupole moment of $^{137}Ba^+$ ion. *Physical Review A*, 88, 05 2013.

[69] Pascal P. Man. Cartesian and Spherical Tensors in NMR Hamiltonians. *Concepts in Magnetic Resonance Part A*, 42(6):197–244, 2013.

[70] Christian Roos. *Controlling the quantum state of trapped ions*. PhD dissertation, University of Innsbruck, 2000. Available at https://www.quantumoptics.at/images/publications/dissertation/roos-diss.pdf.

[71] Brendan Bramman. *Measuring Trapped Ion Qudits*. MSc thesis, University of Waterloo, 2019. Available at https://uwspace.uwaterloo.ca/handle/10012/15165.

[72] D. P. O'Leary, G. K. Brennen, and S. S. Bullock. Parallelism for quantum computation with qudits. *Phys. Rev. A*, 74:032334, Sep 2006.

[73] S. G. Schirmer, A. D. Greentree, V. Ramakrishna, and H. Rabitz. Constructive control of quantum systems using factorization of unitary operators. *J. Phys. A*, 35(39):8315–8339, Sep 2002.

[74] P. A. Ivanov, E. S. Kyoseva, and N. V. Vitanov. Engineering of arbitrary U(N) transformations by quantum Householder reflections. *Phys. Rev. A*, 74:022323, Aug 2006.

[75] Qudit 13Level SPAM Scripts and Data. https://doi.org/10.5281/zenodo.8249564, 2023.

[76] Harrison Ball and Michael J. Biercuk. Walsh-synthesized noise filters for quantum logic. *EPJ Quantum Technology*, 2(1):11, May 2015.

[77] Matthew L. Day, Pei Jiang Low, Brendan White, Rajibul Islam, and Crystal Senko. Limits on atomic qubit control from laser noise. *npj Quantum Information*, 8(1):72, Jun 2022.

APPENDICES

Appendix A

Two-level Transition Equilibrium State

The optical Bloch equations for a two-level system can be constructed in a same manner as Section 3.3, which leads to

$$\begin{aligned}
\frac{d}{dt}\rho_{SS} &= i\frac{\Omega}{2}\left(\rho_{SP} - \rho_{PS}\right) + \gamma\rho_{PP} \\
\frac{d}{dt}\rho_{PP} &= -i\frac{\Omega}{2}\left(\rho_{SP} - \rho_{PS}\right) - \gamma_S\rho_{PP} \\
\frac{d}{dt}\rho_{SP} &= i\frac{\Omega}{2}\left(\rho_{SS} - \rho_{PP}\right) - i\Delta\rho_{SP} - \frac{\gamma}{2}\rho_{SP}.
\end{aligned} \tag{A.1}$$

Solving for ρ_{PP} in Eq. A.1 gives

$$\rho_{PP} = \frac{\Omega^2}{2\Omega^2 + 4\Delta^2 + \gamma^2} \tag{A.2}$$

From Eq. A.2, it can be seen that ρ_{PP} increases monotonically with increasing laser intensity, Ω, and saturates at a value of $\frac{1}{2}$. At large enough laser intensities, Ω dominates over laser frequency detunings Δ, and the P state population stays stable at $\frac{1}{2}$.

Appendix B

Writing Your Own Clebsch-Gordan Coefficients Generator

Clebsch-Gordan coefficients generators are not commonly found in built-in computational packages (not in MATLAB, nor Python). Although custom scripts shared by other users can be found online, it is best to understand how they are generated so that you can verify that they are performing correctly. In this section, I describe an approach I employed to write a custom code for generating Clebsch-Gordan coefficients. I do not claim the approach to be the most efficient computationally, but the calculations are derived in a straightforward manner from first principle derivations of Clebsch-Gordan coefficients that you may find in textbooks, which makes it relatively easily understandable.

A quantum angular momentum system consisting of two sub-systems with angular momentum numbers of J_1 and J_2 can be expressed in the total angular momentum basis $|J, m_J\rangle$ or the uncoupled basis $|J_1, m_1; J_2, m_2\rangle$, where $\vec{J} = \vec{J_1} + \vec{J_2}$ and m_i, $i \in \{1, 2, J\}$ are the projection of the angular momenta components onto the z-axis. The Clebsch-Gordan coefficients are defined by the overlap between each of the states between the two different bases, $C_{Jmm_1m_2} = \langle J_1, m_1; J_2, m_2 | J, m_J\rangle$. Thus, to generate a complete set of Clebsch-Gordan coefficients, we prepare a $(2J_1 + 1)(2J_2 + 1) \times (2J_1 + 1)(2J_2 + 1)$ matrix. Each row corresponds to an uncoupled basis state $|J_1, m_1; J_2, m_2\rangle$ and each row a coupled basis state $|J, m_J\rangle$. The intersection of each row and column corresponds to a Clebsch-Gordan coefficient $C_{Jmm_1m_2}$. Table B.1 illustrates an example of the matrix with $J_1 = 1$ and $J_2 = 1/2$.

		$J=\frac{3}{2}$				$J=\frac{1}{2}$	
		$m_J=\frac{3}{2}$	$m_J=\frac{1}{2}$	$m_J=-\frac{1}{2}$	$m_J=-\frac{3}{2}$	$m_J=\frac{1}{2}$	$m_J=-\frac{1}{2}$
$m_1=1$	$m_2=\frac{1}{2}$						
	$m_2=-\frac{1}{2}$						
$m_1=0$	$m_2=\frac{1}{2}$						
	$m_2=-\frac{1}{2}$						
$m_1=-1$	$m_2=\frac{1}{2}$						
	$m_2=-\frac{1}{2}$						

Table B.1: An example of Clebsch-Gordan coefficients search table, with the coefficients to be computed.

The state with maximal projection along the z-axis are one and the same, giving

$$|J, m_J = J\rangle = |J_1, m_1 = J_1; J_2, m_2 = J_2\rangle \tag{B.1}$$

The subsequent $|J, m_J\rangle$ states expressed in the $|J_1, m_1; J_2, m_2\rangle$ basis with the same J number can be generated with the $\hat{J}_-$ operators,

$$\begin{aligned}
\hat{J}_-|J, m_J\rangle &= \left(\hat{J}_{1-} + \hat{J}_{2-}\right) \sum_{m_1,m_2} C_{Jmm_1m_2}|J_1, m_1; J_2, m_2\rangle \\
|J, m_J - 1\rangle &= \sum_{m_1,m_2} \frac{C_{Jmm_1m_2}\sqrt{J_1(J_1+1) - m_1(m_1-1)}}{\sqrt{J(J+1) - m_J(m_J-1)}}|J_1, m_1 - 1; J_2, m_2\rangle \\
&\quad + \sum_{m_1,m_2} \frac{C_{Jmm_1m_2}\sqrt{J_2(J_2+1) - m_2(m_2-1)}}{\sqrt{J(J+1) - m_J(m_J-1)}}|J_1, m_1; J_2, m_2 - 1\rangle,
\end{aligned} \tag{B.2}$$

By expressing the states $|J_1, m_1\rangle$ and $|J_2, m_2\rangle$ in their vector forms, and the operators $\hat{J}_{1-}$, $\hat{J}_{2-}$, $\hat{I}_1$, and $\hat{I}_2$ in their matrix form, where $\hat{I}_1$ and $\hat{I}_2$ are the identity operators for the first and second angular momentum subspace, we can perform Eq. B.2 straightforwardly using matrix multiplications. This lets us fill up the $J = \frac{3}{2}$ columns in Table B.1 from left to right.

To compute the Clebsch-Gordan coefficient for the next lower J number, we use the property that the $\{|J, m_J\rangle\}$ basis states are orthogonal,

$$\langle J, m_J = J'|J', m_J = J'\rangle = 0 \tag{B.3}$$

for $J \neq J'$. Expressing the state $|J', m_J\rangle$ as a superposition of the $|m_1, m_2\rangle$ states (with the coefficients not known yet), we have

$$|J', m_J = J'\rangle = \sum_{m_1,m_2} a_{m_1,m_2}|m_1, m_2\rangle. \tag{B.4}$$

From selection rule, only the coefficients with $m_J = m_1 + m_2$ will be non-zero. Thus,

$$|J', m_J = J'\rangle = \sum_{m_1+m_2=m_J} a_{m_1,m_2}|m_1, m_2\rangle. \tag{B.5}$$

Now, we multiply both sides of Eq. B.5 by some unknown factor K, and let $b_{m_1,m_2} = Ka_{m_1,m_2}$. By setting the non-zero b_{m_1,m_2} coefficient with the largest m_1 value to 1 (ignoring normalization condition for now), and computing Eq. B.3 for all J states with the Clebsch-Gordan coefficients solved, we obtain the necessary number of independent linear equations to solve for all the b_{m_1,m_2} unknowns. Linear equation solvers can then be used to solve for b_{m_1,m_2}, which I use MATLAB's linsolve() function. K can then be computed by $K = \sum_{m_1,m_2} b^2_{m_1,m_2}$, and finally $a_{m_1,m_2} = b_{m_1,m_2}/K$. The rationale for this approach is because the condition for the states being normalized results in a non-linear equation $1 = \sum_{m_1,m_2} a^2_{m_1,m_2}$. By ignoring the normalization first, we can solve this using a linear equation solver. This method also constrains the coefficient with the largest m_1 value to be positive, leading to coefficients that may have a global sign flip compared to other lookup tables you find elsewhere. However, the relative signs of the coefficients are still the same and thus the physical significance is still the same.

With the next lower J state known, we can then generate the Clebsch-Gordan coefficients for lower m_J states with Eq. B.2 again and fill the $J = \frac{1}{2}$ column in Table B.1 and so on. A script written in MATLAB can be found in the repository [62].

Appendix C

Script For Detecting the Number of Bright Ions in a 2D Image

We find that Ba^+ ion fluorescence rates are sensitive to laser intensities and frequencies, without saturation laser powers where the fluorescing P state population is stable. Thus, the fluorescence rate per ion may easily drift with drifting laser parameters and using detected photon counts may not be a reliable way of detecting the number of bright Ba^+ ions in a linear chain. We developed an algorithm to determine the number of bright ions from a 2D image of the ion captured on a CCD camera. The procedure is as follows:

1. Import the ion image as a 2D array of integers corresponding to the image brightness on each pixel on the image.

2. Find the pixel with the highest brightness count.

3. Extract a 1D array of integers from the 2D image, at the pixel with the highest brightness count, along the ion chain axis.

4. From this 1D array, for each pixel, compute the difference in brightness count with the neighboring pixel after it, and then also compute the brightness difference with the pixel before it. If both values are larger than or equal to zero, it is identified as a local peak.

5. Compute the brightness threshold to determine if a local peak is "truly bright" from an ion fluorescence using the formula $C_{th} = C_{50} + M\,(C_{95} - C_{50})$, where C_{th} is the threshold count, M is a user-defined multiplier factor, typically set to some value

larger than 1, C_{50} and C_{95} are the 50^{th} and 95^{th} percentiles of the brightness counts respectively of the whole 2D image.

6. Local peaks higher than C_{th} are picked out from the 1D array, and the pixel positions of these local peaks are read out. If there are two pixels that are neighboring among these local peaks that are higher than the threshold, they are combined together and counted as one peak.

7. The number of remaining local peaks higher than C_{th} is then treated as the number of bright ions.

The formula in Step 5,

$$C_{th} = C_{50} + M\,(C_{95} - C_{50}) \tag{C.1}$$

is a useful equation for picking out outliers from a quantity with a centralized random distribution (normal distribution, Poisson distribution, etc.), it is the CCD camera background count in this case. The difference $C_{95} - C_{50}$ computes the width of the probability distribution, assuming that less than 5% of the data are outliers. By multiplying $(C_{95} - C_{50})$ with a multiplier $M > 1$ and adding it to the median, we would reach a value where natural manifestations will be extremely rare, and they are thus identified as outliers. The choice of the upper percentile is not unique, and is only chosen as the 95^{th} percentile for this work. If one expects more than 5% of the pixels in the image to not be background counts, a lower percentile can be chosen. The choice of the M multiplier is also typically robust to a wide range of values, as long as the outlier values are much higher than the normal (background) values. On top of having the advantage of being insensitive to fluorescence rate drifts, this algorithm can also detect other dim ions, such as $^{134}Ba^{+}$ or $^{136}Ba^{+}$ when the laser frequencies are set to fluoresce $^{138}Ba^{+}$. Figs. C.1 shows an example of the algorithm at work, and three bright ions are identified by the algorithm.

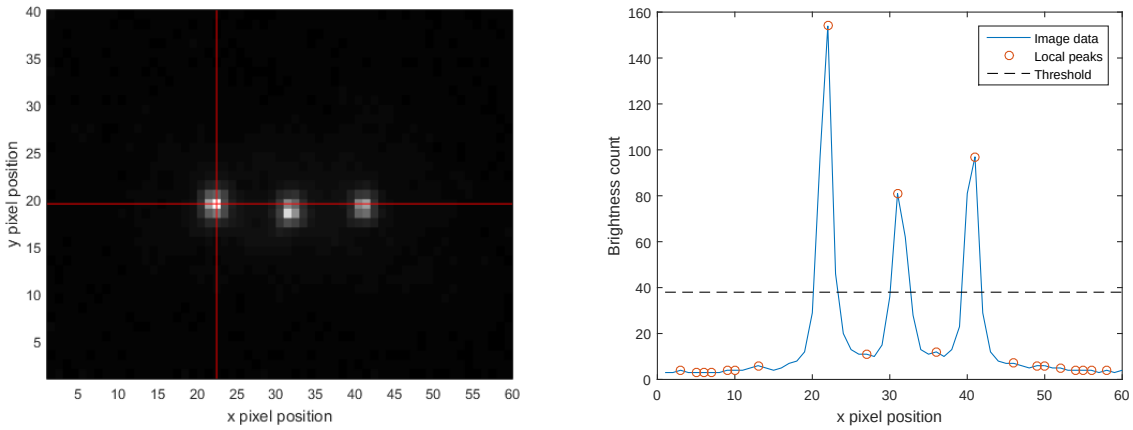

(a) (b)

Figure C.1: (a) A CCD image of three bright ions. The red lines intersect at the point with the highest brightness count as described in Step 2 in the algorithm. (b) A 1D array of brightness count extracted from the horizontal red line in (a), as described in Step 3 in the algorithm. The local peaks are highlighted with circle markers, which are computed in Step 4. The threshold value as shown as dashed line is calculated with $M = 5$, as described in Step 5.

An example of the algorithm coded in the Python language is shown below:

```
import numpy as np
def GetNumberOfIons(A,multiplier):
[max_y_ind,max_x_ind]=np.where(A == np.amax(A))
B = A[max_y_ind,:]
B = B[0]
[peak_positions,local_peaks] = find_peaks(B)
threshold = np.percentile(A,50) + multiplier*(np.percentile(A,95)-np.percentile(A,50))
peak_positions_th = peak_positions[local_peaks > threshold]
peak_positions_th = peak_positions_th.astype(float)
if len(peak_positions_th) > 1:
    peak_positions_th_diff = peak_positions_th[1:]-peak_positions_th[0:-1]
    peak_positions_th_diff_end0 = np.append(peak_positions_th_diff,0)
    peak_positions_th_diff_start0 = np.append(0,peak_positions_th_diff)
    peak_positions_th[peak_positions_th_diff_end0 == 1] = peak_positions_th[peak_positions_th_diff_end0 == 1] + 0.5
    index = np.asarray(range(0,len(peak_positions_th)))
    peak_positions_th = np.delete(peak_positions_th,index[peak_positions_th_diff_start0 == 1])
    number_of_ions = len(peak_positions_th)
    return number_of_ions,peak_positions_th

def find_peaks(in_array):
    in_array = in_array.astype(float)
    a = in_array[1:-1] - in_array[0:-2]
    b = in_array[1:-1] - in_array[2:]
    index = (a>=0) & (b>=0)
    index = np.append(np.insert(index,False,0),False)
    local_peaks = in_array[index]
    c = np.asarray(range(0,len(in_array)))
```

```
peak_positions = c[index]
return [peak_positions,local_peaks]
```

Appendix D

Estimation of Four-rod RF Voltage Amplitude

The radial secular motional frequency of an ion in a Paul trap is related to the RF voltage and amplitude and RF voltage frequency by [49]

$$\omega_s \propto \frac{V_{RF}}{\Omega_{RF}} \tag{D.1}$$

In my earlier work, the a barium ion secular motional frequency in our four-rod trap with $V_{RF} = 200\,\mathrm{V}$ and $\Omega_{RF} = 20\,\mathrm{MHz}$ is determined to be $\omega_s = 1.18\,\mathrm{MHz}$ with simulations using the SIMION software. We have measured our secular frequency to be about $\omega_s = 375\,\mathrm{kHz}$ and we know the RF voltage frequency is $\Omega_{RF} = 20.772\,\mathrm{MHz}$. Using the relation in Eq. D.1, we get $V_{RF} \approx 66\,\mathrm{V}$ for the experiments in Chapter 3. For the experiments in Chapter 4, $\omega_s = 1.3\,\mathrm{kHz}$, which gives $V_{RF} \approx 230\,\mathrm{V}$.

Appendix E

$^{133}Ba^{+}$ Loading Attempts

We had plans to trap $^{133}Ba^{+}$ in our work originally. Another salt target that is not described in the main text was also installed in the vacuum chamber as shown in Fig. E.1. The low-volume target was made from a solution of hydrochloric acid (HCl), with approximately 0.4 mCi of ^{133}Ba. Because HCl corrodes aluminum, we fit a tantalum foil over the tube's end. To apply the solution to the target, we dropped 10 µL in the target cup (which is sitting on a 250 °C hotplate), let it evaporate, leaving 200 ng of $BaCl_2$ salt on the surface, and repeated this process until we had $\sim$ 10 µg on the substrate. With such a low volume, the deposited salt is imperceptible on the substrate tantalum foil (see Fig. E.1b).

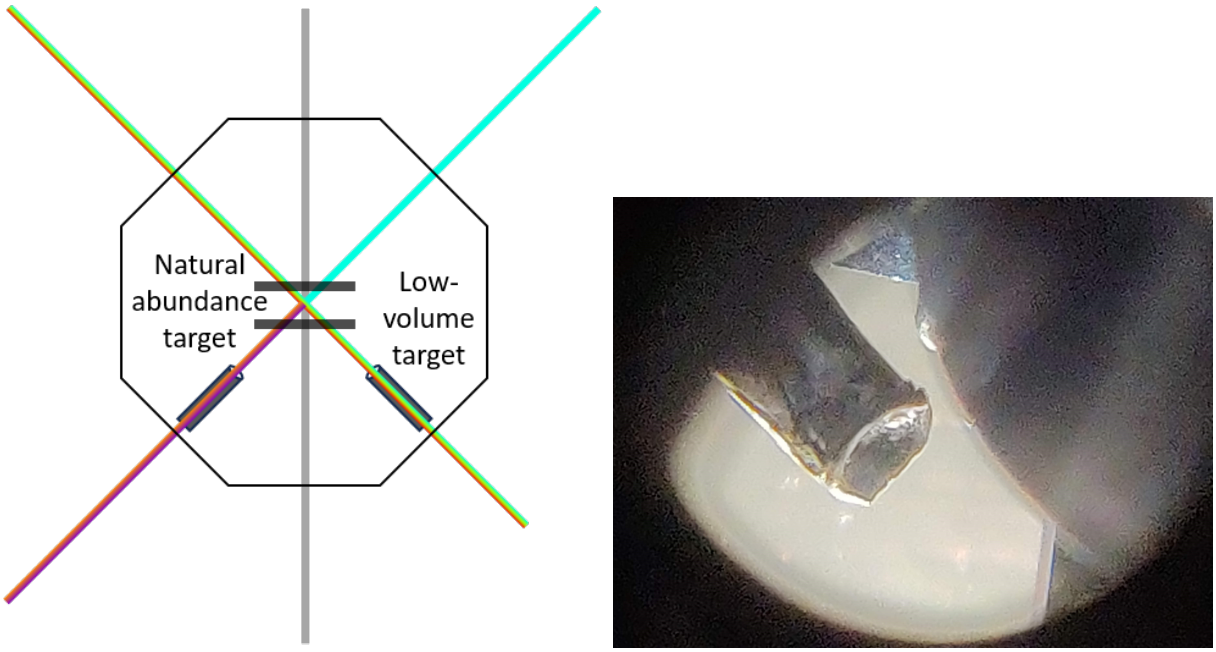

(a) (b)

Figure E.1: (a) An illustration of the vacuum chamber with a ^{133}Ba enriched salt target, labelled as "Low-volume target", that was not shown in the main text. (b) A photograph of the low-volume target.

E.1 Loading Attempts With the Low-volume Target

We attempted to trap barium ions using the two-step photoionization method at various fluences from 0.6 to 3.8 J/cm^2. For a fresh ablation spot, we trap ^{138}Ba$^+$ (which has an abundance of 53.3% on the low-volume target) less than 10 times before being unable to trap, with a loading rate of $\sim$ 0.05 ions/pulse (much lower than from our high-volume target).

To investigate the reliability of an ablation spot on this target, we checked for neutral barium fluorescence rate as we ablate the target. The ablation laser is swept along a line on the low-volume target, ablating along that line. For each ablation pulse, the neutral barium fluorescence from the 554 nm is collected on a PMT with an integration time of 100 ms. The pulse fluence used is 0.59 J cm^{-2}.

On the first sweep of the ablation laser along the line on the target, the peak fluorescence

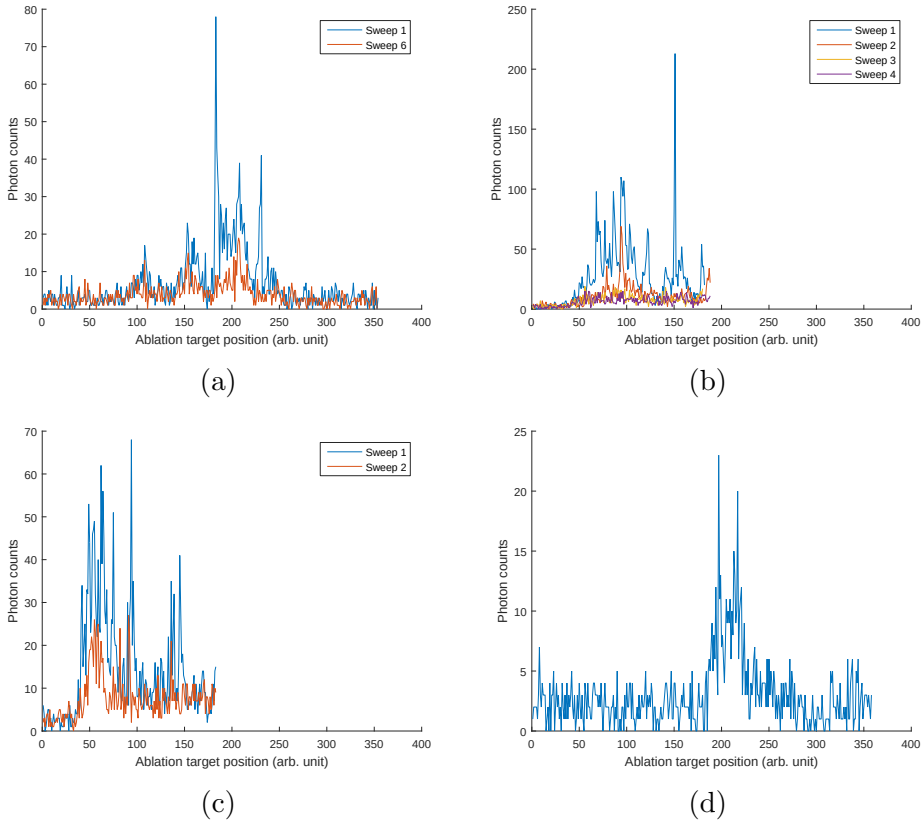

Figure E.2: Neutral barium fluorescence from the low-volume target, sweeping the ablation laser along a line on the target. (a) Initial full-line sweeps at ablation pulse fluence of $0.59\,\mathrm{J\,cm^{-2}}$. (b) Half-line sweeps at ablation pulse fluence of $0.98\,\mathrm{J\,cm^{-2}}$. (c) Half-line sweeps at ablation pulse fluence of $1.44\,\mathrm{J\,cm^{-2}}$. (d) A full-line sweep at ablation pulse fluence of $0.59\,\mathrm{J\,cm^{-2}}$ after the half-line sweeps in (c) and (d).

count detected is approximately 80. On repeat sweep of the ablation laser along the same line, the fluorescence counts decrease rapidly. By the sixth sweep, the peak fluorescence count has dropped to below 20. In an effort to try to condition the target, similar to the procedure done for the high-volume target, the pulse fluence is increased to $0.98\,\mathrm{J\,cm^{-2}}$ and the ablation laser is swept for half of the line. The fluorescence counts are high for the initial scan, at approximately 200 peak fluorescence count, but quickly dropped to below 20 counts on the fourth sweep. This is contrary to the high-volume target, where the neutral barium fluorescence counts would gradually increase and stabilize at a consistent count during the conditioning process. The pulse fluence is further increased to $1.44\,\mathrm{J\,cm^{-2}}$ for the half-line sweep. The peak fluorescence count is approximately 70 for the first scan, but quickly drops to below 30 on the second scan. Going back to the lower pulse fluence at $0.59\,\mathrm{J\,cm^{-2}}$ and performing the full-line scan, we observe that the half-line that went through ablations at high pulse fluence no longer produce any neutral barium fluorescence. In contrast to the high-volume target, instead of conditioning a spot, it shows signs of a spot being depleted of the source material when high pulse fluence is used to ablate it. Attempts to trap $^{138}Ba^{+}$ (which has an abundance of 53.3% on the low-volume target) using the two-step photoionization method follow the same trend, where trapping quickly becomes impossible in the order of tens of pulses, indicating that the source material is depleted.

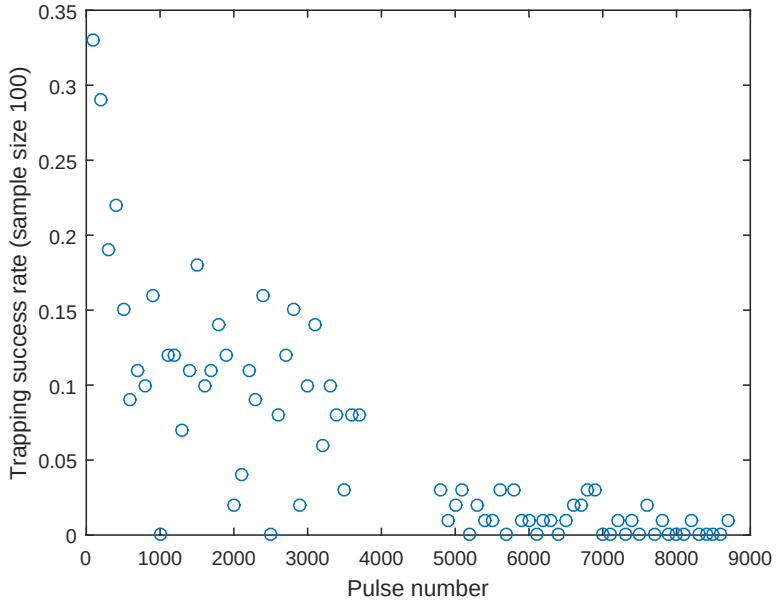

Figure E.3: Trapping probability of $^{138}Ba^{+}$ from the low-volume target using the direct-ion loading method. The horizontal axis denotes the pulse number that is sent to the same spot on the target. The vertical axis shows the trapping success rate out of a sample size of 100. The ablation fluence used is $3.84\,\mathrm{J\,cm^{-2}}$.

To test the low-volume target further, we employ the trapping procedure used by Reference [18]. The ablation laser fluence is increased to $3.84\,\mathrm{J/cm^2}$ to directly generate barium ions. Using the direct ion-loading method, the ion trapping success rate of $^{138}Ba^{+}$ is initially in the order of 10% initially (see Figure E.3). However, it quickly declines to the order of 1% after a few thousand pulses. After about 10,000 pulses, the trapping probability is below 1%. This indicates that a target spot is being depleted quickly with this trapping procedure as well. Furthermore, we are only able to trap single ions and not ion chains as described in [18]. Therefore, with this low-volume target and both loading methods, it is impossible to establish an ion chain. Given the poor trapping performance, low spot lifetimes, and overall expected target lifetime, this target is impractical for loading ions for quantum computing experiments.

E.2 Observation of other excited-state neutral species

By ablating the barium targets at high pulse fluences, on the order of $1\,\mathrm{J/cm^2}$, we also note the presence of some fluorescence after ablation that is not driven by the 554 nm nor the 493 nm lasers, indicating that they are not barium atoms/ions. In these experiments, ablation pulses of pulse fluence $3.84\,\mathrm{J/cm^2}$ are sent to ablate the low-volume target. An imaging system collects light from the trap center. The collected light is detected using a PMT. The PMT is set to detect photons for a time window of 1 µs, starting at different times relative to the arrival time of the ablation pulse to do time-resolved light detection. Different spectral filters are installed in the imaging system to investigate the origin of the detected light. The trap voltages are turned off to allow both charged and uncharged particles to go through the trap.

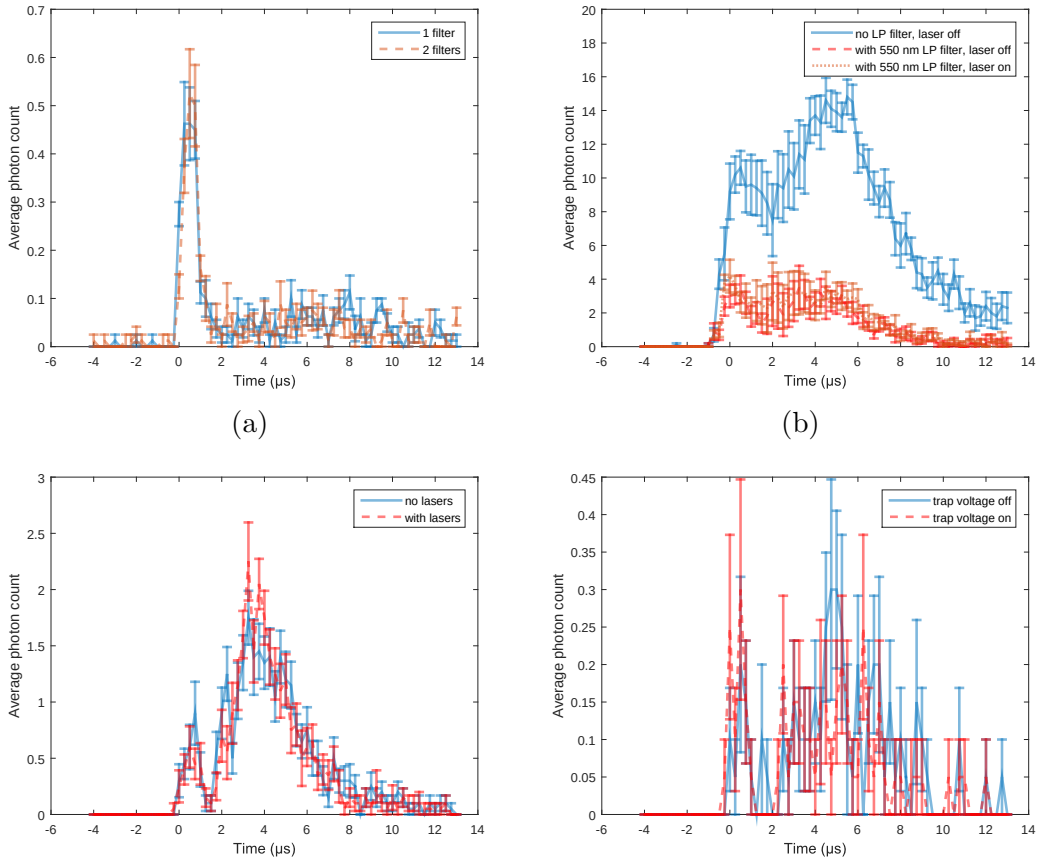

Figure E.4: Time-resolved light detection after ablating the low-volume target with a pulse fluence of 3.84 J/cm^2. (a) Comparison of signals between having 1 and 2 532 nm notch filter in the imaging system. No qualitatively significant difference is found. (b) Comparison of signals between having and not having a 550 nm longpass filter in the imaging system as well as with and without the 554 nm laser turned on. The signal is partially attenuated with the 550 nm longpass filter. No practical difference is observed with or without the 554 nm laser turned on. (c) Comparison of signals with and without the barium ion fluorescence lasers turned on. A 488 nm bandpass filter is installed in the imaging system. No qualitatively significant difference is found. (d) Comparision of signals with and without the trap voltages turned on. A 488 nm bandpass filter is installed in the imaging system. No qualitatively significant difference is found.

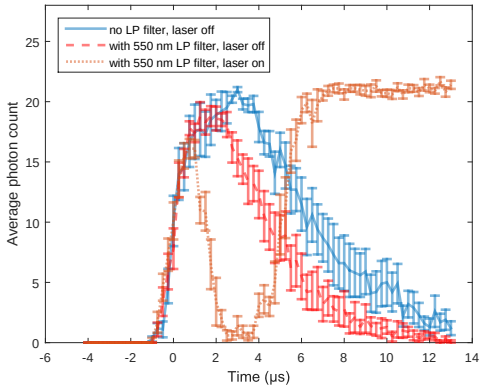

Figure E.5: Time-resolved light detection after ablating the high-volume target with a pulse fluence of 3.84 J/cm^2. Comparison of signals between having and not having a 550 nm longpass filter in the imaging system as well as with and without the 554 nm laser turned on. The signal is partially attenuated with the 550 nm longpass filter. With the 554 nm laser turned on, the early time signal is attenuated while the late time signal is enhanced.

We first observe that there is a photon count peak right after the ablation laser reaches the target, even when all the CW lasers are turned off. We verify that this peak is not 532 nm light by observing that the photon count does not change significantly whether there are 1 or 2 532 nm notch filters (Thorlabs NF533-17) in the imaging system. We also confirm that it is not residual 1064 nm light from the ablation laser by observing that the peak disappears when a 1000 nm longpass filter (Thorlabs FEL1000) is introduced into the imaging system. Our conjecture is that this could be due some up- or down-conversion of the high energy 532 nm pulse, shifting it from the 532 nm frequency and thus getting pass the 532 nm notch filter.

An interesting observation is that there are photon counts detected that last several tens of microseconds after the arrival of the ablation pulse when no CW lasers are turned on. All the experiments discussed from here on in this section are done with 532 nm notch filter to filter off light from the ablation laser. First, we observe that the signal is partially reduced upon the addition of a 550 nm longpass filter (Thorlabs FEL0550). To see if the fluorescence is from barium ions, the experiments are repeated with and without the 493 nm and 650 nm turned on. The imaging system is installed with a 488 nm narrow bandpass filter (Brightline FF01-488/10-25), which allows wavelengths in the range from 481 nm to 495 nm to pass through. It is observed that the signals are not qualitatively different with or without the lasers turned on, indicating that they are likely not barium ions. To further verify if they are ions, the experiments are repeated with and without the trap voltages

being turned on. The same 488 nm narrow bandpass filter is installed and the CW lasers are turned off. No significant qualitative difference in the signals observed is found, whether the trap voltages are turned on or not. This indicates that the fluorescing particles are uncharged. We thus conclude that they are uncharged particles in some excited states, releasing photons as they pass through the trap.

We also repeated the time-resolved experiments on the high-volume target. Three sets of experiments are done, with the following combinations: without 550 nm longpass filter and without 554 nm laser, with 550 nm longpass filter and without 554 nm laser, and with 550 nm longpass filter and with 554 nm laser. Similar to the low-volume target, the signal observed is partially reduced with the 550 nm longpass filter on, without the 554 nm laser. With the 554 nm laser turned on, the signals at earlier times (before 6 µs) are reduced and the signals at later times (after 6 µs) are increased. Our conjecture is that the signals at earlier times are from excited state species. With the 554 nm laser turned on, they are further excited or ionized, leading to them fluorescing at a lower wavelength below 550 nm, or are in an ionic ground state. In both cases, the signal at the PMT would be reduced. The increased signal at later times are most likely coming from neutral barium ions. We also find that it is not advisable to ablate the high-volume target at this high pulse fluence of 3.84 J/cm^2, as it left a visible char mark after these sets of experiments. This is also the reason why no further time-resolved light detection experiments at this pulse fluence is done on the high-volume target.

Appendix F

Evolution of $^{137}Ba^{+}$ Ion $5D_{5/2}$ Level Energy Eigenstates with Magnetic Field Strengths

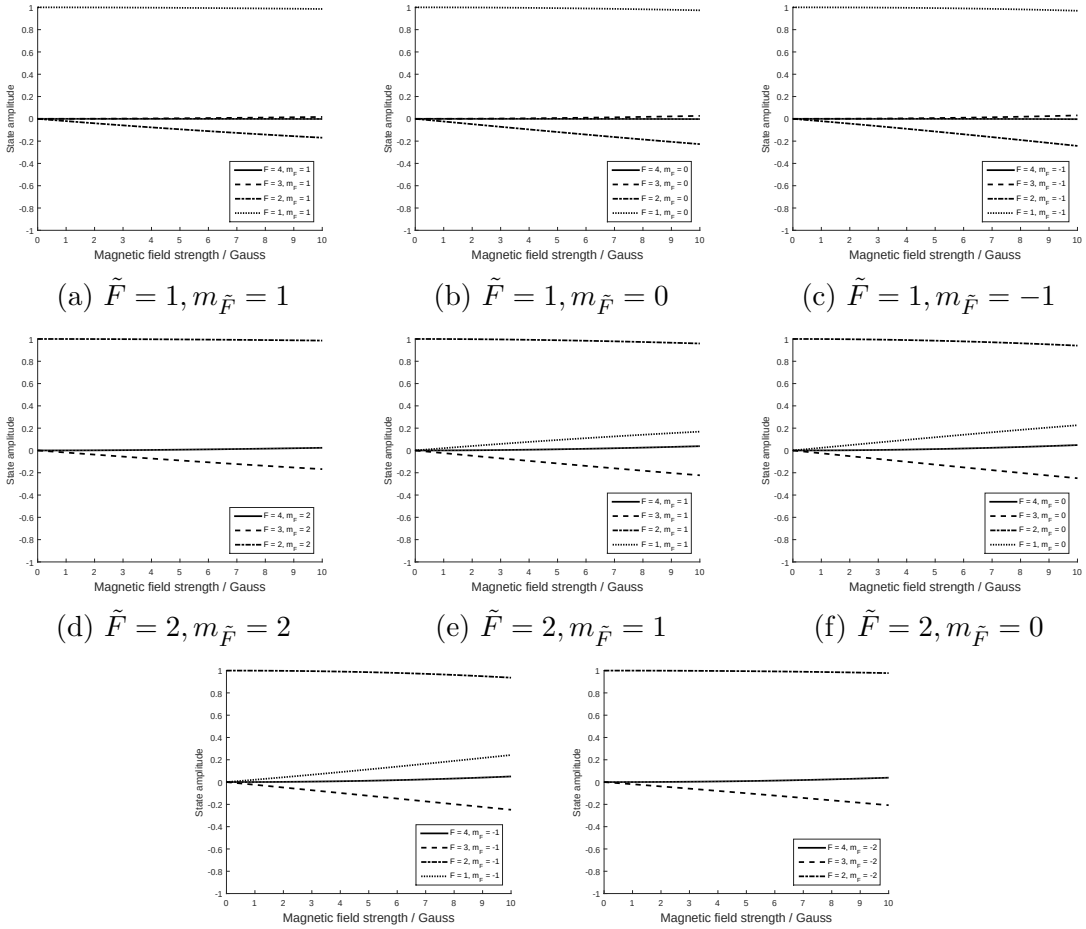

(a) $\tilde{F} = 1, m_{\tilde{F}} = 1$ (b) $\tilde{F} = 1, m_{\tilde{F}} = 0$ (c) $\tilde{F} = 1, m_{\tilde{F}} = -1$

(d) $\tilde{F} = 2, m_{\tilde{F}} = 2$ (e) $\tilde{F} = 2, m_{\tilde{F}} = 1$ (f) $\tilde{F} = 2, m_{\tilde{F}} = 0$

(g) $\tilde{F} = 2, m_{\tilde{F}} = -1$ (h) $\tilde{F} = 2, m_{\tilde{F}} = -2$

Figure F.1: Numerical estimations of the $^{137}\mathrm{Ba}^{+}$ $\tilde{F} = 1$ and $\tilde{F} = 2$ energy eigenstates in the $5D_{5/2}$ level, expressed in the $|F, m_F\rangle$ basis.

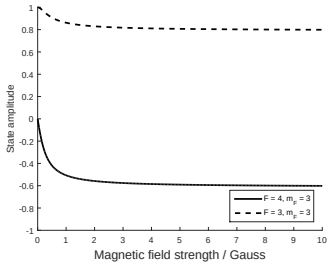

(a) $\tilde{F} = 3, m_{\tilde{F}} = 3$

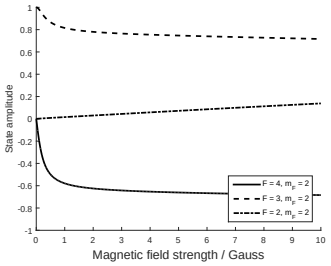

(b) $\tilde{F} = 3, m_{\tilde{F}} = 2$

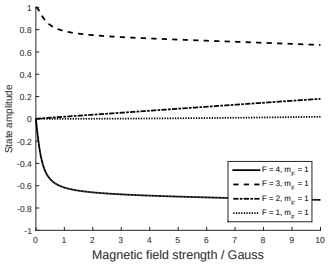

(c) $\tilde{F} = 3, m_{\tilde{F}} = 1$

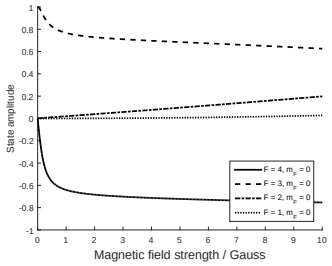

(d) $\tilde{F} = 3, m_{\tilde{F}} = 0$

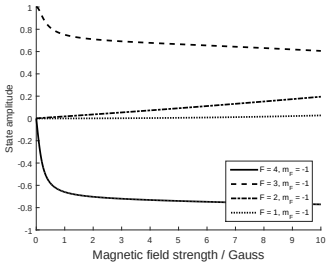

(e) $\tilde{F} = 3, m_{\tilde{F}} = -1$

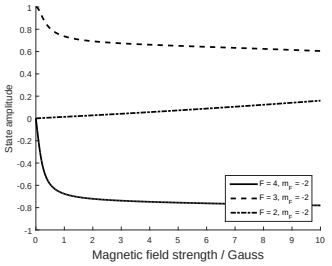

(f) $\tilde{F} = 3, m_{\tilde{F}} = -2$

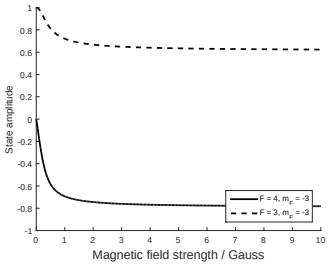

(g) $\tilde{F} = 3, m_{\tilde{F}} = -3$

Figure F.2: Numerical estimations of the $^{137}\mathrm{Ba}^{+}$ $\tilde{F} = 3$ energy eigenstates in the $5D_{5/2}$ level, expressed in the $|F, m_F\rangle$ basis.

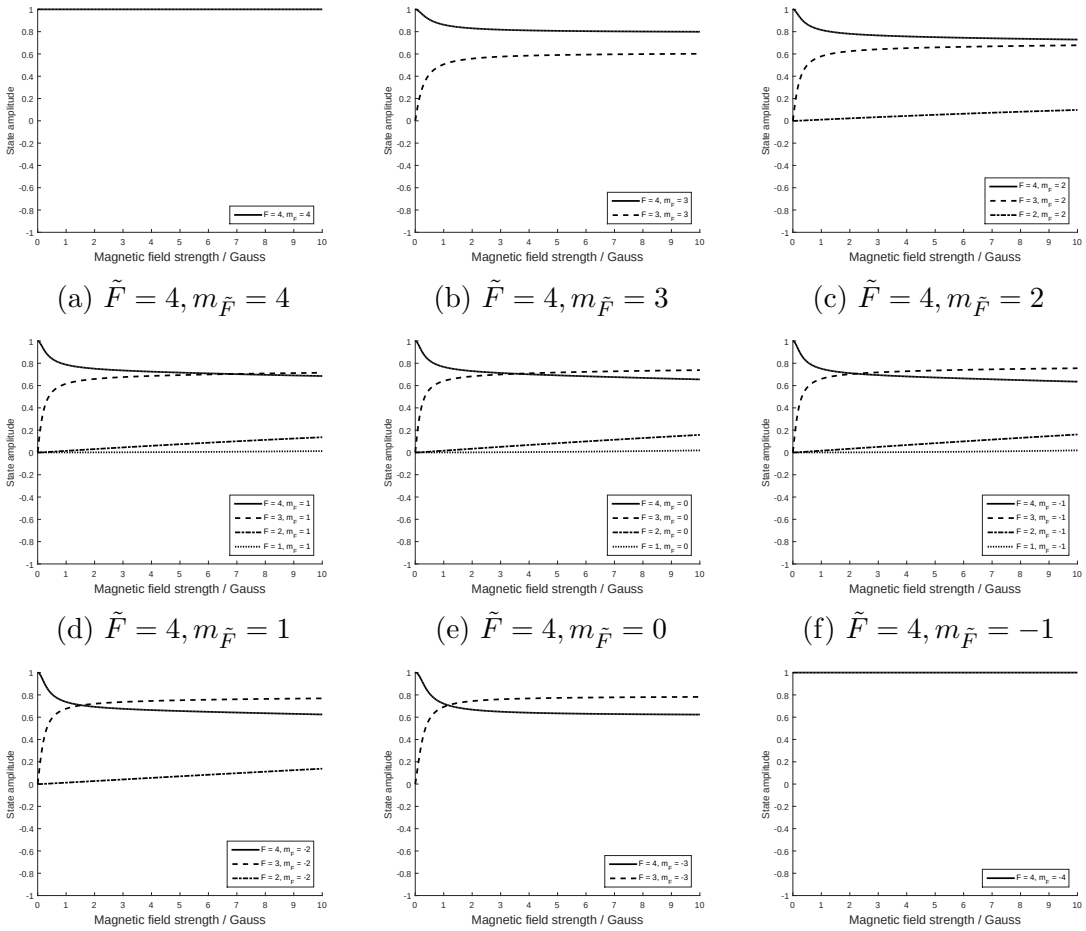

(a) $\tilde{F} = 4, m_{\tilde{F}} = 4$ (b) $\tilde{F} = 4, m_{\tilde{F}} = 3$ (c) $\tilde{F} = 4, m_{\tilde{F}} = 2$

(d) $\tilde{F} = 4, m_{\tilde{F}} = 1$ (e) $\tilde{F} = 4, m_{\tilde{F}} = 0$ (f) $\tilde{F} = 4, m_{\tilde{F}} = -1$

(g) $\tilde{F} = 4, m_{\tilde{F}} = -2$ (h) $\tilde{F} = 4, m_{\tilde{F}} = -3$ (i) $\tilde{F} = 4, m_{\tilde{F}} = -4$

Figure F.3: Numerical estimations of the $^{137}Ba^{+}$ $\tilde{F} = 4$ energy eigenstates in the $5D_{5/2}$ level, expressed in the $|F, m_F\rangle$ basis.

Appendix G

Four-Level Simulations for Studying Fluorescence Flip-Flopping

The same optical Bloch equations construction approach in Section 3.3 was used to study the bright/dark state flip-flopping of a Ba^+ ion when the 493 nm, 650 nm and 1762 nm laser frequencies are turned on. On top of the three levels in Section 3.3.1, another D level is added, simulating the $5D_{5/2}$ state. A Rabi frequency between the S and this new D state drives the transition and this D state is set to decay to the S state with a long decay rate of $0.0286\,\mathrm{s}^{-1}$. The simulated 493 nm and 650 nm Rabi frequencies are set to $2\pi \times 10\,\mathrm{MHz}$ and the 1762 nm Rabi frequency set to $2\pi \times 0.1\,\mathrm{MHz}$.

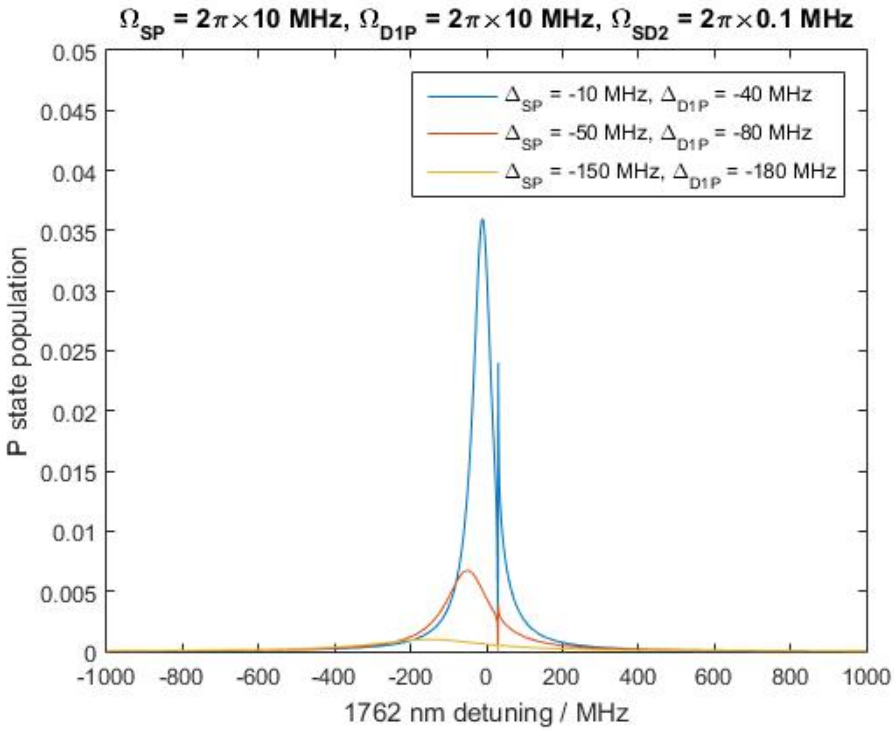

Figure G.1: P state population against the simulated 1762 nm laser detuning in a 4-level toy model.

From Fig. G.1, the average P state population is heavily suppressed when the 1762 nm laser is turned on, when the 1762 nm laser frequency is detuned from resonance. The P state population does not recover at farther detuning of the 1762 nm laser frequency, until machine error is reached. Since this does not fully capture what is observed empirically, I cannot draw any useful conclusions. Using optical Bloch equations to study this phenomenon may be flawed to begin with as we are approximating a steady state dynamics when we do this, which is not what is happening empirically in the time scale of seconds or milliseconds. Perhaps integrating the ion fluorescence over a period much longer then the $D_{5/2}$ decay time at different 1762 nm frequencies may shed more insights to the issue, but it is yet to be seen.

Appendix H

A Dynamic Method for Determining Bright/Dark State Photon Count Threshold

Since Ba^+ ion fluorescence rate is sensitive to both laser intensities and frequencies, it can easily fluctuate with parameter drifts. Therefore, we adopt a method for determining the threshold for differentiating bright/dark states dynamically for the data set that is collected in an experiment, without a need for prior calibrations. The procedure is as follows:

1. Sort the photon count readings in ascending order.
2. Sample the sorted photon count readings in steps of one one-thousandth of the total number of collected photon counts, totalling about one thousand sampled data points.
3. From the sampled data points, compute the difference in photon count of each data point to the next data point.
4. The point where the difference in photon count is the largest is picked out, and the average between these two points are computed and set as the threshold.

The data sampling that is done in Step 2 is necessary for large data sets, where the rarer photon counts (of either bright or dark states) that fall farther along the random distribution probability tails may have manifested, and bridge the gap between the bright and dark states photon count distributions. This would obscure the point where a sudden increase in photon counts is detected in Step 3. As long as the ratio of the bright and dark

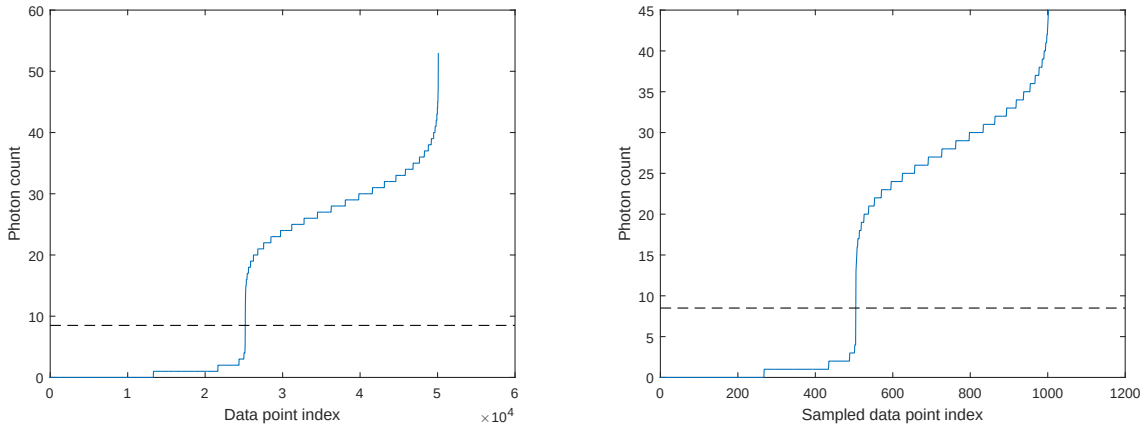

(a) (b)

Figure H.1: (a) Sorted photon count data points of a Rabi cycling experiment. (b) Sampled data points of (a), as described in Step 2 of the procedure. Dashed line marks the computed photon count threshold.

states of the data collected in the experiment is not larger than 1000:1, at least one bright and one dark state will be sampled in Step 2.

Appendix I

6-Level Qudit SPAM with $^{138}Ba^{+}$

The SPAM protocol as discussed in Chapter 4 can be directly applied to $^{138}Ba^{+}$. The encoding scheme and a 6-level qudit SPAM results are summarized in Fig. I.1.

• 6-level qudit results:

Raw

Prepared state	Measured state						Relative B field sensitivity / MHz G^{-1}
	$\|0\rangle$	$\|1\rangle$	$\|2\rangle$	$\|3\rangle$	$\|4\rangle$	$\|5\rangle$	
$\|0\rangle$	100%	0.00%	0.00%	0.00%	0.00%	0.00%	0.00
$\|1\rangle$	6.71%	87.89%	0.00%	0.00%	0.00%	0.00%	-3.92
$\|2\rangle$	3.10%	0.0%	94.99%	0.00%	0.00%	0.00%	-2.24
$\|3\rangle$	2.00%	0.00%	0.00%	97.50%	0.00%	0.00%	-0.56
$\|4\rangle$	3.50%	0.00%	0.10%	0.10%	94.59%	0.0%	1.12
$\|5\rangle$	5.41%	0.00%	0.00%	0.00%	0.00%	90.79%	2.80

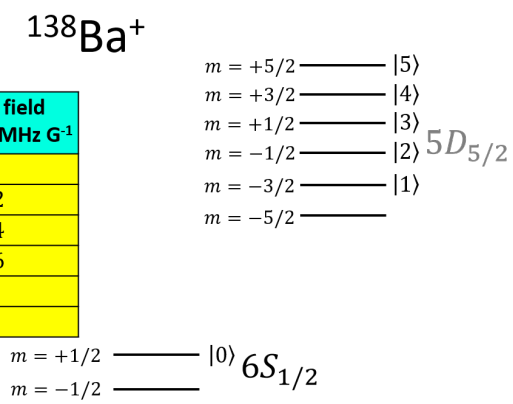

(a)

• 6-level qudit results:

Post-selected

Prepared state	Measured state						Relative B field sensitivity / MHz G^{-1}
	$\|0\rangle$	$\|1\rangle$	$\|2\rangle$	$\|3\rangle$	$\|4\rangle$	$\|5\rangle$	
$\|0\rangle$	100%	0.00%	0.00%	0.00%	0.00%	0.00%	0.00
$\|1\rangle$	7.09%	92.91%	0.00%	0.00%	0.00%	0.00%	-3.92
$\|2\rangle$	3.16%	0.0%	96.84%	0.00%	0.00%	0.00%	-2.24
$\|3\rangle$	2.01%	0.00%	0.00%	97.99%	0.00%	0.00%	-0.56
$\|4\rangle$	3.56%	0.00%	0.10%	0.10%	96.23%	0.0%	1.12
$\|5\rangle$	5.62%	0.00%	0.00%	0.00%	0.00%	94.38%	2.80

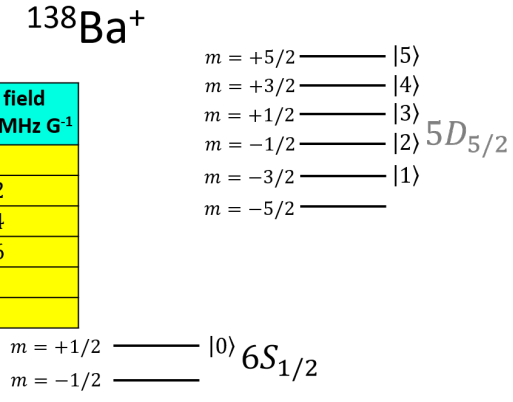

(b)

Figure I.1: 6-level qudit SPAM results. (a) The raw fidelities. (b) Post selected fidelities.

Appendix J

Alternative Interpretation of SPAM Error

In the SPAM experiment performed in Chapter 4, during the measurement process, after checking for fluorescence of the $|0\rangle$ state, each encoded state in the $5D_{5/2}$ level, $|n\rangle$, is de-shelved by sending a π-pulse corresponding to the $|6S_{1/2}, \tilde{F} = 2, m_{\tilde{F}} = 2\rangle \leftrightarrow |n\rangle$ transition. During the de-shelving π-pulse transition, what is effectively performed on the ion is a re-shelving process that is happening simultaneously with the de-shelving process. Thus, there is an alternative method to interpret the measurement fidelity that we initially employed, that turns out to be less robust to ultimately what is used in the main text. In Chapter 4, the measured state is set to be the first instance the ion is bright during the measurement sequence, and disregarding whether the ion is bright or dark for the rest of the sequence in the measurement process. The alternative interpretation treats the cases where the ion is still detected to be bright after the first to be failures of the measurement process, as the ion is supposed to be re-shelved after the first bright event and no other bright events are supposed to be detected. This places an unnecessarily stricter condition, but has the benefit of not having to know the de-shelving sequence to interpret the measured state. Table J.1 summarizes the SPAM fidelity for each prepared state with the same data set presented in the main text, but with the alternative interpretation of a successful measurement event as presented in this section. The overall fidelity is lower than the interpretation used in the main text, as expected. Table J.2 is the post-selected fidelity of Table J.1. Qualitatively, the post-selected fidelities do not differ from the interpretation employed in the main text.

Prepared state	Measured state													
	$\|0\rangle$	$\|1\rangle$	$\|2\rangle$	$\|3\rangle$	$\|4\rangle$	$\|5\rangle$	$\|6\rangle$	$\|7\rangle$	$\|8\rangle$	$\|9\rangle$	$\|10\rangle$	$\|11\rangle$	$\|12\rangle$	Null
$\|0\rangle$	0.951	0	0	0	0	0	0	0	0	0	0	0	0	0.049
$\|1\rangle$	0.059	0.787	0	0	0	0	0	0	0	0	0	0	0	0.154
$\|2\rangle$	0.042	0.002	0.922	0	0	0	0.001	0	0	0	0.001	0	0	0.032
$\|3\rangle$	0.025	0.001	0	0.916	0.001	0	0	0.001	0	0.002	0	0	0	0.054
$\|4\rangle$	0.031	0	0	0	0.852	0	0	0.001	0	0	0	0.001	0	0.115
$\|5\rangle$	0.103	0	0	0	0	0.585	0	0	0	0	0	0	0	0.312
$\|6\rangle$	0.220	0	0.001	0.002	0.002	0.002	0.537	0.001	0.002	0.001	0	0.001	0	0.231
$\|7\rangle$	0.057	0.001	0	0.001	0.001	0.001	0	0.861	0	0	0.001	0	0	0.077
$\|8\rangle$	0.040	0	0.002	0.002	0.001	0	0.003	0.002	0.803	0	0	0	0.001	0.146
$\|9\rangle$	0.147	0.004	0.008	0.003	0	0.003	0.003	0.004	0.005	0.645	0.005	0.004	0.001	0.168
$\|10\rangle$	0.027	0.001	0	0.002	0	0.002	0.002	0.003	0.001	0.002	0.870	0	0	0.090
$\|11\rangle$	0.029	0.003	0.003	0.001	0.002	0.001	0.001	0.001	0	0.003	0.004	0.867	0.001	0.084
$\|12\rangle$	0.030	0.001	0	0	0.001	0	0.001	0	0	0.001	0	0	0.938	0.028

Table J.1: Raw measurement probability of each prepared state from the SPAM data set in the main text, but with the alternative interpretation of a successful measurement. The sample size is 1000. Null indicates not only one bright fluorescence readout during the measurement procedure is obtained.

Prepared state	Measured state												
	$\|0\rangle$	$\|1\rangle$	$\|2\rangle$	$\|3\rangle$	$\|4\rangle$	$\|5\rangle$	$\|6\rangle$	$\|7\rangle$	$\|8\rangle$	$\|9\rangle$	$\|10\rangle$	$\|11\rangle$	$\|12\rangle$
$\|0\rangle$	1	0	0	0	0	0	0	0	0	0	0	0	0
$\|1\rangle$	0.070	0.930	0	0	0	0	0	0	0	0	0	0	0
$\|2\rangle$	0.043	0.002	0.952	0	0	0	0.001	0	0	0	0.001	0	0
$\|3\rangle$	0.026	0.001	0	0.968	0.001	0	0	0.001	0	0.002	0	0	0
$\|4\rangle$	0.035	0	0	0	0.963	0	0	0.001	0	0	0	0.001	0
$\|5\rangle$	0.150	0	0	0	0	0.850	0	0	0	0	0	0	0
$\|6\rangle$	0.286	0	0.001	0.003	0.003	0.003	0.698	0.001	0.003	0.001	0	0.001	0
$\|7\rangle$	0.062	0.001	0	0.001	0.001	0.001	0	0.933	0	0	0.001	0	0
$\|8\rangle$	0.047	0	0.002	0.002	0.001	0	0.004	0.002	0.940	0	0	0	0.001
$\|9\rangle$	0.177	0.005	0.010	0.004	0	0.004	0.004	0.005	0.006	0.775	0.006	0.005	0.001
$\|10\rangle$	0.030	0.001	0	0.002	0	0.002	0.002	0.003	0.001	0.002	0.956	0	0
$\|11\rangle$	0.032	0.003	0.003	0.001	0.002	0.001	0.001	0.001	0	0.003	0.004	0.947	0.001
$\|12\rangle$	0.031	0.001	0	0	0.001	0	0.001	0	0	0.001	0	0	0.965

Table J.2: Post-selected measurement probability of each prepared state from the SPAM data set in the main text, but with the alternative interpretation of a successful measurement.

Appendix K

Frequency Resolution Limitation from Finite AWG Memory

As discussed in Chapter 4, 13 waveforms are stored in the AWG memory for 13-level qudit SPAM experiments. The waveforms have to be periodic and all 13 of them have to share the same clock rate. Let f_R be the frequency resolution that we want to be able to be sent to the 1762 nm laser EOM, i.e. the frequency of the waveform, f_{WF}, that we want to generate is integer multiples of f_R,

$$f_{WF} = nf_R. \tag{K.1}$$

This translates to integer multiples of the waveform period having to match the resolution time period of $T_R = 1/f_R$ from Fourier analysis. To be able to generate the desired waveform with at most the number of sampling points within the resolution time period, integer multiples of the clock/sampling period has to make up $1/f_R$ as well

$$f_{CR} = mf_R, \tag{K.2}$$

where f_{CR} is the clock rate. From Eq. K.2, we immediately see that a better frequency resolution (and thus lower f_R) leads to a higher maximum number of sampling points m, which translates to requiring more digital memory. Thus, this puts a limit on our frequency resolution.

To make use of the limited memory as much as possible, there is a trick to choose some clock rate value that tends to minimize the memory used per waveform. For a waveform to be periodic at a specific clock rate, it has to satisfy

$$n_{WF}T_{WF} = n_{CR}T_{CR} \tag{K.3}$$

where T_{WF} is the period of the waveform, $n_{WF} \in \mathbb{Z}$ is the number of periods of the waveform, T_{CR} is the clock period, and $n_{CR} \in \mathbb{Z}$ is the number of clock periods, which is also the number of points on the waveform. Eq. K.3 can be rewritten as

$$n_{CR} f_{WF} = n_{WF} f_{CR}, \tag{K.4}$$

where $f_{CR} = 1/T_{CR}$ and $f_{WR} = 1/T_{CR}$. Substituting Eqs. K.1 and K.2 into K.4, we get

$$n_{CR} n = n_{WF} m. \tag{K.5}$$

Eq. K.5 can be immediately satisfied by choosing $n_{CR} = m$ and $n_{WF} = n$, which would be the maximum number of sampled points for a waveform. However, if n and m share some common factors, let it be $n = Z \times n'$ and $m = Z \times m'$, then we have

$$n_{CR} n' = n_{WF} m', \tag{K.6}$$

and the number of sampled points on a waveform is reduced by a factor of Z to $n_{CR} = m' = m/Z$. To maximize the probability of m and n sharing some common factors, the clock rate is set to be multiples of many prime numbers, which we chose to be $m = 2^7 \times 3 \times 5 \times 7 \times 11 \times 13 = 1921920$. At $f_R = 1\,\text{kHz}$, the clock rate is $f_{CR} = 1.921\,92\,\text{GHz}$. We find that we are typically unable to save 13 waveforms at 1 kHz resolution onto the AWG without this trick.

Appendix L

Filter Function Construction for Magnetic Field Noise

Consider a total Hamiltonian, $\hat{H}$, comprising the gate Hamiltonian, $\hat{H}_G$, and an error Hamiltonian, , $\hat{H}_e$.

$$\hat{H} = \hat{H}_G + \hat{H}_e \tag{L.1}$$

The error Hamiltonian for a two-level system in general can be modelled as

$$\hat{H}_e = \beta_x(t)\,\hat{\sigma}_x + \beta_y(t)\,\hat{\sigma}_y + \beta_z(t)\,\hat{\sigma}_z. \tag{L.2}$$

The effect of magnetic field noise on two magnetically sensitive atomic energy levels is shifting their relative energy levels, thus contributing to the $\hat{\sigma}_z$ component. The other $\hat{\sigma}_x$ and $\hat{\sigma}_y$ components come from fluctuations in the transition Rabi frequency, which can come from laser intensity noise. We will only consider effects from magnetic field noise here, i.e. $\hat{H}_e(t) = \beta_z(t)\,\hat{\sigma}_z$. The derivations of the general form can be found in Ref. [76].

Going to the interaction picture with respect to $\hat{H}_G$ gives the interaction Hamiltonian

$$\begin{aligned}\hat{H}_I(t) &= \hat{U}_G^{\dagger}(t)\,\hat{H}_e(t)\,\hat{U}_G(t)\\ &= \beta_z(t)\,\hat{U}_G^{\dagger}(t)\,\hat{\sigma}_z\hat{U}_G(t)\end{aligned} \tag{L.3}$$

where $\hat{U}_G(t)$ is the time-evolution operator from the gate Hamiltonian. For a time-independent $\hat{H}_G$, $\hat{U}_G(t) = \exp -i\frac{\hat{H}_G}{\hbar}t$. Defining $\hat{U}_I(t)$ to be the time-evolution operator of $\hat{H}_I(t)$, i.e. $i\hbar\frac{d}{dt}\hat{U}_I(t) = \hat{H}_I(t)\,\hat{U}_I(t)$, the average fidelity of the gate operation with respect to a state in the interaction picture, $|\psi_I\rangle$, is then

$$\mathcal{F} = \langle|\langle\psi_I|\hat{U}_I(t)\,|\psi_I\rangle|^2\rangle, \tag{L.4}$$

where $\langle\cdot\rangle$ denotes ensemble averaging. We evaluate an approximate form of $\hat{U}_I(t)$, assuming that the noise level is small. The functional form of $\hat{U}_I(t)$ from first order approximation of the Magnus expansion is

$$\hat{U}_I(t) \approx \exp\left(-i\int_0^t \frac{\hat{H}_I(t')}{\hbar}dt'\right). \tag{L.5}$$

It is now useful to decompose the $\int_0^t \frac{\hat{H}_I(t')}{\hbar}dt'$ factor in Eq. L.5 to the identity and Pauli operator components

$$\begin{aligned}\int_0^t \frac{\hat{H}_I(t')}{\hbar}dt' &= \frac{1}{\hbar}\int_0^t \beta(t')\,\hat{U}_G^\dagger(t')\,\hat{\sigma}_z\hat{U}_G(t')\,dt' \\ &= a_I(t)\hat{I} + a_x(t)\hat{\sigma}_x + a_y(t)\hat{\sigma}_y + a_z(t)\hat{\sigma}_z,\end{aligned} \tag{L.6}$$

where $a_j(t) = \int_0^t \frac{1}{2}\beta(t')\,\mathrm{Tr}\left(\hat{U}_G^\dagger(t')\,\hat{\sigma}_z\hat{U}_G(t')\,\hat{\sigma}_j\right)dt'$, $j \in \{x,y,z\}$, and $a_I = \int_0^t \frac{1}{2}\beta(t')\,\mathrm{Tr}\left(\hat{U}_G^\dagger(t')\,\hat{\sigma}_z\hat{U}_G(t')\right)dt'$. It is immediately clear that $a_I(t) = 0$ as $\mathrm{Tr}(\hat{\sigma}_z) = 0$ and $\hat{U}_G^\dagger(t)\,\hat{\sigma}_z(t)\,\hat{U}_G(t)$ is just a rotation of $\hat{\sigma}_z$. Eq. L.6 can be further simplified to

$$\int_0^t \frac{\hat{H}_I(t')}{\hbar}dt' = a(t)\,\hat{\sigma}_n, \tag{L.7}$$

where $a(t) = \sqrt{a_x^2(t) + a_y^2(t) + a_z^2(t)}$ and $\hat{\sigma}_n = \frac{a_x(t)}{a(t)}\hat{\sigma}_x + \frac{a_y(t)}{a(t)}\hat{\sigma}_y + \frac{a_z(t)}{a(t)}\hat{\sigma}_z$. It can be straightforwardly verified that $\hat{\sigma}_n^2 = \hat{I}$. Thus, Eq. L.5 can be decomposed to

$$\begin{aligned}\hat{U}_I(t) &\approx \exp\left(-i\int_0^t \frac{\hat{H}_I(t')}{\hbar}dt'\right) \\ &= \exp\left(-ia(t)\,\hat{\sigma}_n\right) \\ &= \cos(a(t))\hat{I} + i\sin(a(t))\hat{\sigma}_n.\end{aligned} \tag{L.8}$$

The gate fidelity from Eq. L.4 can then be evaluated to be

$$\mathcal{F} = \langle\cos^2(a(t))\rangle + \langle\sin^2(a(t))\rangle|\langle\psi_I|\hat{\sigma}_n|\psi_I\rangle|^2. \tag{L.9}$$

Technically, the empirical fidelity would depend on the initial state $|\psi_I\rangle$ from the term $\langle\psi_I|\hat{\sigma}_n|\psi_I\rangle$. For a lower limit estimate of the fidelity, we assume $\langle\psi_I|\hat{\sigma}_n|\psi_I\rangle = 0$, which gives

$$\begin{aligned}\mathcal{F} &= \langle\cos^2(a(t))\rangle \\ &= \frac{1}{2}(1 + \cos(2a(t)))\end{aligned} \tag{L.10}$$

For small noise error, i.e. $a(t) \ll 1$, we have

$$\mathcal{F} \approx 1 - \langle a^2(t) \rangle. \tag{L.11}$$

This gives $\varepsilon = \langle a^2(t) \rangle$ as the estimated average gate error. Evaluating $\langle a^2(t) \rangle$ gives

$$\begin{aligned} \langle a^2(t) \rangle &= \langle a_x^2(t) \rangle + \langle a_y^2(t) \rangle + \langle a_z^2(t) \rangle \\ &= \sum_j \int_{t_1=0}^{t} \int_{t_2=0}^{t} \langle \beta(t_1) \beta^*(t_2) \rangle R_{zj}(t_1) R_{zj}^*(t_2) \, dt_1 dt_2, \end{aligned} \tag{L.12}$$

where $R_{zj}(t) = \frac{1}{2}\mathrm{Tr}\left(\hat{U}_G^\dagger(t) \hat{\sigma}_z \hat{U}_G(t) \hat{\sigma}_j\right)$, and $j \in \{x, y, z\}$. Using Wiener-Khinchin theorem, the factor $\langle \beta(t_1) \beta^*(t_2) \rangle$ can be expressed as

$$\langle \beta(t_1) \beta^*(t_2) \rangle = \frac{1}{2\pi} \int_{\infty}^{\infty} S(\omega) \, e^{i\omega(t_1 - t_2)} d\omega. \tag{L.13}$$

Eqs. L.12 and L.13 give

$$\begin{aligned} \langle a^2(t) \rangle &= \sum_j \frac{1}{2\pi} \int_{-\infty}^{\infty} \frac{1}{\omega^2} S(\omega) \left(-i\omega \int_{t_1=0}^{t} \rangle R_{zj}(t_1) \, e^{i\omega t_1} dt_1 \right) \left(i\omega \int_{t_2=0}^{t} \rangle R_{zj}^*(t_2) \, e^{-i\omega t_2} dt_2 \right) d\omega \\ &= \sum_j \frac{1}{2\pi} \int_{-\infty}^{\infty} \frac{1}{\omega^2} S(\omega) \, \tilde{R}_{zj}(\omega) \, \tilde{R}_{zj}^*(\omega) \, d\omega \\ &= \frac{1}{2\pi} \int_{-\infty}^{\infty} \frac{1}{\omega^2} S(\omega) \, F_{zz}(\omega) \, d\omega, \end{aligned} \tag{L.14}$$

where we have defined $\tilde{R}_{zj}(\omega) = -i\omega \int_0^t \rangle R_{zj}(t') \, e^{i\omega t'} dt'$ following the convention in Ref. [76] and $F_{zz} = \sum_j |\tilde{R}_{zj}(\omega)|^2$.

To evaluate the filter function $F_{zz}(\omega)$, we need to evaluate $\tilde{R}_{zx}(\omega)$, $\tilde{R}_{zy}(\omega)$, and $\tilde{R}_{zz}(\omega)$. Let the gate Hamiltonian be a simple 2-level transition Hamiltonian with and arbitrary phase angle

$$\hat{H}_G = \frac{\Omega}{2} \hat{\sigma}_\phi, \tag{L.15}$$

where $\hat{\sigma}_\phi = \cos(\phi) \, \hat{\sigma}_x + \sin(\phi) \, \hat{\sigma}_y$. This gives

$$\hat{U}_G^\dagger(t) = \left(\cos\left(\frac{\Omega}{2} t\right) \hat{I} + i \sin\left(\frac{\Omega}{2} t\right) (\cos(\phi) \, \hat{\sigma}_x + \sin(\phi) \, \hat{\sigma_y}) \right) \tag{L.16}$$

To evaluate $\tilde{R}_{zj}(\omega)$, we need to first evaluate $R_{zj}(t)$. To do that we use the following useful identities:

1. The trace of any of the Pauli operators is zero, i.e. $Tr\left[\hat{\sigma}_i\right] = 0$.
2. $\hat{\sigma}_i\hat{\sigma}_i = \hat{I}$.
3. $\hat{\sigma}_a\hat{\sigma}_b = i\epsilon_{abc}\hat{\sigma}_c$, where ϵ_{abc} is the Levi-Civita symbol.

With these identities, $R_{zx}(t)$ can be evaluated to be

$$\begin{aligned} R_{zx}(t) &= \frac{1}{2}\mathrm{Tr}\left[\left(\cos\left(\frac{\Omega}{2}t\right)\hat{I} + i\sin\left(\frac{\Omega}{2}t\right)\left(\cos(\phi)\,\hat{\sigma}_x + \sin(\phi)\,\hat{\sigma_y}\right)\right)\hat{\sigma}_z \right. \\ &\quad \left.\left(\cos\left(\frac{\Omega}{2}t\right)\hat{I} - i\sin\left(\frac{\Omega}{2}t\right)\left(\cos(\phi)\,\hat{\sigma}_x + \sin(\phi)\,\hat{\sigma_y}\right)\right)\hat{\sigma}_x\right] \\ &= -\frac{1}{2}\mathrm{Tr}\left[\left(2\sin\left(\frac{\Omega}{2}t\right)\cos\left(\frac{\Omega}{2}t\right)\sin(\phi)\right)\hat{I}\right] \\ &= -2\sin\left(\frac{\Omega}{2}t\right)\cos\left(\frac{\Omega}{2}t\right)\sin(\phi) \\ &= -\sin(\Omega t)\sin(\phi) \end{aligned} \tag{L.17}$$

Evaluating the frequency-domain form gives

$$\begin{aligned} \tilde{R}_{zx}(\omega) &= -i\omega\int_0^t R_{xz}(t')\,e^{i\omega t'}dt' \\ &= i\omega\sin(\phi)\int_0^t \sin(\Omega t')\,e^{i\omega t'}dt' \end{aligned} \tag{L.18}$$

Using

$$\begin{aligned} \int_0^t \sin(\Omega t')\,e^{i\omega t'}dt' &= \frac{1}{2i}\int_0^t\left(e^{i\Omega t'} - e^{-i\Omega t'}\right)e^{i\omega t'}dt' \\ &= \frac{1}{2}\left[\frac{1}{\omega+\Omega}\left(1 - e^{i(\omega+\Omega)t}\right) - \frac{1}{\omega-\Omega}\left(1 - e^{i(\omega-\Omega)t}\right)\right] \\ &= -\frac{i}{\omega^2-\Omega^2}\left[i\Omega e^{i\omega t}\cos(\Omega t) + \omega e^{i\omega t}\sin(\Omega t) - i\Omega\right] \\ &= -\frac{i}{\omega^2-\Omega^2}B(\omega), \end{aligned} \tag{L.19}$$

where $B(\omega) = i\Omega e^{i\omega t}\cos(\Omega t) + \omega e^{i\omega t}\sin(\Omega t) - i\Omega$. Thus, $R_{zx}(\omega)$ simplifies to

$$\tilde{R}_{zx}(\omega) = \frac{\omega}{\omega^2-\Omega^2}\sin(\phi)\,B(\omega) \tag{L.20}$$

Similarly, for $R_{zy}(t)$, we have

$$\begin{aligned}
R_{zy}(t) &= \frac{1}{2}\mathrm{Tr}\left[\left(\cos\left(\frac{\Omega}{2}t\right)\hat{I} + i\sin\left(\frac{\Omega}{2}t\right)\left(\cos(\phi)\,\hat{\sigma}_x + \sin(\phi)\,\hat{\sigma_y}\right)\right)\hat{\sigma}_z\right. \\
&\quad \left.\left(\cos\left(\frac{\Omega}{2}t\right)\hat{I} - i\sin\left(\frac{\Omega}{2}t\right)\left(\cos(\phi)\,\hat{\sigma}_x + \sin(\phi)\,\hat{\sigma_y}\right)\right)\hat{\sigma}_y\right] \\
&= \frac{1}{2}\mathrm{Tr}\left[\left(2\sin\left(\frac{\Omega}{2}t\right)\cos\left(\frac{\Omega}{2}t\right)\cos(\phi)\right)\hat{I}\right] \\
&= 2\sin\left(\frac{\Omega}{2}t\right)\cos\left(\frac{\Omega}{2}t\right)\cos(\phi) \\
&= \sin(\Omega t)\sin(\phi)\,.
\end{aligned} \tag{L.21}$$

Evaluating the frequency domain form gives

$$\begin{aligned}
R_{zy}(\omega) &= -i\omega\int_0^t R_{zy}(t')\,e^{i\omega t'}dt' \\
&= -i\omega\cos(\phi)\int_0^t \sin(\Omega t')\,e^{i\omega t'}dt' \\
&== -\frac{\omega}{\omega^2-\Omega^2}\cos(\phi)\,B(\omega)\,.
\end{aligned} \tag{L.22}$$

For $R_{zz}(t)$, we have

$$\begin{aligned}
R_{zz}(t) &= \frac{1}{2}\mathrm{Tr}\left[\left(\cos\left(\frac{\Omega}{2}t\right)\hat{I} + i\sin\left(\frac{\Omega}{2}t\right)\left(\cos(\phi)\,\hat{\sigma}_x + \sin(\phi)\,\hat{\sigma_y}\right)\right)\hat{\sigma}_z\right. \\
&\quad \left.\left(\cos\left(\frac{\Omega}{2}t\right)\hat{I} - i\sin\left(\frac{\Omega}{2}t\right)\left(\cos(\phi)\,\hat{\sigma}_x + \sin(\phi)\,\hat{\sigma_y}\right)\right)\hat{\sigma}_z\right] \\
&= \frac{1}{2}\mathrm{Tr}\left[\left(\cos^2\left(\frac{\Omega}{2}t\right) - \sin^2(\phi)\sin^2\left(\frac{\Omega}{2}t\right) - \cos^2(\phi)\sin^2\left(\frac{\Omega}{2}t\right)\right)\hat{I}\right] \\
&= \frac{1}{2}\mathrm{Tr}\left[\left(\cos^2\left(\frac{\Omega}{2}t\right) - \sin^2\left(\frac{\Omega}{2}t\right)\right)\hat{I}\right] \\
&= \cos(\Omega t)
\end{aligned} \tag{L.23}$$

Using

$$\begin{aligned}\int_0^t \cos(\Omega t')\, e^{i\omega t'} dt' &= \frac{1}{2}\int_0^t \left(e^{i\Omega t'} + e^{-i\Omega t'}\right) e^{i\omega t'} dt' \\ &= \frac{1}{2}\int_0^t e^{i(\omega+\Omega)t'} + e^{i(\omega-\Omega)t'} dt' \\ &= \frac{i}{2(\omega+\Omega)}\left(1 - e^{i(\omega+\Omega)t}\right) + \frac{i}{2(\omega-\Omega)}\left(1 - e^{i(\omega-\Omega)t}\right) \\ &= \frac{i}{\omega^2-\Omega^2}\left[i\Omega e^{i\omega t}\sin(\Omega t) - \omega e^{i\omega t}\cos(\Omega t) + \omega\right] \\ &= \frac{i}{\omega^2-\Omega^2} V(\omega),\end{aligned} \tag{L.24}$$

where $V(\omega) = i\Omega e^{i\omega t}\sin(\Omega t) - \omega e^{i\omega t}\cos(\Omega t) + \omega$, we have

$$\tilde{R}_{zz}(\omega) = \frac{\omega}{\omega^2-\Omega^2} V(\omega) \tag{L.25}$$

The filter function $F_{zz}(\omega)$ can then be evaluated to be

$$\begin{aligned}F_{zz}(\omega) &= |R_{zx}(\omega)|^2 + |R_{zy}(\omega)|^2 + |R_{zz}(\omega)|^2 \\ &= \frac{\omega^2}{(\omega^2-\Omega^2)^2}\left(|B(\omega)|^2 + |V(\omega)|^2\right) \\ &= \frac{\omega^2}{(\omega^2-\Omega^2)^2}\left(2\omega^2 + 2\Omega^2 - 4\omega\Omega\sin(\omega t)\sin(\Omega t) - 2\left(\omega^2+\Omega^2\right)\cos(\omega t)\cos(\Omega t)\right)\end{aligned} \tag{L.26}$$

For a π-pulse gate, we have $t = \frac{\pi}{\Omega}$, which gives

$$F_{zz}(\omega) = \frac{\omega^2}{(\omega^2-\Omega^2)^2}\left(2\omega^2 + 2\Omega^2 + 2\left(\omega^2+\Omega^2\right)\cos\left(\frac{\omega}{\Omega}\pi\right)\right) \tag{L.27}$$

There are 2 asymptotic behaviour to Eq. L.27. When $\omega \ll \Omega$, $F_{zz}(\omega) \approx \frac{4}{\Omega^2}\omega^2$. When $\omega \gg \Omega$, $F_{zz}(\omega) \approx 2 + 2\cos\left(\frac{\omega}{\Omega}\pi\right)$. Thus, we approximate the filter function to be of a simple form

$$F(\omega) \approx \begin{cases} 4\frac{\omega^2}{\Omega^2}, & \omega < \Omega \\ 2, & \omega \geq \Omega \end{cases} \tag{L.28}$$

Eq. L.27 is also symmetric about $\omega = 0$, which allows us to rewrite Eq. L.14 as

$$\langle a^2(t)\rangle = \frac{1}{\pi}\int_0^\infty \frac{1}{\omega^2} S(\omega) F_{zz}(\omega)\, d\omega. \tag{L.29}$$